UNIVERSIDADE DE SÃO PAULO
ESCOLA DE ENGENHARIA DE SÃO CARLOS

Antonio Carlos Daud Filho

Estudo de uma configuração de VANT com giro de asa: modelagem, simulação, estimador de estados, controle, integração de sistemas e testes de voo

São Carlos

2023

Antonio Carlos Daud Filho

Estudo de uma configuração de VANT com giro de asa: modelagem, simulação, estimador de estados, controle, integração de sistemas e testes de voo

Tese apresentada à Escola de Engenharia de São Carlos da Universidade de São Paulo, para obtenção do título de Doutor em Ciências - Programa de Pós-Graduação em Engenharia Mecânica.

Área de concentração: Aeronaútica

Advisor: Prof. Dr. Eduardo Morgado Belo

São Carlos

2023

Ficha catalográfica elaborada pela Biblioteca Prof. Dr. Sérgio Rodrigues Fontes da EESC/USP com os dados inseridos pelo(a) autor(a).

Daud Filho, Antonio Carlos
D238e Estudo de uma configuração de VANT com giro de asa: modelagem, simulação, estimador de estados, controle, integração de sistemas e testes de voo / Antonio Carlos Daud Filho; orientador Eduardo Morgado Belo. São Carlos, 2022.

Tese (Doutorado) - Programa de Pós-Graduação em Engenharia Mecânica e Área de Concentração em Aeronáutica -- Escola de Engenharia de São Carlos da Universidade de São Paulo, 2022.

1. VTOL. 2. UAV. 3. Voo de transição. 4. Equações de movimento multi-corpos. 5. Simulação. 6. Filtro de Kalman. 7. Controle de voo. 8. Testes de voo. I. Título.

Eduardo Graziosi Silva - CRB - 8/8907

FOLHA DE JULGAMENTO

Candidato: Engenheiro **ANTONIO CARLOS DAUD FILHO.**

Título da tese: "Estudo de uma configuração de VANT com giro de asa: modelagem, simulação, estimador de estados, controle, integração de sistemas e testes de voo"

Data da defesa: 06/02/2023

Comissão Julgadora	**Resultado**
Prof. Titular **Eduardo Morgado Belo** **(Orientador)** (Escola de Engenharia de São Carlos/EESC-USP)	Aprovado
Prof. Titular **Glauco Augusto de Paula Caurin** (Escola de Engenharia de São Carlos/EESC-USP)	Aprovado
Prof. Dr. **Mauricio Andrés Varela Morales** (Instituto Tecnológico de Aeronáutica/ITA)	Aprovado
Prof. Dr. **Fred Nitzsche** (Carleton University/Canada)	Aprovado
Prof. Titular **Flávio José Silvestre** (Technische Universität Berlin/Alemanha)	Aprovado

Coordenador do Programa de Pós-Graduação em Engenharia Mecânica:

Prof. Associado **Adriano Almeida Gonçalves Siqueira**

Presidente da Comissão de Pós-Graduação:

Prof. Titular **Murilo Araujo Romero**

Dedico este trabalho aos meus pais e meu irmão pelo encorajamento, apoio, compreensão e paciência.

AGRADECIMENTOS

Agradeço aos meus pais e meu irmão por me incentivarem e darem a força para continuar com este trabalho de doutorado, e a não desistir mesmo com todas as dificuldades de todo esse processo.

Ao meu orientador Prof. Dr. Eduardo Morgado Belo pelo apoio, disposição, discussões, conselhos e sabedoria, me ajudando sempre que precisei.

Aos meus amigos da pós-graduação Carlos, Fer, Luis, Igor, Natanael, Felipe, Helô, pela amizade, apoio, pelos conselhos, sugestões e bons momentos que passamos juntos.

Aos funcionários da universidade Cláudio, Gi, Gallo, Ana, Rosana, Marlene, Osnan, João e Zé por terem me ensinado muita coisa e ajudado sempre que precisei.

Aos professores Ricardo, Glauco, Hernan, Bidinotto, Álvaro e Catalano pelo incentivo, conselhos, sugestões e disposição em me ajudar com o projeto.

Agradeço também a Escola de Engenharia de São Carlos da Universidade de São Paulo pelo espaço e equipamentos disponibilizados.

À Coordenação de Aperfeiçoamento de Pessoal de Nível Superior (CAPES) pela bolsa de estudos concedida. O presente trabalho foi realizado com apoio da Coordenação de Aperfeiçoamento de Pessoal de Nível Superior – Brasil (CAPES) – Código de Financiamento 001.

Por fim agradeço a todos que contribuíram para o desenvolvimento desse projeto.

The breath within my lungs was so exhausted
from climbing, I could not go on; in fact,
as soon as I had reached that stone, I sat.
"Now you must cast aside your laziness,"
my master said, "for he who rests on down
or under covers cannot come to fame;
and he who spends his life without renown
leaves such a vestige of himself on earth
as smoke bequeaths to air or foam to water.
Therefore, get up; defeat your breathlessness
with spirit that can win all battles if
the body's heaviness does not deter it.
A longer ladder still is to be climbed;
it's not enough to have left them behind;
if you have understood, now profit from it."
Then I arose and showed myself far better
equipped with breath than I had been before:
"Go on, for I am strong and confident."
Dante Alighieri, The Divine Comedy, Inferno - Canto XXIV (1320)

RESUMO

Daud Filho, A. C. **Estudo de uma configuração de VANT com giro de asa: modelagem, simulação, estimador de estados, controle, integração de sistemas e testes de voo**. 2023. 195p. Tese (Doutorado) - Escola de Engenharia de São Carlos, Universidade de São Paulo, São Carlos, 2023.

Esta tese apresenta a configuração de um veículo aéreo não tripulado (VTOL UAV) com decolagem e pouso vertical. Ele tem a capacidade de girar o canard e a asa junto com duas hélices acopladas. Além disso, há duas hélices dianteiras fixas apontando para cima. Um modelo de equações de movimento multi-corpos é derivado para este conceito de aeronave, o que é usado para calcular a trajetória de transição de voo da configuração de voo pairado para cruzeiro. Além disso, é descrito um algoritmo de controle de transição baseado em escalonamento de ganho, que estabiliza a aeronave enquanto ela acelera de voo pairado para cruzeiro, inclinando gradualmente a asa junto com as hélices, alternando sequencialmente entre os estados de equilíbrio. O algoritmo de controle de transição é simulado numericamente para o modelo conceitual da aeronave. Um protótipo de aeronave é projetado e construído. Algoritmos de estimadores de estados baseados no filtro de Kalman discreto são derivados para calcular os estados de voo da aeronave a partir das medições dos sensores embarcados. Algoritmos de controle são descritos para possíveis configurações de voo: configuração de voo pairado com controle de atitude, controle de atitude mais altitude, atitude mais altitude mais controle de posição, e controle de voo de transição. Os algoritmos foram escritos em linguagem de programação C e embarcados no protótipo em placa microcontroladora Arduino Due. Os testes de voo foram conduzidos com sucesso em ambiente interno e externo para a configuração de voo pairado, com os estados de voo sendo transmitidos e salvos em uma estação de solo, assim, os resultados dos testes de voo são apresentados e discutidos.

Palavras-chave: VTOL. UAV. Voo de transição. Equações de movimento multi-corpos. Simulação. Filtro de Kalman. Controle de voo. Testes de voo.

ABSTRACT

Daud Filho, A. C. **A Tilt-wing VTOL UAV configuration study: flight dynamics modeling, simulation, states estimation, control, systems integration and flight testing**. 2023. 195p. Thesis (Doctor) - Escola de Engenharia de São Carlos, Universidade de São Paulo, São Carlos, 2023.

This thesis presents a vertical take-off and landing unmanned aerial vehicle (VTOL UAV) configuration. It has the capacity to tilt the canard and wing along with two attached propellers. Additionally, there are two fixed front propellers pointing upwards. A multi-body equations of motion are derived for this concept of aircraft, which are used to compute the flight transition trajectory from hover to cruise configuration. Furthermore, a transition control algorithm based on gain scheduling is described, which stabilizes the aircraft while it accelerates from hover to cruise, gradually tilting the wing along with the propellers, sequentially switching between equilibrium states. The transition control algorithm is numerically simulated for the conceptual aircraft model. An aircraft prototype is designed and built. States estimation algorithms based on the discrete Kalman filter are derived in order to compute the aircraft flight states from the on-board sensors measurements. Controls algorithms are described for possible flight configurations: hovering configuration with attitude control, attitude plus altitude controls, attitude plus altitude plus position control, and transition flight control. The algorithms were written in C programming language, and embedded in the prototype on-board Arduino Due microcontroller board. Flight tests were successfully conducted in an indoor and outdoor environment for the hovering configuration, the flight states were transmitted and saved in a ground station, so the flight tests results are presented and discussed.

Keywords: VTOL. UAV. Transition flight. Multi-body equations of motion. Simulation. Kalman filter. Flight control. Flight testing.

LIST OF FIGURES

LIST OF TABLES

LIST OF ABBREVIATIONS AND ACRONYMS

ACK	Acknowledgment
CCW	Counterclockwise
CFD	Computational fluid dynamics
CPU	Central processing unit
CW	Clockwise
DC	Direct current
EKF	Extended Kalman filter
ESC	Electronic speed controller
GPS	Global positioning system
I2C	Inter-integrated circuit
IMU	Inertial measurement unit
I/O	Input / Output
IDE	Integrated Development Environment
KF	Kalman filter
LCD	Liquid crystal display
LED	Light-emitting diode
Lipo	Lithium polymer
LQR	Linear quadratic regulator
PID	Proportional integral derivative
PLA	Polylactic acid
PWM	Pulse width modulation
RPM	Revolutions per minute
SD	Secure digital
SPI	Serial peripheral interface

UAM	Urban air mobility
UART	Universal asynchronous receiver-transmitter
UAV	Unmanned aerial vehicle
UKF	Unscented Kalman filter
VTOL	Vertical take-off and landing

LIST OF SYMBOLS

A	Angular motion equation matrix coefficient
$\mathbf{a}$	Acceleration vector
a	Acceleration
B	Angular motion equation matrix coefficient
b	Aerodynamic surface span
C	Angular motion equation matrix coefficient
C_D	Aerodynamic drag coefficient
C_L	Aerodynamic lift coefficient
C_l	Aerodynamic rolling moment coefficient
C_m	Aerodynamic pitch moment coefficient
C_n	Aerodynamic yawing moment coefficient
C_P	Propeller power coefficient
C_Q	Propeller torque coefficient
C_T	Propeller thrust coefficient
C_Y	Aerodynamic side force coefficient
$\bar{c}$	Mean aerodynamic chord
c	Residual binary flag
$cov(x, y)_n$	Covariance between two data series of n measurements
D	Angular motion equation matrix coefficient, aerodynamic drag force, propeller diameter, Controller derivative output
$\mathbf{E}$	Angular motion equation vector coefficient
E	Energy
esc	Output signal to ESC
$\mathbf{F}$	Force vector, Angular motion equation vector coefficient

$\mathbf{f}$	Linear motion equation multi-body coefficient vector
f	Flattening of the planet
$\mathbf{g}$	Gravity acceleration vector
$\mathbf{H}$	Angular momentum vector
h	Altitude
$\tilde{I}$	Inertia tensor
I	Controller integral output
J	Jacobian matrix, propeller advance ratio
K	Aerodynamic surface-body interference factor, gain matrix, Kalman gain
k	Control conversion constant
k_P	Proportional gain
k_I	Integral gain
k_D	Derivative gain
k_1, k_2	Radio input conversion coefficients
L	Aerodynamic lift force
$\bar{L}$	Aerodynamic rolling moment
l	Fuselage length
M	Total mass, aerodynamic pitching moment
m	Part mass, magnetometer reading
N	Aerodynamic yawing moment
n	Propeller speed in revolutions per second, number of measurements
$\mathbf{p}$	Linear momentum vector
O	Origin of reference frame
P	Pivot point, propeller power, roll angular velocity, state uncertainty covariance, Controller proportional output
PID	Controller proportional-integral-derivative output

Q	Propeller torque, pitch angular velocity, process noise covariance matrix
R	Rotation matrix, yaw angular velocity, measurement noise covariance matrix, equatorial radius of the planet
$R_{filtered}$	Radio filtered signal
R_{input}	Radio input signal
R_M	Radius of curvature in the meridian
R_N	Radius of curvature in the prime vertical
$\tilde{R}$	Inertia tensor translation matrix
$\mathbf{r}$	Position vector
r	Residual
S	Main-body to wind axes rotation matrix, aerodynamic surface planform area
$\mathbf{T}$	Torque vector
T	Propeller thrust force, time
$Throttle$	Throttle input signal
t	Time
$\mathbf{U}$	Control vector
U	Control input, velocity in the x_B direction
$\mathbf{u}$	Control disturbance vector
V	Velocity in the y_B direction, projection of flight speed in the propeller axis of rotation
V_{aux}	Auxiliary battery voltage
V_L	Left battery voltage
V_R	Right battery voltage
V_T	Flight speed
$\mathbf{v}$	Velocity vector, measurement noise vector
W	Velocity in the z_B direction

$\mathbf{w}$	Process noise vector
$\mathbf{X}$	State vector
$\mathbf{x}$	State disturbance vector
$\hat{\mathbf{x}}$	State estimate vector
x	Position coordinate in the x direction, measurement
x'	Pitch moment reference coordinate in x direction
Y	Aerodynamic side force
y	Position coordinate in the y direction, measurement
$\mathbf{z}$	Measurement vector
z	Position coordinate in the z direction
z'	Pitch moment reference coordinate in z direction
α	Angle of attack
β	Sideslip angle
γ	Flight path angle
$\Delta Throttle$	Increment in Throttle
ΔV_T	Increment in flight speed at the wing due to canard wake
δ	Deflection or tilt angle
ϵ	Downwash angle, error
ε	Stability criterion function
θ	Pitch angle
λ	Propeller rotation direction (1 counterclockwise or -1 clockwise)
λ_{GPS}	longitude coordinate
μ_{GPS}	latitude coordinate
μ_n	Mean value of a time series of n measurements
ν	Data fusion coefficient
ρ	Air density

σ_n^2	Variance of a data series of n measurements.
τ	First order dynamic system time constant
ϕ	Roll angle
ψ	Yaw angle
Ω	Angular velocity cross product in matrix form
ω	Angular velocity vector
ω	Angular velocity

Subscripts

acc	Accelerometers
aR	Aileron right
aL	Aileron left
avg	Average
B	Main body reference frame
C	Canard
c	Canard
CB	Canard-body interference
E	Earth fixed inertial reference frame
e	Exposed aerodynamic surface, elevator, equilibrium condition
f	Flap
IMU	From IMU
i	Aerodynamic surface moving part index
j	Rotor moving part index
k	time step
LC	Left canard
LW	Left wing
lat	Lateral

$long$	Longitudinal
m	Pitching moment reference
mag	Magnetometer
max	Maximum
min	Minimum
p	Roll angular velocity
$pivot$	Wing or canard pivot point
$press$	From pressure sensor
$props$	Propellers
q	Pitch angular velocity
RC	Right canard
RW	Right wing
$R1, R2, R3, R4$	Rotor 1, 2, 3, 4
r	Rudder, yaw angular velocity
rel	Relative velocity or acceleration
sp	Setpoint
th	Threshold
VT	Vertical tail
W	Wing, wind axes reference frame
w	Wing
WB	Wing-body interference
x	measurement in the x direction
y	measurement in the y direction
z	measurement in the z direction

CONTENTS

1 INTRODUCTION

In recent years, UAV's (Unmanned Aerial Vehicles) have been used in several applications, such as: precision agriculture where drones operators can collect high quality photos from hundred meters height for automatic analysis of individual leaves on a corn plant, for instance, or operate like a sprayer at a very small elevation over a field (KULBACKI *et al.*, 2018; KURKUTE, 2018; MEIVEL *et al.*, 2016; MOGILI; DEEPAK, 2021), photogrammetric data acquisition and 3D mapping of sites and man-made structures (REMONDINO *et al.*, 2011; NEX; REMONDINO, 2014), monitoring of protected areas, remote environments and surveying wildlife (BARRETO *et al.*, 2021; BOLLARD *et al.*, 2022) and inspection of large infrastructures such as power transmission lines (LUQUE-VEGA *et al.*, 2014), oil and gas transmission pipe lines (NOORALISHAHI; LóPEZ; MALDAGUE, 2021), railways (FLAMMINI; PRAGLIOLA; SMARRA, 2016), roads and traffic monitoring (KHAN *et al.*, 2020), parcel delivery (BENARBIA; KYAMAKYA, 2021) and real time object detection and recognition (SONKAR *et al.*, 2022).

Moreover, in order to carry out the different applications, some configurations of UAV's are commonly used, in which the main categories are: fixed wing aircraft, single rotor helicopter, multicopter, and the configurations with vertical take-off and landing (VTOL) capabilities, such as: tail-sitter, lift plus cruise, tilt rotor and tilt wing.

Fixed wing aircraft, in Figure 1a: wings are permanently fixed to the aircraft airframe, so that, the force that sustains the vehicle flight is the wing aerodynamic lift, while the propulsion systems maintain the flight speed. This configuration is very efficient at cruise speed, however does not have the capacity to take-off and land vertically, therefore it requires runways, catapult, parachute or landing net in its operation.

Single rotor helicopter, in Figure 1b: the single rotor provides the vehicle lift, which has four control inputs with complex mechanisms (cyclic, collective, the anti-torque pedals and throttle), so that, one of the core issues in designing a fully autonomous UAV helicopter is to effectively design and implement sophisticated flight control laws (PENG *et al.*, 2009).

Multicopter, in Figure 1c: usually four rotors (quadcopter), but also six or eight rotors can be found (hexacopter, octocopters), sustain the vehicle in the air. Very agile and versatile design, however, does not have long autonomy or range as the fixed wing configuration.

Tail-sitter, in Figure 1d: during take-off and landing the vehicle must be at vertical orientation, while at cruise it must be at horizontal orientation. Therefore, it must perform a complex transition maneuver between the two orientations. The tail-sitter transition

maneuver is considerable more complex than tilt-rotors, since it is required that the complete UAV body tilt around one axis for achieving the transition maneuver, an ordered movement that carries the UAV from hover to cruise mode and vice versa (FLORES; OCA; FLORES, 2018).

Lift plus cruise, in Figure 1e: it is a combination of multicopter and fixed wing, so that, during take-off and landing maneuvers the vertical motors produce the lift required, while at cruise an additional motor produces the necessary horizontal flight speed and the wing sustain the vehicle. Its deficiency is that it only uses the vertical motors during take-off and landing, thus, it has to carry their weight and aerodynamic drag (BACCHINI *et al.*, 2021) for the remaining of cruise condition.

Tilt rotor, in Figure 1f: this configuration is also a combination of multicopter and fixed wing, however it does not have the additional horizontal flight propulsive system. It has tilting mechanism for the rotors only, so that during take-off and landing they are all pointing upwards, and during cruise are horizontally oriented.

Tilt wing, in Figure 1g: much like the tilt rotor, it has tilt mechanisms, but in this configuration the wing tilts along the rotors.

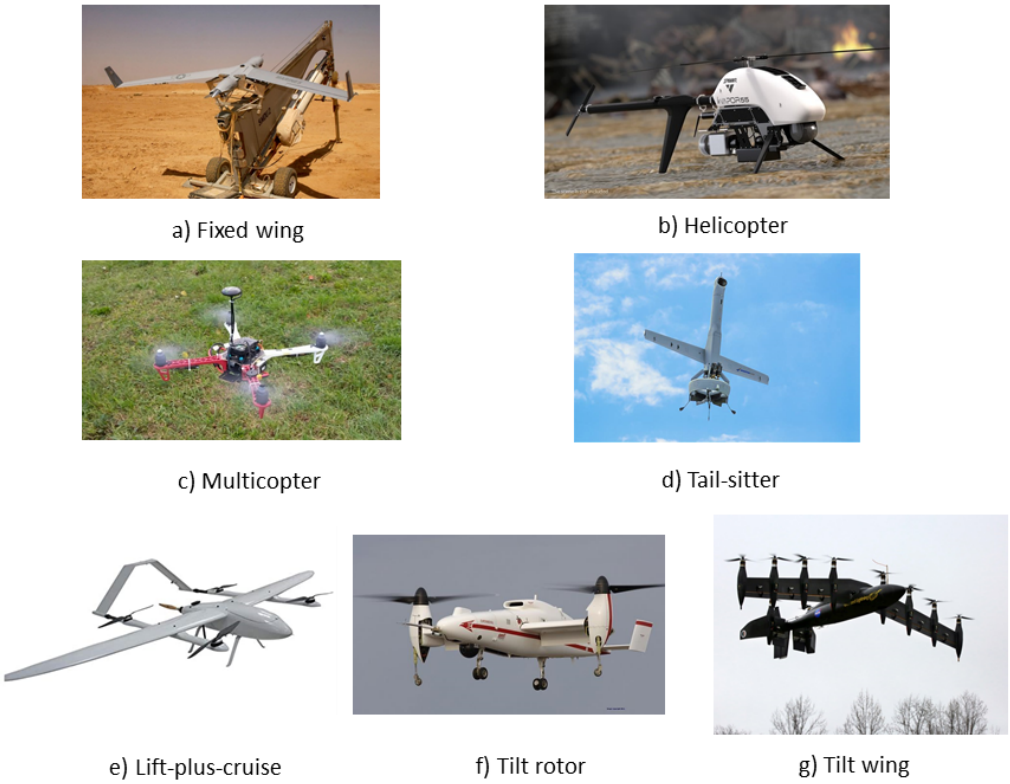

Figure 1 – UAV configurations

Furthermore, the study, simulation, experimentation and operation of UAV's, particularly with VTOL capabilities, can serve as basis for the development of the emerging Urban Air Mobility (UAM) environment, which is the concept of utilizing VTOL aircraft to

transport cargo and passengers quickly over short distances in urban areas (RADOTICH, 2021). In this sense, several designs and configurations are under study, the Vertical Flight Society tracks these aircraft and keeps a directory of current concepts (SOCIETY, 2022).

In the context of Urban Air Mobility (UAM) VTOL projects under development it is important to mention the Embraer EVE eVTOL of Figure 2a, which is a lift-plus-cruise full electric configuration with eight vertical motors and two horizontal motors; the Lilium Jet eVTOL of Figure 2b, which is a fixed wing with canard configuration and distributed electric propulsion with 36 vectored thrust ducted fans. There is also in Figure 2c the Joby Aviation S4 eVTOL, which is a tilt-rotor configuration with six electric rotors and a V-shaped tail.

Figure 2 – Urban Air Mobility (UAM) eVTOL projects under development.

1.1 Thesis Motivation

Therefore, in order to carry out the most diverse applications, several configurations of VTOL aircraft have been developed, each one with its advantages and disadvantages. So, this thesis proposes and presents a vertical take-off and landing unmanned aerial vehicle (VTOL UAV) configuration with tilt-wing along with propellers, tilt-canard and fixed upwards front propellers, which can be an efficient and versatile configuration, that

can combine the agility of the quadcopter and the performance of the fixed wing, being perhaps more stable and controllable than the conventional tilt rotor and tilt wing.

So, in order to study the flight dynamics of this configuration, its is necessary to derive the applicable equations of motion, as well as compute the transition trajectory, a transition flight control strategy for the transition from hover to cruise condition, and from cruise to hover, must be proposed and numerically simulated. Moreover, states estimation and control algorithms must be derived and programmed in a microcontroller board to flight test a prototype of the proposed configuration.

This is significant work because it is inserted in a promising and relevant area in the field of aeronautics, which is the research of technologies that make vertical take-off and landing of unmanned, and manned, aerial vehicles efficient, safe and reliable, mainly because of the complex transition phase that this type of aircraft requires.

Therefore, the study and development of the proposed configuration with the derivation of the equations of motion, transition trajectory and transition flight control algorithms can be applied to both the improvement of small UAV applications as well as contribute to the development of the emerging Urban Air Mobility (UAM) market.

1.2 Objectives and Contributions

The first objective of this thesis is to model the flight dynamics of the proposed aircraft configuration, that is, the derivation of the equations of motion using the multi-body approach, which is more applicable to the proposed configuration, given the tilt movement of the aerodynamic surfaces, along with the rotating propellers.

The second objective is to compute the transition trajectory of the proposed configuration, applicable to a conceptual aircraft to be designed. Therefore, an algorithm to compute the sequence of equilibrium points, or flights states and aerodynamic and propulsive controls, must be selected and applied to the conceptual aircraft. Moreover, a transition flight control algorithm must be developed in order to successfully transition the conceptual aircraft between the sequence of equilibrium states from hover condition to maximum horizontal speed. So, the feasibility of the control algorithm must be verified via numerical simulations.

The third objective is to build an aircraft prototype of the conceptual aircraft, along with the on-board systems in order to test the flight control algorithms for each flight configuration, that is, hovering configuration, transition flight and cruise flight. Therefore, states estimation algorithms must also be developed, which must handle the variables that can be measured via the on-board sensors in order estimate the flight states of interest to control.

Finally, flight tests must be conducted in order to verify the control algorithms for

each flight configuration, seeking finally to carry out a complete transition flight.

Therefore, the intended contributions of this thesis are:

1. The proposed configuration is in itself an important contribution, along with the applicable dynamic modeling and methodology to study the equations of motion of air vehicles with moving aerodynamic surfaces, as well as rotating propellers, therefore increasing the knowledge of VTOL air vehicles flight dynamics and control.
2. The algorithms to control the proposed vehicle during transition flight, with numerical simulations displaying the time series of the whole flight states and controls, so that the dynamics of the flight transition can be analyzed.
3. The construction techniques and prototype design choices and decisions, might give insights and contributions for possible future projects with this kind, or similar UAV designs.
4. The results of flight testing the prototype might provide important data in the study of the flight control of VTOL aircraft in its various phases of flight.

2 LITERATURE REVIEW

There are many UAV configurations, and for each there are specific control algorithms, being that, for the vehicles with VTOL capabilities its is necessary to implement sophisticated transition control maneuvers algorithms.

Particularly, the tilt wing configuration, where the aerodynamic surfaces tilts along with the rotors, has been demonstrating interesting results in terms of performance and versatility (CETINSOY *et al.*, 2012; FREDERICKS *et al.*, 2017; MURAOKA *et al.*, 2012), having performed successfully the transition maneuvers (MCSWAIN *et al.*, 2017). This configuration would have little or no support equipment at all to allow take-off and landing such as runways, catapult, parachute, or landing net, making the UAV operation cheaper and easier than fixed wing configurations, whereas would also have cruise efficiency.

However, the control of such aircraft during the transition from hovering to cruise, and from cruise to hovering, is not an easy task and recently many researchers and companies are working in this topic in order to develop a reliable transition flight control technology.

In this context, the flight control study begins with the aircraft flight dynamic model, which for this configuration would not be exactly the same as in traditional flight dynamics textbooks (ETKIN; REID, 1996; ROSKAM, 2001; STEVENS; LEWIS; JOHNSON, 2016). In other words, most flight dynamic analysis uses the hypothesis that the aircraft behaves like a rigid body in the air, with the hypothesis that the mass of such is constant and there are no structural deformations. However, it would be an oversimplification of the system to apply the 6 degree-of-freedom rigid body equations of motion to this concept of aircraft, since the aerodynamic surfaces are supposed to tilt, along with the spinning rotors, resulting in shifting of the center of gravity and gyroscopic moments (DAUD FILHO, 2018; DROANDI; SYAL; BOWER, 2018).

Therefore, the multi-body equations of motion is a more appropriate approach to dynamic modeling (HAIXU; XIANGJU; WEIJUN, 2010; SU *et al.*, 2019). So, the aircraft is divided in some parts, each with their inertial properties. Such parts are: the aircraft main body, which involves the fuselage, landing gear, vertical tail and all its components; the right and left wing; right and left horizontal stabilizer; and each rotor a separate part. In this way, it is also considered that each part has constant mass. And finally, no structure deformations are considered, that means that the parts dimensions are constant (DAUD FILHO, 2018).

According to (SIMMONS; MURPHY, 2022), the VTOL aircraft aerodynamic modeling is also a challenge due to several vehicle attributes which hamper model development.

These features include many control surfaces and propulsors, propulsion-airframe interactions, high incidence angle propeller aerodynamics, vehicle instability, rapidly changing aerodynamics through transition, and large flight envelopes that need to be characterized by a global aerodynamic model. The author addressed this issue by modeling a tilt wing VTOL aircraft with distributed propulsion using wing tunnel data, whereas (CZYBA *et al.*, 2018) in order to evaluate the aerodynamic performance of the designed UAV, a series of computational fuid dynamics simulations (CFD) were performed in the individual fight modes.

Also, for the transition flight control strategy several authors have been using the concept of transition trajectory, or sometimes referred as transition corridors, that consists of a sequence of equilibrium points, most notably represented by combinations of aerodynamic lifting surfaces tilt angle and airspeed (FREDERICKS *et al.*, 2017; MURAOKA *et al.*, 2012; SOBIESIAK *et al.*, 2019; LIU *et al.*, 2021).

Now, several control techniques are applicable for VTOL aircraft such as Proportional-Integral-Derivative (PID) with gain scheduling to deal with the varying dynamics characteristics along the transition maneuver (LIU *et al.*, 2017; TA; FANTONI; LOZANO, 2012), or a gain-scheduled linear quadratic regulator (LQR) controller, has been under study by other authors as well (LUSTOSA; DEFAÿ; MOSCHETTA, 2015; BENKHOUD; BOUALL'EGUE, 2016; MASAR; STÖHR, 2011). Other relevant techniques that can be mentioned are dynamic inversion (MIKAMI; UCHIYAMA, 2015; LIU *et al.*, 2018; MASUDA; UCHIYAMA, 2018) and H_∞ (YANG; MEJIAS; MOLLOY, 2013; CARDOSO; RAFFO; ESTEBAN, 2016).

Based on the transfer functions of pitch, roll, and yaw control channels, (PAPACHRISTOS; ALEXIS; TZES, 2011) designed a PID controller, and graphic methods, such as root locus method and bode diagram, were used to analyze the control performance, and the effectiveness of these controllers is also tested by hover experiment on the actual flight platform (LIU *et al.*, 2017).

Moreover, from the transition trajectory, or corridors, the dynamic equations can be linearized in the trim points, so that, optimal control theory can be used to design linear quadratic regulators (LQR), to stabilize the nonlinear model near a trim point (ÖNER *et al.*, 2008; DAUD FILHO, 2018). Besides, based on a rotor-tilt law, the suitable linear controller could be switched according to the flight state, and the mode transition would be achieved. In this way (ZHAO; UNDERWOOD, 2014) proposed a switching logic that is to judge if the cruise speed and altitude errors are smaller than a predefined tolerance then switch to the next controller, if not, then keep the current controller. However, it is quite difficult to adjust controller gains for linearized model around equilibrium states depending on the variation of the tilt angle and velocity of the UAV. Furthermore, the discontinuous change of controller gains would result in deterioration of control performance and system

instability during its flight (MASUDA; UCHIYAMA, 2018).

In order to perform controllable flights, the UAV's must be able to estimate their flying states, such as, velocities, attitude, altitude, position, in a way that the control algorithms can be implemented. Therefore, the UAV's have embedded sensors to measure parameters of interest. Nonetheless, it is seldom the case that off-the-shelf sensors are able to measure the aircraft states directly.

In this sense, the most common UAV's embedded sensors are (QUAN, 2017):

- Inertial measurement unit (IMU): include three-axis accelerometer, three-axis gyroscope, and sometimes electronic compass (or three-axis magnetometer). Measure accelerations, angular velocities, and Earth magnetic field.
- Barometer, or pressure sensor: measure the atmospheric pressure and temperature, which can be used to compute altitude.
- Electronic compass (or three-axis magnetometer): measure Earth magnetic field, which is used to compute vehicle heading (or yaw angle).
- GPS receiver: measure the geodetic coordinates of the vehicle.

The measurements must be filtered in order to reduce their noise, and to compute the states of interest. Moreover, there can be more than one sensor to measure the same parameter, which then must be fused. In this sense, sensor fusion is the process of combining information from two or more sensors to obtain improved accuracy and specific inferences that could not be possible using a single sensor alone. The use of multiple sensors helps with overall performance improvement, increases temporal and special coverages, and adds to the robustness of the system (NARKHEDE *et al.*, 2021).

A sensor fusion algorithm is the complementary filter. For instance, a complementary filter for attitude estimation performs low-pass filtering on a low-frequency attitude estimate, obtained from accelerometer data, and high-pass filtering on a biased high-frequency attitude estimate, obtained by direct integration of gyroscope output, and fuses these estimates together to obtain an all-pass estimate of attitude (EUSTON *et al.*, 2008), that is, roll and pitch Euler angles.

Beyond that, there is the Kalman filter (KF) (KALMAN, 1960), and its variants, like the extended Kalman filter (EKF) and unscented Kalman filter (UKF). According to (WELCH; BISHOP, 1995) the Kalman filter is essentially a set of mathematical equations that implement a predictor-corrector type estimator that is optimal in the sense that it minimizes the estimated error covariance, when some presumed conditions are met. Since the time of its introduction, the Kalman filter has been the subject of extensive research and application, particularly in the area of autonomous or assisted navigation. It

can be applied to compute vehicle attitude by fusion of accelerometer, gyroscopes and magnetometer data (DEIBE *et al.*, 2020; JURMAN *et al.*, 2007), altitude by fusion of accelerometer and barometer data (HETéNYI; GóTZY; BLáZOVICS, 2016), and position by fusion of GPS and accelerometer data (CARON *et al.*, 2006).

Also, there is the attitude filter proposed by (MAHONY; HAMEL; PFLIMLIN, 2008) which is formulated as a deterministic kinematic observer on the Special Orthogonal group SO(3) driven by an instantaneous attitude and angular velocity measurements.

A third common attitude filter is the one proposed by (MADGWICK *et al.*, 2010) which uses a quaternion representation, allowing accelerometer and magnetometer data to be used in an analytically derived and optimised gradient-descent algorithm to compute the direction of the gyroscope measurement error as a quaternion derivative.

3 AIRCRAFT CONCEPT

The concept of aircraft studied is a vertical take-off and landing unmanned aerial vehicle (VTOL UAV) with the capacity to tilt the wing and the canard, being that the two front propellers are fixed and the rear propellers tilt along with the wing, as shown in Figure 3 the isometric view for the aircraft with both surfaces in the horizontal, or cruise configuration, and with the aircraft in the vertical, or take-off and landing, or even hovering configuration. Additionally, are show in Figure 4 the aircraft frontal view, in Figure 5 the aircraft side view and in Figure 6 the aircraft upper view. The aircraft has aerodynamic controls such as: flaps, elevator, aileron and rudder, and the payload for this aircraft would be a gimbal and a small camera, with the purpose of filming, monitoring and surveillance. The aircraft model full weight is 6.44 kg.

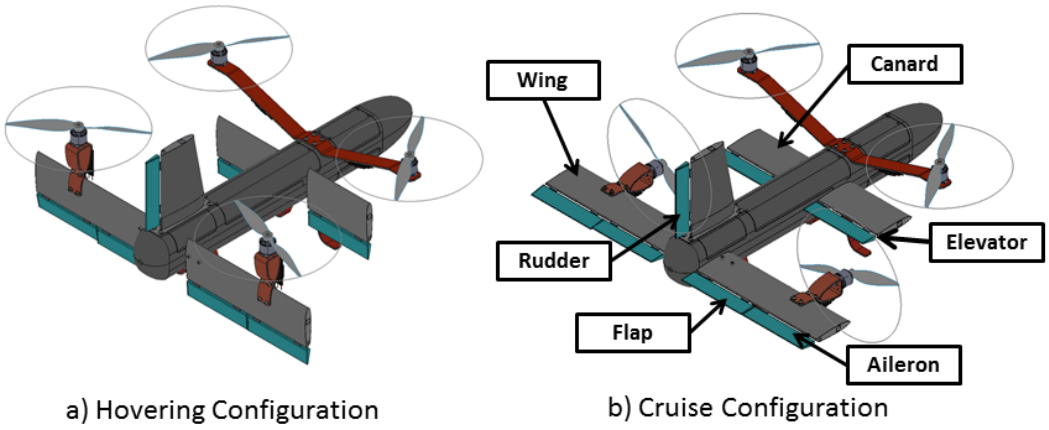

Figure 3 – Aircraft concept, isometric view.

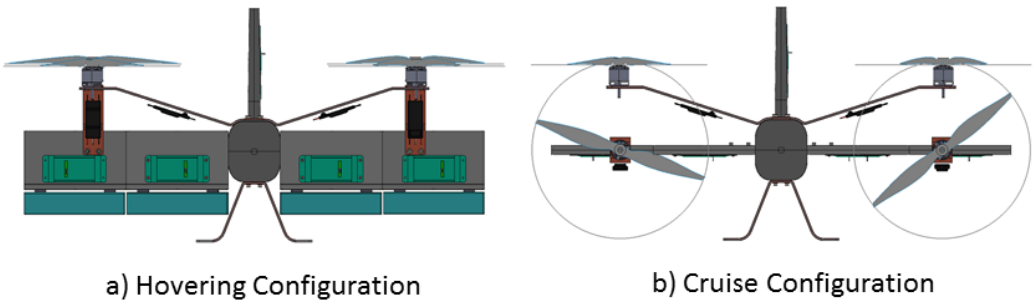

Figure 4 – Aircraft concept, frontal view.

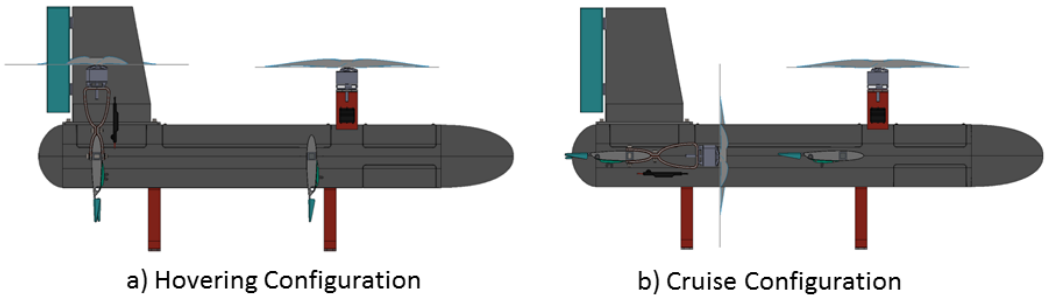

Figure 5 – Aircraft concept, side view.

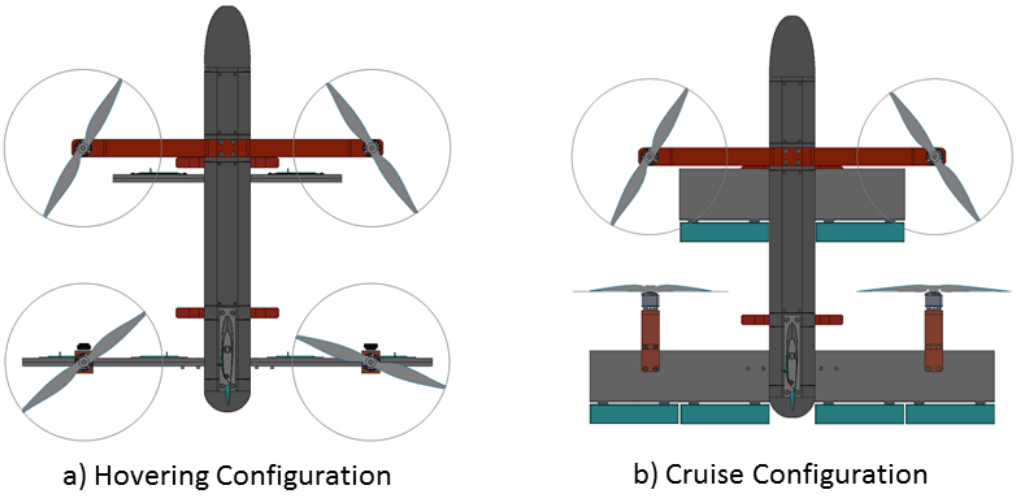

Figure 6 – Aircraft concept, upper view.

This configuration is somewhat a hybrid, or combination, between the tilt wing and lift plus cruise configurations. Nevertheless, as the stabilizing frontal surface (canard) is decoupled from the frontal motors, the transition maneuver should be somehow smoother than the conventional tilt-wing configuration.

At take-off, landing and hovering the aircraft should perform like a quadcopter, with the four motors pointing upwards, and no use of aerodynamic controls to stabilize vehicle attitude. The transition strategy from hover to horizontal flight is that the wing would tilt gradually from the vertical position to horizontal position, so that the motors in the wing would accelerate the vehicle forward. During hovering the canard should be at vertical position in order to reduce the planform area in the wake of the front motors, and at the start of the transition maneuver it should tilt into a horizontal position, so that, it progressively acquire aerodynamic loading to stabilize horizontal flight, in addition, it can be actuated to correct aircraft attitude. Therefore, at horizontal flight it should perform like a fixed wing aircraft with canard, and attitude and trajectory control given primarily

by the aerodynamic control surfaces. Thereby, the transition maneuver from horizontal flight to hovering would be just the opposite strategy.

This way, in this concept compared to the lift plus cruise VTOL configuration, the weight and drag penalty of the exclusive vertical motors might be reduced, although there is the necessity of tilting mechanisms for the wing and canard, which means more weight.

Furthermore, in this configuration there is the possibility for stable and controllable flight in any flight speed from hovering to horizontal flight in maximum speed. In other words, it should not have stall speed provided that the combination of wing and canard tilt angle is well mapped for trimming the aircraft.

The wing was designed with considerable small planform area if compared to fixed wing UAV, because it is expected to tilt, and therefore, conditions with stall and high pitch moment. So, a wing with large planform area would require a powerful servo and tilting mechanism to control its position.

In order to have good hovering control and performance, the center of gravity must be in the longitudinal midpoint between the motors at vertical position, so that, in this condition the four propellers are producing the same thrust. Also, having canard configuration while at horizontal flight, it is possible to have positive static margin even with the center of gravity so far from the aircraft nose.

4 MODELING

This chapter describes the dynamic model develop for the proposed aircraft configuration, that is, the derivation of the equations of motion, the equations of the propulsive and aerodynamic models, and the aircraft model parameters.

4.1 Dynamic Modeling

The aircraft dynamic model shall be divided in parts of constant mass of Figure 7, where there are the origins of the reference frames at the center of mass of each component. In this model there are the Earth fixed inertial reference frame with its origin at O_E, and the aircraft main body coordinate frame fixed at its center of mass O_B. The wing and canard tilts with respect to the fixed pivot points P_W and P_C, which are positioned on the one quarter chord of their exposed root chords. Moreover, the wing and canard are divided in right and left parts, each with its own concentrated mass and coordinate frames $(O_{RW}, O_{LW}, O_{RC}, O_{LC})$ positioned in the respective center of mass, in this manner, when the wing and canard tilts along the pivot points, their coordinate frames follows. Lastly, for every rotor in the wing there is also a coordinate frame (O_{R1}, O_{R2}) at their center of mass, which are fixed with respect to the wing coordinate frame and pivot point (DAUD FILHO, 2018; DAUD FILHO; BELO, 2018), whereas the frontal rotors have their coordinate frames (O_{R3}, O_{R4}) fixed with respect to the main body coordinate frame.

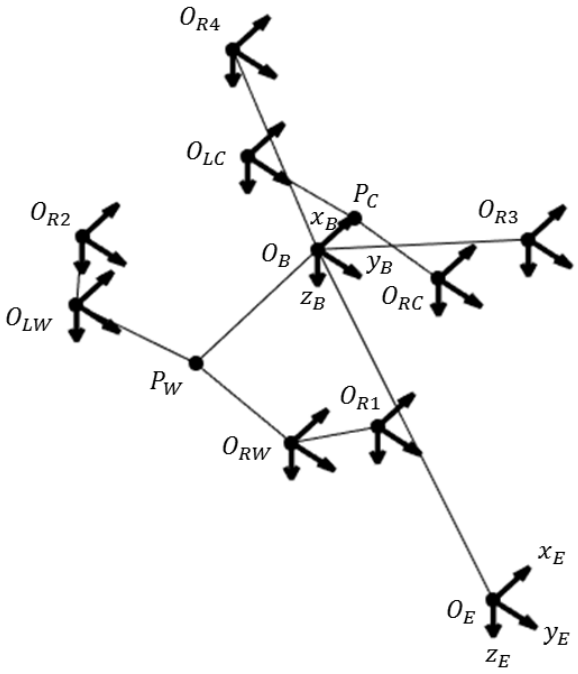

Figure 7 – Aircraft multi-body reference frames and dynamic model.

4.1.1 Linear Motion

The linear motion equation is obtained from the derivation of the total linear momentum of the aircraft with respect to time, therefore in Eq.(4.1) assembles the aircraft total linear momentum in the Earth fixed inertial reference frame ($\mathbf{p}_E$) being the sum of aircraft parts linear momentum.

$$\mathbf{p}_E = m_B\mathbf{v}_{E_B} + m_{LW}\mathbf{v}_{E_{LW}} + m_{RW}\mathbf{v}_{E_{RW}} + m_{LC}\mathbf{v}_{E_{LC}} + m_{RC}\mathbf{v}_{E_{RC}} + \sum_{j=1}^{4} m_{R_j}\mathbf{v}_{E_{R_j}} \tag{4.1}$$

Thereby, the derivation of Eq.(4.1) with respect to time leads to the force equation in the Earth fixed reference frame E in Eq.(4.2), where $\mathbf{F}_E$ is the net applied force vector.

$$\mathbf{F}_E = \frac{d}{dt}(\mathbf{p}_E) = m_B\dot{\mathbf{v}}_{E_B} + m_{LW}\dot{\mathbf{v}}_{E_{LW}} + m_{RW}\dot{\mathbf{v}}_{E_{RW}} + m_{LC}\dot{\mathbf{v}}_{E_{LC}} + m_{RC}\dot{\mathbf{v}}_{E_{RC}} + \sum_{j=1}^{4} m_{R_j}\dot{\mathbf{v}}_{E_{R_j}} \tag{4.2}$$

Now, expanding the equation in terms of the body coordinate frame B fixed at the aircraft main body center of mass, whose position is not affected by the wing or canard tilt. Thus, the acceleration vector written in the body coordinate frame, which rotates with respect to the Earth fixed reference frame at an angular velocity $\omega_B = [P \quad Q \quad R]^T$, is expressed in the Eq.(4.3), which is commonly referred as the theorem of Coriolis.

$$\dot{\mathbf{v}}_E = \dot{\mathbf{v}}_B + \omega_B \times \mathbf{v}_B \tag{4.3}$$

Additionally, applying the definition of acceleration of a moving point A with respect to a moving point B to compute the acceleration of the remaining parts, as in (MERIAM; KRAIGE, 2012), which results in Eq.(4.4), wherein $\mathbf{r}_{i/B}$, $\mathbf{v}_{rel_{i/B}}$ and $\mathbf{a}_{rel_{i/B}}$ are respectively the position vector, relative velocity and relative acceleration of the part with respect to the aircraft main body origin O_B.

$$\dot{\mathbf{v}}_{E_i} = \dot{\mathbf{v}}_B + \omega_B \times \mathbf{v}_B + \dot{\omega}_B \times \mathbf{r}_{i/B} + \omega_B \times (\omega_B \times \mathbf{r}_{i/B}) + 2\omega_B \times \mathbf{v}_{rel_{i/B}} + \mathbf{a}_{rel_{i/B}} \tag{4.4}$$

Moreover, since there are two pivot points in the aircraft, that is, the wing and canard turning points, in Eq.(4.5) is defined the position vector of each part with respect to the main body coordinate frame ($\mathbf{r}_{i/B}$) being the sum of the position of the respective pivot point ($\mathbf{r}_{pivot_i/B}$) with the position of the part to the pivot point ($R^i_B\mathbf{r}_{i/pivot_i}$), which is possible to rotate via the rotation matrix (R^i_B).

$$\mathbf{r}_{i/B} = \mathbf{r}_{pivot_i/B} + R^i_B\mathbf{r}_{i/pivot_i} = \begin{bmatrix} x_{i/B} & y_{i/B} & z_{i/B} \end{bmatrix}^T \tag{4.5}$$

Thus, taking the time derivative of Eq.(4.5), the relative velocity vector ($\mathbf{v}_{rel_{i/B}}$) is obtained in Eq.(4.6), and the second time derivative leads to the relative acceleration vector in Eq.(4.7).

$$\mathbf{v}_{rel_{i/B}} = \frac{d}{dt}(\mathbf{r}_{i/B}) = \frac{d}{dt}(\mathbf{r}_{pivot_i/B} + R^i_B \mathbf{r}_{i/pivot_i}) = \dot{R}^i_B \mathbf{r}_{i/pivot_i} = \begin{bmatrix} \dot{x}_{i/B} & \dot{y}_{i/B} & \dot{z}_{i/B} \end{bmatrix}^T \quad (4.6)$$

$$\mathbf{a}_{rel_{i/B}} = \frac{d}{dt}(\mathbf{v}_{rel_{i/B}}) = \frac{d}{dt}(\dot{R}^i_B \mathbf{r}_{i/pivot_i}) = \ddot{R}^i_B \mathbf{r}_{i/pivot_i} \quad (4.7)$$

As the rotation of the wing and tail are aligned with the y-axis of the main body coordinate frame, the rotation matrix (R^i_B) is defined as shown in the Eq.(4.8), where $\delta_{w,c}$ is the wing or canard tilt angle.

$$R^i_B = \begin{bmatrix} \cos\delta_{w,c} & 0 & \sin\delta_{w,c} \\ 0 & 1 & 0 \\ -\sin\delta_{w,c} & 0 & \cos\delta_{w,c} \end{bmatrix} \quad (4.8)$$

Furthermore, the applied net force vector in Eq.(4.9) is the sum of the aerodynamic and propulsive forces ($\mathbf{F}_B$), the weight of the aircraft main body ($m_B R^E_B \mathbf{g}_E$), the weight of the left and right wing and canard ($\sum_{i=1}^{4} m_i R^E_B \mathbf{g}_E$) and the weight of each rotor ($\sum_{j=1}^{4} m_j R^E_B \mathbf{g}_E$).

$$\mathbf{F}_E = \mathbf{F}_B + m_B R^E_B \mathbf{g}_E + \sum_{i=1}^{4} m_i R^E_B \mathbf{g}_E + \sum_{j=1}^{4} m_j R^E_B \mathbf{g}_E \quad (4.9)$$

In Eq.(4.9) the vector $\mathbf{g}_E$ is the gravity acceleration vector in the Earth fixed reference frame and m is each part mass, in addition to the rotation matrix (R^E_B) of the Earth fixed coordinate frame E to the main body coordinate frame B, expressed in Eq.(4.10) in terms of the Euler angles: roll (ϕ), pitch (θ) and yaw (ψ).

$$R^E_B = \begin{bmatrix} \cos\psi\cos\theta & \sin\psi\cos\theta & -\sin\theta \\ \cos\psi\sin\theta\sin\phi - \sin\psi\cos\phi & \sin\psi\sin\theta\sin\phi + \cos\psi\cos\phi & \cos\theta\sin\phi \\ \cos\psi\sin\theta\cos\phi + \sin\psi\sin\phi & \sin\psi\sin\theta\cos\phi - \cos\psi\sin\phi & \cos\theta\cos\phi \end{bmatrix} \quad (4.10)$$

Now substituting Eq.(4.3), Eq.(4.4), Eq.(4.6), Eq.(4.7) and Eq.(4.9) into Eq.(4.2), making use of the vector cross-product transformation into skew-symmetric matrix representation ($\Omega_B = \omega_B\times$) and ($\dot{\Omega}_B = \dot{\omega}_B\times$), and rearranging terms gives the resulting Eq.(4.11).

$$\mathbf{F}_B = -\left(m_B + \sum_{i=1}^{4} m_i + \sum_{j=1}^{4} m_j\right) R_B^E \mathbf{g}_E + \left(m_B + \sum_{i=1}^{4} m_i + \sum_{j=1}^{4} m_j\right) \dot{\mathbf{v}}_B + \left(m_B + \sum_{i=1}^{4} m_i + \sum_{j=1}^{4} m_j\right) \Omega_B \mathbf{v}_B + \sum_{i=1}^{4} m_i [(\dot{\Omega}_B + \Omega_B \Omega_B)\mathbf{r}_{i/B} + (2\Omega_B \dot{R}_B^i + \ddot{R}_B^i)\mathbf{r}_{i/pivot_i}] + \sum_{j=1}^{6} m_j [(\dot{\Omega}_B + \Omega_B \Omega_B)\mathbf{r}_{j/B} + (2\Omega_B \dot{R}_B^j + \ddot{R}_B^j)\mathbf{r}_{j/pivot_j}] \quad (4.11)$$

In Eq.(4.12) is defined the aircraft total mass (M) being the sum of each mass part.

$$M = m_B + \sum_{i=1}^{4} m_i + \sum_{j=1}^{4} m_j \quad (4.12)$$

Finally, isolating the aircraft main body acceleration vector in the left-hand side, the translational motion equation is obtained in Eq.(4.13), where are grouped the dynamic terms with respect to the wing, canard and rotors parts in the vector $\mathbf{f}$ defined in Eq.(4.14).

$$\dot{\mathbf{v}}_B = -\Omega_B \mathbf{v}_B + \frac{\mathbf{F}_B}{M} + R_B^E \mathbf{g}_E - \mathbf{f} \quad (4.13)$$

$$\begin{aligned} \mathbf{f} = & \frac{1}{M} \sum_{i=1}^{4} \{m_i [(\dot{\Omega}_B + \Omega_B \Omega_B)\mathbf{r}_{i/B} + (2\Omega_B \dot{R}_B^i + \ddot{R}_B^i)\mathbf{r}_{i/pivot_i}]\} \\ & + \frac{1}{M} \sum_{j=1}^{4} \{m_j [(\dot{\Omega}_B + \Omega_B \Omega_B)\mathbf{r}_{j/B} + (2\Omega_B \dot{R}_B^j + \ddot{R}_B^j)\mathbf{r}_{j/pivot_j}]\} \end{aligned} \quad (4.14)$$

4.1.2 Angular Motion

Similarly to the translational motion equation, the derivation of the angular motion equation begins by defining the aircraft total angular momentum ($\mathbf{H}_B$) being the sum of the angular momentum of each part as in in Eq.(4.15), where the reference frame is the aircraft main body coordinate frame B. The terms of the form ($\tilde{I}_B$) are the inertia tensors of each part with respect to the main body coordinate frame. Additionally, the aircraft parts around the main body have an additional term regarding the angular momentum due to the distance of the mass, which has linear momentum at a distance from the main body coordinate frame.

$$\mathbf{H}_B = \tilde{I}_B \omega_B + \sum_{i=1}^{4} \{\tilde{I}_{B_i} \omega_{B_i} + \mathbf{r}_{i/B} \times (m_i \mathbf{v}_{B_i})\} + \sum_{j=1}^{4} \{\tilde{I}_{B_j} \omega_{B_j} + \mathbf{r}_{j/B} \times (m_j \mathbf{v}_{B_j})\} \quad (4.15)$$

So, the velocity vector of each part in the main body coordinate frame is defined in Eq.(4.16).

$$\mathbf{v}_{B_i} = \mathbf{v}_B + \omega_B \times \mathbf{r}_{i/B} + \mathbf{v}_{rel_{i/B}} = \mathbf{v}_B + \omega_B \times \mathbf{r}_{i/B} + \dot{R}^i_B \mathbf{r}_{i/pivot_i} \tag{4.16}$$

The time derivative of the aircraft total angular momentum gives the net torque acting at the aircraft main body center of mass ($\mathbf{T}_B$) and the moments due to the parts weight distant to the main body center of mass in Eq.(4.17)

$$\frac{d}{dt}(\mathbf{H}_B) = \mathbf{T}_B + \sum_{i=1}^{4}\{\mathbf{r}_{i/B} \times m_i R^E_B \mathbf{g}_E\} + \sum_{j=1}^{4}\{\mathbf{r}_{j/B} \times m_j R^E_B \mathbf{g}_E\} \tag{4.17}$$

Furthermore, the time derivative of the Eq.(4.15) leads to Eq.(4.18).

$$\begin{aligned}\frac{d}{dt}(\mathbf{H}_B) &= \tilde{I}_B\dot{\omega}_B + \omega_B \times (\tilde{I}_B\omega_B) \\ &+ \sum_{i=1}^{4}\left\{\frac{d}{dt}(\tilde{I}_{B_i}\omega_{B_i}) + \omega_B \times (\tilde{I}_{B_i}\omega_{B_i}) + m_i\left[\frac{d}{dt}(\mathbf{r}_{i/B}) \times \mathbf{v}_{B_i} + \mathbf{r}_{i/B} \times \frac{d}{dt}(\mathbf{v}_{B_i})\right]\right\} \\ &+ \sum_{j=1}^{4}\left\{\frac{d}{dt}(\tilde{I}_{B_j}\omega_{B_j}) + \omega_B \times (\tilde{I}_{B_j}\omega_{B_j}) + m_j\left[\frac{d}{dt}(\mathbf{r}_{j/B}) \times \mathbf{v}_{B_j} + \mathbf{r}_{j/B} \times \frac{d}{dt}(\mathbf{v}_{B_j})\right]\right\}\end{aligned} \tag{4.18}$$

It is also necessary to define the inertia tensor in Eq.(4.19), which must be defined with respect to the main body coordinate frame. Therefore, each part inertia tensor is taken in its own reference frame ($\tilde{I}_i$), which is more easily computed, and make a rotation operation ($R^i_B \tilde{I}_i R^{i^T}_B$) in order to have it in the same orientation of the main body coordinate frame, and through the parallel axis theorem take into account the distance of the part to the origin of the main body coordinate frame ($m_i \tilde{R}^i_B$).

$$\tilde{I}_{B_i} = R^i_B \tilde{I}_i R^{i^T}_B + m_i \tilde{R}^i_B \tag{4.19}$$

Additionally, in Eq.(4.20) is defined the inertia tensor translation matrix, where the $x_{i/B}$, $y_{i/B}$ and $z_{i/B}$ components are given by the Eq.(4.5).

$$\tilde{R}^i_B = \begin{bmatrix} y^2_{i/B} + z^2_{i/B} & -x_{i/B}y_{i/B} & -x_{i/B}z_{i/B} \\ -y_{i/B}x_{i/B} & x^2_{i/B} + z^2_{i/B} & -y_{i/B}z_{i/B} \\ -z_{i/B}x_{i/B} & -z_{i/B}y_{i/B} & x^2_{i/B} + y^2_{i/B} \end{bmatrix} \tag{4.20}$$

Moreover, the inertia tensor time derivative is defined in Eq.(4.21), in which is used the time derivative of the inertia tensor translation matrix shown in Eq.(4.22), where the subscripts (i/B) are omitted to make it easier to understand.

$$\frac{d}{dt}(\tilde{I}_{B_i}) = \dot{R}^i_B \tilde{I}_i {R^i_B}^T + R^i_B \tilde{I}_i \dot{R^i_B}^T + m_i \frac{d}{dt}(\tilde{R}^i_B) \tag{4.21}$$

$$\frac{d}{dt}(\tilde{R}^i_B) = \begin{bmatrix} 2y\dot{y} + 2z\dot{z} & -(\dot{x}y + x\dot{y}) & -(\dot{x}z + x\dot{z}) \\ -(\dot{y}x + y\dot{x}) & 2x\dot{x} + 2z\dot{z} & -(\dot{y}z + y\dot{z}) \\ -(\dot{z}x + z\dot{x}) & -(\dot{z}y + z\dot{y}) & 2x\dot{x} + 2y\dot{y} \end{bmatrix} \tag{4.22}$$

Similarly to the inertia tensor, the aircraft parts angular velocity is defined with respect to the main body coordinate frame, thus in Eq.(4.23) the left and right wing and canard angular velocity vector are the sum of the main body angular velocity (ω_B) and the angular velocity of the respective surface tilting movement. Also, the time derivative is taken in order to obtain the angular acceleration in Eq.(4.24).

$$\omega_{B_i} = R^i_B \omega_i + \omega_B = \begin{bmatrix} 0 & \dot{\delta}_i & 0 \end{bmatrix}^T + \omega_B \tag{4.23}$$

$$\dot{\omega}_{B_i} = \frac{d}{dt}\left(R^i_B \omega_i + \omega_B \right) = \begin{bmatrix} 0 & \ddot{\delta}_i & 0 \end{bmatrix}^T + \dot{\omega}_B \tag{4.24}$$

Now, for the angular velocity of the rotors in Eq.(4.25) it is necessary to take into account the angular velocity of the rotors themselves (ω_{R_j}) and the direction of rotation ($\lambda_1 = -1$, $\lambda_2 = 1$, $\lambda_3 = 1$, $\lambda_4 = -1$). Its time derivative is shown in Eq.(4.26).

$$\omega_{B_j} = R^j_B \omega_{R_j} + R^j_B \omega_j + \omega_B = R^j_B \begin{bmatrix} \lambda_j \omega_{R_j} & 0 & 0 \end{bmatrix}^T + \begin{bmatrix} 0 & \dot{\delta}_j & 0 \end{bmatrix}^T + \omega_B \tag{4.25}$$

$$\dot{\omega}_{B_j} = \frac{d}{dt}\left(R^j_B \omega_{R_j} + R^j_B \omega_j + \omega_B \right) = \dot{R}^j_B \begin{bmatrix} \lambda_j \omega_{R_j} & 0 & 0 \end{bmatrix}^T + R^j_B \begin{bmatrix} \lambda_j \dot{\omega}_{R_j} & 0 & 0 \end{bmatrix}^T + \begin{bmatrix} 0 & \ddot{\delta}_j & 0 \end{bmatrix}^T + \dot{\omega}_B \tag{4.26}$$

Finally, substituting Eq.(4.18), Eq.(4.23), Eq.(4.24), Eq.(4.25) and Eq.(4.26) into Eq.(4.17) and rearranging it obtain the Eq.(4.27).

$$\mathbf{T}_B = A\dot{\omega}_B + B\omega_B + C\dot{\mathbf{v}}_B + D\mathbf{v}_B + \mathbf{E} - \mathbf{F} \tag{4.27}$$

The coefficients A, B, C, D, $\mathbf{E}$ and $\mathbf{F}$ in Eq.(4.27) are defined respectively in Eq.(4.28), Eq.(4.29), Eq.(4.30), Eq.(4.31), Eq.(4.32) and Eq.(4.33).

$$A = \tilde{I}_B + \sum_{i=1}^{4} \tilde{I}_{B_i} + \sum_{j=1}^{4} \tilde{I}_{B_j} \tag{4.28}$$

$$B = \Omega_B \tilde{I}_B + \sum_{i=1}^{4} \left\{ \frac{d}{dt}(\tilde{I}_{B_i}) + \Omega_B \tilde{I}_{B_i} \right\} + \sum_{j=1}^{4} \left\{ \frac{d}{dt}(\tilde{I}_{B_j}) + \Omega_B \tilde{I}_{B_j} \right\} \tag{4.29}$$

$$C = \sum_{i=1}^{4} \left\{ m_i \mathbf{r}_{i/B} \times \right\} + \sum_{j=1}^{4} \left\{ m_j \mathbf{r}_{j/B} \times \right\} \tag{4.30}$$

$$D = \sum_{i=1}^{4} \left\{ m_i \left[(\dot{R}^i_B \mathbf{r}_{i/pivot_i} \times) + \mathbf{r}_{i/B} \times \Omega_B \right] \right\} + \sum_{j=1}^{4} \left\{ m_j \left[(\dot{R}^j_B \mathbf{r}_{j/pivot_j} \times) + \mathbf{r}_{j/B} \times \Omega_B \right] \right\} \tag{4.31}$$

$$\begin{aligned} \mathbf{E} = \sum_{i=1}^{4} \Bigg\{ \Bigg[\frac{d}{dt}(\tilde{I}_{B_i}) + \Omega_B \tilde{I}_{B_i} \Bigg] R^i_B \omega_i + \tilde{I}_{B_i} \frac{d}{dt}(R^i_B \omega_i) + m_i \Bigg[\dot{R}^i_B \mathbf{r}_{i/pivot_i} \times (\Omega_B \mathbf{r}_{i/B} + \dot{R}^i_B \mathbf{r}_{i/pivot_i}) \\ + \mathbf{r}_{i/B} \times \Big((\dot{\Omega}_B + \Omega_B \Omega_B) \mathbf{r}_{i/B} + (2\Omega_B \dot{R}^i_B + \ddot{R}^i_B) \mathbf{r}_{i/pivot_i} \Big) \Bigg] \Bigg\} \\ + \sum_{j=1}^{4} \Bigg\{ \Bigg[\frac{d}{dt}(\tilde{I}_{B_j}) + \Omega_B \tilde{I}_{B_j} \Bigg] (R^j_B \omega_{R_j} + R^j_B \omega_j) + \tilde{I}_{B_j} \frac{d}{dt}(R^j_B \omega_{R_j} + R^j_B \omega_j) \\ + m_j \Bigg[\dot{R}^j_B \mathbf{r}_{j/pivot_j} \times (\Omega_B \mathbf{r}_{j/B} + \dot{R}^j_B \mathbf{r}_{j/pivot_j}) + \mathbf{r}_{j/B} \times \Big((\dot{\Omega}_B + \Omega_B \Omega_B) \mathbf{r}_{j/B} + (2\Omega_B \dot{R}^j_B + \ddot{R}^j_B) \mathbf{r}_{j/pivot_j} \Big) \Bigg] \Bigg\} \end{aligned} \tag{4.32}$$

$$\mathbf{F} = \sum_{i=1}^{4} \left\{ \mathbf{r}_{i/B} \times m_i R^E_B \mathbf{g}_E \right\} + \sum_{j=1}^{4} \left\{ \mathbf{r}_{j/B} \times m_j R^E_B \mathbf{g}_E \right\} \tag{4.33}$$

Isolating the aircraft main body angular acceleration vector in the left-hand side gives the angular motion equation in Eq.(4.34).

$$\dot{\omega}_B = A^{-1}(-B\omega_B - C\dot{\mathbf{v}}_B - D\mathbf{v}_B - \mathbf{E} + \mathbf{F} + \mathbf{T}_B) \tag{4.34}$$

4.1.3 Forces and Torques

Additionally, the net force vector ($\mathbf{F}_B$) is the sum of the aircraft aerodynamic forces of drag (D), side force (Y) and lift (L), and the propellers propulsive forces, as in Eq.(4.35), where is defined the propellers thrust aligned with the x-axis of their own coordinate frame.

$$\mathbf{F}_B = S^T \begin{bmatrix} -D \\ Y \\ -L \end{bmatrix} + \sum_{j=1}^{4} \left\{ R^j_B \begin{bmatrix} T_j \\ 0 \\ 0 \end{bmatrix} \right\} \tag{4.35}$$

Moreover, the propeller thrust and torque are defined according to Eq.(4.36) and Eq.(4.37) respectively, where C_T is the thrust coefficient and C_Q the torque coefficient,

both obtained from performance data of the APC 12x5 propeller from (APC, 2022). In these equations ρ is the air density, n the propeller speed in revolutions per second and D the propeller diameter.

$$T_j = C_T \rho n^2 D^4 \tag{4.36}$$

$$Q_j = C_Q \rho n^2 D^5 \tag{4.37}$$

Also, the power required by the propeller is defined as in Eq.(4.38), for C_P the propeller power coefficient.

$$Pj = C_P \rho n^3 D^5 \tag{4.38}$$

The propellers thrust, torque and power coefficients are computed with respect to the propellers advance ratio of Eq.(4.39), where V is the projection of the flight speed in the propeller axis of rotation. In case the projection is null or negative, the propeller was considered in static condition.

$$J = \frac{V}{nD} \tag{4.39}$$

Furthermore, it is important to define the net torque vector acting at the aircraft main body center of mass ($\mathbf{T}_B$), in Eq.(4.40) being the sum of the aerodynamic roll, pitch and yaw moments ($\bar{L}, M, N$), and the propellers torque and moments due to their thrust with respect to the main body coordinate frame origin. In here λ_j defines the propeller rotation direction, that i, clockwise or counter-clockwise.

$$\mathbf{T}_B = S^T \begin{bmatrix} \bar{L} \\ M \\ N \end{bmatrix} + \sum_{j=1}^{4} \left\{ R_B^j \begin{bmatrix} \lambda_j Q_j \\ 0 \\ 0 \end{bmatrix} + \mathbf{r}_{j/B} \times R_B^j \begin{bmatrix} T_j \\ 0 \\ 0 \end{bmatrix} \right\} \tag{4.40}$$

It is important to note that the front propellers of the tilt-wing UAV configuration under study are expected to operate under high angle of attack conditions, which would have effects in the thrust, torque and moments acting in the propeller, particularly at high flight speeds. So, a blade element model of a helicopter rotor would be more precise, however it would make the modeling and simulation much more complex.

4.1.4 Attitude Propagation Equation

The aircraft angular velocity and Euler angle rates are not the same, they relate through the attitude propagation equation of Eq.(4.41), whose demonstration can be found in (STEVENS; LEWIS; JOHNSON, 2016).

$$\begin{bmatrix} \dot{\phi} \\ \dot{\theta} \\ \dot{\psi} \end{bmatrix} = \begin{bmatrix} 1 & \tan\theta\sin\phi & \tan\theta\cos\phi \\ 0 & \cos\phi & -\sin\phi \\ 0 & \sin\phi\sec\theta & \cos\phi\sec\theta \end{bmatrix} \begin{bmatrix} P \\ Q \\ R \end{bmatrix} \tag{4.41}$$

4.1.5 Navigation Equation

Additionally, it is possible to keep track of the aircraft main body trajectory in the Earth fixed reference frame integrating the aircraft velocity, therefore is defined the x position, y position and z position in E reference frame respectively (x_E, y_E, z_E), whose time derivatives are the components of the velocity vector in the E reference frame. So, applying the rotation of reference frames to the main body velocity vector we obtain the navigation equation in Eq.(4.42). It is worth mentioning that the rotation matrix applied here is the transpose of Eq.(4.10), that is $R_E^B = (R_B^E)^T$.

$$\mathbf{v}_E = \begin{bmatrix} \dot{x}_E & \dot{y}_E & \dot{z}_E \end{bmatrix}^T = R_E^B \mathbf{v}_B \tag{4.42}$$

Furthermore, the aircraft altitude h is defined as in Eq.(4.43), since in the Earth fixed inertial reference frame, the z_E coordinate points downwards.

$$h = -z_E \tag{4.43}$$

4.1.6 Controls Dynamic Equation

Every aerodynamic control surface actuation and rotor angular velocity are modeled as first order dynamic systems, whose equations are in Eq.(4.44) for the aerodynamic controls deflection angles (δ) and in Eq.(4.45) for the rotors angular velocity, where τ is the time constant. In here there are the actuator and propeller commanded signals U_δ and U_{ω_R} converted to deflection angle and propeller angular velocity via the conversion constants k_δ and k_{ω_R}

$$\dot{\delta} = \frac{1}{\tau_\delta}(k_\delta U_\delta - \delta) \tag{4.44}$$

$$\dot{\omega}_R = \frac{1}{\tau_R}(k_{\omega_R} U_{\omega_R} - \omega_R) \tag{4.45}$$

4.1.7 Torque at tilting surfaces

It is important to compute the torque acting at the tilting surfaces, that is, the torque at the wing and canard axis, in order to choose a fitting servo. The torque at the wing axis is defined in Eq.(4.46) and in Eq.(4.47) for the canard axis. Both torques are functions of the aerodynamic moments at those surfaces, as well as the moments relative

to the propellers for the wing, where $r_{j/pivot}$ is the distance vector of the propeller to the pivot point of the wing or canard.

$$\mathbf{T}_w = S^T \begin{bmatrix} \bar{L}_w \\ M_w \\ N_w \end{bmatrix} + \sum_{j=1}^{2} \left\{ R_B^j \begin{bmatrix} \lambda_j Q_j \\ 0 \\ 0 \end{bmatrix} + \mathbf{r}_{j/pivot} \times R_B^j \begin{bmatrix} T_j \\ 0 \\ 0 \end{bmatrix} \right\} \tag{4.46}$$

$$\mathbf{T}_c = S^T \begin{bmatrix} \bar{L}_c \\ M_c \\ N_c \end{bmatrix} \tag{4.47}$$

4.1.8 Energy consumed during flight

The propellers require power to produce the thrust and torque, which is provided by the on-board batteries, which have total energy capacity. Thus, the aircraft range and autonomy must be computed with respect to the energy capacity.

The energy is the integral of the power over time, as defined in Eq.(4.48). However, the energy capacity of the batteries are defined in $mmAh$, so, in Eq.(4.48) the power must be divided by the battery nominal voltage (considered Lipo 4S = 14.8V) to compute the current, and divide by 3.6 to convert to $mmAh$.

$$E(mmAh) = \int_{T_0}^{T_{end}} P\, dt = \int_{T_0}^{T_{end}} \frac{P}{3.6V}\, dt \tag{4.48}$$

4.2 Aircraft Model Parameters

In this section are listed the parameters needed to test the equations in transition flight simulation for the conceptual VTOL aircraft designed for this study. Firstly in Table 1 are listed each aircraft parts weight and its position with respect to aircraft nose and with wing and canard horizontal, that is $\delta_w = 0°$ and $\delta_c = 0°$. The aircraft full weight is 6.44 kg.

Also, the pivot points positions in meters with respect to aircraft nose are for the wing: $P_W(x, y, z) = [0.691 \quad 0 \quad 0]^T$, and for the canard $P_C(x, y, z) = [0.335 \quad 0 \quad 0]^T$.

Additionally, are listed in Table 2 the aircraft parts inertia tensor parameters with respect to their own coordinate frame, where the inertia tensor ($\tilde{I}$) is defined as in Eq.(4.49), and the relevant geometric parameters are listed in Table 3.

$$\tilde{I} = \begin{bmatrix} I_{xx} & I_{xy} & I_{xz} \\ I_{xy} & I_{yy} & I_{yz} \\ I_{xz} & I_{yz} & I_{zz} \end{bmatrix} \tag{4.49}$$

Table 1 – Aircraft parts weight and position with respect to aircraft nose (wing and canard horizontal, $\delta_w = 0°$ and $\delta_c = 0°$)

part	m, kg	x, m	y, m	z, m
m_B	4.24	0.448	0	0.0163
m_{RW}	0.507	0.719	0.211	0
m_{LW}	0.507	0.719	-0.211	0
m_{RC}	0.185	0.361	0.146	0
m_{LC}	0.185	0.361	-0.146	0
m_{R1}	0.203	0.577	0.278	0
m_{R2}	0.203	0.577	-0.278	0
m_{R3}	0.203	0.172	0.280	-0.098
m_{R4}	0.203	0.172	-0.280	-0.098

Table 2 – Aircraft parts components of the inertia tensor in their own coordinate frames.

part	I_{xx}	I_{yy}	I_{zz}	I_{xy}	I_{xz}	I_{yz}
B	0.022	0.3964	0.3946	0	-0.0162	0
RW	0.0034	6.25e-4	0.0040	1.22e-4	0	0
LW	0.0034	6.25e-4	0.0040	-1.22e-4	0	0
RC	3.93e-4	2.46e-4	6.30e-4	-4.76e-5	0	0
LC	3.93e-4	2.46e-4	6.30e-4	4.76e-5	0	0
$R1$	4.71e-5	4.71e-5	3.43e-5	0	0	0
$R2$	4.71e-5	4.71e-5	3.43e-5	0	0	0
$R3$	4.71e-5	4.71e-5	3.43e-5	0	0	0
$R4$	4.71e-5	4.71e-5	3.43e-5	0	0	0

Table 3 – Aircraft geometric parameters.

S_B, m^2	0.0074	b_W, m	0.794	K_{CB}	1.449
S_W, m^2	0.112	b_C, m	0.441	x'_{W_e}, m	0.691
S_{W_e}, m^2	0.100	b_{VT}, m	0.28	z'_{W_e}, m	0
S_C, m^2	0.0626	l_B, m	0.787	x'_{C_e}, m	0.335
S_{C_e}, m^2	0.0498	$\bar{c}_W, m$	0.142	z'_{C_e}, m	0
S_{VT}, m^2	0.0438	$\bar{c}_C, m$	0.142	x_{m_B}, m	0.335
D_{props}, m	0.3048	K_{WB}	1.239	z_{m_B}, m	0

The time constants used in the simulations are listed in Table 4, in which for the brushless motors they were obtained from (QUAN, 2017) for a similar propulsion system. For the servo actuators it has been found time constants ranging from 0.119 to 0.520 s (GREULICH, 2016; FRANCO *et al.*, 2007).

Table 4 – Controls time constants used in the simulations

Parameter	Value
$\tau_{\delta_w}, \tau_{\delta_c}$	0.520 s
$\tau_{\delta_f}, \tau_{\delta_e}, \tau_{\delta_r}, \tau_{\delta_{aR}}, \tau_{\delta_{aL}}$	0.25 s
$\tau_{R_1}, \tau_{R_2}, \tau_{R_3}, \tau_{R_4}$	0.098 s

In Table 5 are listed the actuators limits, and in Table 6 the control input limits and conversion constants.

Table 5 – Actuators limits

Control	Range
δ_w	0° to 90°
δ_c	-10° to 90°
$\delta_f, \delta_e, \delta_r, \delta_{aR}, \delta_{aL}$	-30° to 30°
$\omega_{R_1}, \omega_{R_2}, \omega_{R_3}, \omega_{R_4}$	0 to 13860 RPM

Table 6 – Control input limits

Control	Range	Conversion Constants	Value
U_{δ_w}	0 to 1	k_{δ_w}	1.5708
U_{δ_c}	-1 to 1	k_{δ_c}	1.5708
$U_{\delta_f}, U_{\delta_e}, U_{\delta_r}, U_{\delta_{aR}}, U_{\delta_{aL}}$	-1 to 1	$k_{\delta_f}, k_{\delta_e}, k_{\delta_r}, k_{\delta_{aR}}, k_{\delta_{aL}}$	0.5236
$U_{\omega_{R_1}}, U_{\omega_{R_2}}, U_{\omega_{R_3}}, U_{\omega_{R_4}}$	0 to 1	$k_{\omega_{R_1}}, k_{\omega_{R_2}}, k_{\omega_{R_3}}, k_{\omega_{R_4}}$	1451

4.3 Aerodynamic Modeling

The aerodynamic forces and moments are modeled according to the following equations of this section, where there are aircraft drag (D) in Eq.(4.50), aerodynamic side force (Y) in Eq.(4.51), aerodynamic lift (L) in Eq.(4.52), rolling moment ($\bar{L}$) in Eq.(4.53), pitching moment (M) in Eq.(4.54) and yawing moment (N) in Eq.(4.55). Also, the equations, aerodynamic coefficients and dynamic derivatives were obtained using the extensive methods of (HOAK, 1960; HOERNER, 1965; HOUGHTON; CARPENTER, 2003).

The wing and canard have constant chord Naca 0012 airfoils, which is a widely used airfoil in aircraft wings and stabilizers. Moreover, airfoils with camber were avoided, since during the hovering configuration in which the wings and canard are in the vertical position, the effect of the wake coming from the propellers (pointing upwards) could produce unintended aerodynamic forces in the longitudinal axis of the aircraft.

In this context, the aerodynamic forces and moments are firstly computed for the main aircraft components, that is, the main body or fuselage, the wing, canard and vertical tail, and then added to form the full vectors to be inserted in the dynamic equations of motion. The resulting aerodynamic coefficients as functions of angle of attack are shown in the Appendix A.

$$D = \frac{1}{2}\rho(V_T + \Delta V_T)^2 C_{D_{W_e}} S_{W_e} + \frac{1}{2}\rho V_T^2 \left(C_{D_B} S_B + C_{D_{C_e}} S_{C_e} \right) + \frac{1}{4}\rho V_T S_W \bar{c}_W C_{D_q} Q \quad (4.50)$$

$$Y = \frac{1}{2}\rho V_T^2 S_W \left(C_{Y_\beta}\beta + C_{Y_{\delta_r}}\delta_r \right) + \frac{1}{4}\rho V_T S_W b_W \left(C_{Y_p}P + C_{Y_r}R + C_{Y_{\dot{\beta}}}\dot{\beta} \right) \tag{4.51}$$

$$L = \frac{1}{2}\rho V_T^2 K_{CB} \left(C_{L_B}S_B + C_{L_{C_e}}S_{C_e} \right) + \frac{1}{2}\rho (V_T + \Delta V_T)^2 K_{WB} C_{L_{W_e}} S_{W_e} + \frac{1}{4}\rho V_T S_W \bar{c}_W \left(C_{L_q}Q + C_{L_{\dot{\alpha}}}\dot{\alpha} \right) \tag{4.52}$$

$$\bar{L} = \frac{1}{4}\rho V_T S_W b_W^2 \left(C_{l_p}P + C_{l_r}R + C_{l_{\dot{\beta}}}\dot{\beta} \right) + \frac{1}{2}\rho V_T^2 S_W b_W \left(C_{l_\beta}\beta + C_{l_{\delta_{a_L}}}\delta_{a_L} - C_{l_{\delta_{a_R}}}\delta_{a_R} + C_{l_{\delta_r}}\delta_r \right) \tag{4.53}$$

$$\begin{aligned} M = \frac{1}{2}\rho V_T^2 \Big(& (x_B - x_{m_B}) S_B K_{CB} (C_{L_B}\cos\alpha + C_{D_B}\sin\alpha) \\ & - (z_B - z_{m_B}) S_B K_{CB} (C_{L_B}\sin\alpha - C_{D_B}\cos\alpha) \\ & + C_{m_B}\bar{c}_W S_B + (x_B - x_{C_e}^{'}) S_{C_e} K_{CB} (C_{L_{C_e}}\cos\alpha + C_{D_{C_e}}\sin\alpha) \\ & - (z_B - z_{C_e}^{'}) S_{C_e} K_{CB} (C_{L_{C_e}}\sin\alpha - C_{D_{C_e}}\cos\alpha) + C_{m_{C_e}}\bar{c}_C S_{C_e} \Big) \\ & + \frac{1}{2}\rho (V_T + \Delta V_T)^2 S_{W_e} \Big((x_B - x_{W_e}^{'}) K_{WB} (C_{L_{W_e}}\cos(\alpha - \epsilon) + C_{D_{W_e}}\sin(\alpha - \epsilon)) \\ & - (z_B - z_{W_e}^{'}) K_{WB} (C_{L_{W_e}}\sin(\alpha - \epsilon) - C_{D_{W_e}}\cos(\alpha - \epsilon)) + C_{m_{W_e}}\bar{c}_W \Big) \\ & + \frac{1}{4}\rho V_T S_W \bar{c}_W^2 \left(C_{m_q}Q + C_{m_{\dot{\alpha}}}\dot{\alpha} \right) \end{aligned} \tag{4.54}$$

$$N = \frac{1}{4}\rho V_T S_W b_W^2 \left(C_{n_p}P + C_{n_r}R + C_{n_{\dot{\beta}}}\dot{\beta} \right) + \frac{1}{2}\rho V_T^2 S_W b_W \left(C_{n_\beta}\beta + C_{n_{\delta_{a_L}}}\delta_{a_L} - C_{n_{\delta_{a_R}}}\delta_{a_R} + C_{n_{\delta_r}}\delta_r \right) \tag{4.55}$$

4.3.1 Transformation Between Reference Axes

The aerodynamic forces and moments are defined with respect to the wind axes, which is defined as a transformation from the aircraft main body coordinate frame. So, the aircraft main body velocity vector and its components $\mathbf{v}_B = [U \quad V \quad W]^T$ is defined, being that the same vector can be described in wind axes as $\mathbf{v}_W = [V_T \quad 0 \quad 0]^T$, where V_T is the aircraft main body flight speed, defined in Eq.(4.58).

The transformation between this vectors are possible using Eq.(4.56), where the main body-to-wind-axes rotation matrix (S) is defined in Eq.(4.57), which is a function of the aircraft main body angle of attack (α) and sideslip angle (β). We make use of the same transformation for the angular velocity vector $\omega_W = S\omega_B = [P_W \quad Q_W \quad R_W]^T$.

$$\mathbf{v}_W = S\mathbf{v}_B \tag{4.56}$$

$$S = \begin{bmatrix} \cos\alpha\cos\beta & \sin\beta & \sin\alpha\cos\beta \\ -\cos\alpha\sin\beta & \cos\beta & -\sin\alpha\sin\beta \\ -\sin\alpha & 0 & \cos\alpha \end{bmatrix} \tag{4.57}$$

$$V_T = \sqrt{U^2 + V^2 + W^2} \tag{4.58}$$

The aircraft main body angle of attack (α) and sideslip angle (β) are defined in Eq.(4.59) and Eq.(4.60) respectively.

$$\alpha = \tan^{-1}\left(\frac{W}{U}\right) \tag{4.59}$$

$$\beta = \sin^{-1}\left(\frac{V}{V_T}\right) \tag{4.60}$$

5 SIMULATION

This chapter describes the method to compute the aircraft transition trajectory, the linearization of the equations of motion, stability analysis, the transition flight control algorithm and numerical simulations of the transition flight from hover to maximum speed, and from maximum speed to hover.

5.1 Aircraft Transition Trajectory

Aircraft transition trajectory, or steady state flight conditions, is the sequence of equilibrium points or trim conditions, which in turn are the combination of state variables that makes the flight state derivatives equal to zero. Moreover, is also important because it provides an initial condition for flight simulation and a flight condition to linearize the aircraft dynamics equations of motion (STEVENS; LEWIS; JOHNSON, 2016).

So, the trim conditions are defined by the combination of variables of the state vector of Eq.(5.1), with a corresponding control vector of Eq.(5.2), that result in the scalar cost function of Eq.(5.3) equal to zero. Note that this scalar is the sum of the time derivatives squared of the states related to translational and angular motion, which can be computed using Eq.(4.13) and Eq.(4.34) for a given input state vector $\mathbf{X}$.

$$\mathbf{X} = (U, V, W, P, Q, R, \phi, \theta, \psi, x_E, y_E, z_E, \delta_f, \delta_e, \delta_r, \delta_{a_L}, \delta_{a_R}, \delta_w, \delta_c, \omega_{R_1}, \omega_{R_2}, \omega_{R_3}, \omega_{R_4}) \quad (5.1)$$

$$\mathbf{U} = (U_{\delta_f}, U_{\delta_e}, U_{\delta_r}, U_{\delta_{a_L}}, U_{\delta_{a_R}}, U_{\delta_w}, U_{\delta_c}, U_{\omega_{R_1}}, U_{\omega_{R_2}}, U_{\omega_{R_3}}, U_{\omega_{R_4}}) \quad (5.2)$$

$$\jmath = \dot{U}^2 + \dot{V}^2 + \dot{W}^2 + \dot{P}^2 + \dot{Q}^2 + \dot{R}^2 \quad (5.3)$$

The equilibrium points were computed in the range of transition flight with zero rate of climb or descent, that is flight path angle (γ) zero. For the longitudinal flight only, the flight path angle is defined as $\gamma = \theta - \alpha$, thus for $\gamma = 0 \Rightarrow \theta = \alpha$.

Furthermore, for the longitudinal flight condition, are set as input (β, P, Q, R, ϕ) equal to zero because they are related to lateral and angular motion. The yaw angle ψ and aircraft positions x_E and y_E are arbitrary, and h is the altitude desired for the simulation, which has a direct effect in the air density ρ. Additionally, the controls of the lateral motion $(\delta_r, \delta_{a_L}, \delta_{a_R})$ are also null.

So being, it is necessary to compute the combination of the remaining non-zero state variables for an input of flight velocity U, this way it is possible to obtain the equilibrium points for the intended range of longitudinal flight conditions.

An effective algorithm to solve this problem, which is the minimization of the scalar cost function of Eq.(5.3) for inputs of the state vector $\mathbf{X}$ with the constraints previously mentioned, is the Sequential Simplex, described in (WALTERS *et al.*, 1991; NELDER; MEAD, 1965), which is based on the search of optimum from sequential experimentation and measurement of system outcome from a combination of variables. The algorithm starting procedure implemented was the Corner Initial Method, described in (WALTERS *et al.*, 1991), and the stopping criterion used was scalar cost function value less than $1e-10$.

The equilibrium trajectory is computed in steps of $U_e = 0.1\,m/s$, from hover (0 m/s) to 20 m/s. And from 20 m/s to 30 m/s the steps are of 1.0 m/s, therefore the equilibrium points are corresponding to the markers in Figure 8, Figure 9, Figure 10, Figure 11 and Figure 12. The reference altitude is 100 m.

The canard tilt angle (δ_c) was given as fixed input to the algorithm, this because the system is over-actuated, which means that there are more than one solution for the equilibrium condition for a given input flight speed. By fixing the canard tilt angle as an input, it is possible to obtain a smoother resultant curve of flight states as a function of flight speed.

The algorithm was applied to the conceptual VTOL aircraft under study which resulted in the following results of Figure 8 for wing and canard tilt angle (δ_w, δ_c), as function of reference flight speed U_e, being that, the flap and elevator are not used to trim the aircraft, and in Figure 9 for the propellers RPM at wing (ω_{Wing}) and at the front of the aircraft (ω_{Front}). Note that at flight speed zero, that is, hovering condition both wing and canard are at tilt angle 90° having the propellers pointing upwards, and as the flight speed increases the wing gradually lean forward until is close to horizontal position at higher speeds. At low flight speeds the propellers at wing and front have similar angular velocities, up until the wing is close to horizontal position, where the angular velocity of the wing propellers have to increase in order to keep track of the horizontal velocity of the aircraft, whilst the front propellers reduce its angular velocity in order to reduce thrust.

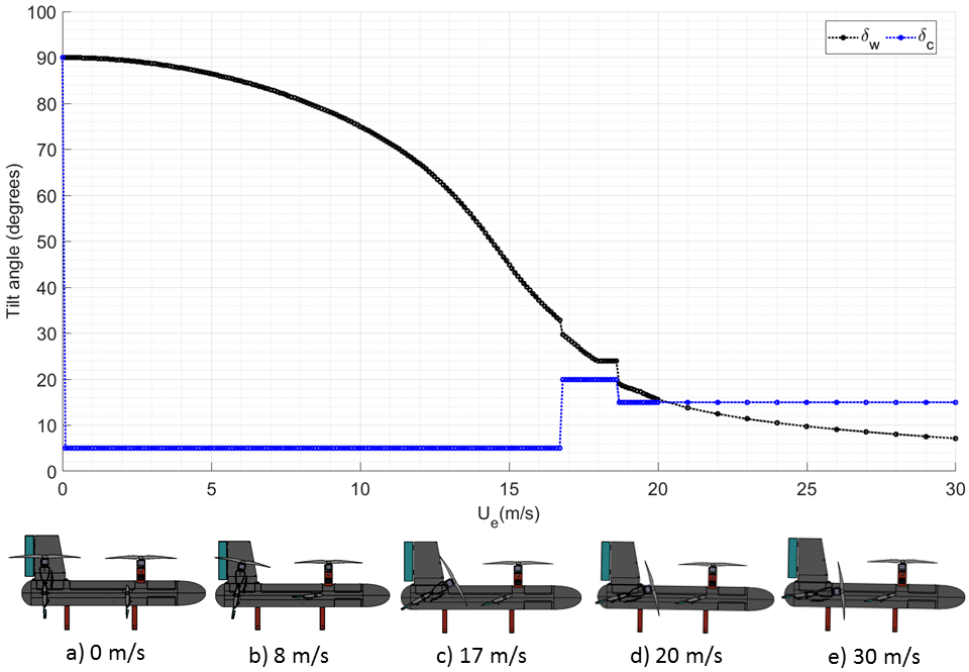

Figure 8 – Aircraft wing and canard tilt angle trim data as function of reference flight speed U_e.

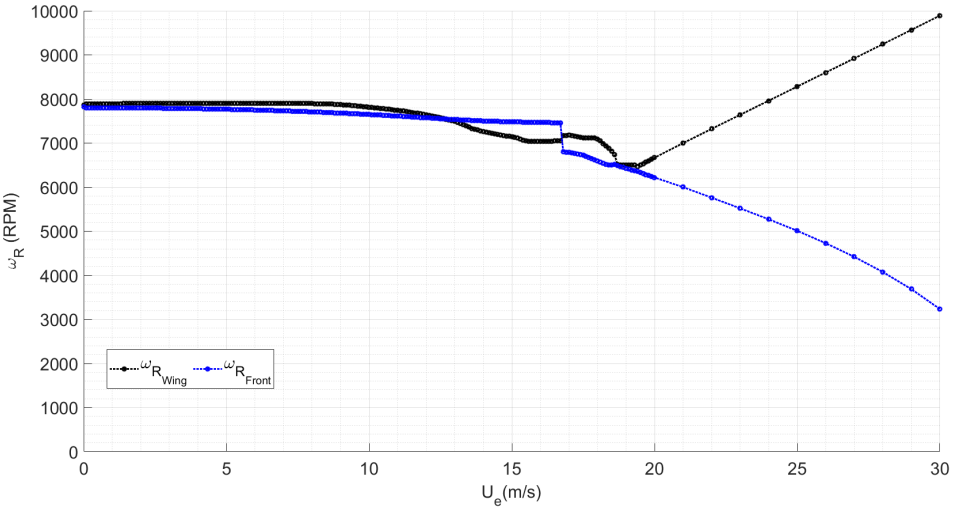

Figure 9 – Aircraft propellers angular velocity trim data as function of reference flight speed U_e.

Moreover, the strategy for the canard tilt angle at the transition is to move it completely in one step from the vertical position to a more horizontal position at the beginning of the transition so that it would have low drag during acceleration. So, it tilts to 5° at the beginning of the maneuver. At flight speed close to $U_e = 16.7\,m/s$ the wing is at the maximum lift coefficient condition, so the canard must increase its tilt angle and angle of attack in order to trim the vehicle, which allows the continued acceleration and gradual wing tilting to more horizontal position, while maintaining negative main body

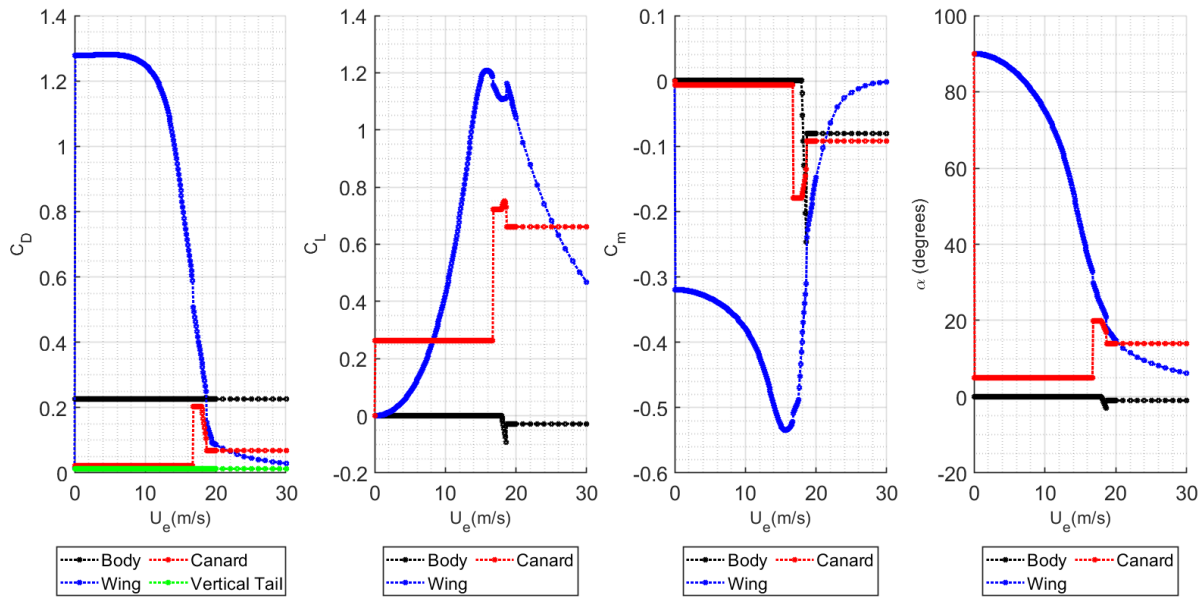

Figure 10 – Aerodynamic longitudinal coefficients at transition trajectory.

angle of attack, which is important to keep the front propellers producing thrust upwards and forward.

Furthermore, it is noticeable that there are two distinct regions of equilibrium conditions, that is, from hover up until $U_e = 16.7\,m/s$ where the wing is in the aerodynamic stalled region and the main body is kept at $0°$ angle of attack, therefore, most of the vehicle lifting force comes from the propellers, and the total power required is progressively reduced. The aerodynamic coefficients and angle of attack of the main body, wing and canard are shown in Figure 10, where the wing reaches its maximum lift coefficient close to the frontier between regions of equilibrium conditions, and at higher flight speeds the drag coefficients are significantly reduced.

During the transition maneuver from hover to maximum speed the total vertical force that sustains the vehicle switches between mostly propulsive to mostly aerodynamic, which is shown in Figure 11 for the fraction of total vertical force with respect to aircraft weight. The contribution of each vehicle component is also shown in this figure.

As most of the vertical force is provided by the propellers at low flight speed, the power required is also greater, and as the vehicle flight speed gradually increases, simultaneously to the increases of the portion of aerodynamic vertical force, the power required for flight reduces, which is depicted in Figure 12.

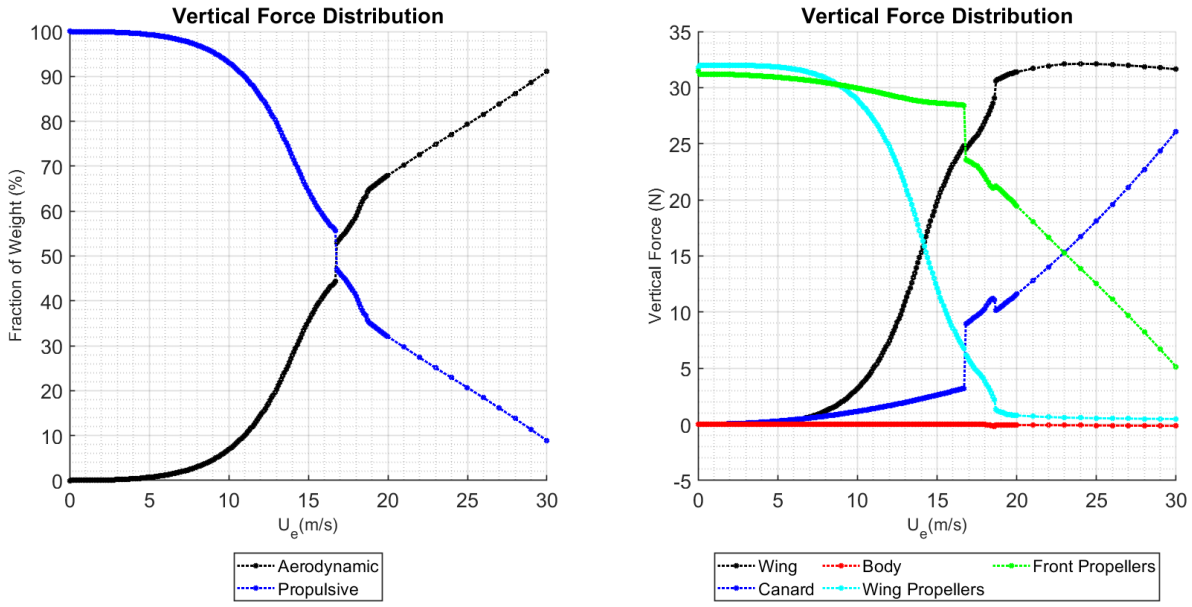

Figure 11 – Total vertical force, propulsive or aerodynamic.

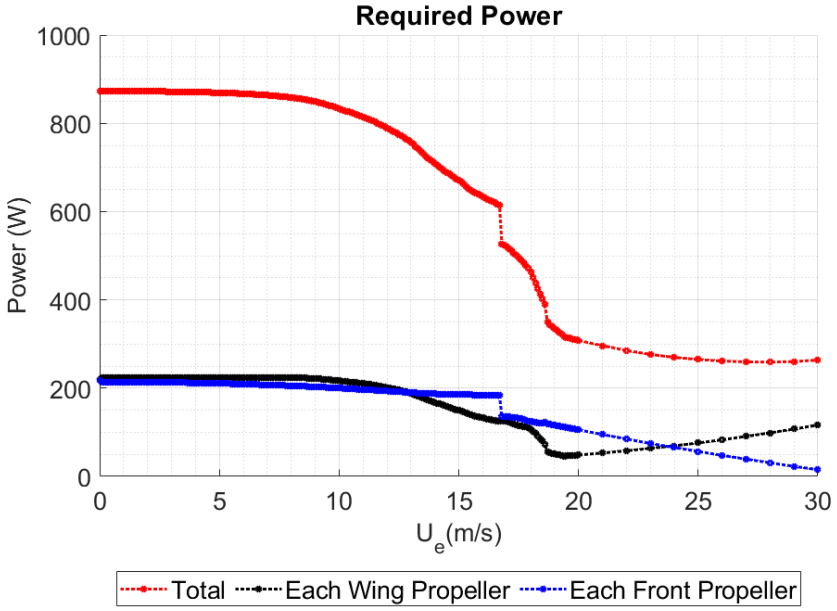

Figure 12 – Required power from the propellers.

5.2 Equations of motion linearization

In order to linearize the equations of motion, it is assumed that a series of nonlinear equation that describe the aircraft system dynamics can be expressed as follows, being that, $\mathbf{f}$ is a vector of n scalar nonlinear functions f_i.

$$\mathbf{f}\left(\dot{\mathbf{X}}, \mathbf{X}, \mathbf{U}\right) = 0 \tag{5.4}$$

It is now considered small perturbations from the steady-state condition X_e, U_e and derive a set of linear constant-coefficient state equations. If expand the nonlinear state equations in a Taylor series about the equilibrium point (X_e, U_e) and keep only the first-order terms, it is found that the perturbations in the state, state derivative, and control vectors must satisfy, according to (STEVENS; LEWIS; JOHNSON, 2015).

$$\nabla_{\dot{\mathbf{X}}} f_1 \delta\dot{\mathbf{X}} + \nabla_{\mathbf{X}} f_1 \delta\mathbf{X} + \nabla_{\mathbf{U}} f_1 \delta\mathbf{U} = 0 \tag{5.5}$$

$$\nabla_{\dot{\mathbf{X}}} f_2 \delta\dot{\mathbf{X}} + \nabla_{\mathbf{X}} f_2 \delta\mathbf{X} + \nabla_{\mathbf{U}} f_2 \delta\mathbf{U} = 0 \tag{5.6}$$

$$\vdots \tag{5.7}$$

$$\nabla_{\dot{\mathbf{X}}} f_n \delta\dot{\mathbf{X}} + \nabla_{\mathbf{X}} f_n \delta\mathbf{X} + \nabla_{\mathbf{U}} f_n \delta\mathbf{U} = 0 \tag{5.8}$$

The 'delta' operator represents (δ) small perturbations, and the 'nabla' operator (∇) represents a row vector of first partial derivatives, as in Eq.(5.9).

$$\nabla_{\mathbf{X}} f_i = \begin{bmatrix} \frac{\partial f_i}{\partial X_1} & \frac{\partial f_i}{\partial X_2} & \cdots & \frac{\partial f_n}{\partial X_n} \end{bmatrix} \tag{5.9}$$

The system of equations can be written in implicit linear state-variable form as in Eq.(5.10).

$$J_E \dot{\mathbf{x}} = J_A \mathbf{x} + J_B u \tag{5.10}$$

Wherein, $\dot{\mathbf{x}}$, $\mathbf{x}$ and $\mathbf{u}$ are perturbation vectors from the equilibrium point, defined as in Eq.(5.11) and Eq.(5.12).

$$\mathbf{X} = \mathbf{X}_e + \mathbf{x} \tag{5.11}$$

$$\mathbf{U} = \mathbf{U}_e + \mathbf{u} \tag{5.12}$$

And the coefficient matrices, or Jacobian matrices, must be calculated at the equilibrium point. So,

$$J_E = -\begin{bmatrix} \nabla_{\dot{\mathbf{X}}} f_1 \\ \vdots \\ \nabla_{\dot{\mathbf{X}}} f_n \end{bmatrix}_{\mathbf{X}=\mathbf{X}_e, \mathbf{U}=\mathbf{U}_e} \tag{5.13}$$

$$J_A = \begin{bmatrix} \nabla_{\mathbf{X}} f_1 \\ \vdots \\ \nabla_{\mathbf{X}} f_n \end{bmatrix}_{\mathbf{X}=\mathbf{X}_e, \mathbf{U}=\mathbf{U}_e} \tag{5.14}$$

$$J_B = \begin{bmatrix} \nabla_{\mathbf{U}} f_1 \\ \vdots \\ \nabla_{\mathbf{U}} f_n \end{bmatrix}_{\mathbf{X}=\mathbf{X}_e, \mathbf{U}=\mathbf{U}_e} \tag{5.15}$$

The resulting system of equation can be decoupled in longitudinal and lateral states, which are then defined in Eq.(5.16) and Eq.(5.17), and their respective controls in Eq.(5.18) and Eq.(5.19).

$$\mathbf{X}_{long} = (U, W, Q, \theta, h) \tag{5.16}$$

$$\mathbf{X}_{lat} = (U, V, P, R, \phi, \psi) \tag{5.17}$$

$$\mathbf{U}_{long} = (\delta_f, \delta_e, \delta_c, \omega_{R_1}, \omega_{R_2}, \omega_{R_3}, \omega_{R_4}) \tag{5.18}$$

$$\mathbf{U}_{lat} = (\delta_r, \delta_{a_L}, \delta_{a_R}, \omega_{R_1}, \omega_{R_2}, \omega_{R_3}, \omega_{R_4}) \tag{5.19}$$

Finally, decoupling the systems of equations and rearranging terms, it is defined in Eq.(5.20) the linearized system of equations of motion for the longitudinal states and controls disturbances, and in Eq.(5.21) the linearized system of equations of motion for the lateral states and controls disturbances.

$$\dot{\mathbf{x}}_{long} = A_{long}\mathbf{x}_{long} + B_{long}u_{long} \tag{5.20}$$

$$\dot{\mathbf{x}}_{lat} = A_{lat}\mathbf{x}_{lat} + B_{lat}u_{lat} \tag{5.21}$$

5.3 Stability analysis

A important analysis of the stability of the aircraft is the open-loop evaluation of the flight modes eigenvalues of the linearized system of equations of motion for the longitudinal and lateral states. So, the system of equations of motion were linearized over the range of trim conditions for flight speeds ranging from 0 to 30 m/s, and the eigenvalues of the A_{long} and A_{lat} were evaluated, that is, the plant open-loop stability analysis, they are shown in Figure 13.

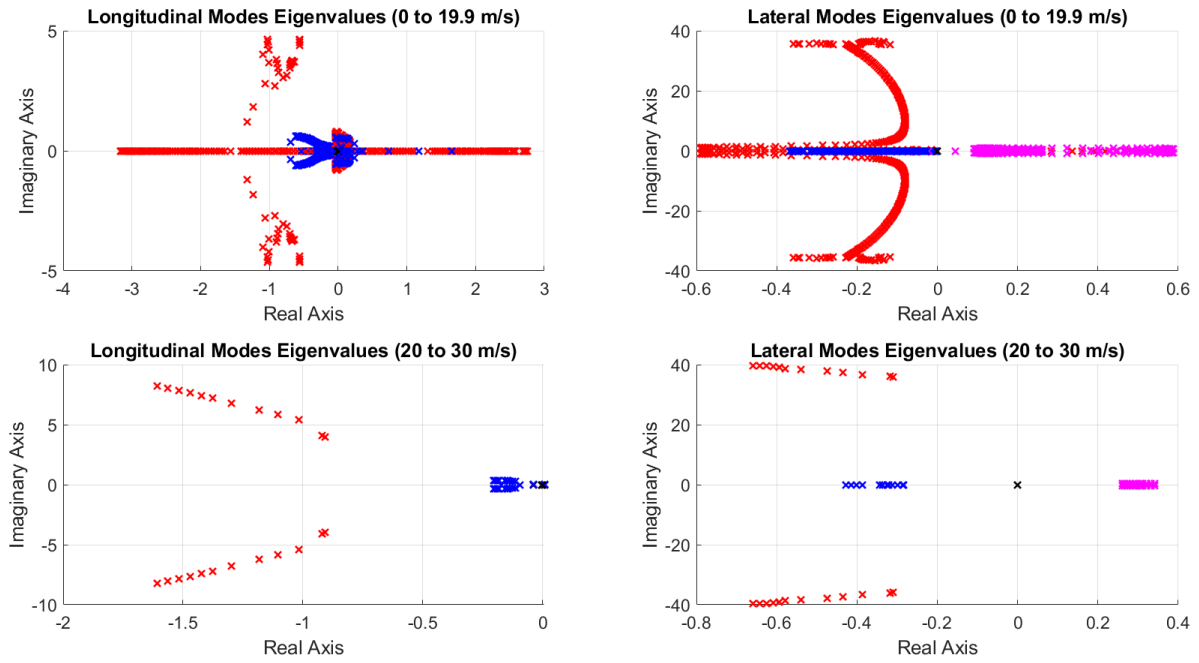

Figure 13 – Open-loop longitudinal and lateral flight modes eigenvalues.

From 0 to 19.9 m/s there are some longitudinal and lateral modes eigenvalues that have positive real part, which means natural instability. Therefore, there must be active control to stabilize the aircraft. From 20 to 30 m/s all longitudinal flight modes have negative real parts, thus are all stable, whereas some lateral modes eigenvalues have positive real part, therefore, unstable.

5.4 Transition Flight Control Simulation

The equilibrium points were computed which allows for a steady state flight in some given aircraft flight speed, now it is important to be able to transition between the given points. The strategy to control the flight is shown in Figure 14 with the control architecture diagram used for simulation, which has the following main blocks: aircraft dynamics, controller and reference scheduler.

The aircraft dynamics block is the grouping of the dynamic equations previously described, that is, Eq.(4.13), Eq.(4.34), Eq.(4.41), Eq.(4.42), Eq.(4.44), Eq.(4.45), which can be numerically integrated to obtain the state variables over time.

Furthermore, the controller block for simulation is expanded in Figure 15, whose purpose is to compute the control vector $\mathbf{U}$ in order to stabilize the aircraft in the current steady state reference $\mathbf{X}_e$, remembering that in the trimmed condition there is a control reference $\mathbf{U}_e$ that must be complemented by $\mathbf{u}$ in order to control the aircraft given some state variables disturbances ($\mathbf{U} = \mathbf{U}_e + \mathbf{u}$). Thus the control system must compute the

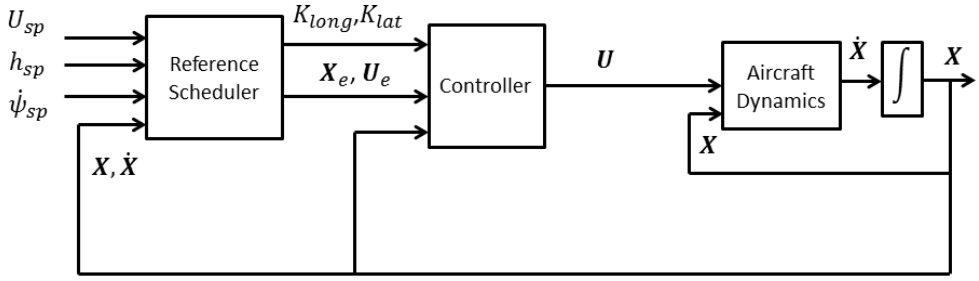

Figure 14 – Control architecture diagram for simulation.

disturbance $\mathbf{x}$ from reference condition ($\mathbf{x} = \mathbf{X} - \mathbf{X}_e$).

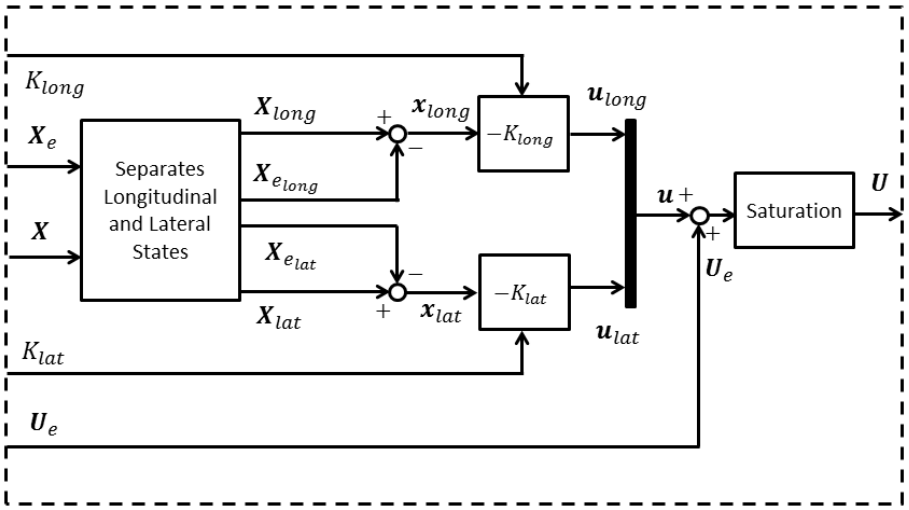

Figure 15 – Controller block diagram for simulation.

The state vector is separated in longitudinal and lateral states of Eq.(5.16) and Eq.(5.17), in order to have a decoupled system with longitudinal and lateral control. Lastly, the disturbances in the longitudinal and lateral motion are multiplied by longitudinal and lateral gain matrices in order to compute the controls: ($\mathbf{u}_{long} = -K_{long}\mathbf{x}_{long}$) and ($\mathbf{u}_{lat} = -K_{lat}\mathbf{x}_{lat}$). In this way, every aerodynamic actuator and propeller command is computed and assembled in the resulting $\mathbf{u}$ and final full control vector $\mathbf{U}$, which must then be saturated in order to avoid exceed the maximum possible values.

The longitudinal and lateral gain matrices (K_{long}, K_{lat}), to apply in the simulations, were computed using the linear quadratic regulator theory (LQR) (OGATA, 2010; STEVENS; LEWIS; JOHNSON, 2016) applied to linearized equations of motion at the equilibrium points, for each pair of longitudinal and lateral equilibrium vectors of the set of equilibrium points. The gain matrices must be selected by the reference scheduler block. The resulting gain matrices (K_{long}, K_{lat}) for the range of reference flight speeds are shown in the Appendix C.

Finally, the remaining block of the control architecture is the reference scheduler

block described in Figure 16, whose purpose is to select the proper gain matrices and state reference vectors from the pilot commands. The control architecture would have primarily three inputs: the aircraft flight speed setpoint (U_{sp}), the desired altitude setpoint (h_{sp}) and the desired turn rate setpoint ($\dot{\psi}_{sp}$), however in this work only flight speed control is simulated.

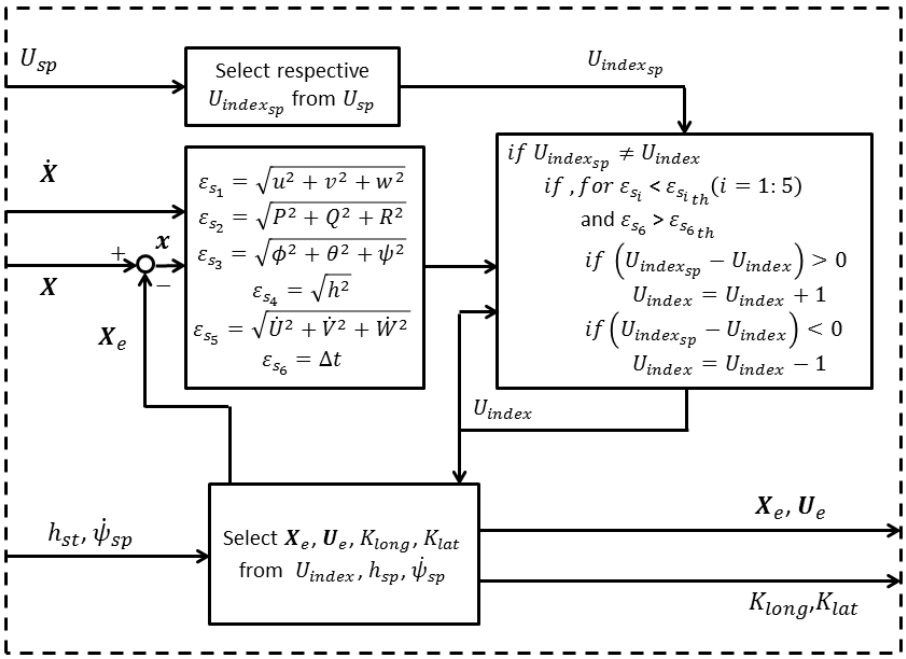

Figure 16 – Reference scheduler block diagram for simulation.

The flight speed setpoint is the desired speed to be achieved by the aircraft. So, in order to accelerate or decelerate, the chosen flight transition concept is to gradually move from equilibrium points, that is, accelerate towards the next equilibrium point $\mathbf{X}_e$ slightly tilting the aerodynamic surfaces and wait until the control system diminishes the state disturbances $\mathbf{x}$ from the current equilibrium reference $\mathbf{X}_e$, and only allows the acceleration to continue until the next equilibrium vector if the dynamic system is sufficiently stabilized. The stability criteria to permit the change in state reference are the following cost functions: ε_1 (velocity disturbance from reference), ε_2 (angular velocity disturbance from reference), ε_3 (attitude disturbance from reference), ε_4 (altitude disturbance from reference), ε_5 (acceleration disturbance from reference) and ε_6 (time since last transition) grouped in Eq.(5.22), being less than thresholds $\varepsilon_{1_{th}}$, $\varepsilon_{2_{th}}$, $\varepsilon_{3_{th}}$, $\varepsilon_{4_{th}}$, $\varepsilon_{5_{th}}$ and greater than $\varepsilon_{6_{th}}$.

$$\begin{cases} \varepsilon_1 = \sqrt{u^2 + v^2 + w^2} \\ \varepsilon_2 = \sqrt{P^2 + Q^2 + R^2} \\ \varepsilon_3 = \sqrt{\phi^2 + \theta^2 + \psi^2} \\ \varepsilon_4 = \sqrt{h^2} \\ \varepsilon_5 = \sqrt{\dot{U}^2 + \dot{V}^2 + \dot{W}^2} \\ \varepsilon_6 = \Delta t \end{cases} \tag{5.22}$$

Additionally, the reference vectors are grouped with respect to the equilibrium flight velocity, so that each equilibrium vector is related to an auxiliary variable named U_{index}. Therefore, for an accelerated flight the U_{index} must increase gradually, whereas for a decelerated flight the U_{index} must decrease. This concept is better illustrated in Figure 17; in this figure we show that each U_{index} is associated to a flight speed and longitudinal and lateral states and controls. Thus, the flight speed setpoint aims the objective U_{index}, and the control system switches between U_{index} which updates the current controller parameters $(\mathbf{X}_e, \mathbf{U}_e, K_{long}, K_{lat})$ gradually as the aircraft becomes sufficiently stable. Moreover, the inputs h_{sp} and $\dot{\psi}_{sp}$ updates the corresponding equilibrium state variables for the current U_{index}, causing the aircraft to climb, descend or turn.

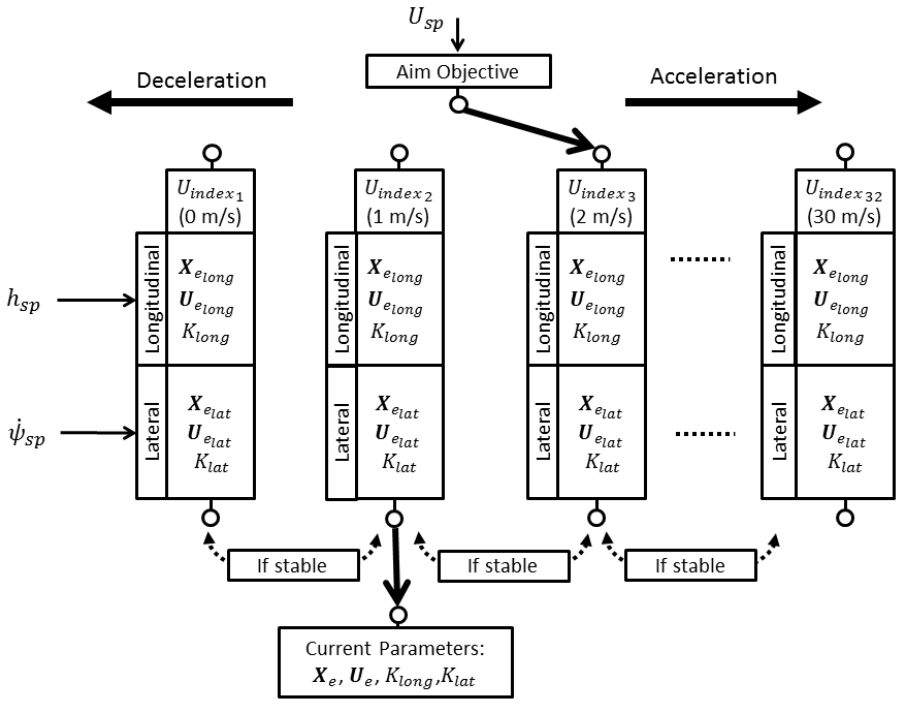

Figure 17 – Reference scheduler parameters selection for simulation.

5.5 Simulation Results

So, the control architecture diagram of Figure 14 was implemented in the MATLAB/Simulink software environment (MATLAB, 2010) in order to simulate the transition flight from hover to cruise condition, and from cruise to hover condition, where the trim conditions are previously computed and stored in matrix form to be selected by the transition algorithm. The gain matrices (K_{long}, K_{lat}) as function of reference flight speeds are shown in Appendix C. Furthermore, results are presented only for transition flight simulation, where the integration time steps were 0.0001 seconds, and the transition stability thresholds applied are listed in Table 7. Moreover, the aerodynamic coefficients and derivatives at the transition trajectory are shown in the Appendix A, and the reference altitude is 100 m.

Table 7 – Transition stability thresholds

Cost function	Definition	ε_{th} (Threshold)
ε_1	$\sqrt{u^2 + v^2 + w^2}$	8
ε_2	$\sqrt{P^2 + Q^2 + R^2}$	0.1
ε_3	$\sqrt{\phi^2 + \theta^2 + \psi^2}$	0.1
ε_4	$\sqrt{h^2}$	6
ε_5	$\sqrt{\dot{U}^2 + \dot{V}^2 + \dot{W}^2}$	1
ε_6	Δt	0.5

5.5.1 Transition Flight

First, in Figure 18 there are the results for the flight states for transition simulation of 0 to 30 m/s, and in Figure 20 the controls. There is also the simulation for transition from cruise to hover (30 m/s to 0 m/s), with the flight states in Figure 24 and the controls in Figure 26. The cost functions that govern the transition between trim points are shown in Figure 22 and Figure 28. Moreover, each of these results are followed by graphs with a closer look at the most critical transition phase, for the accelerated flight for the simulation time from 85 to 95 seconds, and for the decelerated flight for the simulation time from 20 to 30 seconds.

The complete transition from take-off (0 m/s) to maximum speed (30 m/s) takes 125 seconds and 1530 m of horizontal distance, and from maximum speed to landing (0 m/s) takes also 125 seconds and 1469 m. The results are summarized in Table 8.

Table 8 – Longitudinal flight simulation results summary

U_e (m/s)	Time to transition (s)	Horizontal distance (m)	Energy Consumed (mmAh)
0 to 30	125	1530	1635
30 to 0	125	1469	1644

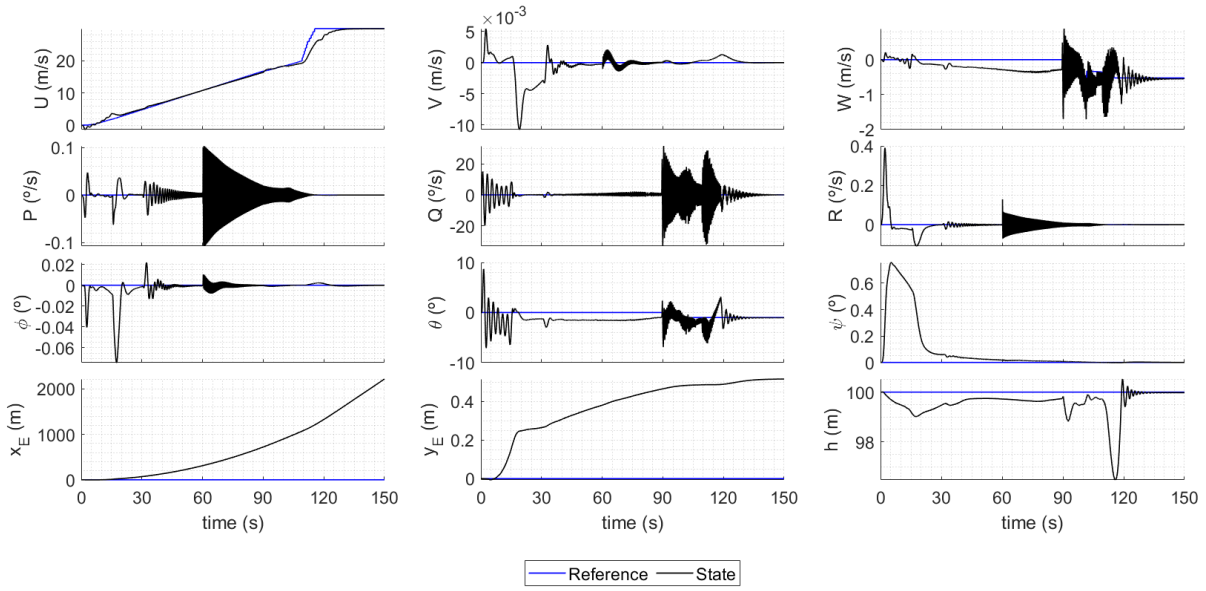

Figure 18 – Simulation flight states, transition from 0 to 30 m/s.

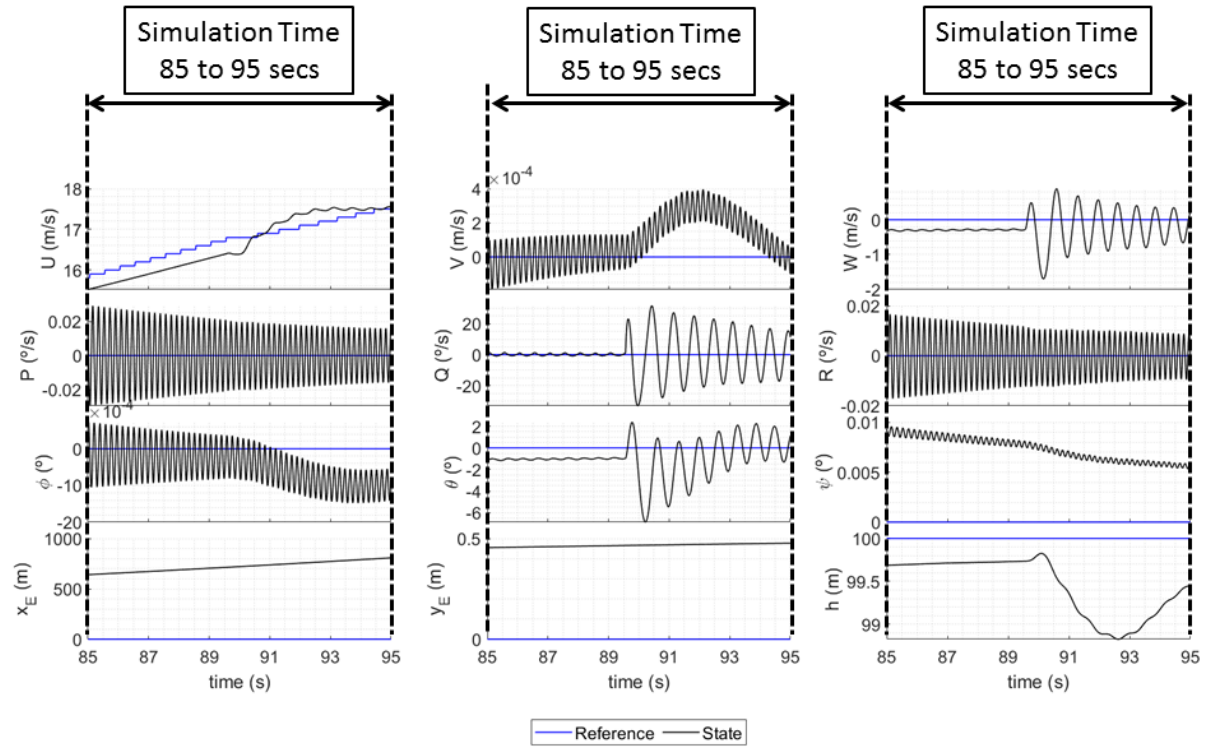

Figure 19 – Simulation flight states, transition from 0 to 30 m/s (Simulation time 85 to 95 seconds).

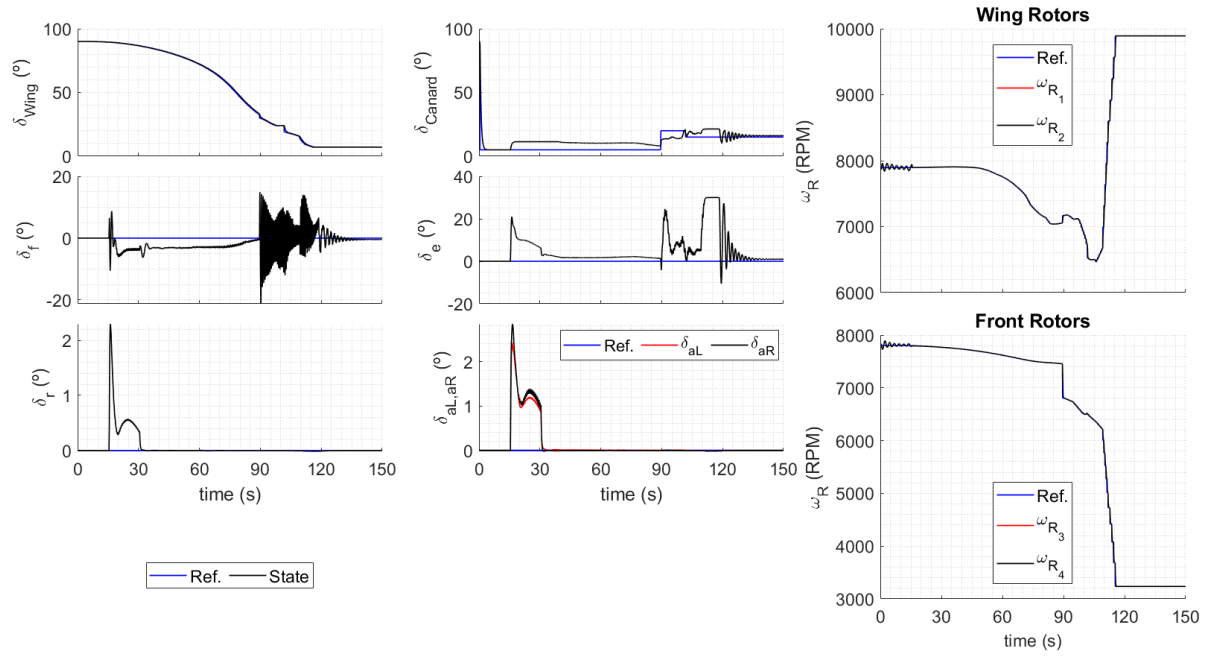

Figure 20 – Simulation controls, transition from 0 to 30 m/s.

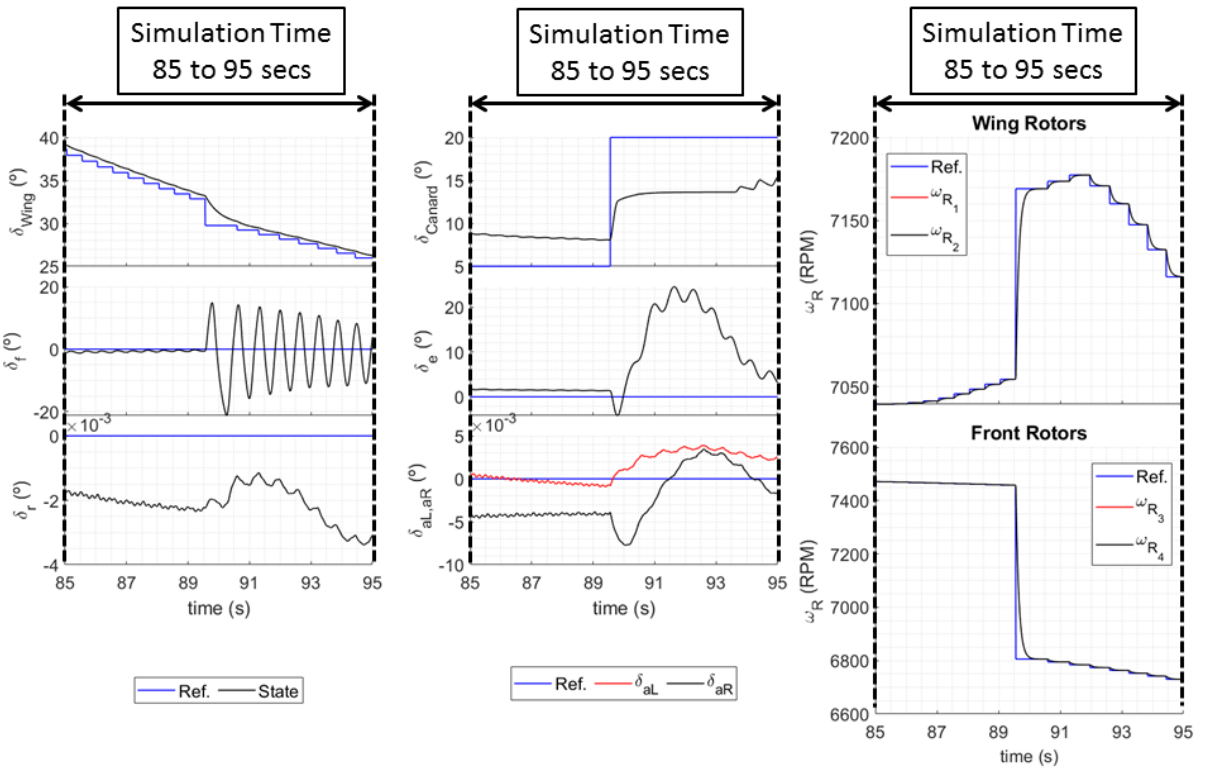

Figure 21 – Simulation controls, transition from 0 to 30 m/s (Simulation time 85 to 95 seconds).

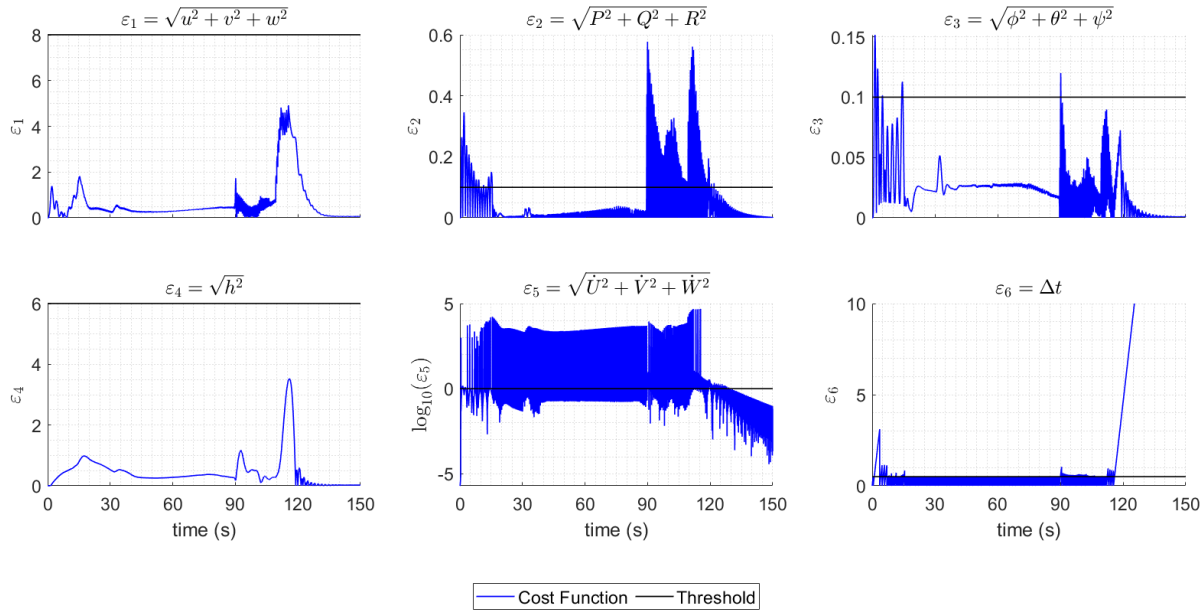

Figure 22 – Simulation transition cost functions, transition from 0 to 30 m/s.

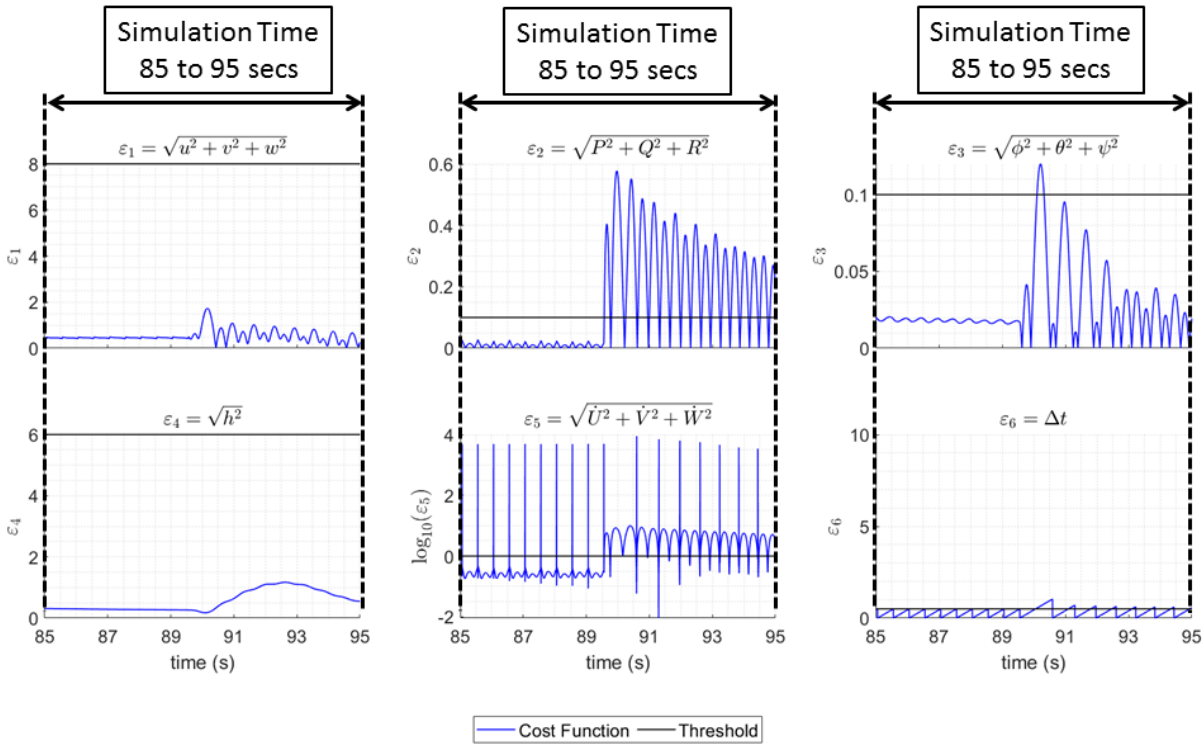

Figure 23 – Simulation transition cost functions, transition from 0 to 30 m/s (Simulation time 85 to 95 seconds).

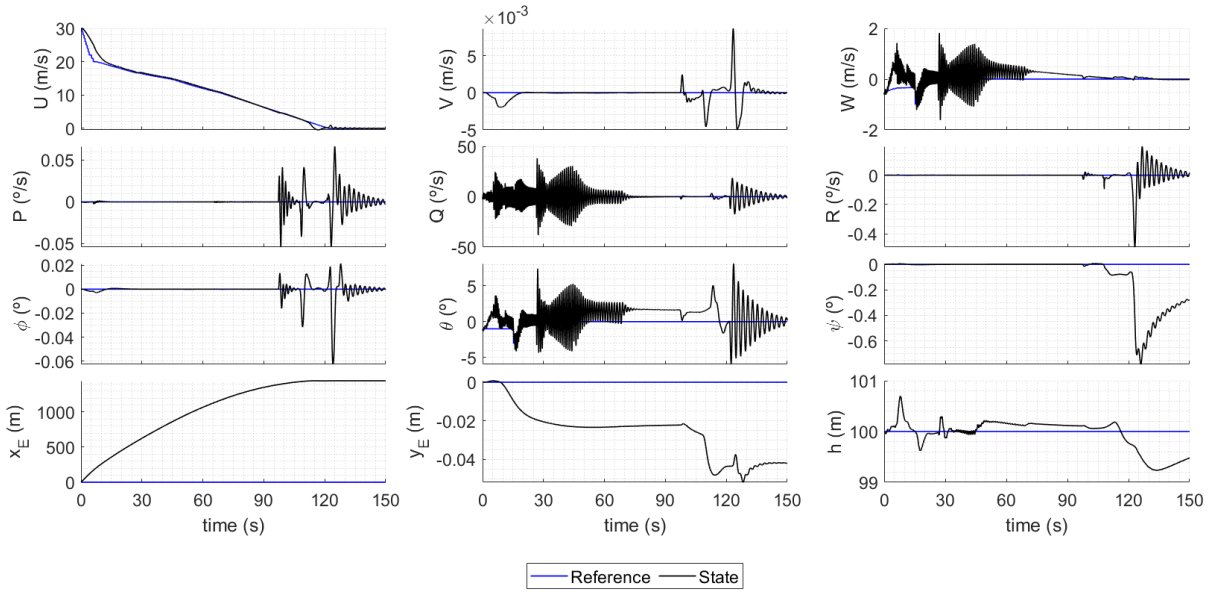

Figure 24 – Simulation flight states, transition from 30 to 0 m/s.

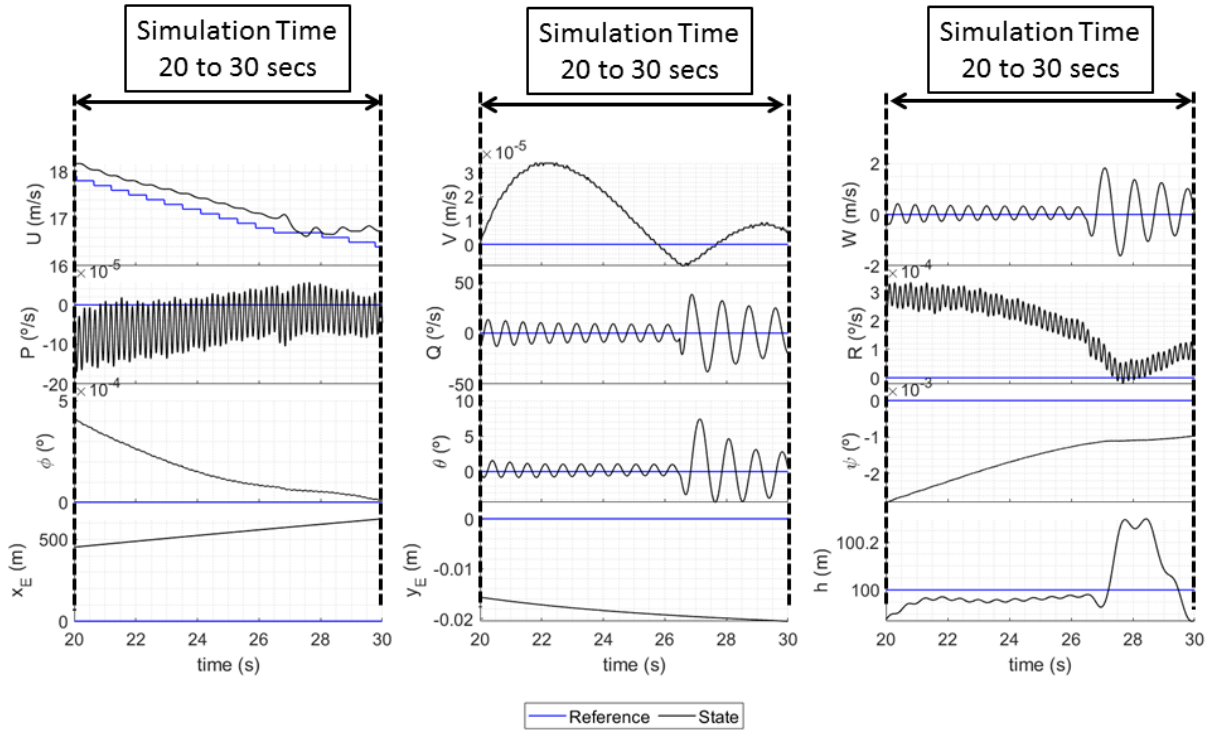

Figure 25 – Simulation flight states, transition from 30 to 0 m/s (Simulation time 20 to 30 seconds).

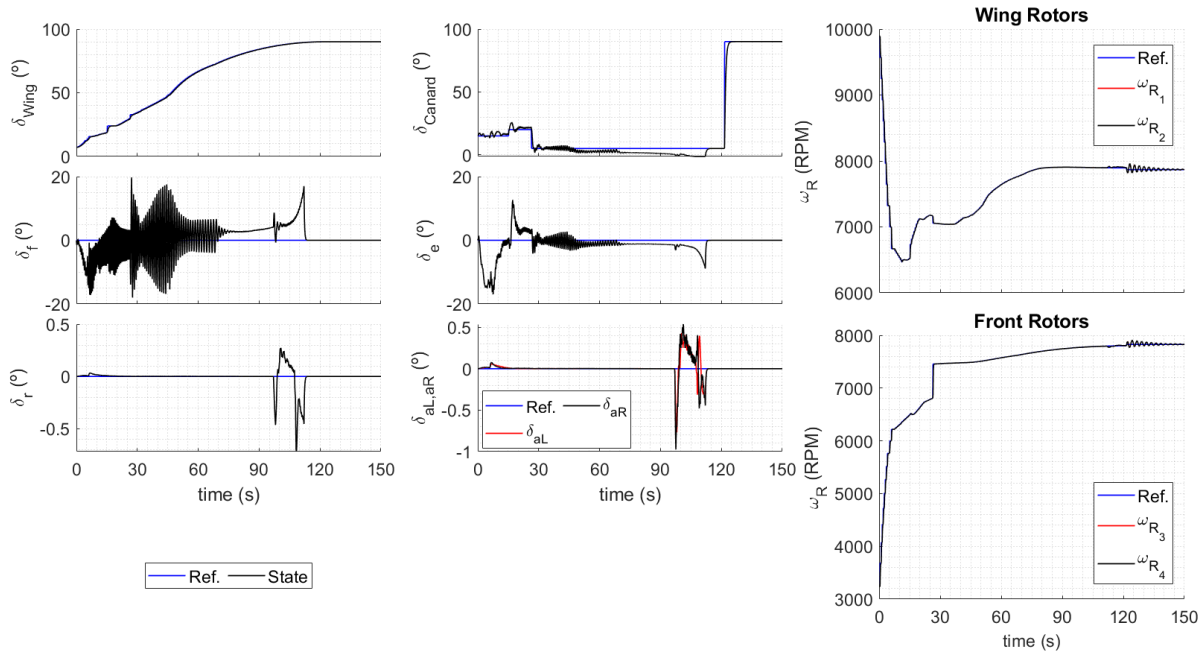

Figure 26 – Simulation controls, transition from 30 to 0 m/s.

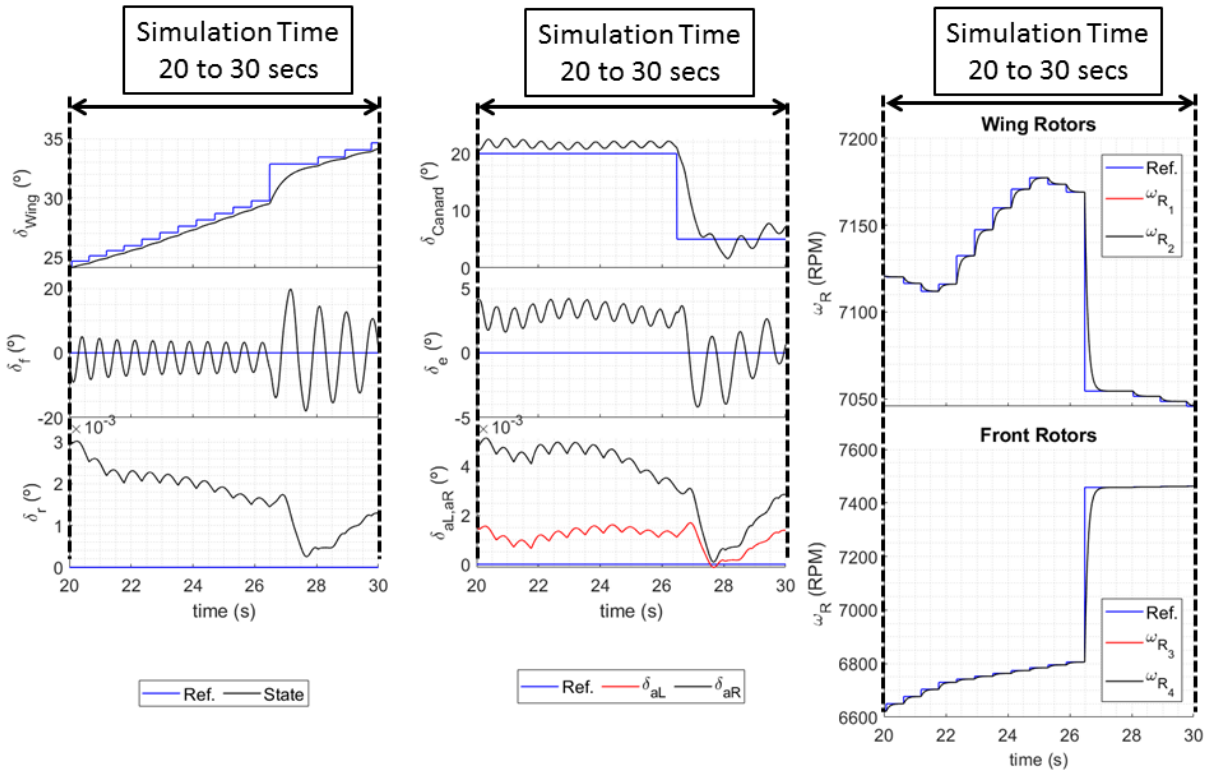

Figure 27 – Simulation controls, transition from 30 to 0 m/s (Simulation time 20 to 30 seconds).

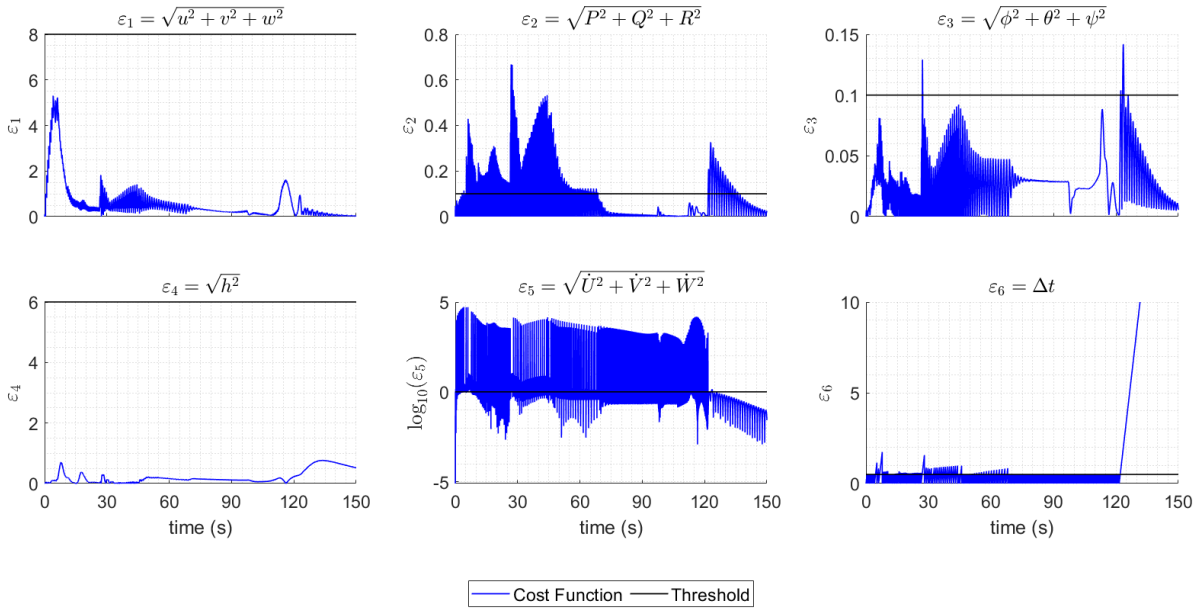

Figure 28 – Simulation transition cost functions, transition from 30 to 0 m/s.

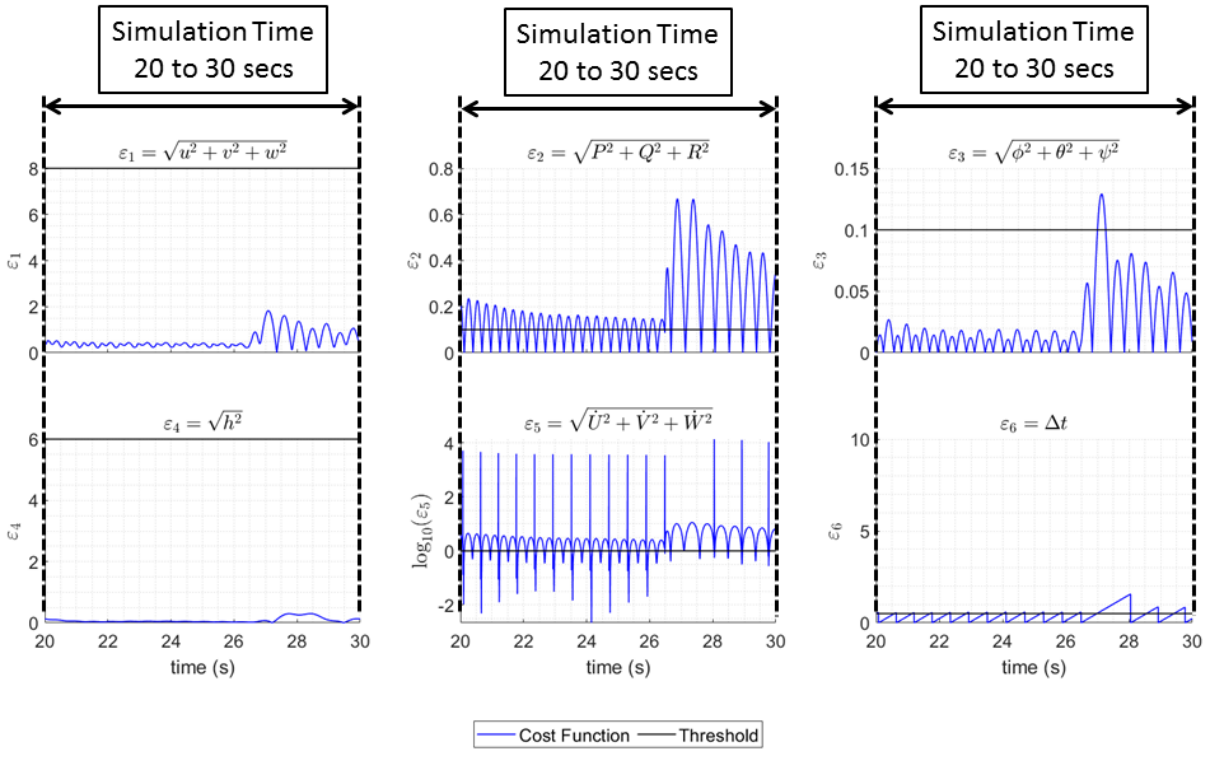

Figure 29 – Simulation transition cost functions, transition from 30 to 0 m/s (Simulation time 20 to 30 seconds).

There are two main control stages to complete the full transition flight from hover (0 m/s) to maximum flight speed (30 m/s), which are defined with respective to the

reference flight speed U_e, so that at each stage there are some active controls and some remain neutral. They are defined in Table 9.

From reference flight speed U_e from 0 to 1.9 m/s, the active controls are the four propellers, and no aerodynamic actuator is active, therefore remaining in the reference position. That is because the aerodynamic dynamic pressure is too small to have an effective control. For U_e from 2.0 to 30.0 m/s, the active controls are the four propellers, the flaps, elevators, rudder, ailerons and canard, being that the canard can only tilt -10° to +10° from the reference tilt angle to control the vehicle.

Table 9 – Longitudinal flight active controls as function of reference flight speed

Transition Stage	U_e (m/s)	Active Controls
1	0 to 1.9	ω_{R_1},ω_{R_2}, ω_{R_3}, ω_{R_4}
2	2.0 to 30.0	$\omega_{R_1}, \omega_{R_2}, \omega_{R_3}, \omega_{R_4}, \delta_f, \delta_e, \delta_c, \delta_r, \delta_{aR}, \delta_{aL}$

Moreover, there is an important phase which is the transition from inclined wing aerodynamic stalled to more horizontal and aerodynamic loaded. This can be noticed in the trim data of Figure 8 where the wing position goes from 90° tilt angle at hover (0 m/s), gradually decreases the tilt angle until 24° at $U_e = 16.7m/s$, where the canard must increase its tilt angle from 5° to 20° in order to trim the vehicle. In Figure 18 the vehicle keeps a continuous acceleration up until $U_e = 20m/s$, whilst having oscillations in attitude and altitude given that the wing is in the nonlinear range of angle of attack (close to the maximum lift coefficient). From $U_e = 20m/s$ to maximum flight speed at $U_e = 30m/s$ there is an even higher acceleration rate, where the wing is at the linear range of angle of attack. Moreover, in order to keep the continuous acceleration and transition the aircraft main body pitch angle is kept at negative values, so that the front propellers thrust point upwards and forward.

For the decelerated flight in Figure 24 there is also two regions with almost constant rate of deceleration, from $U_e = 30m/s$ to $U_e = 20m/s$, and from $U_e = 20m/s$ to $U_e = 0m/s$, where the aircraft pitch angle is kept at positive values for the most of the maneuver, so that the front propellers would point upwards and backwards. The altitude oscillates for roughly -1.0 to +1.0 m for the full transition.

The wing tilting at the low flight speeds causes oscillations in attitude, and even in the lateral directional flight states such as roll and yaw Euler angles and angular velocities, causing sideslip, which is a result of the gyroscopic moments of the tilting of the propellers at high angular speeds.

The actuators and rotors controls are depicted in Figure 20 for the accelerated flight and in Figure 26 for the decelerated flight, where it is noticeable the gradual wing tilting close to the reference tilt angle during transitional flight, as well as the active tilting of the canard with considerable displacement in relation to the reference, which is due to

the action of the controller to stabilize the flight. Also, during high flight speeds the flaps and elevator are actuated in a high frequency and deflection angles, in response to the tilting of the wing in conditions of considerable aerodynamic loading.

In order to have a better understanding of the aircraft dynamics, its oscillatory movement and controls action, the states, controls and cost functions were highlighted at the critical phase of the transition in Figure 19, Figure 21 and in Figure 23 for the accelerated flight for simulation time 85 to 95 seconds and in Figure 25, Figure 27 and Figure 29 for the decelerated flight for simulation time 20 to 30 seconds. In this critical phase the aircraft performs the maneuver of wing at high lift coefficient and canard is tilted at high angle of attack. This maneuver causes a change in the dynamic response noticeable by the amplitude of the states and controls oscillations.

The switching between reference states and controls occurs when the transition cost functions reach their thresholds, being their time series depicted in Figure 22 for the accelerated flight and in Figure 28 for the decelerated flight. It is worth mentioning that the cost functions that mostly govern the transition are related to attitude and acceleration instabilities, that is, cost functions ε_2, ε_3 and ε_5. The cost function ε_6 (minimum time between transitions switching) is important to impose a time constraint in order to wait for some stabilization before switching to the next equilibrium point, otherwise the switching would occur before the dynamics of the system can develop.

The torque at wing and canard axis was also computed and shown in Figure 30 for the transition from hover to maximum speed, and in Figure 31 from maximum speed to hover. It is noticeable that the maximum torque at wing occur at the critical phase where the wing moves from fully horizontal to inclined. In this figures are also depicted the total energy consumed by the propellers to perform the maneuver, being that the total energy consumed is displayed in Table 8.

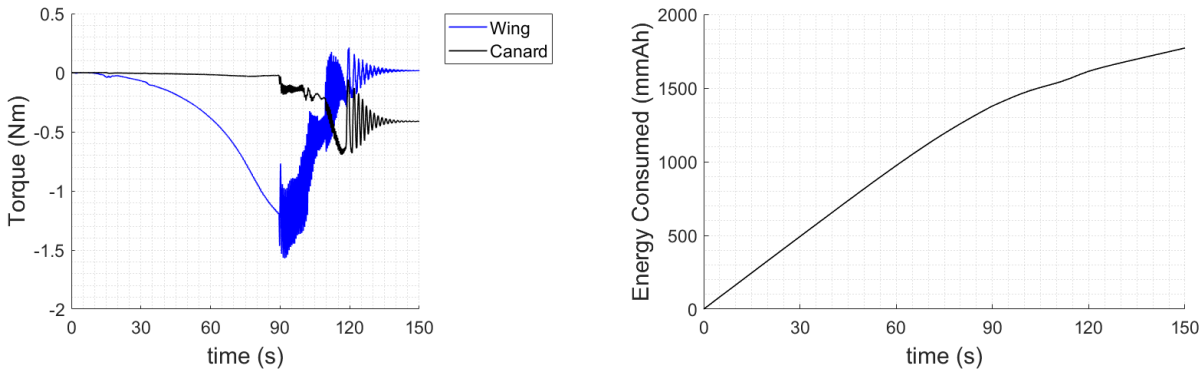

Figure 30 – Simulation torque at wing and canard axis, and energy consumed, transition from 0 to 30 m/s.

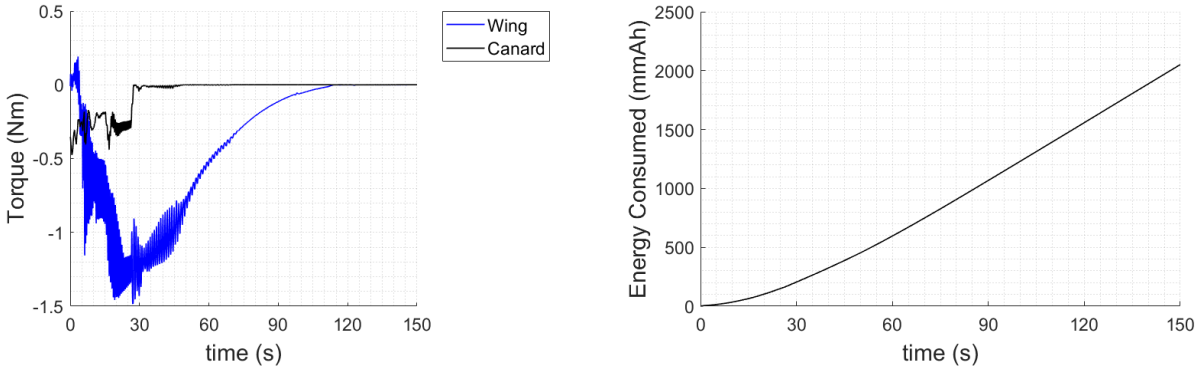

Figure 31 – Simulation torque at wing and canard axis, and energy consumed, transition from 30 to 0 m/s.

5.5.2 Longitudinal Full Transition Flight

The aircraft shall have two Lipo 4S batteries for the propulsion system, one for the right wing and front motors, and the other for the left wing and front motors. Each battery have 5200 mmAh energy capacity, therefore, a total of 10400 mmAh.

From Table 8 the transition from hover to cruise takes 125 seconds (2.08 minutes), 1530 m, and 1635 mmAh of energy, and the transition for landing 125 seconds (2.08 minutes), 1445 m and 1641 mmAh, so there is left 7124 mmAh for cruise at maximum speed ($U_e = 30m/s$). The power required at this speed is 263.7 W, from Fig. 12. Dividing the total required power by the batteries rated voltage (14.8 V), gives the required current of 17.81 A. Therefore, the available time for cruise flight is,

$$t_{cruise} = \frac{7.124\,Ah}{17.81\,A} = 0.40\,h = 23.98\,minutes \tag{5.23}$$

So, the vehicle autonomy would be,

$$t_{autonomy} = t_{0to30} + t_{cruise} + t_{30to0} = 2.08 + 23.98 + 2.08 = 28.14\,minutes \tag{5.24}$$

Also, the vehicle range would be,

$$\Delta x_{total} = \Delta x_{0to30} + \Delta\Delta x_{cruise} + x_{30to0} = 1530 + 30 * t_{cruise} + 1469 = 46163\,m \tag{5.25}$$

5.5.3 Lateral Stability

The lateral stability was analyzed by simulating the aircraft controllability from disturbance in a lateral state, being applied in the simulations 5° in roll angle. The

simulations were carried for conditions of constant reference flight speed U_e of 0, 7.5, 15, 22 and 30 m/s. The results are shown in Appendix B.

6 AIRCRAFT PROTOTYPE

In this chapter the aircraft prototype airframe and on-board systems are described, along with the microcontroller board, sensors, communication systems, actuators, motors, batteries and ground station.

The final prototype assembled is shown in Figure 32, Figure 33 and Figure 34.

Figure 32 – Aircraft prototype hover configuration (left), cruise configuration (right).

Figure 33 – Aircraft prototype front view, hover configuration (left), cruise configuration (right).

6.1 Airframe

The aircraft fairings are made of a carbon fiber and glass fiber sandwich composite structure with polyester based fleece in the core. Moreover, the wing and canard have alu-

Figure 34 – Aircraft prototype side view, hover configuration (left), cruise configuration (right).

minum spars, from which the surfaces are attached to the shafts of the tilting mechanisms, that makes the surfaces very stiff.

The fairing were manufactured using vacuum bagging and epoxy resin. In this sense, the molds also needed to be manufactured, which were made using composites of glass fiber and epoxy resin, by the process of hand laminate, where the mold plugs were 3D printed using Polylactic Acid (PLA) filaments. The manufactured molds are shown in Figure 35.

Figure 35 – Molds used to manufacture aircraft fairings.

6.2 Prototype Weight

The final aircraft prototype has a weight of 6.44 kg. Each aircraft prototype part weight are listed in Table 10.

Table 10 – Aircraft prototype parts weight.

Part	Weight (g)
Right Canard	193
Left Canard	180
Right Wing	704
Left Wing	711
Vertical Stabilizer	286
Front Motors Frame	645
Main body	2795
Right Battery	369
Left Battery	371
Auxiliary Battery	185
Total	6439

6.3 Systems architecture

Is this section are described the architecture of important on-board systems: propulsion powering systems, auxiliary battery powering systems and on-board systems communication architecture.

The vehicle has three batteries, and each battery powers specific systems. So, in Figure 36 is the diagram of the propulsion electric systems, in which the left side Lipo 4S 5200 mAh battery powers the left side motors and electronic speed controllers (ESC), and its voltage can be monitored by the microcontroller board by measurement of the voltage output of a voltage divider circuit, shown in Figure 37, which outputs 3.3V (maximum input voltage allowed in the Arduino Due analog input ports) when the battery is fully loaded at 16.8V. For the right side battery, the circuit is exactly the same, powering the right side motors and ESC's.

There is a third battery, the auxiliary battery, which powers all the remaining on-board systems, including the microcontroller board, whose electric diagram is shown in Figure 38.

It is important to mention some circuits of this diagram, which are:

- Voltage divider circuit of Figure 39: from a P4 plug the auxiliary battery is connected and its voltage can be measured by a Arduino Due analog input port, from the output of the voltage divider circuit (max 12.6V to 3.3V).

- Red LED strip optocoupler (TIL111) circuit of Figure 40: the optocoupler is triggered by a digital input from a Arduino Due digital port, which closes the red LED strip circuit.

- Step down circuit for telemetry module of Figure 41: the telemetry module nRF24L01+

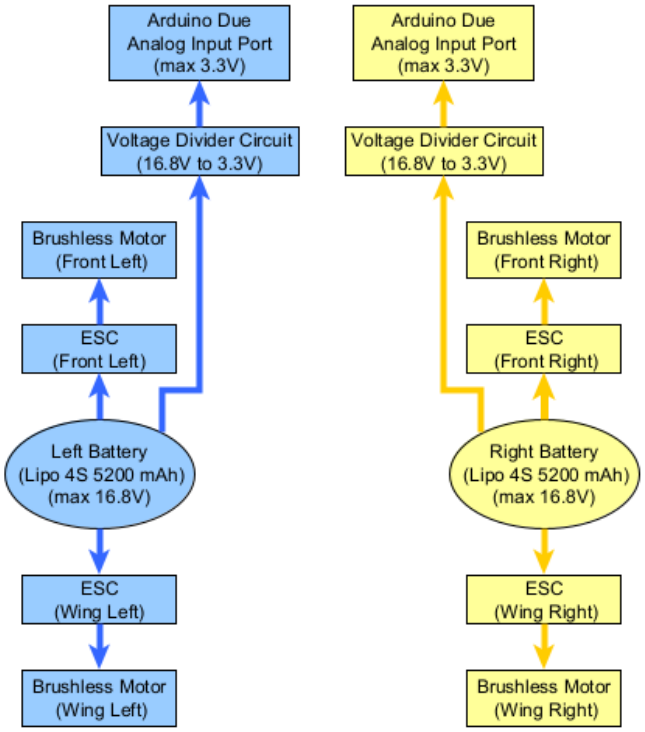

Figure 36 – Propulsion powering systems

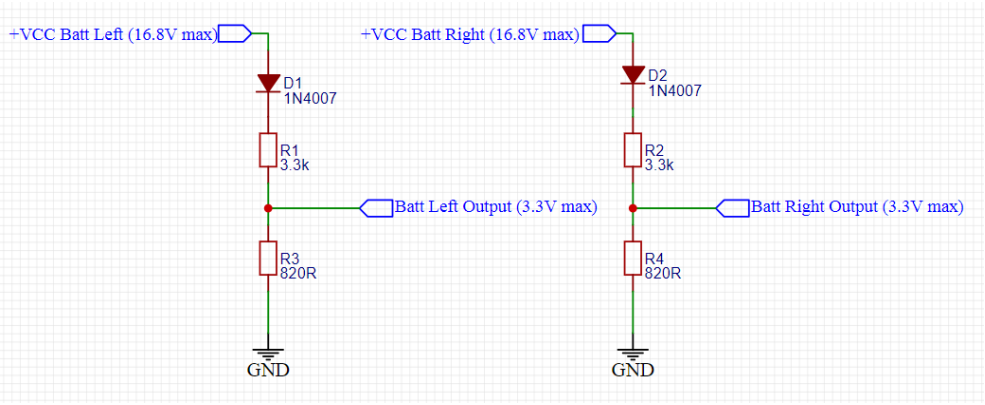

Figure 37 – Voltage divider circuits (max 16.8V to 3.3V)

is powered by this circuit, which has a voltage regulator to output 3.3V (AMS1117-3.3V), from an input of 6.0V. Moreover, it has bypass capacitors to reduce output noise.

Furthermore, there is the on-board systems communication architecture in the diagram of Figure 42, in which the microcontroller board (Arduino Due) communicates with the sensors, radio receiver, electronic speed controllers and servos, using the required communication protocols, being: I2C, UART, SPI and PWM.

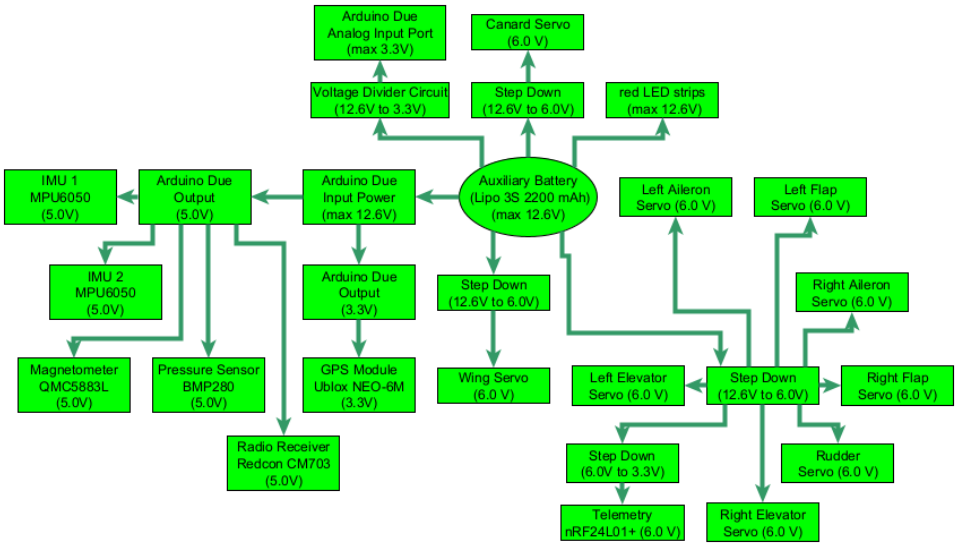

Figure 38 – Auxiliary battery powering systems

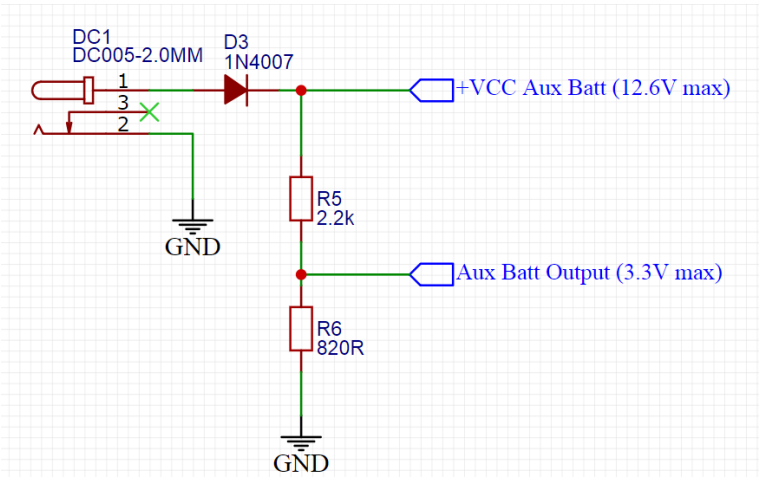

Figure 39 – Voltage divider circuit (max 12.6V to 3.3V)

6.4 Microcontroller board

An Arduino Due, shown in Figure 43, is the control board used to integrate all the others systems of the vehicle, which also holds the control software. Is is a microcontroller board based on the Atmel SAM3X8E ARM Cortex-M3 CPU, 32-bit ARM core microcontroller, whose features are detailed in Table 11.

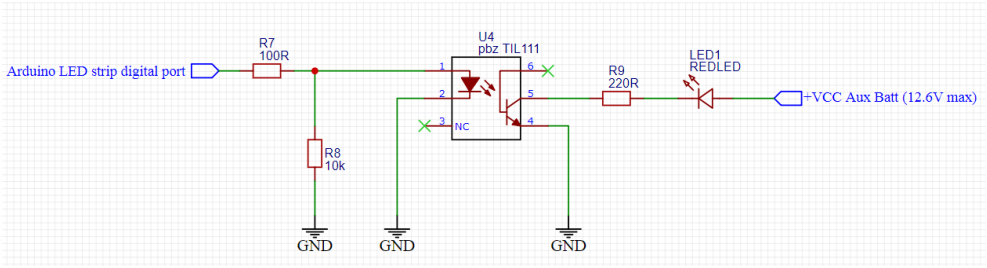

Figure 40 – Red LED strip optocoupler circuit

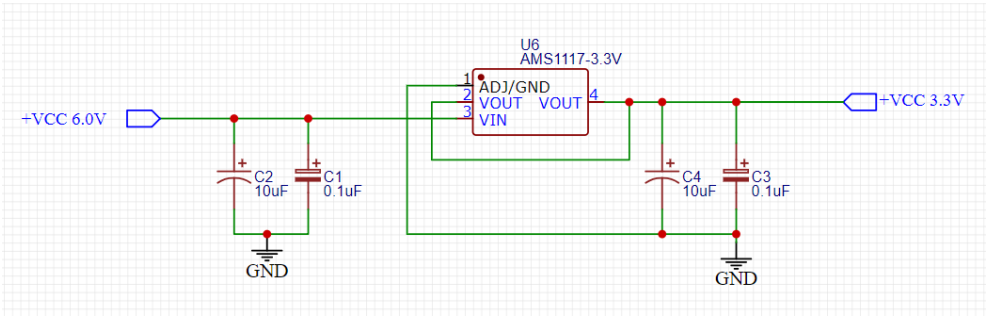

Figure 41 – Step down circuit for telemetry module

Table 11 – Arduino Due microcontroller board features

Microcontroller	AT91SAM3X8E 32-bit
Digital I/O Pins	54
PWM pins	12
Analog input pins I/O	12
UART	yes, 4 serial ports
I2C	yes
SPI	yes
I/O Voltage	3.3V
Input voltage (nominal)	7-12V
Processor clock speed	84 MHz
Memory	96KB SRAM, 512KB flash

6.5 Inertial Measurement Unit (IMU)

On-board the vehicle there are two MPU-6050 Inertial Measurement Unit (IMU), shown in Figure 44. It is an integrated 6-axis motion tracking device that combines a 3-axis gyroscope, 3-axis accelerometer, and a Digital Motion Processor, whose features are detailed in Table 12. Therefore, its purpose is to measure the vehicle accelerations in the 3-axis of the body coordinate frame, and the 3-axis angular velocities.

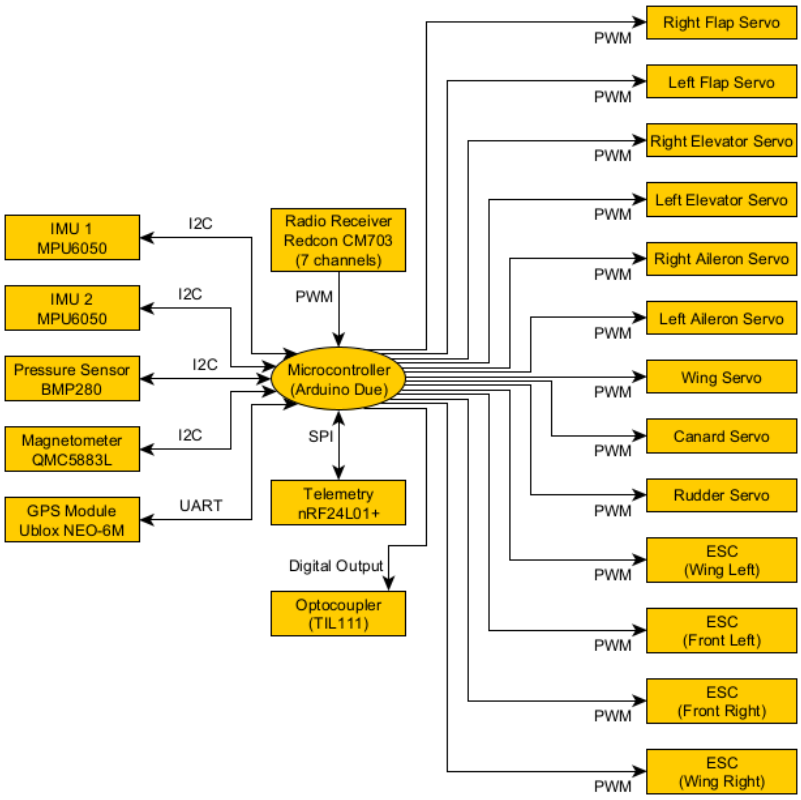

Figure 42 – On-board systems communication architecture

Figure 43 – Arduino Due microcontroller board

Table 12 – MPU-6050 Inertial Measurement Unit features

Input voltage	3-5V
Communication	I2C protocol
Gyroscope range	±250, ±500, ±1000, ±2000 (degrees/s)
Accelerometer range	±2, ±4, ±8, ±16 (g)
Gyroscope measurement rate	up to 8,0 kHz
Accelerometer measurement rate	up to 1,0 kHz

Figure 44 – MPU-6050 Inertial Measurement Unit

6.6 Pressure sensor

The BMP280, shown in Figure 45, is an absolute barometric pressure sensor especially designed for mobile applications, whose features are detailed in Table 13. Its purpose is to compute vehicle altitude, which is obtained from measurements of temperature and atmospheric pressure.

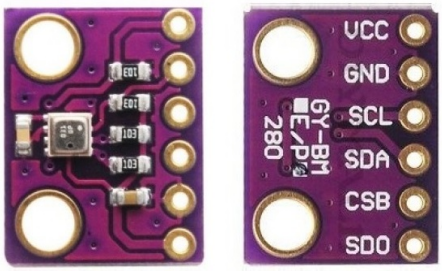

Figure 45 – BMP280 pressure sensor

Table 13 – BMP280 Pressure sensor features

Input voltage	3.3V
Communication	I2C protocol
Pressure range	300 to 1100 hPa (+9000 to -500 m above/below sea level)
Relative accuracy	± 0.12 hPa (equiv. to ± 1,0 m)
Temperature range	-40 to +85°C
Measurement rate	up to 157 Hz

6.7 Magnetometer

The QMC5883L, shown in Figure 46 is a multi-chip three-axis magnetic sensor, whose features are detailed in Table 14. Its purpose is to measure the composition of the local Earth magnetic field, in order to compute the vehicle heading, or yaw angle.

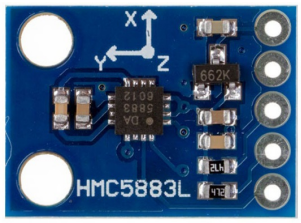

Figure 46 – QMC5883L Magnetometer

Table 14 – QMC5883L Magnetometer features

Input voltage	3-5V
Communication	I2C protocol
Magnetic field range	± 8.0 (gauss)
Heading accuracy	1.0°to 2.0°
Temperature range	-40 to +85°C
Measurement rate	up to 200 Hz

6.8 GPS module

The Ublox GPS module NEO-6M, with antenna, is used, shown in Figure 47, whose features are detailed in Table 15. Its purpose is to measure the vehicle position coordinates, that is, latitude and longitude.

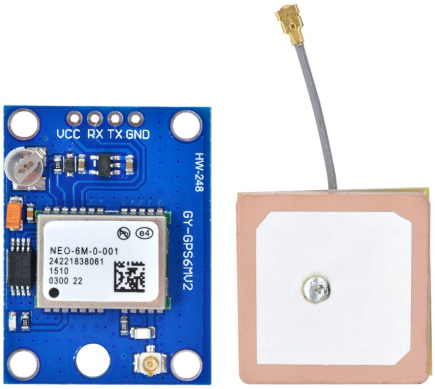

Figure 47 – Ublox NEO-6M GPS module

Table 15 – Ublox NEO-6M GPS module features

Input voltage	3-5V
Communication	UART protocol
Horizontal position accuracy	2.5 m
Measurement rate	1.0 to 5.0 Hz

6.9 Radio transmitter and receiver

The radio transmitter used is the JR X9503 2.4, shown in Figure 48, whose features are detailed in Table 16, and the radio receiver, shown in Figure 49, which goes on-board the vehicle, whose features are detailed in Table 17. The purpose of the pair radio transmitter and receiver is to send command input from the pilot to the vehicle.

Figure 48 – JR X9503 2.4 radio transmitter

Table 16 – JR X9503 2.4 Radio transmitter features

Modulation technology	DSM2/DSM1 protocol
Number of channels	9
Band	2.4 to 2.483 GHz

Figure 49 – Redcon CM703 DSM2/DSMX micro receiver

Table 17 – Redcon CM703 DSM2/DSMX micro receiver features

Modulation technology	DSM2/DSMX protocol
Number of channels	7
Band	2.4 GHz
Input voltage	3.3-10V

6.10 Telemetry system

A pair of nRF24L01+ transceiver, shown in Figure 50, whose features are detailed in Table 18, are used as telemetry system between the vehicle and a ground station. Its purpose is to transmit flight data from the vehicle to the ground station.

Figure 50 – NRF24L01+ transceiver

Table 18 – nRF24L01+ transceiver features

Modulation technology	GFSK protocol
Number of channels	126
Band	2.4 to 2.4835 GHz
Input voltage	1.9-3.6V
Communication	SPI protocol
Air data rate	250 kbps, 1.0 Mbps, 2.0 Mbps
Transmitter output	-18, -12, -6, 0 dBm
Payload	1 to 32 bytes dynamic payload length

6.11 Canard and wing tilt mechanism

The canard and wing have tilt mechanisms, which are driven by servos, shown in Figure 51, whose features are detailed in Table 19. Whereas, the mechanisms are four-bar linkages (TANG, 2010), which is shown in Figure 52.

Figure 51 – Canard and wing tilt mechanism servos

Table 19 – Canard and wing servos features

	Canard	Wing
Input voltage	4.8-6.0V	4.8-6.0V
Stall torque	6.0V/26kg.cm	6.0V/35kg.cm
Blocking current	2.5A	3.5A
Weight	60 g	60 g

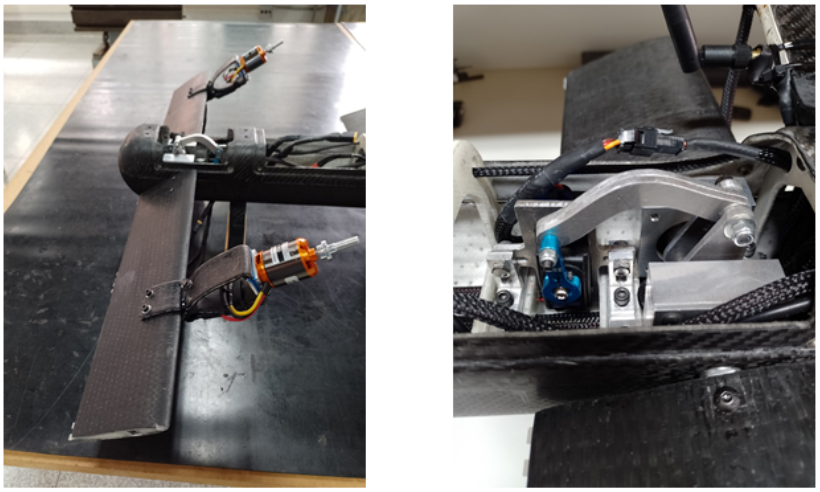

Figure 52 – Wing and canard tilt mechanism

6.12 Aerodynamic control servos

The aerodynamic controls, that is, flap, ailerons, elevators and rudder, are actuated by servos of Figure 53, whose features are detailed in Table 20.

Figure 53 – Aerodynamic control servos (Tower Pro MG90S)

Table 20 – Aerodynamic control servos (Tower Pro MG90S) features

Input voltage	3.0-6.0V
Stall torque	6.0V/2.2kg.cm
Blocking current	1.2A
Weight	14 g

6.13 Propulsion system

6.13.1 Brushless motor

There are in the vehicle four D3548-4 1100 kV brushless motor, shown in Figure 54, whose features are detailed in Table 21. Being that, the two in front are in fixed positions, and the two rear motors tilt along the wing.

Figure 54 – Brushless motor D3548-4 1100 kV

Table 21 – Brushless motor D3548-4 1100 kV features

Input voltage	11.1-18.5V
Maximum power	911 W
Weight	156 g
Maximum thrust (12x6 prop/Lipo battery)	2150 g

6.13.2 Electronic Speed Controller (ESC)

For each brushless motor it is necessary a Electronic Speed Controller, in case being the Hobbywing skywalker 60A ESC shown in Figure 55, whose features are detailed in Table 22. Its purpose is to receive input signal from the control board and consequently drive the motor in the corresponding speed.

Figure 55 – Hobbywing skywalker 60A ESC

Table 22 – Hobbywing skywalker 60A ESC features

Battery cell	2-6S (Lipo)
Continuous current	60 A
Burst current ($\leq$ 10s)	80 A
Weight	63 g

6.13.3 Propeller

The four propellers are Aeronaut CAM Carbon Light 12x5 (inches), shown in Figure 56, being the front left and rear right clockwise, and the front right and rear left counter-clockwise.

Figure 56 – Aeronaut CAM Carbon Light 12x5 propeller (CW and CCW)

6.14 Vehicle batteries

There are three batteries on-board the vehicle, shown in Figure 57, being that two are used to power the motors, and the third, auxiliary battery, powers the remaining systems. Their features are detailed in Table 23.

Figure 57 – Vehicle batteries

Table 23 – Vehicle batteries features

	Propulsion batteries	Auxiliary battery
Number of batteries	2	1
Lipo cells	4S (14.8V)	3S (11.1V)
Capacity	5200 mAh	2200 mAh
Discharge	12C	30C
Weight	370 g	185 g

6.15 Warning lights

There are red LED strips in the front motor support, as shown in Figure 58, which blink to warn the pilot when the setup is running, and when there is low battery voltage.

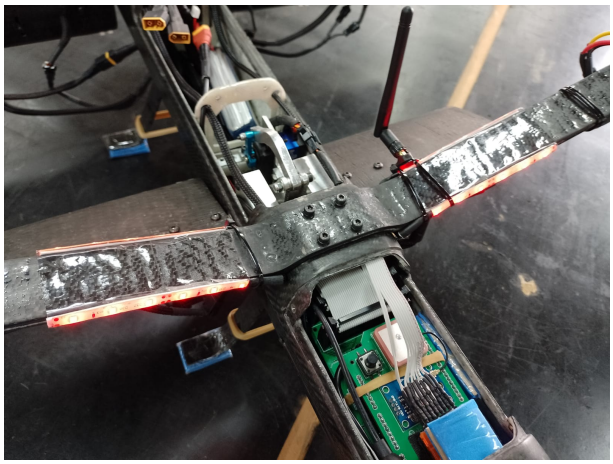

Figure 58 – Vehicle warning lights (red LED strips)

6.16 Integration boards

In order to integrate all the vehicle on-board systems, printed circuit boards were designed, which are attached to the microcontroller board (Arduino Due). So, in Figure 59 is shown the base board that attaches to the Arduino Due, and in Figure 60 the board that goes on top.

They were manufactured in a fiberglass composite (FR4), with 1.6 mm thickness and two layers of copper trails.

In it are coupled the on board systems: IMU 1, IMU 2, pressure sensor, magnetometer, GPS module and radio receiver.

Additionally, there are the following electronics:

- Step down voltage regulator (XL4005-5A) from 3S Lipo battery (max 12.6V) to 6.0V: powering of wing servo.

- Step down voltage regulator (XL4005-5A) from 3S Lipo battery (max 12.6V) to 6.0V: powering of canard servo.
- Step down voltage regulator (XL4005-5A) from 3S Lipo battery (max 12.6V) to 6.0V: powering of aerodynamic control servos and telemetry.
- 2 voltage divider circuits, reduce Lipo 4S (max 16.8V) to input 3.3V in the Arduino Due analog input ports to measure batteries voltage.
- 1 voltage divider circuit, reduce Lipo 3S (max 12.6V) to input 3.3V in the Arduino Due analog input port to measure battery voltage.
- Circuit with optocoupler (TIL111) to light up the vehicle warning red LED strips.
- P4 plug to connect the auxiliary battery (Lipo 3S) to power the systems.
- 2 IDC header 34-pins to connect the vehicle distributed systems.
- Reset button.

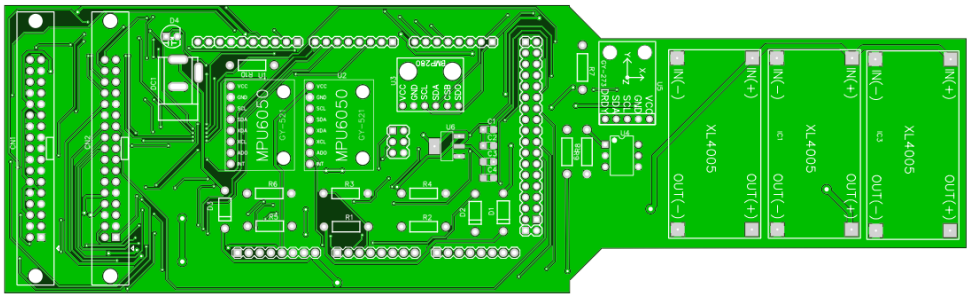

Figure 59 – Vehicle systems integration board (base)

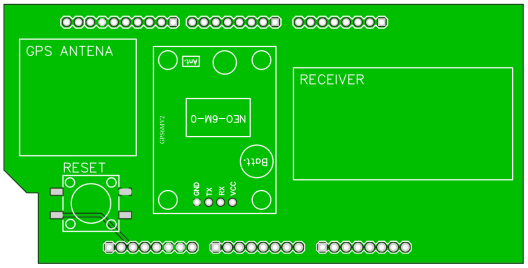

Figure 60 – Vehicle systems integration board (top)

The boards with soldered electronics are shown in Figure 61, and the integrated and embedded systems in the vehicle are shown in Figure 62.

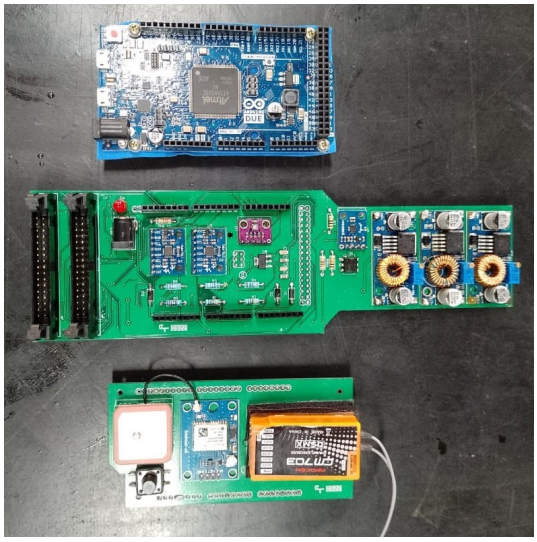

Figure 61 – Vehicle printed circuit integration boards

Figure 62 – On-board integrated control systems

6.17 Ground station

A ground station was designed to display important vehicle information to the pilot. Is is attached to the radio transmitter, as shown in Figure 63. Is is composed of a microcontroller board, LCD display shield, a telemetry system, data logger, buzzer and battery, whose communication diagram is shown in Figure 64.

Figure 63 – Ground station

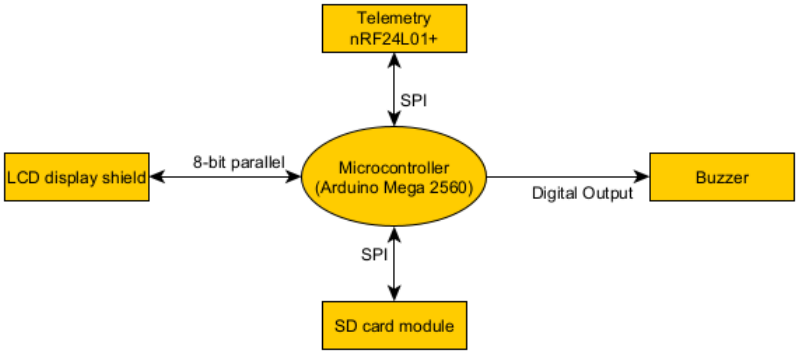

Figure 64 – Ground station systems communication architecture

6.17.1 Micro controller board

An Arduino Mega 2560, shown in Figure 65, is the control board used to integrate the systems of the ground station, which also holds a control software. Is is a microcontroller board based on the ATMega2560 8-bit, whose features are detailed in Table 24.

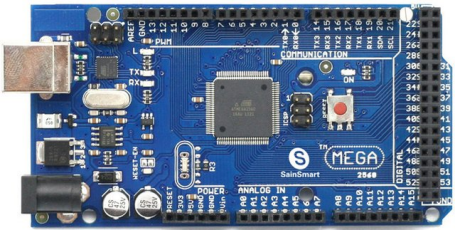

Figure 65 – Arduino Mega 2560

Table 24 – Arduino Mega 2560 microcontroller board features

Microcontroller	ATMega2560 8-bit
Digital I/O Pins	54
PWM pins	15
Analog input pins I/O	16
UART	yes, 4 serial ports
I2C	yes
SPI	yes
I/O Voltage	5.0V
Input voltage (nominal)	7-12V
Processor clock speed	16 MHz
Memory	8KB SRAM, 256KB flash, 8KB EEPROM

6.17.2 LCD display shield

The LCD display shield, shown in Figure 66, is used in the ground station, attached to the control board Arduino Mega 2560, to visually inform the pilot of the vehicle and ground station status.

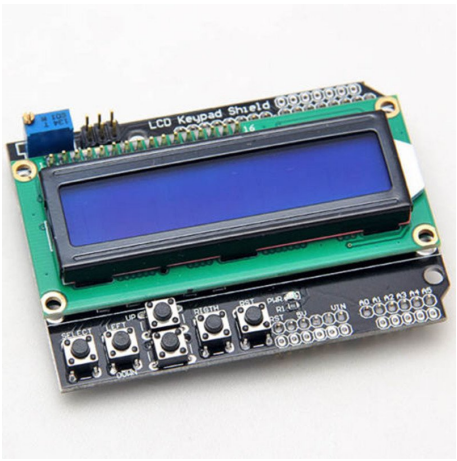

Figure 66 – LCD display shield

6.17.3 Telemetry system

A nRF24L01+ transceiver, described in section 6.10, is used in the ground station to receive flight data from the vehicle, and transmit it to the ground station microcontroller board.

6.17.4 Data logger

The ground station has a data logger to save flight test data. Its the module shown in Figure 67, whose features are detailed in Table 25, which save flight data to a Micro SDHC Card of 32 GB.

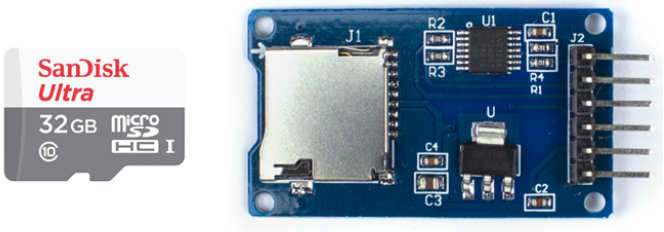

Figure 67 – SD card module

Table 25 – SD card module features

Input voltage	3-5.0V
Communication	SPI protocol
Card	Micro SDHC 32 GB

6.17.5 Buzzer

A 5V DC buzzer of Figure 68 is used in the ground station to warn the pilot of low battery condition in the vehicle, or low battery in the ground station.

Figure 68 – Buzzer 5V DC

6.17.6 Battery

The Lipo battery of Figure 69, whose features are detailed in Table 26, is used to power the ground station.

Figure 69 – Ground station battery

Table 26 – Ground station battery features

Lipo cells	3S (11.1V)
Capacity	850 mAh
Discharge (peak)	60C (120C)
Weight	80 g

7 STATES ESTIMATION ALGORITHMS

In this chapter the vehicle states estimation algorithms are presented, which are programmed in the vehicle controller board software.

7.1 Data Filtering

First of all, it is important to present the methods to handle the measurements data from the sensors, so that it can be used in the states estimation algorithms. In this sense, sensors measurement data are filtered in order to compute data series mean, variance and covariance.

7.1.1 Data measurements mean

The mean, or moving average, value μ_n of a data series of n measurements $(x_1, x_2, ..., x_n)$ is given by Eq. (7.1).

$$\mu_n = \frac{1}{n}\sum_{i=1}^{n} x_i \tag{7.1}$$

Given a new measurement x_{n+1}, the mean value is recomputed, as in Eq. (7.2).

$$\mu_{n+1} = \frac{1}{n+1}\sum_{i=1}^{n+1} x_i = \frac{n}{n+1}\left(\frac{1}{n}\sum_{i=1}^{n} x_i + \frac{1}{n}x_{n+1}\right) \tag{7.2}$$

Therefore, the recursive mean value μ_{n+1} can be recomputed at each step using Eq. (7.3).

$$\mu_{n+1} = \frac{1}{n+1}\mu_n + \frac{1}{n+1}x_{n+1} \tag{7.3}$$

7.1.2 Data measurements variance

Also, the variance σ_n^2 of a data series of n measurements is defined by Eq. (7.4).

$$\sigma_n^2 = \frac{1}{n}\sum_{i=1}^{n}\left(x_i - \mu_n\right)^2 \tag{7.4}$$

So, given a new measurement x_{n+1}, the variance is recomputed in Eq. (7.5).

$$\sigma_{n+1}^2 = \frac{1}{n+1}\sum_{i=1}^{n+1}\left(x_i - \mu_{n+1}\right)^2 = \frac{1}{n+1}\sum_{i=1}^{n+1}\left(x_i - \frac{1}{n+1}\mu_n - \frac{1}{n+1}x_{n+1}\right)^2 \tag{7.5}$$

Rearranging the terms, the recursive variance is computed as in Eq. (7.6).

$$\sigma_{n+1}^2 = \frac{1}{n+1}\sigma_n^2 + \frac{n}{(n+1)(n+1)}\Big(x_{n+1} - \mu_n\Big)^2 \tag{7.6}$$

7.1.3 Data measurements covariance

The covariance between two given data series $(x_1, x_2, ..., x_n)$ and $(y_1, y_2, ..., y_n)$ is defined in Eq. (7.7), according to (WALPOLE *et al.*, 2007).

$$cov(x, y)_n = \frac{1}{n}\sum_{i=1}^{n} x_i y_i - \mu_{n_x}\mu_{n_y} \tag{7.7}$$

So, for new measurements x_{n+1} and y_{n+1}, the covariance is recomputed as in Eq. (7.8).

$$cov(x, y)_{n+1} = \frac{1}{n+1}\sum_{i=1}^{n+1} x_i y_i - \mu_{n+1_x}\mu_{n+1_y} \tag{7.8}$$

Multiplying Eq. (7.7) by -1, adding to Eq. (7.8) and rearranging terms, gives the recursive covariance in Eq. (7.9).

$$cov(x, y)_{n+1} = \frac{n}{n+1}cov(x, y)_n + \frac{1}{n}\Big(x_{n+1} - \mu_{n+1_x}\Big)\Big(y_{n+1} - \mu_{n+1_y}\Big) \tag{7.9}$$

7.1.4 Data fusion from two sensors

When the same information is measured from two instruments, the resulting quantity $\hat{x}$ is the linear combination of the two measurements x_1 and x_2, for a given data fusion coefficient $(0 \leq \nu \leq 1)$, as in Eq. (7.10).

$$\hat{x} = \nu x_1 + (1 - \nu)x_2 \tag{7.10}$$

It is important that the resulting data is more reliable than the previous measured data, which means that the resulting variance is less than the individual measurements, that is,

$$\sigma^2(\hat{x}) < max(\sigma^2(x_1); \sigma^2(x_2)) \tag{7.11}$$

So, the resulting variance is computed in Eq. (7.12).

$$\sigma^2(\hat{x}) = \nu^2\sigma^2(x_1) + (1 - \nu)^2\sigma^2(x_2) + 2\nu(1 - \nu)cov(x_1, x_2) \tag{7.12}$$

Therefore, Eq. (7.12) is derived with respect to ν, in order to find the minimum.

$$\frac{\partial \sigma^2(\hat{x})}{\partial \nu} = 2\nu\sigma^2(x_1) + 2(1-\nu)\sigma^2(x_2) + 2(1-2\nu)cov(x_1, x_2) \tag{7.13}$$

The minimum is found at $\frac{\partial var(\hat{x})}{\partial \nu} = 0$. So, equating Eq. (7.13) to zero, and rearranging the terms, the final ν is obtained in Eq. (7.14).

$$\nu = \frac{\sigma^2(x_1) - cov(x_1, x_2)}{\sigma^2(x_1) + \sigma^2(x_2) - 2cov(x_1, x_2)} \tag{7.14}$$

7.2 Data fusion from IMU 1 and IMU 2

The data fusion algorithm of section 7.1.4 is applied to measured data from both embedded IMU's, that is, angular velocities and accelerations in the x, y, z axes. Therefore, the resulting angular velocities ω_x, ω_y, ω_z and accelerations a_x, a_y, a_z are linear combinations between the measurements of both IMU's, which are defined in Eq. (7.16), Eq. (7.15), Eq. (7.17), Eq. (7.18), Eq. (7.19) and Eq. (7.20), respectively.

$$\omega_x = \nu_{\omega_x}\omega_x^{IMU1} + (1-\nu_{\omega_x})\omega_x^{IMU2} \tag{7.15}$$

$$\omega_y = \nu_{\omega_y}\omega_y^{IMU1} + (1-\nu_{\omega_y})\omega_y^{IMU2} \tag{7.16}$$

$$\omega_z = \nu_{\omega_z}\omega_z^{IMU1} + (1-\nu_{\omega_z})\omega_z^{IMU2} \tag{7.17}$$

$$a_x = \nu_{a_x}a_x^{IMU1} + (1-\nu_{a_x})a_x^{IMU2} \tag{7.18}$$

$$a_y = \nu_{a_y}a_y^{IMU1} + (1-\nu_{a_y})a_y^{IMU2} \tag{7.19}$$

$$a_z = \nu_{a_z}a_z^{IMU1} + (1-\nu_{a_z})a_z^{IMU2} \tag{7.20}$$

Consequently, at each control loop it is necessary to update the measured mean, variance and covariance for the angular velocities and accelerations measured from both IMU's, in order to compute the data fusion coefficients, thus applying Eq. (7.14).

7.3 Discrete Kalman filter algorithm

Most of the state estimators employed make use of the discrete Kalman filter algorithm, derived in (WELCH; BISHOP, 1995). In this section the algorithm is described.

The Kalman filter addresses the general problem of trying to estimate the state of $x \in \Re^n$ a discrete-time controlled process that is governed by the linear stochastic difference equation, of Eq. (7.21), and measurements $z \in \Re^m$ in the form of Eq. (7.22).

$$\mathbf{x}_k = A\mathbf{x}_{k-1} + B\mathbf{u}_k + \mathbf{w}_{k-1} \tag{7.21}$$

$$\mathbf{z}_k = H\mathbf{x}_k + \mathbf{v}_k \tag{7.22}$$

The random variables $\mathbf{w}_k$ and $\mathbf{v}_k$ represent the process and measurement noise respectively. They are assumed to be independent of each other, white, and with normal probability distributions, as in Eq. (7.23) and Eq. (7.24), where Q is the process noise covariance matrix and R the measurement noise covariance matrix.

$$p(w) \sim N(0, Q) \tag{7.23}$$

$$p(v) \sim N(0, R) \tag{7.24}$$

The Kalman filter estimates a process by using a form of feedback control: the filter estimates the process state at some time and then obtains feedback in the form of noisy measurements. As such, the equations for the Kalman filter fall into two groups: time update equations and measurement update equations. The time update equations are responsible for projecting forward in time the current state and error covariance estimates to obtain the a prediction of the state for the next time step. The measurement update equations are responsible for the feedback, that is, for incorporating a new measurement into the prediction of the state to obtain a correction of it.

7.3.1 Prediction step

Therefore, the first step of the algorithm is to make a prediction of the state forward in time, that is, from time step $k-1$ to step k. So, in Eq. (7.25), $\hat{\mathbf{x}}_k^-$ is the predicted state from the current state $\hat{\mathbf{x}}_{k-1}$.

$$\hat{\mathbf{x}}_k^- = A\hat{\mathbf{x}}_{k-1} + B\mathbf{u}_k \tag{7.25}$$

In Eq. (7.26) there is the projection forward in time of the state uncertainty covariance P_k^-. In this equation the process noise covariance matrix Q might chance each time step.

$$P_k^- = AP_{k-1}A^T + Q_k \tag{7.26}$$

7.3.2 Correction step

From the projected state uncertainty covariance matrix, the Kalman gain K_k is computed, as in Eq. (7.27). In this equation the measurement noise covariance matrix R might change each time step.

$$K_k = P_k^- H^T (HP_{k-1}H^T + R_k)^{-1} \tag{7.27}$$

The final state estimate $\hat{\mathbf{x}}$ is corrected through Eq. (7.28), also using the measurements $\mathbf{z}_k$.

$$\hat{\mathbf{x}} = \hat{\mathbf{x}}_k^- + K_k(\mathbf{z}_k - H\hat{\mathbf{x}}_k^-) \tag{7.28}$$

Lastly, the state uncertainty covariance must be updated using Eq. (7.29).

$$P_k = (I - HK_k)P_k^- \tag{7.29}$$

7.4 Accelerations and angular velocities filtering

Accelerations and angular velocities measured from the IMU's have noise, therefore it is important to reduce the incoming noise from the measurements in order to compute the attitude of the vehicle.

In this context, it is applied the discrete Kalman filter described in the section 7.3, for a one-dimensional state, applied to each axis.

Thus, for this case the process is defined according to Eq. (7.30).

$$\hat{x}_k^- = \hat{x}_{k-1} + w_k \tag{7.30}$$

With a measurement equation defined in Eq. (7.31).

$$z_k = x_k + v_k \tag{7.31}$$

In the case of the discrete Kalman filter applied to Accelerations and angular velocities measured by the IMU's there is no control input, so $u = 0$, and the state does

not change from step to step, so $A = 1$. Additionally, the measurement is directly of the state, so $H = 1$.

Which, results in the simplification of the algorithm:

7.4.1 Prediction step

State prediction in Eq. (7.32).

$$\hat{x}_k^- = \hat{x}_{k-1} \tag{7.32}$$

Projected state uncertainty covariance matrix in Eq. (7.33). In this case, the process noise covariance Q is a scalar and assumed constant, small but non-zero, which must be tuned, being defined in the algorithm setup.

$$P_k^- = P_{k-1} + Q_k \tag{7.33}$$

7.4.2 Correction step

Kalman gain in Eq. (7.34). In this case the measurement noise covariance R is a scalar, and equal to the variance of the state measurement $\sigma_k^2(z)$. Thus, it is necessary to recursively compute the measurements mean, and variance, using Eq. (7.3) and Eq. (7.6), respectively.

$$K_k = \frac{P_k^-}{P_{k-1} + R_k} \tag{7.34}$$

State correction in Eq. (7.35).

$$\hat{x}_k = \hat{x}_k^- + K_k(z_k - \hat{x}_k^-) \tag{7.35}$$

Update state uncertainty covariance in Eq. (7.36).

$$P_k = (1 - K_k)P_k^- \tag{7.36}$$

Therefore, this algorithm is applied for the accelerations in each axes (a_x^{IMU}, a_y^{IMU}, a_z^{IMU}) and angular velocities in each axes (ω_x^{IMU}, ω_y^{IMU}, ω_z^{IMU}).

7.5 Attitude discrete Kalman filter

7.5.1 Roll and pitch angle from accelerations

In the steady state condition, where gravity is the only acceleration affecting the accelerometers, it is possible to derive the roll and pitch angle from the projection of

the gravity acceleration vector in each accelerometer axis. In this context, the measured accelerations would be a rotation of the acceleration vector through the rotation matrix from the Earth fixed inertial frame to the body coordinate frame R_B^E, as in Eq. (7.37).

$$\begin{bmatrix} a_x \\ a_y \\ a_z \end{bmatrix} = \begin{bmatrix} \cos\psi\cos\theta & \sin\psi\cos\theta & -\sin\theta \\ \cos\psi\sin\theta\sin\phi - \sin\psi\cos\phi & \sin\psi\sin\theta\sin\phi + \cos\psi\cos\phi & \cos\theta\sin\phi \\ \cos\psi\sin\theta\cos\phi + \sin\psi\sin\phi & \sin\psi\sin\theta\cos\phi - \cos\psi\sin\phi & \cos\theta\cos\phi \end{bmatrix} \begin{bmatrix} 0 \\ 0 \\ g \end{bmatrix} \tag{7.37}$$

Also, in this situation, the gravity acceleration is the same as the vector sum of the measured acceleration in each axis, as in Eq. (7.38).

$$g = \sqrt{a_x^2 + a_y^2 + a_z^2} \tag{7.38}$$

Therefore, multiplying and rearranging terms, the roll and pitch angle from accelerometers are defined in Eq. (7.39) and Eq. (7.40), respectively.

$$\phi_{acc} = \arctan\left(\frac{a_y}{a_z}\right) \tag{7.39}$$

$$\theta_{acc} = -\arcsin\left(\frac{a_x}{\sqrt{a_x^2 + a_y^2 + a_z^2}}\right) \tag{7.40}$$

7.5.2 Magnetometer calibration

According to (CARUSO, 1997) when a compass is operating in a open area in the absence of any ferrous metals there is no distortion effects on the earth's magnetic field. In reality, though, compasses are mounted in vehicles, aircraft, and platforms that most likely have ferrous materials nearby. The effects of ferrous metals (iron, nickel, steel, cobalt) will distort, or bend, the earth's field which will alter the compass heading. These effects can be thought of as a magnetic field that is added to the earth's field. If the compass is securely mounted in the vehicle, the ferrous effects can be accounted for and removed from the magnetic readings.

Therefore, one way of calibrating the magnetometer readings is by using the following Eq. (7.41), Eq. (7.42) and Eq. (7.43), in which $(m^B_{x_{raw}}, m^B_{y_{raw}}, m^B_{z_{raw}})$ are the magnetometer readings in the body coordinate frame.

$$m_x^B = \left(m^B_{x_{raw}} - m^B_{x_{offset}}\right) m^B_{x_{scale}} \tag{7.41}$$

$$m_y^B = \left(m^B_{y_{raw}} - m^B_{y_{offset}}\right) m^B_{y_{scale}} \tag{7.42}$$

$$m_z^B = \left(m_{z_{raw}}^B - m_{z_{offset}}^B\right) m_{z_{scale}}^B \tag{7.43}$$

The $(m_{x_{offset}}^B, m_{y_{offset}}^B, m_{z_{offset}}^B)$ are the permanent hard iron distortion in each axis, or bias, which can be computed using Eq. (7.44), Eq. (7.45) and Eq. (7.46), where $(m_{x_{max}}^B, m_{y_{max}}^B, m_{z_{max}}^B)$ and $(m_{x_{min}}^B, m_{y_{min}}^B, m_{z_{min}}^B)$ are the maximum and minimum measurements in each axis obtained by fully rotating the magnetometer, that is, the vehicle, in every direction.

$$m_{x_{offset}}^B = \frac{m_{x_{max}}^B + m_{x_{min}}^B}{2} \tag{7.44}$$

$$m_{y_{offset}}^B = \frac{m_{y_{max}}^B + m_{y_{min}}^B}{2} \tag{7.45}$$

$$m_{z_{offset}}^B = \frac{m_{z_{max}}^B + m_{z_{min}}^B}{2} \tag{7.46}$$

Furthermore, the $(m_{x_{scale}}^B, m_{y_{scale}}^B, m_{z_{scale}}^B)$ are scale factors resulting from the soft iron distortion, which is the result of material that distorts a magnetic field but does not necessarily generate a magnetic field itself, so it is dependent upon the orientation of the material relative to the magnetometer. They are computed using the following Eq. (7.47), Eq. (7.48) and Eq. (7.49).

$$m_{x_{scale}}^B = \frac{\Delta m_{avg}}{\Delta m_{avg_x}} \tag{7.47}$$

$$m_{y_{scale}}^B = \frac{\Delta m_{avg}}{\Delta m_{avg_y}} \tag{7.48}$$

$$m_{z_{scale}}^B = \frac{\Delta m_{avg}}{\Delta m_{avg_z}} \tag{7.49}$$

Being that the scale factors the defined using Eq. (7.50), Eq. (7.51), Eq. (7.52) and Eq. (7.53).

$$\Delta m_{avg_x} = \frac{m_{x_{max}}^B - m_{x_{min}}^B}{2} \tag{7.50}$$

$$\Delta m_{avg_y} = \frac{m_{y_{max}}^B - m_{y_{min}}^B}{2} \tag{7.51}$$

$$\Delta m_{avg_z} = \frac{m_{z_{max}}^B - m_{z_{min}}^B}{2} \tag{7.52}$$

$$\Delta m_{avg_z} = \frac{\Delta m_{avg_x} + \Delta m_{avg_y} + \Delta m_{avg_z}}{3} \tag{7.53}$$

7.5.3 Yaw angle from magnetometer

Magnetometers are devices capable of sensing the Earth's magnetic field vector, which are measured in the body coordinate frame (m_x^B, m_y^B, m_z^B). So, the measurements must be converted to the Earth fixed inertial frame (m_x^E, m_y^E, m_z^E) in order to compute the vehicle heading, which is the rotation of the vector with respect to roll and pitch angles (ϕ, θ), according to Eq. (7.54).

$$\begin{bmatrix} m_x^E \\ m_y^E \\ m_z^E \end{bmatrix} = \begin{bmatrix} \cos\theta & \sin\theta\sin\phi & \sin\theta\cos\phi \\ 0 & \cos\phi & -\sin\phi \\ -\sin\theta & \cos\theta\sin\phi & \cos\theta\cos\phi \end{bmatrix} \begin{bmatrix} m_x^B \\ m_y^B \\ m_z^B \end{bmatrix} \tag{7.54}$$

Thus, the vehicle heading, or yaw angle, is defined as the direction of the resulting vector in the horizontal projection, as in Eq. (7.55), according to (QUAN, 2017) and (WAHDAN *et al.*, 2014).

$$\psi_{mag} = \arctan 2\left(m_y^E, m_x^E\right) \tag{7.55}$$

The yaw angle is considered in the range: $\psi_{mag} \in [0, 2\pi]$, so if $\psi_{mag} < 0$ in the result of Eq. (7.55), $\psi_{mag} = \psi_{mag} + 2\pi$.

7.5.4 Euler angles data fusion algorithm

The Euler angles rates and angular velocities have the following relationship of Eq. (7.56), according to (QUAN, 2017).

$$\begin{bmatrix} \dot{\phi} \\ \dot{\theta} \\ \dot{\psi} \end{bmatrix} = \begin{bmatrix} 1 & \tan\theta\sin\phi & \tan\theta\cos\phi \\ 0 & \cos\phi & -\sin\phi \\ 0 & \sin\phi\sec\theta & \cos\phi\sec\theta \end{bmatrix} \begin{bmatrix} \omega_x \\ \omega_y \\ \omega_z \end{bmatrix} \tag{7.56}$$

Therefore, the integration of Eq. (7.56) would provide Euler angles from gyroscopes measurements of the angular velocities. However, such integration also entails numerical errors, which causes measurement drift, that is, the errors are also summed which results in Euler angles that increases indefinitely over time.

So, this information must be corrected using computed Euler angles from accelerometers and magnetometers. In this sense, the discrete Kalman filter algorithm of section 7.3 is applied (JURMAN *et al.*, 2007).

7.5.5 Prediction step

In the prediction step the Euler angles are computed from integration of Eq. (7.56), resulting in Eq. (7.57).

$$\begin{bmatrix}\phi_k^- \\ \theta_k^- \\ \psi_k^-\end{bmatrix} = \begin{bmatrix}1 & 0 & 0 \\ 0 & 1 & 0 \\ 0 & 0 & 1\end{bmatrix}\begin{bmatrix}\phi_{k-1} \\ \theta_{k-1} \\ \psi_{k-1}\end{bmatrix} + \begin{bmatrix}1 & \tan\theta_{k-1}\sin\phi_{k-1} & \tan\theta_{k-1}\cos\phi_{k-1} \\ 0 & \cos\phi_{k-1} & -\sin\phi_{k-1} \\ 0 & \sin\phi_{k-1}\sec\theta_{k-1} & \cos\phi_{k-1}\sec\theta_{k-1}\end{bmatrix}\begin{bmatrix}\omega_{x_k}dt \\ \omega_{y_k}dt \\ \omega_{z_k}dt\end{bmatrix} \tag{7.57}$$

Additionally, the projection forward in time of the state uncertainty covariance matrix P_k^- is computed the same way, repeated here in Eq. (7.58).

$$P_k^- = AP_{k-1}A^T + Q_k \tag{7.58}$$

Therefore, in this application, Eq. (7.59) is defined.

$$A = \begin{bmatrix}1 & 0 & 0 \\ 0 & 1 & 0 \\ 0 & 0 & 1\end{bmatrix} \tag{7.59}$$

Moreover, assuming no covariance between measurement of different axes, Eq. (7.60) is defined.

$$Q_k = \begin{bmatrix}\sigma_k^2(\omega_x dt) & cov_k(\omega_x dt, \omega_y dt) & cov_k(\omega_x dt, \omega_z dt) \\ cov_k(\omega_y dt, \omega_x dt) & \sigma_k^2(\omega_y dt) & cov_k(\omega_y dt, \omega_z dt) \\ cov_k(\omega_z dt, \omega_x dt) & cov_k(\omega_z dt, \omega_y dt) & \sigma_k^2(\omega_z dt)\end{bmatrix} = dt^2\begin{bmatrix}\sigma_k^2(\omega_x) & 0 & 0 \\ 0 & \sigma_k^2(\omega_y) & 0 \\ 0 & 0 & \sigma_k^2(\omega_z)\end{bmatrix} \tag{7.60}$$

7.5.6 Correction step

The measurements are defined in Eq. (7.61).

$$\begin{bmatrix}\phi_{acc_k} \\ \theta_{acc_k} \\ \psi_{mag_k}\end{bmatrix} = \begin{bmatrix}1 & 0 & 0 \\ 0 & 1 & 0 \\ 0 & 0 & 1\end{bmatrix}\begin{bmatrix}\phi_k \\ \theta_k \\ \psi_k\end{bmatrix} \tag{7.61}$$

Therefore, in this application,

$$H = \begin{bmatrix}1 & 0 & 0 \\ 0 & 1 & 0 \\ 0 & 0 & 1\end{bmatrix} \tag{7.62}$$

From the projected state uncertainty covariance matrix, the Kalman gain K_k is computed, as in Eq. (7.63).

$$K_k = P_k^- H^T (H P_{k-1} H^T + R_k)^{-1} \tag{7.63}$$

Where R_k, the measurement noise covariance matrix, is defined as in Eq. (7.64).

$$R_k = \begin{bmatrix} \sigma_k^2(\phi_{acc}) & cov_k(\phi_{acc}, \theta_{acc}) & cov_k(\phi_{acc}, \psi_{mag}) \\ cov_k(\theta_{acc}, \phi_{acc}) & \sigma_k^2(\theta_{acc}) & cov_k(\theta_{acc}, \psi_{mag}) \\ cov_k(\psi_{mag}, \phi_{acc}) & cov_k(\psi_{mag}, \theta_{acc}) & \sigma_k^2(\psi_{mag}) \end{bmatrix} = \begin{bmatrix} \sigma_k^2(\phi_{acc}) & 0 & 0 \\ 0 & \sigma_k^2(\theta_{acc}) & 0 \\ 0 & 0 & \sigma_k^2(\psi_{mag}) \end{bmatrix} \tag{7.64}$$

The final state estimate is corrected through Eq. (7.65).

$$\begin{bmatrix} \phi_k \\ \theta_k \\ \psi_k \end{bmatrix} = \begin{bmatrix} \phi_k^- \\ \theta_k^- \\ \psi_k^- \end{bmatrix} + K_k \left(\begin{bmatrix} \phi_{acc_k} \\ \theta_{acc_k} \\ \psi_{mag_k} \end{bmatrix} - \begin{bmatrix} 1 & 0 & 0 \\ 0 & 1 & 0 \\ 0 & 0 & 1 \end{bmatrix} \begin{bmatrix} \phi_k^- \\ \theta_k^- \\ \psi_k^- \end{bmatrix} \right) \tag{7.65}$$

Lastly, the state uncertainty covariance must be updated using Eq. (7.66).

$$P_k = (I - H K_k) P_k^- \tag{7.66}$$

In Figure 70 the attitude discrete Kalman filter is shown in diagram form.

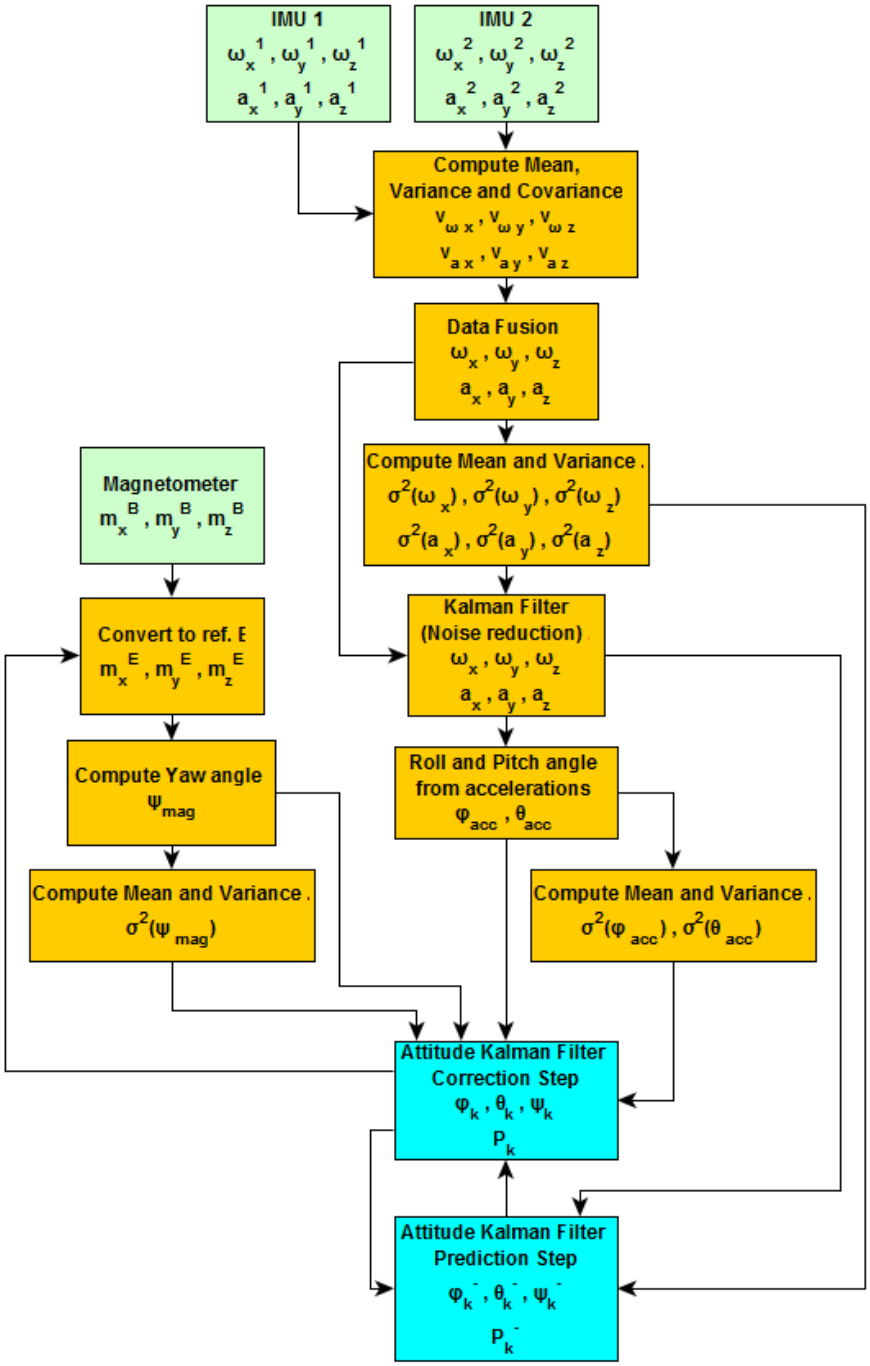

Figure 70 – Attitude discrete Kalman filter diagram

7.6 Vehicle accelerations

It is important to compute the vehicle accelerations in body coordinate frame $(\dot{U}, \dot{V}, \dot{W})$, that is, to remove the gravity acceleration from the measurements of the accelerometers (a_x, a_y, a_z). This can be done once the Euler angles are computed, as in Eq. (7.67).

$$\begin{bmatrix}\dot{U}\\ \dot{V}\\ \dot{W}\end{bmatrix} = \begin{bmatrix}a_x\\ a_y\\ a_z\end{bmatrix} - \begin{bmatrix}\cos\psi\cos\theta & \sin\psi\cos\theta & -\sin\theta\\ \cos\psi\sin\theta\sin\phi - \sin\psi\cos\phi & \sin\psi\sin\theta\sin\phi + \cos\psi\cos\phi & \cos\theta\sin\phi\\ \cos\psi\sin\theta\cos\phi + \sin\psi\sin\phi & \sin\psi\sin\theta\cos\phi - \cos\psi\sin\phi & \cos\theta\cos\phi\end{bmatrix}\begin{bmatrix}0\\ 0\\ g\end{bmatrix} \tag{7.67}$$

Now, the accelerations in body coordinate frame can be converted to Earth fixed inertial frame $(\ddot{x}_E, \ddot{y}_E, \ddot{z}_E)$, as in Eq. (7.68).

$$\begin{bmatrix}\ddot{x}_{E_{IMU}}\\ \ddot{y}_{E_{IMU}}\\ \ddot{z}_{E_{IMU}}\end{bmatrix} = \begin{bmatrix}\cos\psi\cos\theta & \cos\psi\sin\theta\sin\phi - \sin\psi\cos\phi & \cos\psi\sin\theta\cos\phi + \sin\psi\sin\phi\\ \sin\psi\cos\theta & \sin\psi\sin\theta\sin\phi + \cos\psi\cos\phi & \sin\psi\sin\theta\cos\phi - \cos\psi\sin\phi\\ -\sin\theta & \cos\theta\sin\phi & \cos\theta\cos\phi\end{bmatrix}\begin{bmatrix}\dot{U}\\ \dot{V}\\ \dot{W}\end{bmatrix} \tag{7.68}$$

7.7 Altitude and vertical velocity discrete Kalman filter

In order to estimate the vehicle altitude h, and also the vertical velocity $\dot{h}$, a discrete Kalman filter is applied. In this sense, the prediction step makes use of integration of the vehicles vertical acceleration to compute the vertical velocity, and additionally, double integration to compute altitude. But first the vertical acceleration $\ddot{z}_E$ must be converted to $\ddot{h}$, since in the Earth fixed inertial frame the positive direction of $\ddot{z}_E$ points downward.

$$\ddot{h}_{IMU_k} = -\ddot{z}_{E_{IMU_k}} \tag{7.69}$$

7.7.1 Prediction step

Thus, in the prediction step the altitude and vertical velocity are computed in Eq. (7.70), following (HETéNYI; GóTZY; BLáZOVICS, 2016).

$$\begin{bmatrix}h_k^-\\ \dot{h}_k^-\end{bmatrix} = \begin{bmatrix}1 & dt\\ 0 & 1\end{bmatrix}\begin{bmatrix}h_{k-1}\\ \dot{h}_{k-1}\end{bmatrix} + \begin{bmatrix}\frac{dt^2}{2}\\ dt\end{bmatrix}\ddot{h}_{IMU_k} \tag{7.70}$$

The projection forward in time of the state uncertainty covariance matrix P_k^- is computed the same way, repeated here in Eq. (7.71).

$$P_k^-(h) = AP_{k-1}(h)A^T + Q_k(h) \tag{7.71}$$

Where, the process noise covariance is defined as in Eq. (7.72), following (RAJAMANI, 2007).

$$Q_k(h) = \begin{bmatrix} \frac{dt^2}{2} \\ dt \end{bmatrix} \begin{bmatrix} \frac{dt^2}{2} & dt \end{bmatrix} \sigma_k^2(\ddot{h}_{IMU}) = \begin{bmatrix} \frac{dt^4}{4} & \frac{dt^3}{2} \\ \frac{dt^3}{2} & dt^2 \end{bmatrix} \sigma_k^2(\ddot{h}_{IMU}) \tag{7.72}$$

And, in this application, Eq. (7.73).

$$A = \begin{bmatrix} 1 & dt \\ 0 & 1 \end{bmatrix} \tag{7.73}$$

7.7.2 Correction step

The measurements are defined in Eq. (7.74), results from pressure sensor measurements.

$$\begin{bmatrix} h_{press_k} \\ \dot{h}_{press_k} \end{bmatrix} = \begin{bmatrix} 1 & 0 \\ 0 & 1 \end{bmatrix} \begin{bmatrix} h_k \\ \dot{h}_k \end{bmatrix} \tag{7.74}$$

Therefore, in this application,

$$H = \begin{bmatrix} 1 & 0 \\ 0 & 1 \end{bmatrix} \tag{7.75}$$

From the projected state uncertainty covariance matrix, the Kalman gain K_k is computed, as in Eq. (7.76).

$$K_k(h) = P_k^-(h)H^T(HP_{k-1}(h)H^T + R_k(h))^{-1} \tag{7.76}$$

Where R_k, the measurement noise covariance matrix, is defined as in Eq. (7.77), assuming no covariance between altitude and vertical velocity measurements.

$$R_k(h) = \begin{bmatrix} \sigma_k^2(h_{press}) & cov_k(h_{press}, \dot{h}_{press}) \\ cov_k(h_{press}, \dot{h}_{press}) & \sigma_k^2(\dot{h}_{press}) \end{bmatrix} = \begin{bmatrix} \sigma_k^2(h_{press}) & 0 \\ 0 & \sigma_k^2(\dot{h}_{press}) \end{bmatrix} \tag{7.77}$$

The final state estimate is corrected through Eq. (7.78).

$$\begin{bmatrix} h_k \\ \dot{h}_k \end{bmatrix} = \begin{bmatrix} h_k^- \\ \dot{h}_k^- \end{bmatrix} + K_k(h) \left(\begin{bmatrix} h_{press_k} \\ \dot{h}_{press_k} \end{bmatrix} - \begin{bmatrix} 1 & 0 \\ 0 & 1 \end{bmatrix} \begin{bmatrix} h_k^- \\ \dot{h}_k^- \end{bmatrix} \right) \tag{7.78}$$

The state uncertainty covariance must be updated using Eq. (7.79).

$$P_k(h) = (I - HK_k(h))P_k^-(h) \tag{7.79}$$

Finally, the resulting vertical velocity is converted back to Earth fixed inertial frame in Eq. (7.80) in order to obtain the complete velocity vector.

$$\dot{z}_{E_k} = -\dot{h}_k \tag{7.80}$$

In Figure 71 the altitude discrete Kalman filter is shown in diagram form.

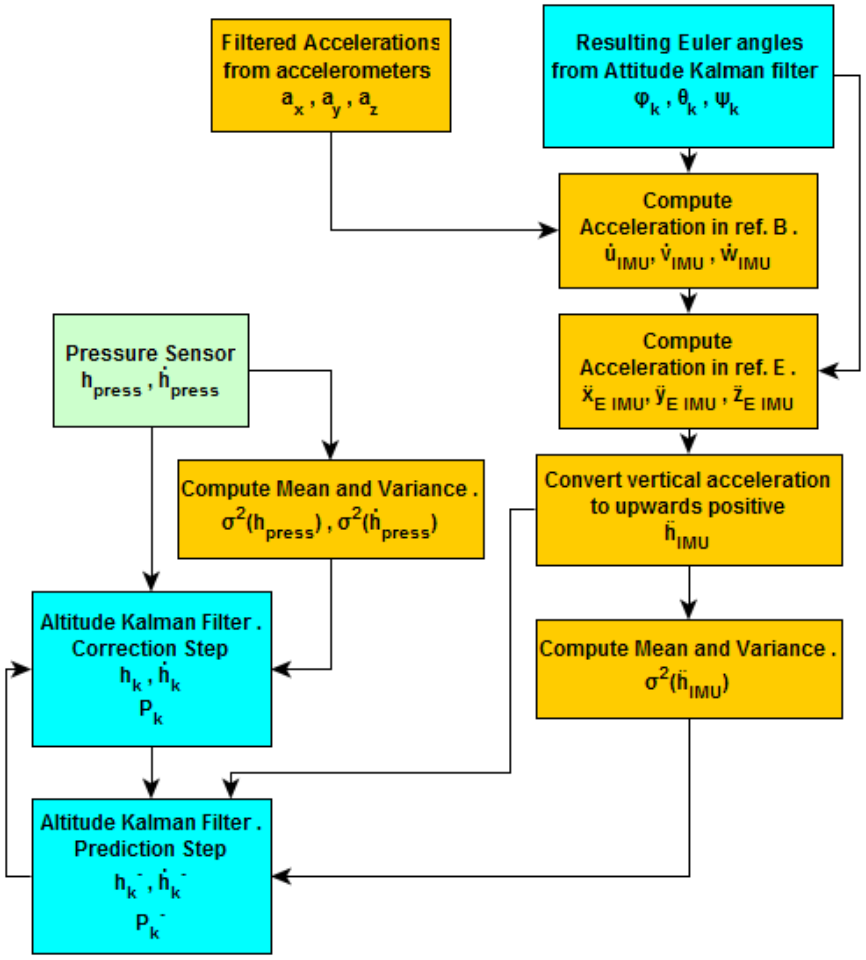

Figure 71 – Altitude discrete Kalman filter diagram

7.8 Position and horizontal velocity from GPS

The GPS module outputs the vehicle current geodetic coordinates, that is, latitude μ_{GPS} and longitude λ_{GPS}, which can be converted to $x_{E_{GPS}}$ and $y_{E_{GPS}}$ position in the Earth fixed inertial reference frame, through flat Earth approximation from the initial position, or geodetic coordinates $(\mu_{GPS_0}, \lambda_{GPS_0})$, following the method of (STEVENS; LEWIS; JOHNSON, 2015) and (ETKIN, 2012).

Therefore, the $(x_{E_{GPS}}, y_{E_{GPS}})$ coordinates are defined in Eq. (7.81) and Eq. (7.82), so that, at initial coordinates $(\mu_{GPS_0}, \lambda_{GPS_0}) \rightarrow (x_{E_{GPS}}, y_{E_{GPS}}) = (0, 0)$.

$$x_{E_{GPS}} = \frac{1}{\arctan 2(1, R_M)} (\mu_{GPS} - \mu_{GPS_0}) \tag{7.81}$$

$$y_{E_{GPS}} = \frac{1}{\arctan 2(1, R_N \cos \mu_{GPS_0})} (\lambda_{GPS} - \lambda_{GPS_0}) \tag{7.82}$$

Where R_N is the radius of curvature in the prime vertical and R_M the radius of curvature in the meridian, computed as in Eq. (7.83) and Eq. (7.84) respectively.

$$R_N = \frac{R}{\sqrt{1 - (2f - f^2) \sin^2 \mu_{GPS_0}}} \tag{7.83}$$

$$R_M = R_N \frac{1 - (2f - f^2)}{1 - (2f - f^2) \sin^2 \mu_{GPS_0}} \tag{7.84}$$

Furthermore, R is the equatorial radius of the planet ($R = 6378137m$) and f the flattening of the planet ($f = 0.00335281$).

The horizontal velocity measured from GPS data is the time derivative of the horizontal position, that is, Eq. (7.85) and Eq. (7.86).

$$\dot{x}_{E_{GPS}} = \frac{\partial x_{E_{GPS}}}{\partial t} \tag{7.85}$$

$$\dot{y}_{E_{GPS}} = \frac{\partial y_{E_{GPS}}}{\partial t} \tag{7.86}$$

7.9 Position and horizontal velocity discrete Kalman filter

The horizontal position and velocity can be measured from GPS data, as shown is the previous section 7.8, however GPS modules measures valid position in frequencies usually from $1,0Hz$ to $5,0Hz$, which might be insufficient for high flight speeds, and besides, there can be degradation of the GPS signal, causing positioning errors which quickly drift with time (CARON *et al.*, 2006). Therefore, the discrete Kalman filter is an important tool to fuse data from GPS and IMU in order to obtain continuous and more reliable position and horizontal velocity.

The data fusion algorithm structure is the same as applied in section 7.7, being that, in the prediction step there is integration of horizontal accelerations in Earth fixed inertial frame ($\ddot{x}_{E_{IMU_k}}, \ddot{y}_{E_{IMU_k}}$) from section 7.6, and the correction step makes use of position and horizontal velocities measured from GPS data ($x_{E_{GPS_k}}, \dot{x}_{E_{GPS_k}}, y_{E_{GPS_k}}, \dot{y}_{E_{GPS_k}}$) from section 7.8.

As mentioned before, there can be faults in the GPS signal which might results in inaccuracies in the GPS fix position. Therefore, in order to detect faulty GPS signal, the

residual is computed, that is, the difference between the position estimates from correction step (from GPS) and estimates from the prediction step (from IMU). The residual must be monitored by computing its mean and variance, so that, if the variance is beyond a defined threshold, GPS signal should be faulty (QUAN, 2017). Consequently, the fusion process algorithm remains at the prediction stage, and subsequently, the position computed from IMU is not corrected (SUKKARIEH; NEBOT; DURRANT-WHYTE, 1999).

7.9.1 Prediction step

Thus, in the prediction step the horizontal position $(x_{E_k}^-, y_{E_k}^-)$ and velocity $(\dot{x}_{E_k}^-, \dot{y}_{E_k}^-)$ are computed in Eq. (7.87) and Eq. (7.88).

$$\begin{bmatrix} x_{E_k}^- \\ \dot{x}_{E_k}^- \end{bmatrix} = \begin{bmatrix} 1 & dt \\ 0 & 1 \end{bmatrix} \begin{bmatrix} x_{E_{k-1}} \\ \dot{x}_{E_{k-1}} \end{bmatrix} + \begin{bmatrix} \frac{dt^2}{2} \\ dt \end{bmatrix} \ddot{x}_{E_{IMU_k}} \tag{7.87}$$

$$\begin{bmatrix} y_{E_k}^- \\ \dot{y}_{E_k}^- \end{bmatrix} = \begin{bmatrix} 1 & dt \\ 0 & 1 \end{bmatrix} \begin{bmatrix} y_{E_{k-1}} \\ \dot{y}_{E_{k-1}} \end{bmatrix} + \begin{bmatrix} \frac{dt^2}{2} \\ dt \end{bmatrix} \ddot{y}_{E_{IMU_k}} \tag{7.88}$$

The projection forward in time of the state uncertainty covariance matrix P_k^- is computed the same way for both x_E and y_E directions, repeated here in Eq. (7.89) and Eq. (7.90).

$$P_k^-(x_E) = AP_{k-1}(x_E)A^T + Q_k(x_E) \tag{7.89}$$

$$P_k^-(y_E) = AP_{k-1}(y_E)A^T + Q_k(y_E) \tag{7.90}$$

Where, the process noise covariance is defined as in Eq. (7.91) and Eq. (7.92), following (RAJAMANI, 2007).

$$Q_k(x_E) = \begin{bmatrix} \frac{dt^2}{2} \\ dt \end{bmatrix} \begin{bmatrix} \frac{dt^2}{2} & dt \end{bmatrix} \sigma_k^2(\ddot{x}_{E_{IMU}}) = \begin{bmatrix} \frac{dt^4}{4} & \frac{dt^3}{2} \\ \frac{dt^3}{2} & dt^2 \end{bmatrix} \sigma_k^2(\ddot{x}_{E_{IMU}}) \tag{7.91}$$

$$Q_k(y_E) = \begin{bmatrix} \frac{dt^2}{2} \\ dt \end{bmatrix} \begin{bmatrix} \frac{dt^2}{2} & dt \end{bmatrix} \sigma_k^2(\ddot{y}_{E_{IMU}}) = \begin{bmatrix} \frac{dt^4}{4} & \frac{dt^3}{2} \\ \frac{dt^3}{2} & dt^2 \end{bmatrix} \sigma_k^2(\ddot{y}_{E_{IMU}}) \tag{7.92}$$

Moreover, for both directions, the Eq. (7.93) is applied.

$$A = \begin{bmatrix} 1 & dt \\ 0 & 1 \end{bmatrix} \tag{7.93}$$

7.9.2 Correction step

The measurements are defined in Eq. (7.94) and Eq. (7.95), results from GPS measurements.

$$\begin{bmatrix} x_{E_{GPS_k}} \\ \dot{x}_{E_{GPS_k}} \end{bmatrix} = \begin{bmatrix} 1 & 0 \\ 0 & 1 \end{bmatrix} \begin{bmatrix} x_{E_k} \\ \dot{x}_{E_k} \end{bmatrix} \tag{7.94}$$

$$\begin{bmatrix} y_{E_{GPS_k}} \\ \dot{y}_{E_{GPS_k}} \end{bmatrix} = \begin{bmatrix} 1 & 0 \\ 0 & 1 \end{bmatrix} \begin{bmatrix} y_{E_k} \\ \dot{y}_{E_k} \end{bmatrix} \tag{7.95}$$

Therefore, in this application,

$$H = \begin{bmatrix} 1 & 0 \\ 0 & 1 \end{bmatrix} \tag{7.96}$$

From the projected state uncertainty covariance matrix, the Kalman gain K_k for each direction is computed, as in Eq. (7.97) and Eq. (7.98).

$$K_k(x_E) = P_k^-(x_E)H^T(HP_{k-1}(x_E)H^T + R_k(x_{E_{GPS}}))^{-1} \tag{7.97}$$

$$K_k(y_E) = P_k^-(y_E)H^T(HP_{k-1}(y_E)H^T + R_k(y_{E_{GPS}}))^{-1} \tag{7.98}$$

Where R_k, the measurement noise covariance matrix, is defined as in Eq. (7.99) and Eq. (7.100), assuming no covariance between position and horizontal velocity measurements.

$$R_k(x_{E_{GPS}}) = \begin{bmatrix} \sigma_k^2(x_{E_{GPS}}) & cov_k(x_{E_{GPS}}, \dot{x}_{E_{GPS}}) \\ cov_k(\dot{x}_{E_{GPS}}, x_{E_{GPS}}) & \sigma_k^2(\dot{x}_{E_{GPS}}) \end{bmatrix} = \begin{bmatrix} \sigma_k^2(x_{E_{GPS}}) & 0 \\ 0 & \sigma_k^2(\dot{x}_{E_{GPS}}) \end{bmatrix} \tag{7.99}$$

$$R_k(y_{E_{GPS}}) = \begin{bmatrix} \sigma_k^2(y_{E_{GPS}}) & cov_k(y_{E_{GPS}}, \dot{y}_{E_{GPS}}) \\ cov_k(\dot{y}_{E_{GPS}}, y_{E_{GPS}}) & \sigma_k^2(\dot{y}_{E_{GPS}}) \end{bmatrix} = \begin{bmatrix} \sigma_k^2(y_{E_{GPS}}) & 0 \\ 0 & \sigma_k^2(\dot{y}_{E_{GPS}}) \end{bmatrix} \tag{7.100}$$

The residuals are computed in Eq. (7.101), Eq. (7.102), Eq. (7.103) and Eq. (7.104).

$$r_{x_{E_k}} = x_{E_{GPS_k}} - x_{E_k}^- \tag{7.101}$$

$$r_{\dot{x}_{E_k}} = \dot{x}_{E_{GPS_k}} - \dot{x}_{E_k}^- \tag{7.102}$$

$$r_{y_{E_k}} = y_{E_{GPS_k}} - y_{E_k}^- \tag{7.103}$$

$$r_{\dot{y}_{E_k}} = \dot{y}_{E_{GPS_k}} - \dot{y}^-_{E_k} \tag{7.104}$$

So that, if the variance of a residual is higher than a defined threshold, the respective IMU position or horizontal velocity must not be corrected. Therefore, the following algorithm is applied.

$$c_{r_{x_{E_k}}} = \begin{cases} 1 & \text{if } \sigma_k^2(r_{x_E}) \leq \sigma_k^2(r_{x_E})_{threshold} \\ 0 & \text{else} \end{cases} \tag{7.105}$$

$$c_{r_{\dot{x}_{E_k}}} = \begin{cases} 1 & \text{if } \sigma_k^2(r_{\dot{x}_E}) \leq \sigma_k^2(r_{\dot{x}_E})_{threshold} \\ 0 & \text{else} \end{cases} \tag{7.106}$$

$$c_{r_{y_{E_k}}} = \begin{cases} 1 & \text{if } \sigma_k^2(r_{y_E}) \leq \sigma_k^2(r_{y_E})_{threshold} \\ 0 & \text{else} \end{cases} \tag{7.107}$$

$$c_{r_{\dot{y}_{E_k}}} = \begin{cases} 1 & \text{if } \sigma_k^2(r_{\dot{y}_E}) \leq \sigma_k^2(r_{\dot{y}_E})_{threshold} \\ 0 & \text{else} \end{cases} \tag{7.108}$$

The final state estimate is corrected through Eq. (7.109) and Eq. (7.110).

$$\begin{bmatrix} x_{E_k} \\ \dot{x}_{E_k} \end{bmatrix} = \begin{bmatrix} x^-_{E_k} \\ \dot{x}^-_{E_k} \end{bmatrix} + K_k(x_E) \begin{bmatrix} c_{r_{x_{E_k}}} r_{x_{E_k}} \\ c_{r_{\dot{x}_{E_k}}} r_{\dot{x}_{E_k}} \end{bmatrix} \tag{7.109}$$

$$\begin{bmatrix} y_{E_k} \\ \dot{y}_{E_k} \end{bmatrix} = \begin{bmatrix} y^-_{E_k} \\ \dot{y}^-_{E_k} \end{bmatrix} + K_k(y_E) \begin{bmatrix} c_{r_{y_{E_k}}} r_{y_{E_k}} \\ c_{r_{\dot{y}_{E_k}}} r_{\dot{y}_{E_k}} \end{bmatrix} \tag{7.110}$$

Lastly, the state uncertainty covariance matrices must be updated using Eq. (7.111) and Eq. (7.112).

$$P_k(x_E) = (I - HK_k(x_E))P_k^-(x_E) \tag{7.111}$$

$$P_k(y_E) = (I - HK_k(y_E))P_k^-(y_E) \tag{7.112}$$

In Figure 72 the position and horizontal velocity discrete Kalman filter is shown in diagram form.

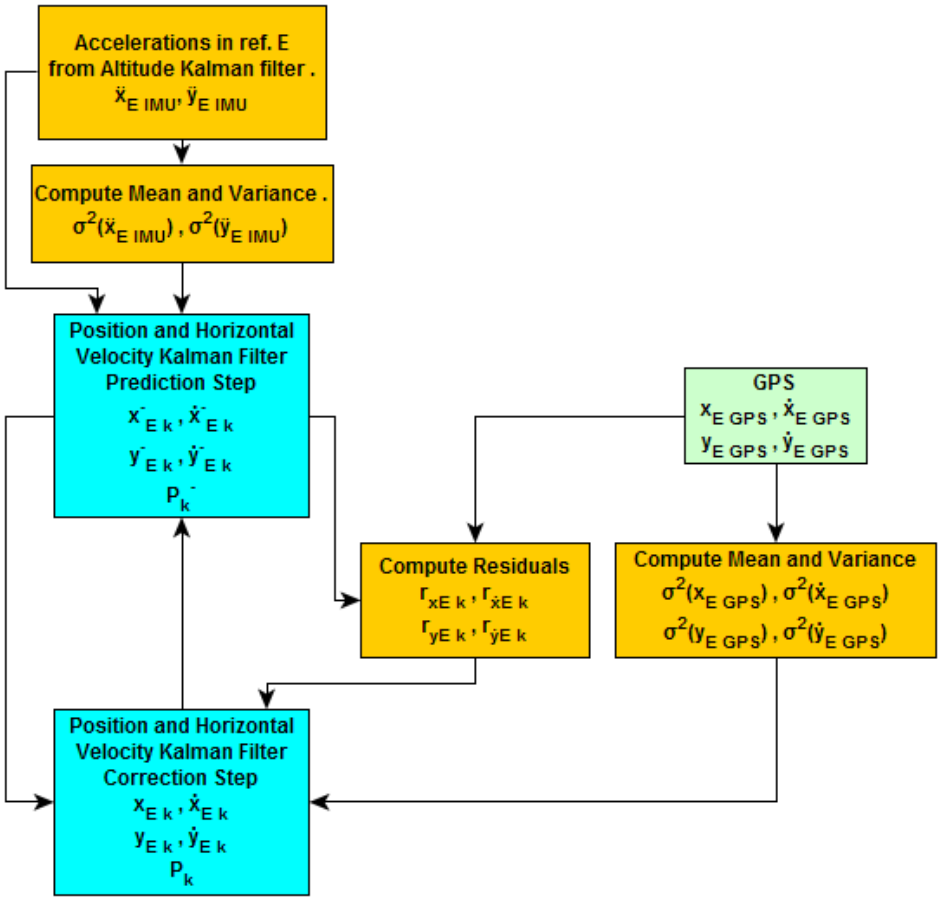

Figure 72 – Position and horizontal velocity discrete Kalman filter diagram

7.10 Vehicle velocity in body coordinate frame

Once the vehicle's horizontal and vertical velocities have been computed $(\dot{x}_E, \dot{y}_E, \dot{z}_E)$, the vector can be converted to body coordinate frame (U, V, W) in order to obtain vehicle resulting velocity V_T, angle of attack α and sideslip angle β. So, this is done using Eq. (7.113).

$$\begin{bmatrix} U \\ V \\ W \end{bmatrix} = \begin{bmatrix} \cos\psi\cos\theta & \sin\psi\cos\theta & -\sin\theta \\ \cos\psi\sin\theta\sin\phi - \sin\psi\cos\phi & \sin\psi\sin\theta\sin\phi + \cos\psi\cos\phi & \cos\theta\sin\phi \\ \cos\psi\sin\theta\cos\phi + \sin\psi\sin\phi & \sin\psi\sin\theta\cos\phi - \cos\psi\sin\phi & \cos\theta\cos\phi \end{bmatrix} \begin{bmatrix} \dot{x}_E \\ \dot{y}_E \\ \dot{z}_E \end{bmatrix} \tag{7.113}$$

In Eq. (7.114) is defined the vehicle resulting velocity, in Eq. (7.115) the angle of attack and in Eq. (7.116) the sideslip angle, following (STEVENS; LEWIS; JOHNSON, 2015).

$$V_T = \sqrt{U^2 + V^2 + W^2} \tag{7.114}$$

$$\alpha = \arctan 2\left(W, U\right) \tag{7.115}$$

$$\beta = \arcsin\left(\frac{V}{V_T}\right) \tag{7.116}$$

8 CONTROL ALGORITHM

In this chapter are presented the control algorithms to by applied in the aircraft prototype, being: hovering configuration attitude control; attitude plus attitude control; attitude plus altitude plus position control, and transition control, along with the embedded software architecture.

8.1 Radio receiver input signals

The aircraft radio receiver has seven channels, whose respective sticks in the radio transmitter are shown in Figure 73, and the channels specifications are listed in Table 27. Every channel use pulse width modulation (PWM) with the frequency of 45.45 Hz.

The radio receiver channel 1 PWM signal range is shown in Figure 74, where is displayed in Figure 74a the signal at minimum throttle with 930 μs and in Figure 74b the stick at maximum throttle with 2070 μs. Therefore each channel range must be measured and then scaled to the normalized range (1000 μs to 2000 μs).

Each radio receiver channel is connected to a digital port in the on-board microcontroller board (Arduino Due), so that the pulse widths are measured on each channel by measuring the instant of time when the signal changes from low to high, and then back, from high to low, and thus making the time difference between the two occurrences. This procedure is possible due to the interrupt function of the processor, so that, when a change in the digital input signal is detected, the code interrupts the current action, and proceeds with a bypass function, in this case, measure the time of the occurrence, then returns to the previous action.

Figure 73 – Radio transmitter channels

Table 27 – Radio receiver channels specifications.

Channel	Control	Pulse Width Modulation (PWM) Range (μs)
Channel 1	Throttle	1000μs - 2000μs (continuous)
Channel 2	Roll	1000μs - 1500μs - 2000μs (return to center automatically)
Channel 3	Pitch	1000μs - 1500μs - 2000μs (return to center automatically)
Channel 4	Yaw	1000μs - 1500μs - 2000μs (return to center automatically)
Channel 5	Flight Mode	1100μs or 1900μs (two positions)
Channel 6	Flap	1100μs or 1500μs or 1900μs (three positions)
Channel 7	Tilt	1100μs or 1500μs or 1900μs (three positions)

a) Channel 1 minimum throttle (930us) b) Channel 1 maximum throttle (2070 us)

Figure 74 – Radio receiver channel 1 input PWM signal range

Furthermore, every channel input signal is noisy, so it is important to implement digital filters to dampen it. Thus, a simple filter to do it is the complementary filter, defined in Eq. (8.1). It has two filtration intensities, so that, when the variance of the radio input signal R_{input} is less then a threshold, the signal is highly attenuated, which correspond to the situation that the pilot makes no movement in the respective stick. When the pilot moves a stick, the variance of the corresponding signal increases, so the filter intensity must be reduced in order to have a quick response.

$$R^k_{filtered} = \begin{cases} 0.995R^{k-1}_{filtered} + 0.005R^k_{input} & \text{if } \sigma^2_k(R_{input}) \leq \sigma^2_{threshold}(R_{input}) \\ 0.30R^{k-1}_{filtered} + 0.70R^k_{input} & \text{else} \end{cases} \tag{8.1}$$

In Figure 75 is displayed an example of the radio receiver channel 1 (throttle) input and the same signal using the filter of Eq. (8.1), by moving the radio throttle stick with the hand. The mean and variance are computed using the last 10 measurements, and the variance threshold $R_{input_{threshold}}$ is 40. It is possible to observe that the unfiltered signal has noise when the stick remains in static position, which is removed by the filter.

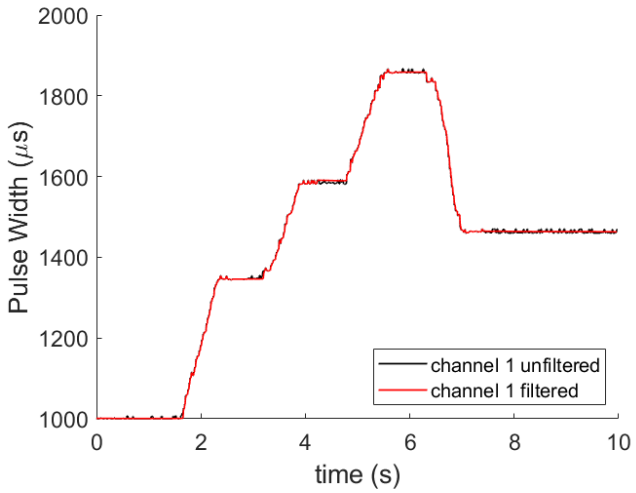

Figure 75 – Radio receiver channel 1 signal unfiltered and filtered

8.2 ESC's input signals

The electronic speed controllers (ESC's), that drive the brushless motors, are also controlled via PWM signals, with modulation in the range of 1000 μs to 2000 μs. The input in the range of 1000 μs to 1100 μs, keeps the motors off, so the motors start spinning with input signal of 1100 μs, and the maximum rotational speed is with input signal of 2000 μs.

8.3 Hovering Configuration Control

8.3.1 Attitude Control

The objective of the control in the aircraft hovering configuration is to stabilize the attitude of the vehicle, that is, to keep it leveled when there is no control inputs from the pilot and to lean or turn to a given direction when commanded.

At hovering configuration the attitude is controlled using only the motors and propellers, that is, the aerodynamic actuators such as flaps, ailerons, elevators and rudders are not used, therefore remaining in the neutral position.

The attitude hovering configuration control diagram is depicted in Figure 76, which is described in this section.

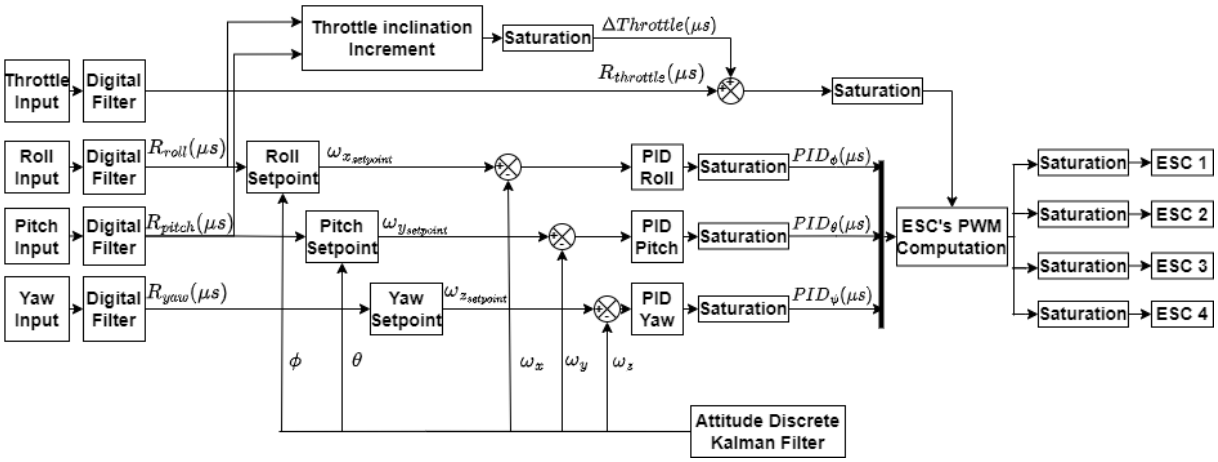

Figure 76 – Attitude hovering configuration control diagram

Therefore, the error to be regulated is the angular velocity in the three axis of rotation, as defined in Eq. (8.2), Eq. (8.3) and Eq. (8.4) for the error is roll, pitch and yaw directions respectively. The errors are defined with respect to setpoints.

$$\epsilon_{\phi}^{k} = \omega_{x}^{k} - \omega_{x_{setpoint}}^{k} \tag{8.2}$$

$$\epsilon_{\theta}^{k} = \omega_{y}^{k} - \omega_{y_{setpoint}}^{k} \tag{8.3}$$

$$\epsilon_{\psi}^{k} = \omega_{z}^{k} - \omega_{z_{setpoint}}^{k} \tag{8.4}$$

Each axis setpoint is defined in Eq. (8.5), Eq. (8.6) and Eq. (8.7), being functions of the estimated Euler roll ϕ and pitch θ angles, and the motion commands received from the radio. The value of setpoints different from zero on each of the axes imposes an inclination movement to the vehicle, that is, it means that even with the vehicle in an initially level situation, when applied in $\omega_{x_{setpoint}}^{k}$ a positive value will result in a negative error in ϵ_{ϕ}^{k}, so the controller interpret as a need to tilt the vehicle on that axis. Therefore, varying the setpoint values through the radio command signals, or detecting inclination angle, is possible to order the inclination and rotation of the vehicle on each axis.

$$\omega_{x_{setpoint}}^{k} = \frac{R_{roll}^{k} - k_1(\phi)\phi^{k}}{k_2(\phi)} \tag{8.5}$$

$$\omega_{y_{setpoint}}^{k} = \frac{R_{pitch}^{k} - k_1(\theta)\theta^{k}}{k_2(\theta)} \tag{8.6}$$

$$\omega^k_{z_{setpoint}} = \frac{R^k_{yaw}}{k_2(\psi)} \tag{8.7}$$

However, it is important that this forced turn command is self-limiting, that is, the movement of slope starts with the aircraft level and with a maximum error ϵ due to the signal command of the radio at the setpoint, and as it tilts it is important that this tilt error decreases progressively until it reaches a maximum incline and remains inclined, resulting in a movement forward, for example. These motion limitations are made through the equations that define the setpoints (Eq. (8.5), Eq. (8.6) and Eq. (8.7)), where the difference between the radio input commands and the respective Euler angle sets the maximum slope limit, so that, the resulting angular velocity setpoints is zero in an inclined condition at the same time the radio stick is actuated. In these equations the normalized input signals from the radio receiver in the roll, pitch and yaw directions (PWM from 1000 μs to 2000 μs), must be adjusted so that when the input signal falls below the center value of 1500 μs results in a negative command, and if it is above the center value of 1500 μs result in a positive command. Furthermore, it is important to use a positive and negative 10 μs dead band around the central 1500 μs value to avoid unintentional commands. This adjustment is shown in the following equations (Eq. (8.8), Eq. (8.9) and Eq. (8.10)).

$$R^k_{roll} = \begin{cases} R^k_{roll_{filtered}} - 1510 & \text{if} \quad R^k_{roll_{filtered}} > 1510 \\ R^k_{roll_{filtered}} - 1490 & \text{else if} \quad R^k_{roll_{filtered}} < 1490 \\ 0 & \text{else} \end{cases} \tag{8.8}$$

$$R^k_{pitch} = \begin{cases} R^k_{pitch_{filtered}} - 1510 & \text{if} \quad R^k_{pitch_{filtered}} > 1510 \\ R^k_{pitch_{filtered}} - 1490 & \text{else if} \quad R^k_{pitch_{filtered}} < 1490 \\ 0 & \text{else} \end{cases} \tag{8.9}$$

$$R^k_{yaw} = \begin{cases} R^k_{yaw_{filtered}} - 1510 & \text{if} \quad R^k_{yaw_{filtered}} > 1510 \\ R^k_{yaw_{filtered}} - 1490 & \text{else if} \quad R^k_{yaw_{filtered}} < 1490 \\ 0 & \text{else} \end{cases} \tag{8.10}$$

Moreover, in the equation defining the angular velocity setpoints (Eq. (8.5), Eq. (8.6) and Eq. (8.7)) there are conversion coefficients k_1 and k_2. The first converts the vehicle respective estimated Euler angle, roll or pitch in degrees, to an equivalent value in μs to make the difference with the radio input signal in μs. It is related to the maximum input signal (2000 μs - 1510 μs), to the maximum desired inclination angle in the respective axis, $\phi_{desired_{max}}$ and $\theta_{desired_{max}}$, given by Eq. (8.11) and Eq. (8.12).

$$k_1(\phi) = \frac{2000[\mu s] - 1510[\mu s]}{\phi_{desired_{max}}[^\circ]} \tag{8.11}$$

$$k_1(\theta) = \frac{2000[\mu s] - 1510[\mu s]}{\theta_{desired_{max}}[^\circ]} \tag{8.12}$$

The k_2 coefficient converts the resulting difference of the numerator in μs into angular velocity setpoint to an equivalent value in degrees/s. Similarly, this coefficient is computed relating the maximum input signal (2000 μs - 1510 μs) to the maximum desired angular velocity in the respective axis, $\omega_{x_{max}}$, $\omega_{y_{max}}$ and $\omega_{z_{max}}$, given by Eq. (8.13), Eq. (8.14) and Eq. (8.15).

$$k_2(\phi) = \frac{2000[\mu s] - 1510[\mu s]}{\omega_{x_{max}}[^\circ/s]} \tag{8.13}$$

$$k_2(\theta) = \frac{2000[\mu s] - 1510[\mu s]}{\omega_{y_{max}}[^\circ/s]} \tag{8.14}$$

$$k_2(\psi) = \frac{2000[\mu s] - 1510[\mu s]}{\omega_{z_{max}}[^\circ/s]} \tag{8.15}$$

The applied control methodology is the Proportional-Integral-Derivative (PID), whose equations are defined in Eq. (8.16), Eq. (8.17) and Eq. (8.18), for the roll, pitch and yaw axis respectively, making use of the gains k_P (proportional), k_I (integral) and k_D (derivative). In these equations the outputs PID_ϕ, PID_θ and PID_ψ are resulting PWM signals in μs.

$$PID_\phi^k = k_{P_\phi}\epsilon_\phi^k + I_\phi^k + k_{D_\phi}\left(\epsilon_\phi^k - \epsilon_\phi^{k-1}\right) \tag{8.16}$$

$$PID_\theta^k = k_{P_\theta}\epsilon_\theta^k + I_\theta^k + k_{D_\theta}\left(\epsilon_\theta^k - \epsilon_\theta^{k-1}\right) \tag{8.17}$$

$$PID_\psi^k = k_{P_\psi}\epsilon_\psi^k + I_\psi^k + k_{D_\psi}\left(\epsilon_\psi^k - \epsilon_\psi^{k-1}\right) \tag{8.18}$$

The integral parts I_ϕ, I_θ and I_ψ must be saturated, that is, if the sum reaches a value above a certain upper limit, or below the lower limit, the value is forced to equal the corresponding limit. Therefore, they are defined in Eq. (8.19), Eq. (8.20) and Eq. (8.21).

$$I_\phi^k = \begin{cases} k_{I_\phi}\left(\epsilon_\phi^k + \sum_{i=0}^{k-1}\epsilon_{\phi_i}\right) & \text{if} \quad I_{\phi_{min}} \leq I_\phi^k \leq I_{\phi_{max}} \\ I_{\phi_{max}} & \text{else if} \quad I_\phi^k > I_{\phi_{max}} \\ I_{\phi_{min}} & \text{else if} \quad I_\phi^k < I_{\phi_{min}} \end{cases} \tag{8.19}$$

$$I_{\theta}^{k} = \begin{cases} k_{I_\theta}\left(\epsilon_{\theta}^{k} + \sum_{i=0}^{k-1}\epsilon_{\theta_i}\right) & \text{if} \quad I_{\theta_{min}} \leq I_{\theta}^{k} \leq I_{\theta_{max}} \\ I_{\theta_{max}} & \text{else if} \quad I_{\theta}^{k} > I_{\theta_{max}} \\ I_{\theta_{min}} & \text{else if} \quad I_{\theta}^{k} < I_{\theta_{min}} \end{cases} \tag{8.20}$$

$$I_{\psi}^{k} = \begin{cases} k_{I_\psi}\left(\epsilon_{\psi}^{k} + \sum_{i=0}^{k-1}\epsilon_{\psi_i}\right) & \text{if} \quad I_{\psi_{min}} \leq I_{\psi}^{k} \leq I_{\psi_{max}} \\ I_{\psi_{max}} & \text{else if} \quad I_{\psi}^{k} > I_{\psi_{max}} \\ I_{\psi_{min}} & \text{else if} \quad I_{\psi}^{k} < I_{\psi_{min}} \end{cases} \tag{8.21}$$

Moreover, the resulting PID output must also be saturated, which is done in Eq. (8.22), Eq. (8.23) and Eq. (8.24).

$$PID_{\phi}^{k} = \begin{cases} PID_{\phi}^{k} & \text{if} \quad PID_{\phi_{min}} \leq PID_{\phi}^{k} \leq PID_{\phi_{max}} \\ PID_{\phi_{max}} & \text{else if} \quad PID_{\phi}^{k} > PID_{\phi_{max}} \\ PID_{\phi_{min}} & \text{else if} \quad PID_{\phi}^{k} < PID_{\phi_{min}} \end{cases} \tag{8.22}$$

$$PID_{\theta}^{k} = \begin{cases} PID_{\theta}^{k} & \text{if} \quad PID_{\theta_{min}} \leq PID_{\theta}^{k} \leq PID_{\theta_{max}} \\ PID_{\theta_{max}} & \text{else if} \quad PID_{\theta}^{k} > PID_{\theta_{max}} \\ PID_{\theta_{min}} & \text{else if} \quad PID_{\theta}^{k} < PID_{\theta_{min}} \end{cases} \tag{8.23}$$

$$PID_{\psi}^{k} = \begin{cases} PID_{\psi}^{k} & \text{if} \quad PID_{\psi_{min}} \leq PID_{\psi}^{k} \leq PID_{\psi_{max}} \\ PID_{\psi_{max}} & \text{else if} \quad PID_{\psi}^{k} > PID_{\psi_{max}} \\ PID_{\psi_{min}} & \text{else if} \quad PID_{\psi}^{k} < PID_{\psi_{min}} \end{cases} \tag{8.24}$$

The output signals computed using the PID methodology are controls with respect to a steady vehicle condition, that is the hovering condition. Thus, it must be added to the input that makes the vehicle hover (the *Throttle* input signal to the motors that corresponds to propellers at total thrust equivalent to the vehicle weight). Therefore, the resulting PWM signals to each electronic speed controller (ESC) are defined in Eq. (8.25), Eq. (8.26), Eq. (8.27) and Eq. (8.28). The ESC's numbering are defined in Figure 77, as well as the rotations directions.

$$esc_{1}^{k} = Throttle^{k} + PID_{\phi}^{k} + PID_{\theta}^{k} + PID_{\psi}^{k} \tag{8.25}$$

$$esc_{2}^{k} = Throttle^{k} - PID_{\phi}^{k} + PID_{\theta}^{k} - PID_{\psi}^{k} \tag{8.26}$$

$$esc_{3}^{k} = Throttle^{k} + PID_{\phi}^{k} - PID_{\theta}^{k} - PID_{\psi}^{k} \tag{8.27}$$

$$esc_4^k = Throttle^k - PID_\phi^k - PID_\theta^k + PID_\psi^k \tag{8.28}$$

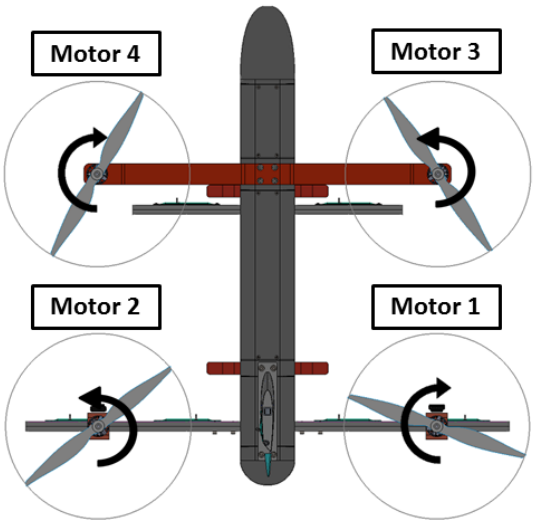

Figure 77 – Numbering of the aircraft motors and rotation directions.

The positive and negative signs of the sums of the PID_ϕ, PID_θ and PID_ψ outputs in Eq. (8.25), Eq. (8.26), Eq. (8.27) and Eq. (8.28), are given by the effects of the thrusts and torques of each propeller on the attitude (respective Euler angles) of the vehicle. In other words, for instance, given a flight situation with a positive error in pitch direction ϵ_θ, the correction is to reduce esc_3 and esc_4 inputs, and increase esc_1 and esc_2.

Additionally, if the pilot orders the vehicle to lean in some direction, in order to move forward, backwards, to the left or to the right, it will lean and the sum of the thrusts of the propellers will no longer sustain completely the aircraft weight, in other words, the tendency shall be to move in the respective direction whilst descend. Therefore, the input to lean must be followed with a throttle increment.

The roll (R_{roll}) and pitch (R_{pitch}) inputs from the radio is equivalent to a desired roll ($\phi_{desired}$) and pitch ($\theta_{desired}$) angle respectively, defined in Eq. (8.29) and Eq. (8.30), where $k_1(\phi)$ and $k_2(\theta)$ are the same as in Eq. (8.11) and Eq. (8.12). Similarly, for the yaw axis is defined the yaw angular rate desired in Eq. (8.31).

$$\phi_{desired}^k = \frac{R_{roll}^k}{k_1(\phi)} \tag{8.29}$$

$$\theta_{desired}^k = \frac{R_{pitch}^k}{k_1(\theta)} \tag{8.30}$$

$$\omega^k_{z_{desired}} = \frac{R^k_{yaw}}{k_2(\psi)} \tag{8.31}$$

As the input signals R_{roll} and R_{pitch} have upper and bottom limits, there are maximum and minimum desired inclination angles, which were previously used in Eq. (8.11) and Eq. (8.12), in the definition of $k_1(\phi)$ and $k_1(\theta)$.

So, the increment to the $Throttle$ is defined in Eq. (8.32), whose outcome must be saturated via Eq. (8.33).

$$\Delta Throttle^k_{lean} = \left(\frac{\|\phi^k_{desired}\|}{\phi_{desired_{max}}} + \frac{\|\theta^k_{desired}\|}{\theta_{desired_{max}}} \right) \Delta Throttle_{max} \tag{8.32}$$

$$\Delta Throttle^k_{lean} = \begin{cases} \Delta Throttle^k_{lean} & \text{if} \quad \Delta Throttle^k_{lean} \leq \Delta Throttle_{lean_{max}} \\ \Delta Throttle_{lean_{max}} & \text{else} \end{cases} \tag{8.33}$$

The result is then summed to the radio throttle filtered input, as in Eq. (8.34).

$$Throttle^k = R^k_{throttle_{filtered}} + \Delta Throttle^k_{lean} \tag{8.34}$$

Still, it is important to leave a margin for the increments due to the PID controller in relation to the $Throttle$ signal, since the maximum input signal at each ESC is 2000 μs. Thus, the maximum signal allowed is limited to $Throttle$ of 1800 μs, which is the saturation of Eq. (8.35).

$$Throttle^k = \begin{cases} Throttle^k & \text{if} \quad Throttle^k \leq 1800\mu s \\ 1800 & \text{else} \end{cases} \tag{8.35}$$

Moreover, when the $Throttle$ signal is such that the resulting propellers thrust is equivalent to the vehicle weight, the vehicle should remain hovering. So, if it is greater then this value, the vehicle shall climb vertically, and if smaller it shall go down.

It is also important to saturate the signal to the ESC's resulting from the PID's, so if the result is below 1100 μs, this minimum input value must be forced so that the motors do not shut down in flight. Furthermore, if the result is above 2000 μs, this maximum input value must be forced, since the maximum input value allowed for the ESC's is 2000 μs.

8.3.2 Attitude plus altitude control

The aircraft has also the capacity to control its altitude, or height. This capability is activated via the flight mode radio input, which is given by the the radio receiver channel 5. It has two positions, that is, flight mode 1 and flight mode 2, summarized in Table 28.

So, the aircraft must take-off in flight mode 1, with the channel 5 stick in high position. Once the vehicle acquire altitude in a hover condition, the pilot can put the channel 5 stick in low position activating flight mode 2, which sets the current estimated height (h^k) via the altitude discrete Kalman filter as the height setpoint ($h^k_{setpoint}$) to be controlled.

Table 28 – Aircraft transition desired index as functions of channel 7 stick position

Channel	Flight Mode	Control
Channel 5 Stick High	Flight Mode 1	Attitude Control
Channel 5 Stick Low	Flight Mode 2	Attitude + Altitude Control

The full attitude plus altitude control diagram is depicted in Figure 78, which has a complementary part to the attitude control diagram.

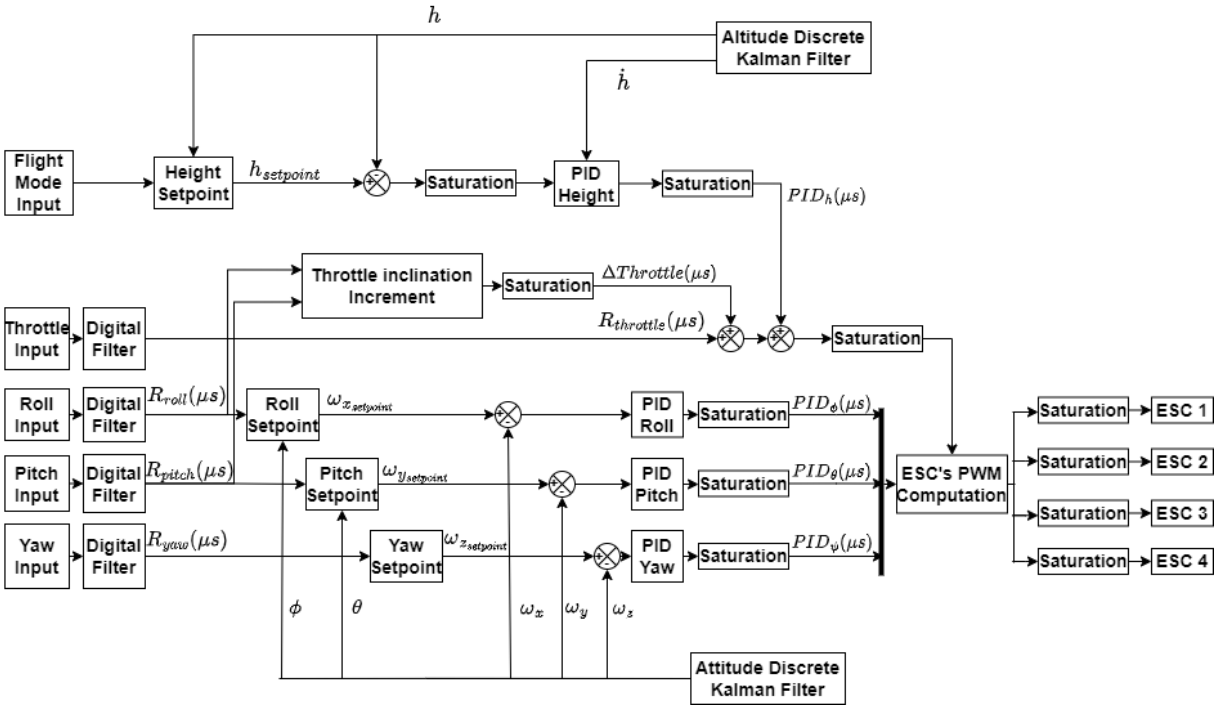

Figure 78 – Attitude plus altitude hovering configuration control diagram

Therefore, the error to be regulated is the difference between the current estimated height h^k to the height setpoint $h_{setpoint}$ defined at the moment the pilot activated flight mode 2, as in Eq. (8.36). The minus sign multiplying the difference is because when the

error is positive, the outcome must be to reduce throttle input, and if the error is negative, the outcome must be to increase throttle input.

$$\epsilon_h^k = -(h^k - h_{setpoint}) \tag{8.36}$$

It is important to saturate the error in height to avoid excessive correction, as in Eq. (8.37).

$$\epsilon_h^k = \begin{cases} \epsilon_h^k & \text{if} \quad \epsilon_{h_{min}} \leq \epsilon_h^k \leq \epsilon_{h_{max}} \\ \epsilon_{h_{max}} & \text{else if} \quad \epsilon_h^k > \epsilon_{h_{max}} \\ \epsilon_{h_{min}} & \text{else if} \quad \epsilon_h^k < \epsilon_{h_{min}} \end{cases} \tag{8.37}$$

The control methodology is the Proportional-Integral-Derivative (PID), whose equation is defined in Eq. (8.38), making use of the gains k_{P_h} (proportional), k_{I_h} (integral) and k_{D_h} (derivative). The PID_h^k is the resulting PWM signal, and $\dot{h}^k$ is the estimated vertical velocity, which is an outcome from the altitude discrete Kalman filter.

$$PID_h^k = k_{P_h}\epsilon_h^k + I_h^k + k_{D_h}\left(-\dot{h}^k\right) \tag{8.38}$$

The I_h^k is the integral part, which is saturated via Eq. (8.39).

$$I_h^k = \begin{cases} k_{I_h}\left(\epsilon_h^k + \sum_{i=0}^{k-1}\epsilon_{h_i}\right) & \text{if} \quad I_{h_{min}} \leq I_h^k \leq I_{h_{max}} \\ I_{h_{max}} & \text{else if} \quad I_h^k > I_{h_{max}} \\ I_{h_{min}} & \text{else if} \quad I_h^k < I_{h_{min}} \end{cases} \tag{8.39}$$

The outcome PID_h^k, must also be saturated as in Eq. (8.40).

$$PID_h^k = \begin{cases} PID_h^k & \text{if} \quad PID_{h_{min}} \leq PID_h^k \leq PID_{h_{max}} \\ PID_{h_{max}} & \text{else if} \quad PID_h^k > PID_{h_{max}} \\ PID_{h_{min}} & \text{else if} \quad PID_h^k < PID_{h_{min}} \end{cases} \tag{8.40}$$

Finally, the result is added to the *Throttle* input, as in Eq. (8.41), which is then used to compute the PWM signals to each ESC, as in Eq. (8.25), Eq. (8.26), Eq. (8.27) and Eq. (8.28).

$$Throttle^k = R^k_{throttle_{filtered}} + \Delta Throttle^k_{lean} + PID_h^k \tag{8.41}$$

8.3.3 Attitude, altitude and position control

There is also the possibility to activate position control, which is an addition to the attitude plus altitude control. The diagram of this flight mode is shown in Figure 79. Moreover, since the channel 5 stick has only two available positions, the embedded code can either have Flight Mode 2 with Attitude + Altitude control, or Flight Mode 2 with Attitude + Altitude + Position control, as in Table 29.

Table 29 – Aircraft hovering configuration flight modes with attitude, altitude and position

Channel	Flight Mode	Control
Channel 5 Stick High	Flight Mode 1	Attitude Control
Channel 5 Stick Low	Flight Mode 2	Attitude + Altitude + Position Control

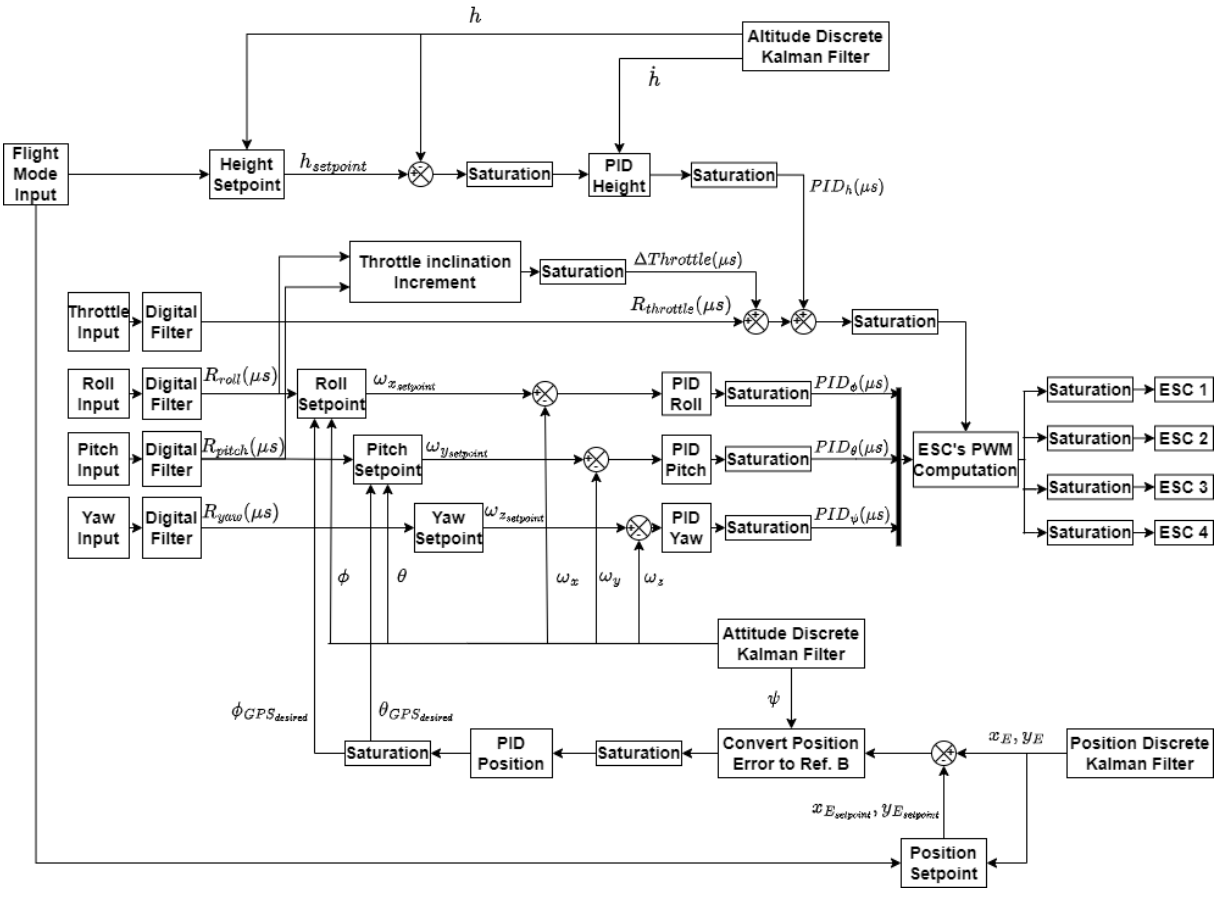

Figure 79 – Attitude, altitude and position control during hovering configuration diagram

The position error is defined with respect to the coordinates of a defined setpoint $(x^k_{E_{setpoint}}, y^k_{E_{setpoint}})$ in the Earth fixed inertial frame. Thus, the errors in x_E and y_E directions are defined in Eq. (8.42) and Eq. (8.43). The setpoints are defined as the position when the pilot activate flight mode 2, therefore with the purpose to hold position.

$$\epsilon_{x_E}^k = x_E^k - x_{E_{setpoint}}^k \tag{8.42}$$

$$\epsilon_{y_E}^k = y_E^k - y_{E_{setpoint}}^k \tag{8.43}$$

The errors in Earth fixed inertial frame must be converted to body coordinate frame, via Eq. (8.44).

$$\begin{bmatrix} \epsilon_{x_B}^k \\ \epsilon_{y_B}^k \end{bmatrix} = \begin{bmatrix} \cos\psi^k & \sin\psi^k \\ -\sin\psi^k & \cos\psi^k \end{bmatrix} \begin{bmatrix} \epsilon_{x_E}^k \\ \epsilon_{y_E}^k \end{bmatrix} \tag{8.44}$$

The results must be saturated in order to avoid correction of long displacements, which is done in Eq. (8.45) and Eq. (8.46).

$$\epsilon_{x_B}^k = \begin{cases} \epsilon_{x_B}^k & \text{if} \quad \epsilon_{x_{B_{min}}} \leq \epsilon_{x_B}^k \leq \epsilon_{x_{B_{max}}} \\ \epsilon_{x_{B_{max}}} & \text{else if} \quad \epsilon_{x_B}^k > \epsilon_{x_{B_{max}}} \\ \epsilon_{x_{B_{min}}} & \text{else if} \quad \epsilon_{x_B}^k < \epsilon_{x_{B_{min}}} \end{cases} \tag{8.45}$$

$$\epsilon_{y_B}^k = \begin{cases} \epsilon_{y_B}^k & \text{if} \quad \epsilon_{y_{B_{min}}} \leq \epsilon_{y_B}^k \leq \epsilon_{y_{B_{max}}} \\ \epsilon_{y_{B_{max}}} & \text{else if} \quad \epsilon_{y_B}^k > \epsilon_{y_{B_{max}}} \\ \epsilon_{y_{B_{min}}} & \text{else if} \quad \epsilon_{y_B}^k < \epsilon_{y_{B_{min}}} \end{cases} \tag{8.46}$$

Furthermore, there are the saturation of the integral parts in Eq. (8.47) and Eq. (8.48).

$$I_{x_B}^k = \begin{cases} k_{I_{x_B}} \left(\epsilon_{x_B}^k + \sum_{i=0}^{k-1} \epsilon_{x_{B_i}} \right) & \text{if} \quad I_{x_{B_{min}}} \leq I_{x_B}^k \leq I_{x_{B_{max}}} \\ I_{x_{B_{max}}} & \text{else if} \quad I_{x_B}^k > I_{x_{B_{max}}} \\ I_{x_{B_{min}}} & \text{else if} \quad I_{x_B}^k < I_{x_{B_{min}}} \end{cases} \tag{8.47}$$

$$I_{y_B}^k = \begin{cases} k_{I_{y_B}} \left(\epsilon_{y_B}^k + \sum_{i=0}^{k-1} \epsilon_{y_{B_i}} \right) & \text{if} \quad I_{y_{B_{min}}} \leq I_{y_B}^k \leq I_{y_{B_{max}}} \\ I_{y_{B_{max}}} & \text{else if} \quad I_{y_B}^k > I_{y_{B_{max}}} \\ I_{y_{B_{min}}} & \text{else if} \quad I_{y_B}^k < I_{y_{B_{min}}} \end{cases} \tag{8.48}$$

Likewise, the control methodology is the Proportional-Integral-Derivative (PID), whose equation is defined in Eq. (8.49) that results in the desired pitch angle $\theta_{GPS_{desired}}$ to correct the vehicle position in the x_B direction, and in Eq. (8.50) that results in the desired roll angle $\phi_{GPS_{desired}}$ to correct the vehicle position in the y_B direction.

$$\theta^k_{GPS_{desired}} = k_{P_{x_B}}\epsilon^k_{x_B} + I^k_{x_B} + k_{D_{x_B}}\left(\epsilon^k_{x_B} - \epsilon^{k-1}_{x_B}\right) \tag{8.49}$$

$$\phi^k_{GPS_{desired}} = -k_{P_{y_B}}\epsilon^k_{y_B} - I^k_{y_B} - k_{D_{y_B}}\left(\epsilon^k_{y_B} - \epsilon^{k-1}_{y_B}\right) \tag{8.50}$$

Both results must be saturated, which is done in Eq. (8.51) and Eq. (8.52).

$$\theta^k_{GPS_{desired}} = \begin{cases} \theta^k_{GPS_{desired}} & \text{if} \quad \theta_{GPS_{desired_{min}}} \leq \theta^k_{GPS_{desired}} \leq \theta_{GPS_{desired_{max}}} \\ \theta_{GPS_{desired_{max}}} & \text{else if} \quad \theta^k_{GPS_{desired}} > \theta_{GPS_{desired_{max}}} \\ \theta_{GPS_{desired_{min}}} & \text{else if} \quad \theta^k_{GPS_{desired}} < \theta_{GPS_{desired_{min}}} \end{cases} \tag{8.51}$$

$$\phi^k_{GPS_{desired}} = \begin{cases} \phi^k_{GPS_{desired}} & \text{if} \quad \phi_{GPS_{desired_{min}}} \leq \phi^k_{GPS_{desired}} \leq \phi_{GPS_{desired_{max}}} \\ \phi_{GPS_{desired_{max}}} & \text{else if} \quad \phi^k_{GPS_{desired}} > \phi_{GPS_{desired_{max}}} \\ \phi_{GPS_{desired_{min}}} & \text{else if} \quad \phi^k_{GPS_{desired}} < \phi_{GPS_{desired_{min}}} \end{cases} \tag{8.52}$$

Lastly, the resulting desired roll and pitch angle must be inserted in the angular velocity setpoints, as in Eq. (8.53) and Eq. (8.54).

$$\omega^k_{x_{setpoint}} = \frac{R^k_{roll} + k_1(\phi)(\phi^k_{GPS_{desired}} - \phi^k)}{k_2(\phi)} \tag{8.53}$$

$$\omega^k_{y_{setpoint}} = \frac{R^k_{pitch} + k_1(\theta)(\theta^k_{GPS_{desired}} - \theta^k)}{k_2(\theta)} \tag{8.54}$$

8.4 Transition Control

The first aspect of the transition flight is the way the wing and canard should tilt as the vehicle transitions. So, this movement follows the curves of Figure 80, which are the results of the combination of equilibrium states as functions of flight speed, described in section 5.1. However, in this figure the wing and canard tilt angles are functions of a control variable named transition Index.

The transition Index is controlled via the radio channel 7 input, which has three positions (stick high, middle and low). So, each channel 7 stick position relates to a transition index desired, as shown in Table 30. That is, the vehicle takes-off with the channel 7 stick in the high position (Hovering Configuration: wing and canard at 90°). Once the pilot decides to start the transition, the stick is put in the middle position, thus pointing the desired transition Index to 0.5 (Transition Configuration), but the current Index shall transition following the Eq. (8.55), which is an increase or decrease in the

Index at a constant rate given by the tilt rate K_{tilt}, if the desired Index ($Index^k_{desired}$) differs from the current Index ($Index^{k-1}$). The stick positioned to low gradually makes the full transition to horizontal flight. Likewise, putting the stick back to middle and high, makes the vehicle back to transition and then hovering configuration.

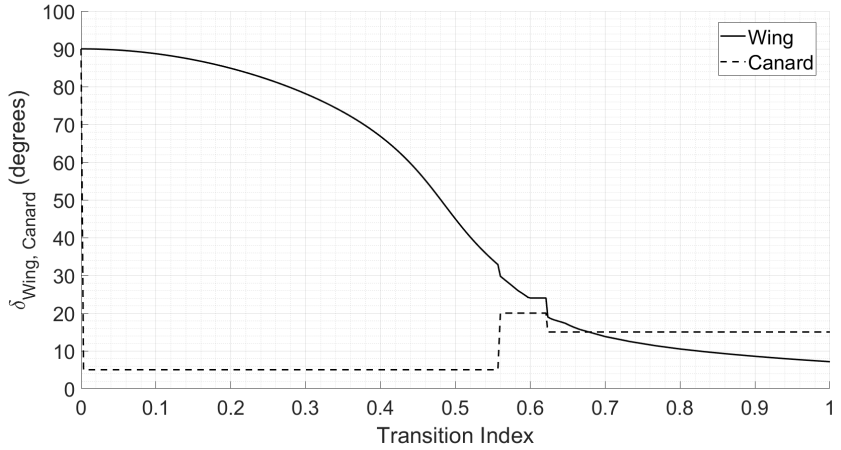

Figure 80 – Transition wing and canard tilt angle with respect to transition index

$$Index^k = \begin{cases} Index^{k-1} & \text{if} \quad Index^k_{desired} = Index^{k-1} \\ Index^{k-1} + K_{tilt}dt & \text{else if} \quad Index^k_{desired} > Index^{k-1} \\ Index^{k-1} - K_{tilt}dt & \text{else if} \quad Index^k_{desired} < Index^{k-1} \end{cases} \tag{8.55}$$

Table 30 – Aircraft transition index desired as function of channel 7 stick

Channel	Transition Index Desired	Control
Channel 7 Stick High	0	Hovering Configuration
Channel 7 Stick Middle	0.5	Transition Configuration
Channel 7 Stick Low	1.0	Horizontal Flight Configuration

There is also the flap position during transition, which is controlled via radio input channel 6 stick, whose positions are related to flap deflections as in Table 31.

Table 31 – Aircraft flap position as function of channel 6 stick

Channel	Flap Position
Channel 6 Stick High	Flap retracted (0°)
Channel 6 Stick Middle	Flap middle position (30°)
Channel 6 Stick Low	Flap full (60°)

The aerodynamic controls (ailerons, elevators and rudder) are only used when the aircraft is in transition or horizontal flight configuration, which means transition Index other than zero. So, the PWM signals to the their servos are defined as in Eq. (8.56) for the ailerons (pwm_A), which are controlled using the radio roll input (channel 2), in Eq.

(8.57) for the elevators (pwm_E), which are controlled using the radio pitch input (channel 3), and in Eq. (8.58) for the rudder (pwm_R), which is controlled using the radio yaw input (channel 4). The PWM input to the servos of 1500 μs keeps then in the neutral position.

$$pwm_A = \begin{cases} 1500 \quad \mu s & \text{if} \quad Index^{k-1} = 0 \\ R^k_{roll_{filtered}} & \text{else} \end{cases} \tag{8.56}$$

$$pwm_E = \begin{cases} 1500 \quad \mu s & \text{if} \quad Index^{k-1} = 0 \\ R^k_{pitch_{filtered}} & \text{else} \end{cases} \tag{8.57}$$

$$pwm_R = \begin{cases} 1500 \quad \mu s & \text{if} \quad Index^{k-1} = 0 \\ R^k_{yaw_{filtered}} & \text{else} \end{cases} \tag{8.58}$$

The Throttle input should not be applied equally between the four motors during transition maneuver, which must then be scaled according to the trim curves as function of wing tilt angle and transition Index, as in Figure 81, which is the relation between front motors RPM to wing motors RPM obtained from the transition trajectory.

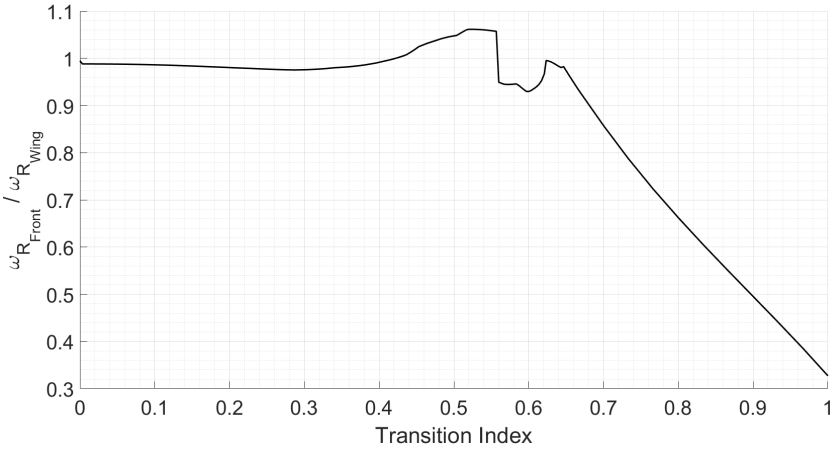

Figure 81 – Transition throttle input scale between front motors and wing motors at equilibrium

Moreover, the attitude control using the four propellers must have proportional gains scheduled according to transition Index and wing tilt angle. Therefore, in Figure 82 is shown the vehicle angular velocities (P, Q, R) derivatives with respect to each propeller angular velocity at equilibrium condition. So, once the control gains are calibrated for the hovering configuration, they shall be scaled for the transition maneuver according to their derivatives with respect to the vehicle angular velocities.

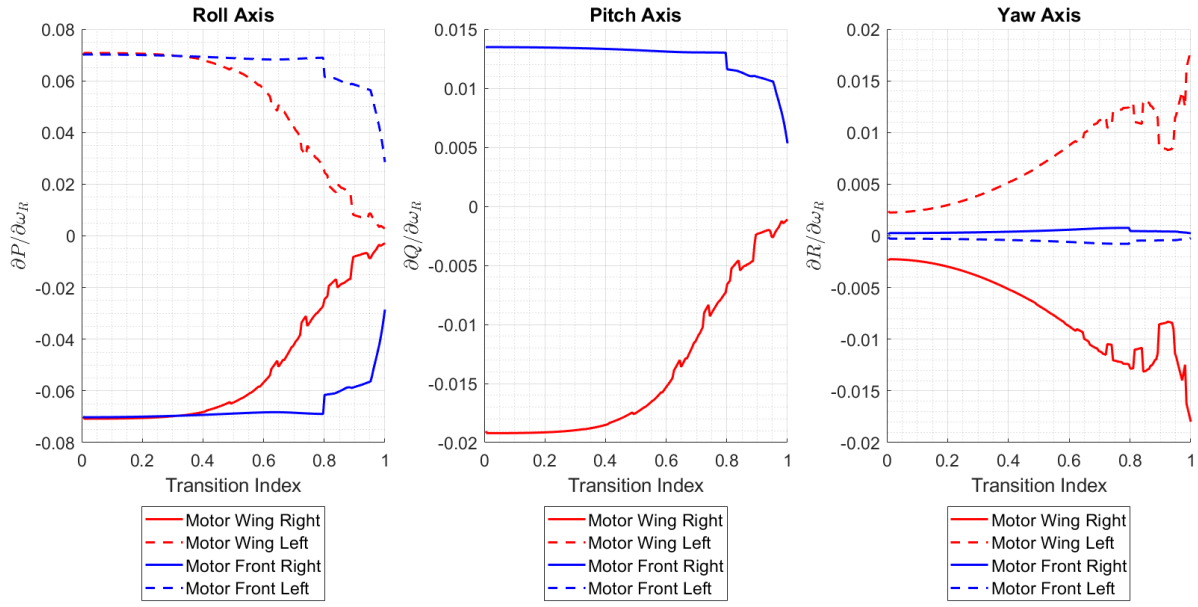

Figure 82 – Angular velocities derivatives with respect to propellers angular velocities for the transition trajectory.

8.5 Embedded Software

The on-board sensors readings, data handling, filtering, flight states estimation, radio inputs processing, control computations, telemetry data transmission and control signals outputs, are all actions to be performed by the vehicle microcontroller board through a embedded software, which are written in a code in C programming language, using the Arduino IDE (Integrated Development Environment), which also performs the code compilation and upload to the microcontroller board.

It is a single code that is divided in two main functions:

1. Setup, that runs only once when starting the code, whose actions are shown in Figure 83.

2. Control loop, which runs indefinitely until the system shuts down, whose actions are shown in Figure 84.

Immediately after the setup ends, the control loop starts.

In the setup the on-board systems and sensors must be started and configured:

1. It starts by enabling the interrupts to allow the radio inputs PWM signals readings.

2. Defines which analog ports are inputs and which digital ports are inputs and outputs.

3. Aircraft warning lights are turned on to inform the operator that the setup has started.

4. Start the serial communication bus at 400 kHz clock speed.

5. Start the IMU 1 with gyroscopes full scale range of ± 2000 degrees/s and accelerometers full scale range of ± 16 g.

6. Start the IMU 2 with gyroscopes full scale range of ± 2000 degrees/s and accelerometers full scale range of ± 16 g.

7. Configure the radio inputs, that is, save the minimum, center and maximum PWM signal at channel 1, 2, 3 and 4.

8. Configure the motors, that is, program each ESC individually in the range of 1000 μs to 2000 μs PWM signals, and check rotation directions.

9. IMU 1 calibration, which is the measurement of the bias in each axis of the gyroscopes and accelerometers in a stationary condition, to be removed during the control loop. In this sense, a 1000 readings are taken to compute the mean value, which is the bias.

10. IMU 2 calibration, which is the measurement of the bias in each axis of the gyroscopes and accelerometers in a stationary condition, to be removed during the control loop. In this sense, a 1000 readings are taken to compute the mean value, which is the bias.

11. Start pressure sensor.

12. Start GPS module at 5 Hz refresh rate.

13. Start magnetometer at 10 Hz output rate and full scale range of ± 8 gauss.

14. Calibrate magnetometer, which is the rotation of the vehicle in every direction in order to measure the full range of possible readings, and save the maximum and minimum readings to be used in the yaw angle computation.

15. Start the telemetry system configuring it to apply 2.0 Mbps of air data transmission rate, power amplifier level at 0 dBm, the frequency of the channel at 2476 MHz and a 40-bit address.

16. Turn off the aircraft warning lights to inform the operator that the setup has ended.

17. Then starts the control loops.

Once the software setup is finished, the code begins the control loops, whose actions are depicted in Figure 84.

Moreover, it is important that the embedded software runs in real time, that is, every loop takes the same amount of time to perform all the tasks. It is crucial because of the numerical integrations to be consistent with the applied integration time period (dt). Therefore, the maximum time to perform each task were measured, which are shown next to the tasks of Figure 84.

The GPS module is the one with the lowest refresh rate (5 Hz) and is only read when new data is available, otherwise it reads the pressure sensor. Therefore, the full control loop takes a maximum of 7669 μs when it reads GPS data, and 7766 μs when it reads pressure sensor. Lastly, the code waits until the loop timer reads 8000 μs (which is the numerical integration time period used) to end the control loop and start a new one, which means that the code runs at 125 Hz.

Therefore, the software is a single code that has the structure of Figure 85, which has the main parts being: include libraries (necessary libraries to run specific functions), define variables (type, size, name), setup and loop.

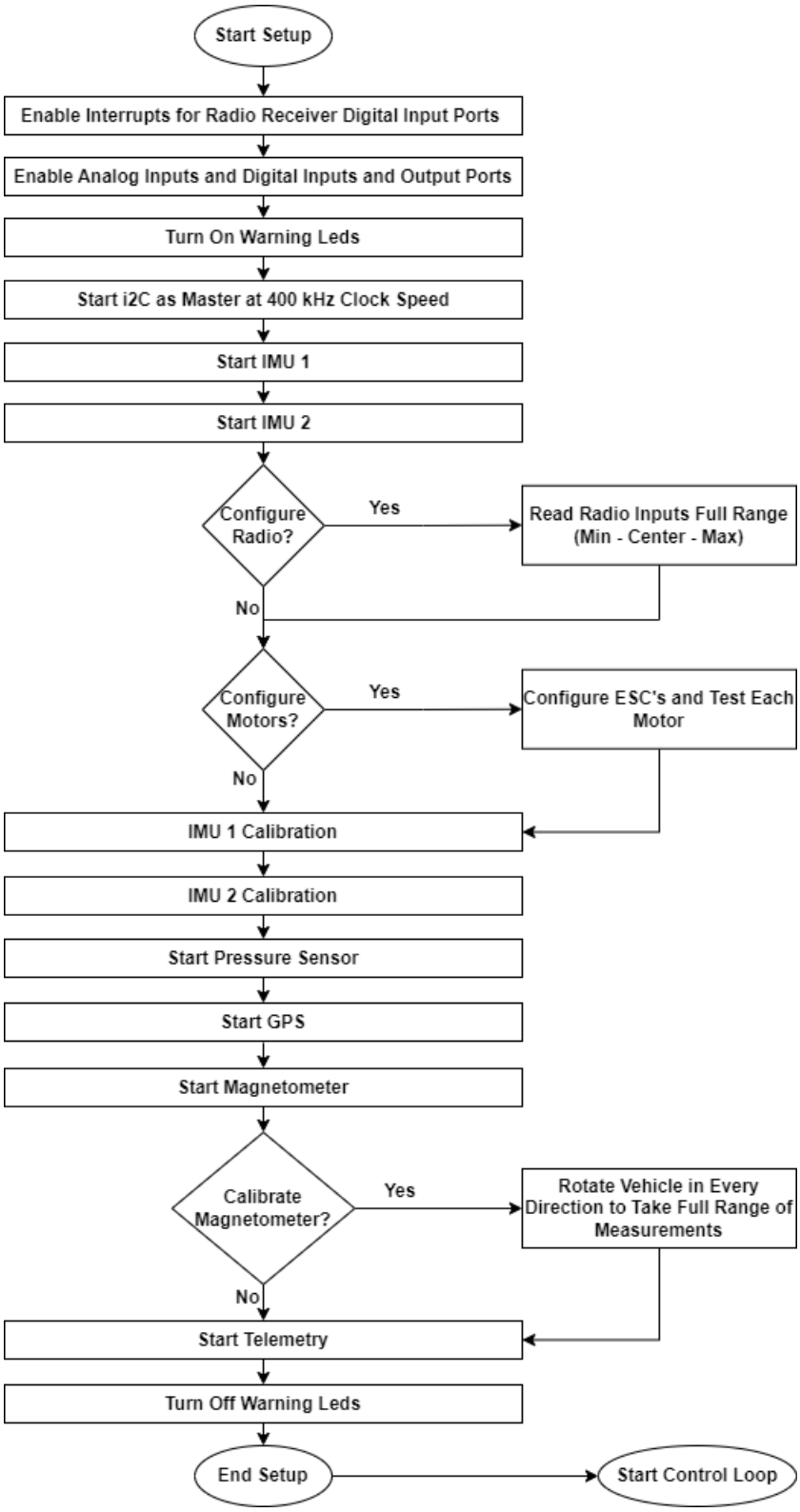

Figure 83 – Embedded software setup.

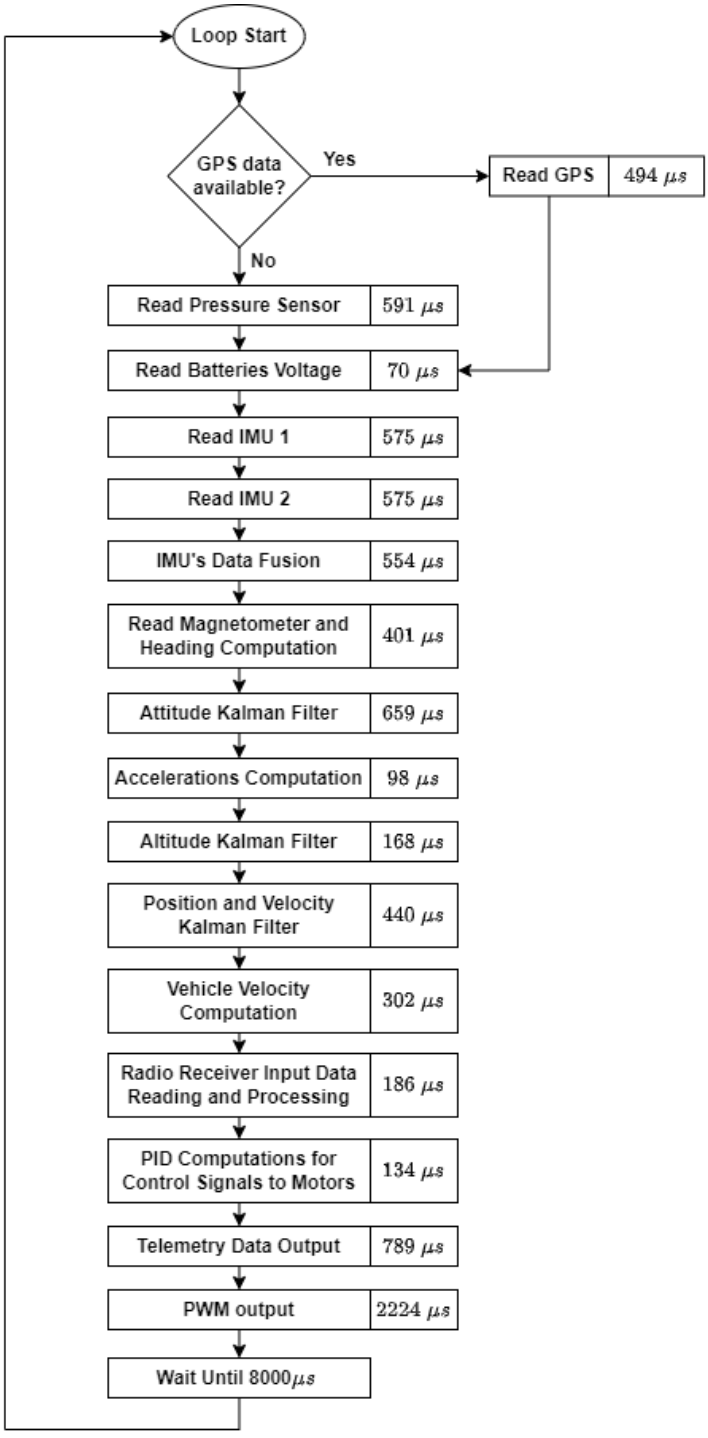

Figure 84 – Embedded software control loop diagram, with maximum time to perform each task.

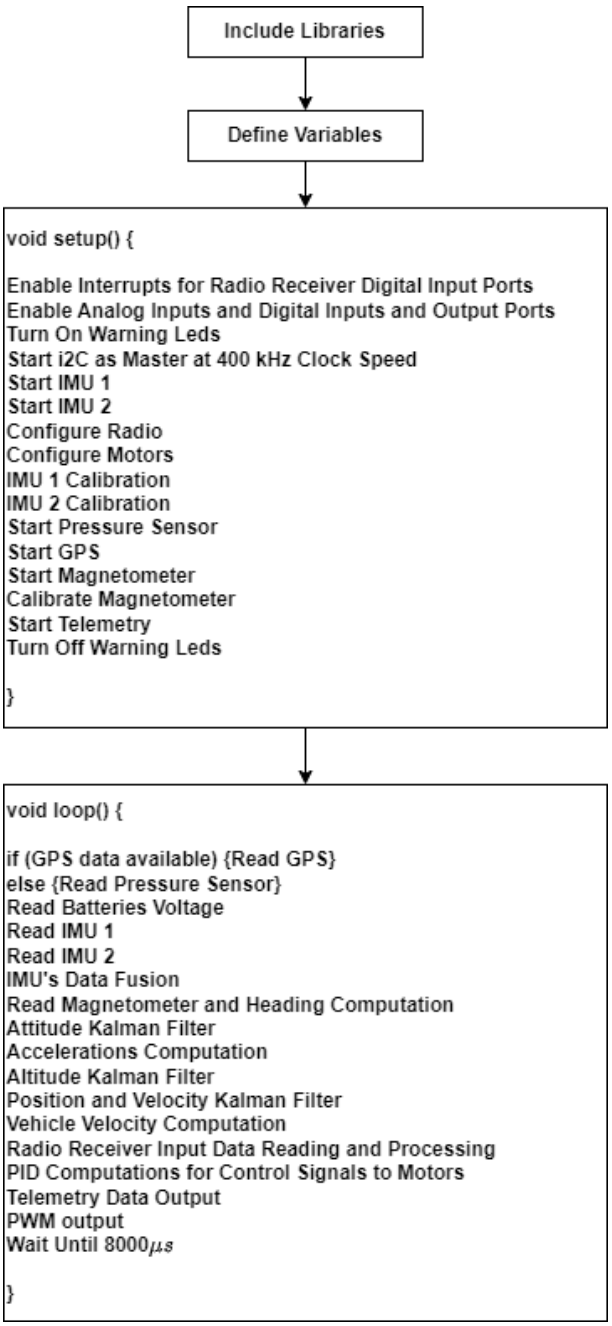

Figure 85 – Embedded software structure.

9 FLIGHT TESTING

In this chapter is presented the method to transmit and save the flight tests data.

9.1 Flight Data

The aircraft flight condition and states estimated by the embedded microcontroller board are transmitted to the ground station via the telemetry system. Some information is displayed in the ground station display screen so that the pilot is aware of important flight conditions such as:

- if telemetry data is being received.
- if SD card is working.
- available aircraft batteries charge.
- aircraft height from the take-off altitude.
- aircraft heading.
- number of GPS valid satellites.
- aircraft horizontal displacement from take-off position.
- ground station available battery charge.

The telemetry system uses a pair of nRF24L01+ transceiver, being that one is on-board the vehicle, and the other in the ground station. It was configured to use 2.0 Mbps, the power amplifier level at 0 dBm, the frequency of the channel at 2476 MHz and a 40-bit address at the transmitter and receiver.

Moreover, this radio module has auto-acknowledgment feature, in which the transmitter sends payload data to the receiver, and the receiver responds with an acknowledgment (ACK) packet that has received the payload data. The transmission of the same payload data package is retried up until 15 times (default), at intervals of 250 μs, until an acknowledgment packet is received.

So, the auto-acknowledgment feature was disabled to not interfere with the microcontroller control loop frequency, which must be constant to ensure the control system operate in real time, that is, fixed time period to perform every control loop. Thus, the transmission of each payload data package is attempted only once.

This transceiver has a maximum payload size of 32 bytes, therefore in each control loop only one packet of 32 bytes is sent. A total of four packets are defined in the following tables (Table 32, Table 33, Table 34 and Table 35), being that every packet has 12 variables of integer 16-bits (2-bytes) and 2 variables of integer 32-bits (4-bytes), thus a total of 32 bytes. The telemetry data transmission protocol is depicted in Figure 86. So, it takes four control loops to send the full flight data of a single control loop. The strategy of splitting the transmission of flight data through subsequent loops was adopted to avoid individual loops with long time periods.

Furthermore, some of the variables of the packets are multiplied by a constant (100) in order to convert float variables to integers, without losing decimal place information. Therefore, once the data is received in the ground station, they are converted back to float and divided by the same constant. An integer 16-bit stores a value in the range of -32,768 to 32,767, and a integer 32-bit stores a value in the range of -2,147,483,648 to 2,147,483,647.

The data packets are recognized at the ground station by the first integer 16-bits data of each packet which contains its tag, that is, data tag 1, 2, 3 or 4.

At the ground station there is the SD card which saves the received flight data from the aircraft in a text file. The incoming flight data, that is, the set of four packets, was saved in the frequency of 10 Hz.

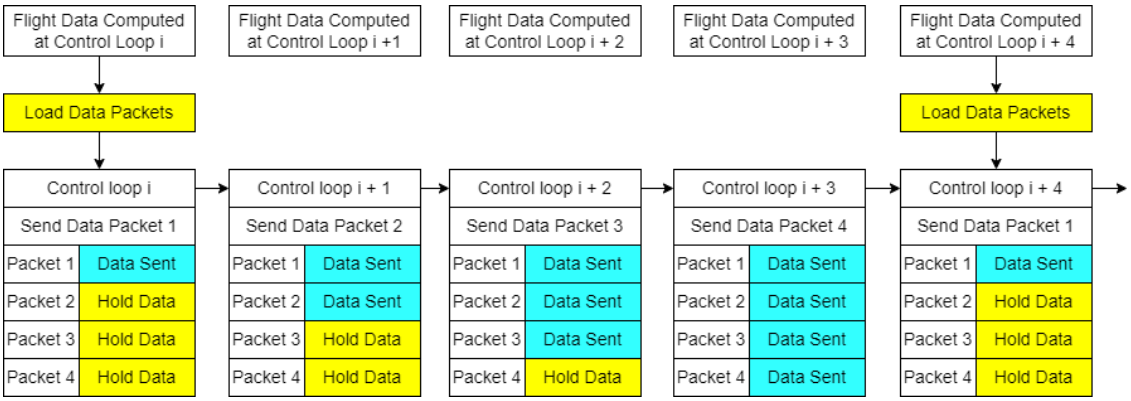

Figure 86 – Telemetry data transmission protocol

Table 32 – Telemetry data packet 1

Data	Name	Size	Units
1	Data Tag 1	int 16 bits	adm
$\phi * 100$	roll angle × 100	int 16 bits	$degrees * 100$
$\theta * 100$	pitch angle × 100	int 16 bits	$degrees * 100$
$\psi * 100$	yaw angle × 100	int 16 bits	$degrees * 100$
$\omega_x * 100$	roll angular velocity × 100	int 16 bits	$degrees/s * 100$
$\omega_y * 100$	pitch angular velocity × 100	int 16 bits	$degrees/s * 100$
$\omega_z * 100$	yaw angular velocity × 100	int 16 bits	$degrees/s * 100$
$h * 100$	height × 100	int 16 bits	$m * 100$
$\dot{h} * 100$	vertical velocity × 100	int 16 bits	$m/s * 100$
$V_{aux} * 100$	auxiliary battery voltage × 100	int 16 bits	$V * 100$
$V_L * 100$	left battery voltage × 100	int 16 bits	$V * 100$
$V_R * 100$	right battery voltage × 100	int 16 bits	$V * 100$
t_{loop}	loop timer	int 32 bits	μs
t_{end}	loop period	int 32 bits	μs

Table 33 – Telemetry data packet 2

Data	Name	Size	Units
2	Data Tag 2	int 16 bits	adm
pwm_W	PWM servo wing	int 16 bits	μs
pwm_C	PWM servo canard	int 16 bits	μs
$Throttle$	PWM throttle	int 16 bits	μs
pwm_E	PWM elevator	int 16 bits	μs
pwm_A	PWM aileron	int 16 bits	μs
pwm_F	PWM flap	int 16 bits	μs
pwm_R	PWM rudder	int 16 bits	μs
esc_1	PWM esc 1 (front left)	int 16 bits	μs
esc_2	PWM esc 2 (wing left)	int 16 bits	μs
esc_3	PWM esc 3 (front right)	int 16 bits	μs
esc_4	PWM esc 4 (wing right)	int 16 bits	μs
μ_{GPS}	GPS latitude	int 32 bits	$degrees * 1.0e7$
λ_{GPS}	GPS longitude	int 32 bits	$degrees * 1.0e7$

Table 34 – Telemetry data packet 3

Data	Name	Size	Units
3	Data Tag 3	int 16 bits	adm
$V_T * 100$	flight speed × 100	int 16 bits	$m/s * 100$
$\beta * 100$	sideslip angle × 100	int 16 bits	$degrees * 100$
$\alpha * 100$	angle of attack × 100	int 16 bits	$degrees * 100$
$\delta_W * 100$	wing angle × 100	int 16 bits	$degrees * 100$
$\delta_C * 100$	canard angle × 100	int 16 bits	$degrees * 100$
$N_{satellites}$	number of valid GPS satellites	int 16 bits	adm
$\phi_{desired} * 100$	desired roll angle × 100	int 16 bits	$degrees * 100$
$\theta_{desired} * 100$	desired pitch angle × 100	int 16 bits	$degrees * 100$
$\omega_{z_{desired}} * 100$	yaw angular velocity desired × 100	int 16 bits	$degrees/s * 100$
$h_{setpoint} * 100$	height setpoint × 100	int 16 bits	$m * 100$
FM	flight mode	int 16 bits	adm
x_E	x position in ref. E	int 32 bits	m
y_E	y position in ref. E	int 32 bits	m

Table 35 – Telemetry data packet 4

Data	Name	Size	Units
4	Data Tag 4	int 16 bits	adm
PID_ϕ	PID output roll	int 16 bits	μs
PID_θ	PID output pitch	int 16 bits	μs
PID_ψ	PID output yaw	int 16 bits	μs
P_h	P output height	int 16 bits	μs
D_h	D output height	int 16 bits	μs
$\phi_{GPS_{desired}} * 100$	roll desired position control × 100	int 16 bits	$degrees * 100$
$\theta_{GPS_{desired}} * 100$	pitch desired position control × 100	int 16 bits	$degrees * 100$
$R_{throttle}$	throttle input	int 16 bits	μs
R_{roll}	roll input	int 16 bits	μs
R_{pitch}	pitch input	int 16 bits	μs
R_{yaw}	yaw input	int 16 bits	μs
$x_{E_{setpoint}} * 100$	x position setpoint in ref. E × 100	int 32 bits	$m * 100$
$y_{E_{setpoint}} * 100$	y position setpoint in ref. E × 100	int 32 bits	$m * 100$

10 RESULTS

In this chapter the results of the aircraft flight testing are presented. The tests were:

1. Aircraft prototype in the hovering configuration in an indoor environment, the drone cage of the Department of Aeronautical Engineering of the Engineering School of São Carlos, University of São Paulo.

   Algorithms tested: section 8.3.1 and section 8.3.2, that is, attitude control and attitude plus altitude control.

2. Aircraft prototype in the hovering configuration in an outdoor environment, the surroundings of the Department of Aeronautical, in the city of São Carlos.

   Algorithms tested: section 8.3.1 and section 8.3.2, that is, attitude control and attitude plus altitude control.

At this stage of the project the aircraft had a crash with significant damage, therefore, the tests had to be interrupted for writing the thesis, repairing of the prototype and finalizing the project.

Furthermore, the PID controller gains were tuned experimentally, that is, by trial and errors, gradually modifying the gains, and testing it in the indoor environment.

10.1 Flight Test at Hovering Configuration, Indoor Environment

The aircraft was tested in an indoor environment, using the control algorithm of section 8.3.1 and section 8.3.2, that is, attitude control and attitude plus altitude automatic control, being that, the position and orientation is controlled by the pilot. In this indoor environment there is no GPS signal available, therefore the horizontal position and velocity of the aircraft are not computed.

In Figure 87 and in Figure 88 are shown two photographs of the indoor flight test. It lasted roughly 100 seconds.

The aircraft flight states were transmitted via telemetry system to a ground station that recorded the flight data at the rate of 10 Hz. In Figure 89 are shown the results of the attitude states, that is, roll, pitch and yaw (heading) angles and angular rates. During the test the attitude is well controlled, being that the yaw angles is slightly disturbed from its starting orientation, so that the pilot had to give a little control input to correct its orientation.

Figure 87 – Flight test, indoor environment (1).

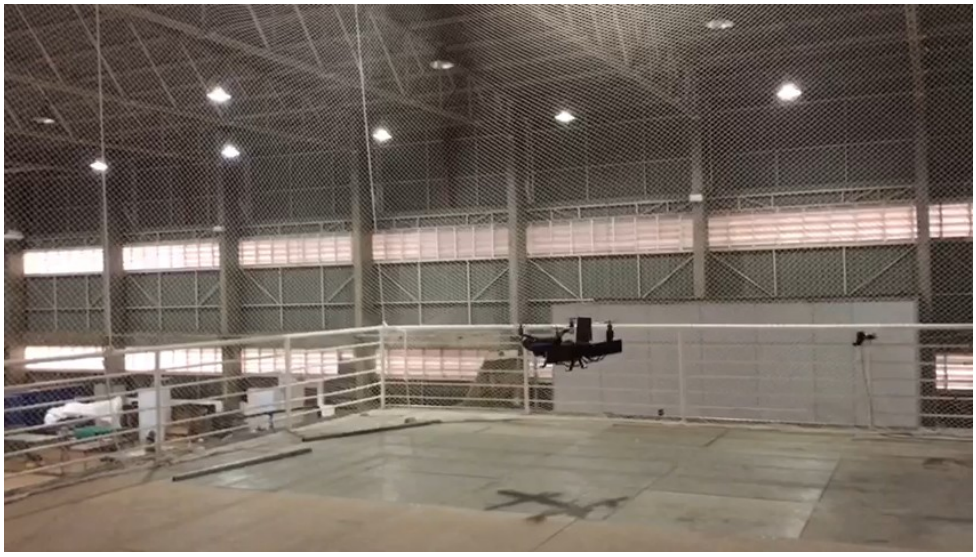

Figure 88 – Flight test, indoor environment (2).

In Figure 90 are shown the height and climb rate, along with the height setpoint when the pilot sets the flight mode to attitude plus altitude control (Flight Mode = 2). Because of the proximity to the ground, and the indoor environment, the pressure readings are somewhat less precise, given the air turbulence created by the propellers. This condition caused the starting height to read -0.5 m, which would deviate from the starting condition at 0 m from the embedded code at setup.

In Figure 91 are depicted the input signals (PWM) to the ESC's, where the black line is the throttle controlled by the pilot, from where the height can be indirectly controlled. The difference between the signals from the throttle input shows that the embedded code is actively controlling the errors in attitude.

Finally, in Figure 92 shows the on-board batteries voltage and the time to perform the embedded code control loop. The left and right propulsion batteries (4S Lipo, max 16.8V) are heavily demanded in the hovering configuration, so that their voltage drops significantly from the starting condition, which is a consequence of the battery internal resistance and the high current demanded. Moreover, during the hover their voltages continue to drop continuously at a lower rate, given the discharge. Once the aircraft lands and turn off the motors the voltage increases because there is no current being demanded from the batteries.

Furthermore, the time to perform the embedded software control loop is kept under 8000 μs during the whole flight test, therefore the code is correctly running in 125 Hz.

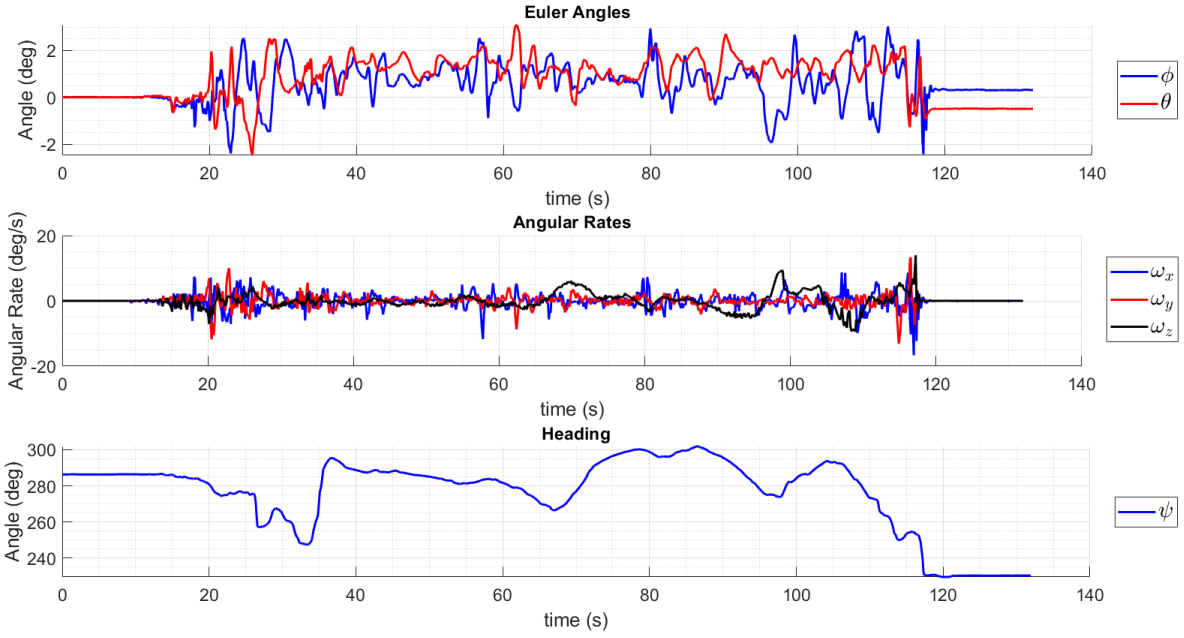

Figure 89 – Flight test, indoor environment, attitude states.

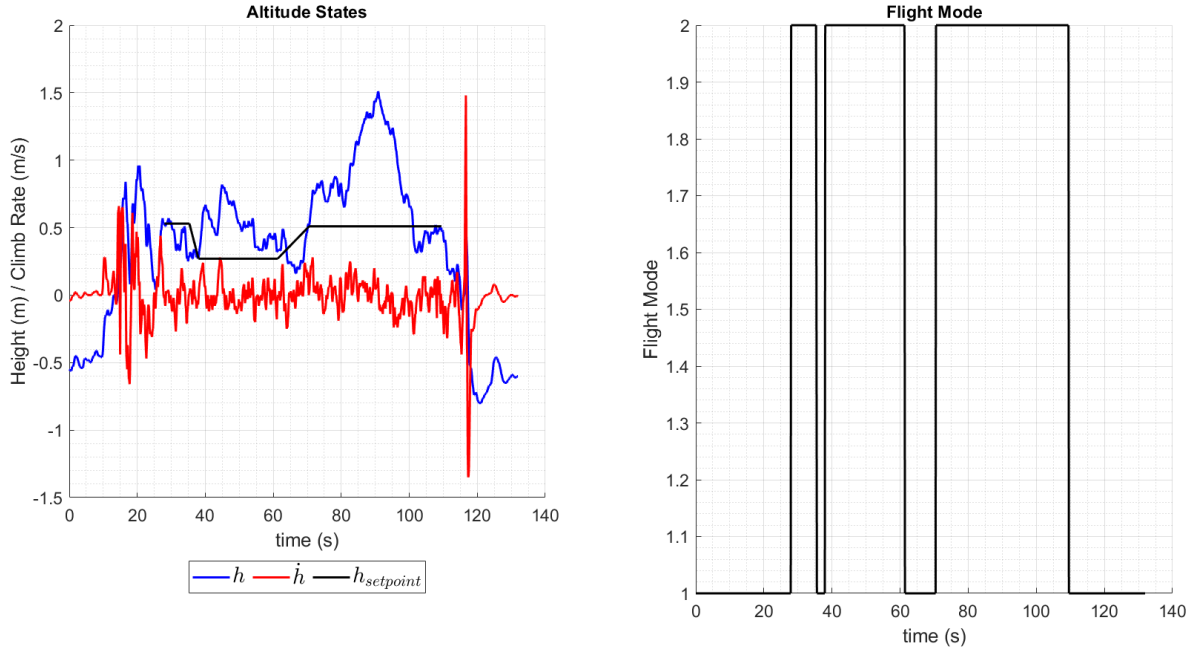

Figure 90 – Flight test, indoor environment, altitude states.

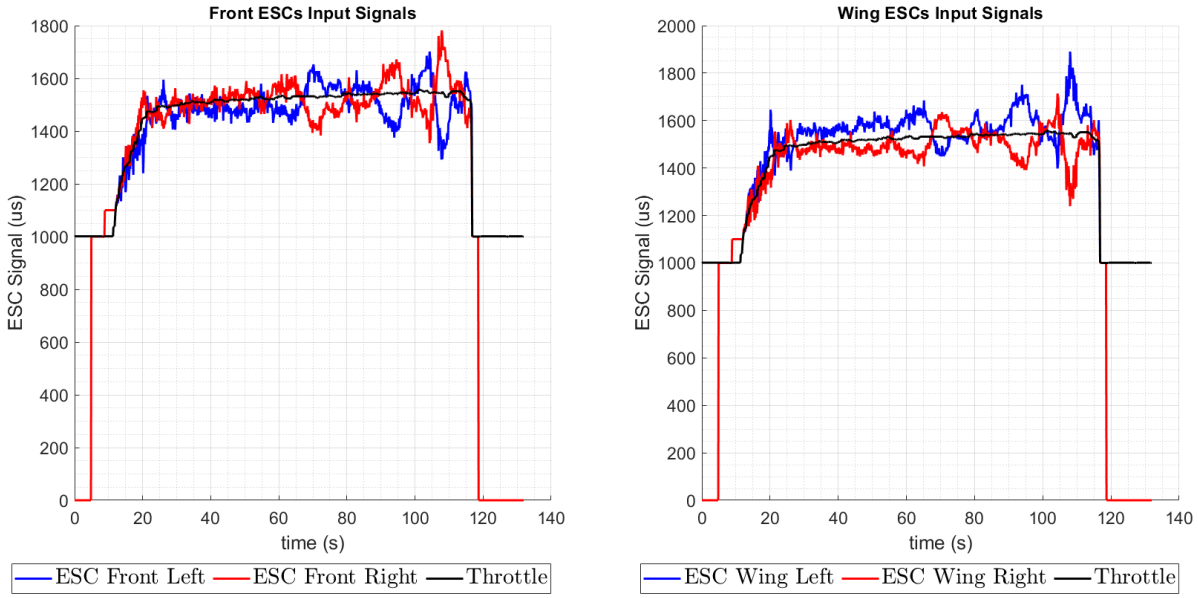

Figure 91 – Flight test, indoor environment, ESC's input signals.

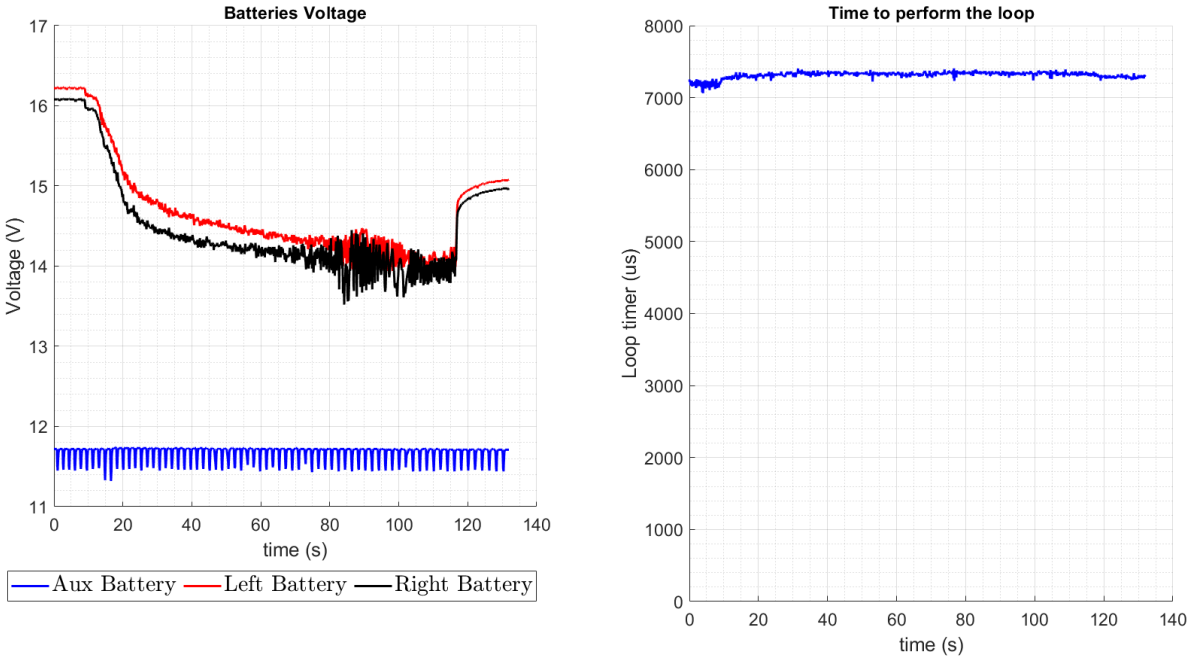

Figure 92 – Flight test, indoor environment, batteries voltage and time to perform the embedded code control loop.

10.2 Flight Test at Hovering Configuration, Outdoor Environment

The aircraft was also tested in an outdoor environment, in the surroundings of the Department of Aeronautical Engineering of the Engineering School of São Carlos, University of São Paulo. The algorithms applied were the same as in the flight tests in the indoor environment, that is, attitude control and attitude plus altitude automatic control in the hovering configuration. In the outdoor environment the GPS signal is available, therefore the aircraft coordinates, horizontal position and velocity can be computed.

So, in Figure 93, Figure 94, Figure 95 and Figure 96 are depicted photographs of the flight test, which lasted for roughly 130 seconds.

The attitude states results are shown in Figure 97, where is observed that the disturbances in attitude were more visible than the flight test in the indoor environment, which is a consequence of the wind gusts acting in the exposed aerodynamic surfaces of the aircraft, that is, the wing, canard, vertical tail, as well as the fuselage.

In Figure 98 are shown the results for the altitude states, where the aircraft reached a peak height of 21.4 meters. The altitude automatic control were not performing very well, so the pilot disengaged it to manually control its altitude. Therefore, the altitude automatic control still requires calibration.

In Figure 99 are shown the input signals to the motors ESC's. In this flight test the throttle input from the pilot was more triggered, which reflects the pilot's attempt

Figure 93 – Flight test, outdoor environment (1).

Figure 94 – Flight test, outdoor environment (2).

to control the aircraft altitude. Beyond that, the input signals to the ESC's are more oscillatory and with higher peaks than the flight test in the indoor environment, which demonstrates that the control system had to impose higher inputs to control the aircraft attitude.

In Figure 100 are shown the on-board batteries voltage over the flight test. As in the indoor test, the voltage of the propulsion batteries drops dramatically for take off, and then the discharge rate continues at a lower value. Voltage fluctuations can also be due to throttle commands by the pilot. In this test both propulsion batteries started at roughly

Figure 95 – Flight test, outdoor environment (3).

Figure 96 – Flight test, outdoor environment (4).

maximum charge at 16.8 V, and at the end they were both at 15.1 V. The minimum available voltage is 13.6 V, therefore the flight test consumed 53 % of the available charge. It is worth mentioning that the rated capacity of the propulsion batteries is 5200 mmAh, however, they have in practice only 3000 mmAh, which could be measured during charging procedure. Therefore the autonomy of the prototype in the hovering configuration should be 245 seconds (4.0 minutes).

In Figure 101 are shown the aircraft velocities in the main body coordinate frame, where the peak velocity is for the landing movement, remembering that positive W is

downward. Also in this figure is shown the available satellites to measure the aircraft coordinates from the GPS. The minimum number of satellites programmed in the code in order to compute the aircraft position was 8. if there are less than 8 satellites the positioning will have considerable drift, which degrades the precision of the measurements. for a short time the number of available satellites became less than 8, which probably happened when the aircraft came closer to the building, that has a metallic hoof, which can disturb the GPS signal.

The aircraft trajectory is shown in Figure 102 with the trajectory from the take off position at coordinates $(x_E, y_E) = (0, 0)$, where the measured coordinates are plotted with arrows representing the horizontal flight speed vector. And in Figure 103 for the trajectory over the map of the surrounding of the Department of Aeronautical Engineering in the city of São Carlos.

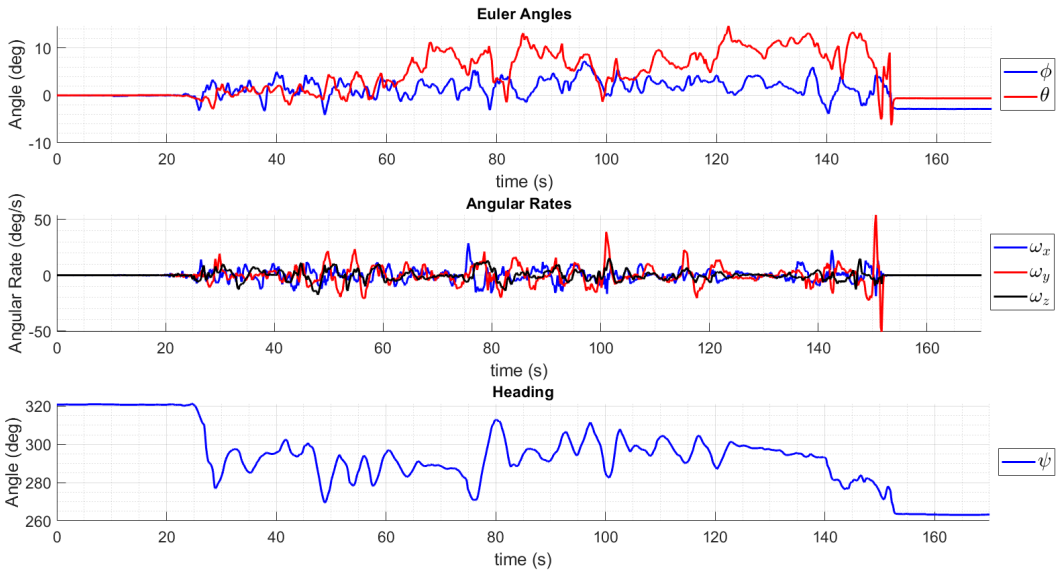

Figure 97 – Flight test, outdoor environment, attitude states.

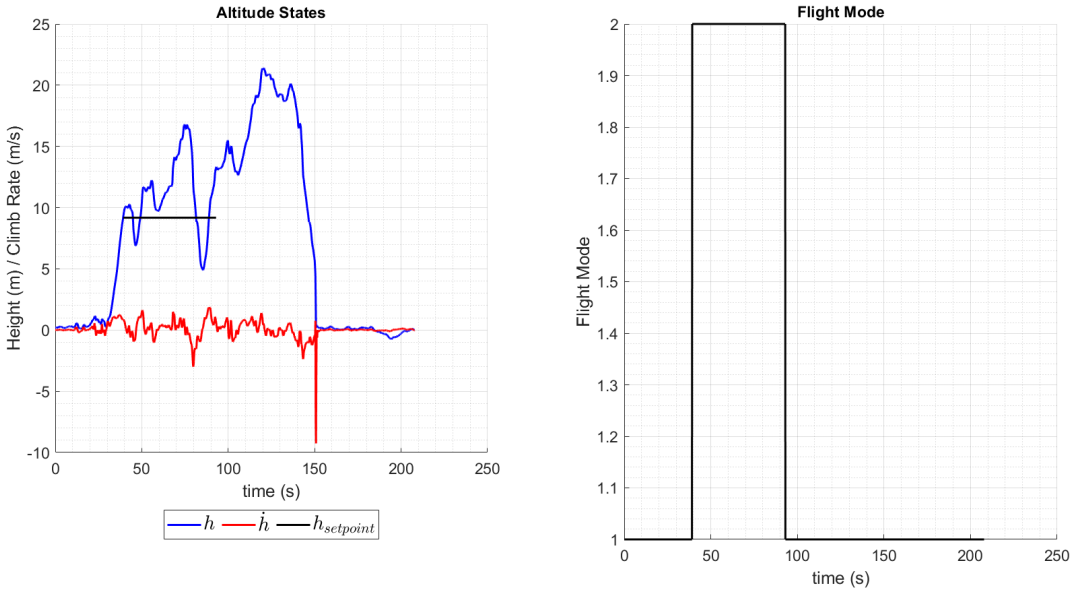

Figure 98 – Flight test, outdoor environment, altitude states.

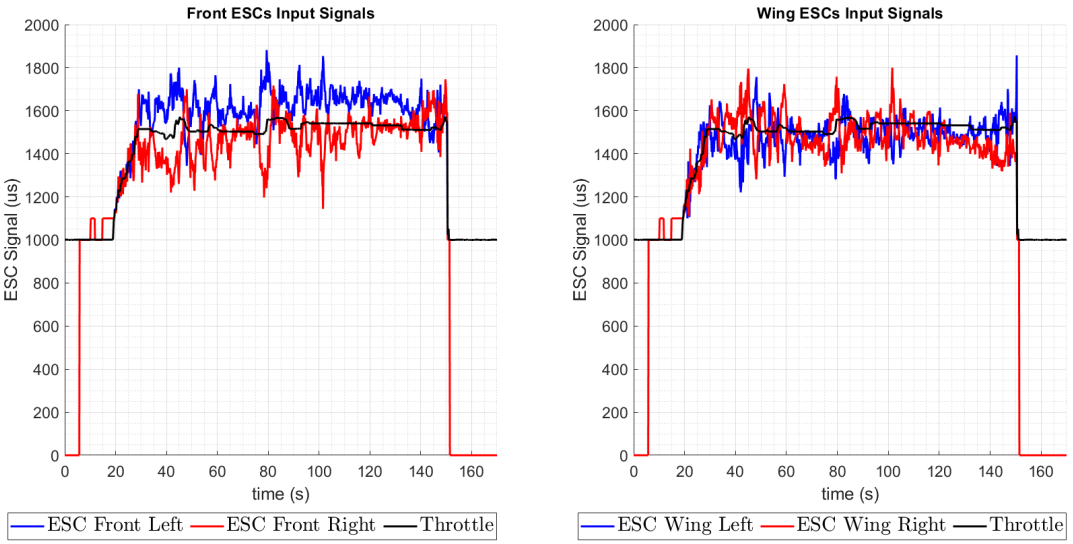

Figure 99 – Flight test, outdoor environment, ESC's input signals.

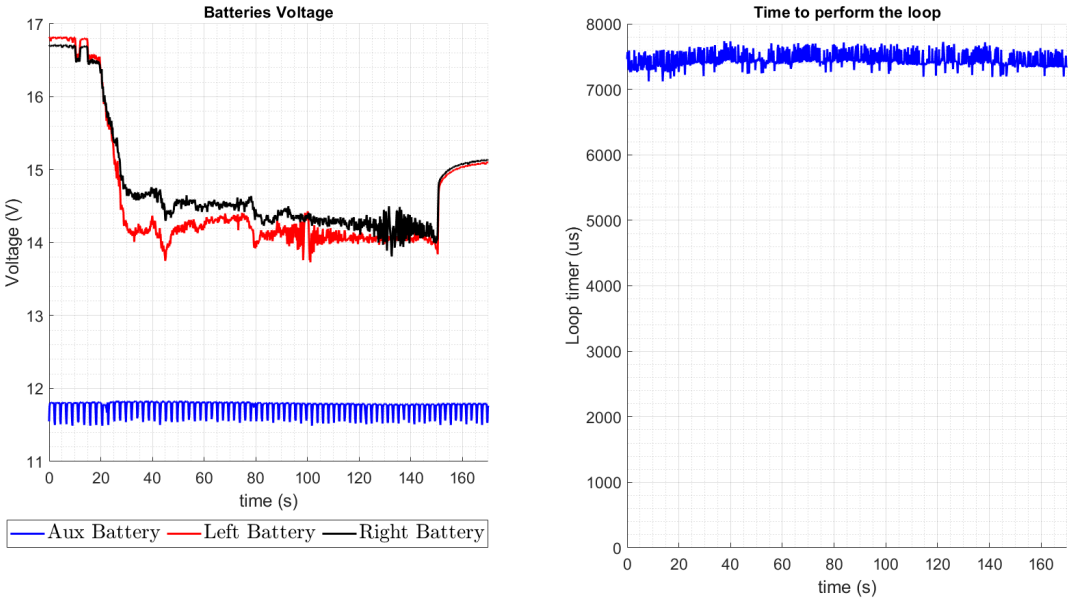

Figure 100 – Flight test, outdoor environment, batteries voltage and time to perform embedded code control loop.

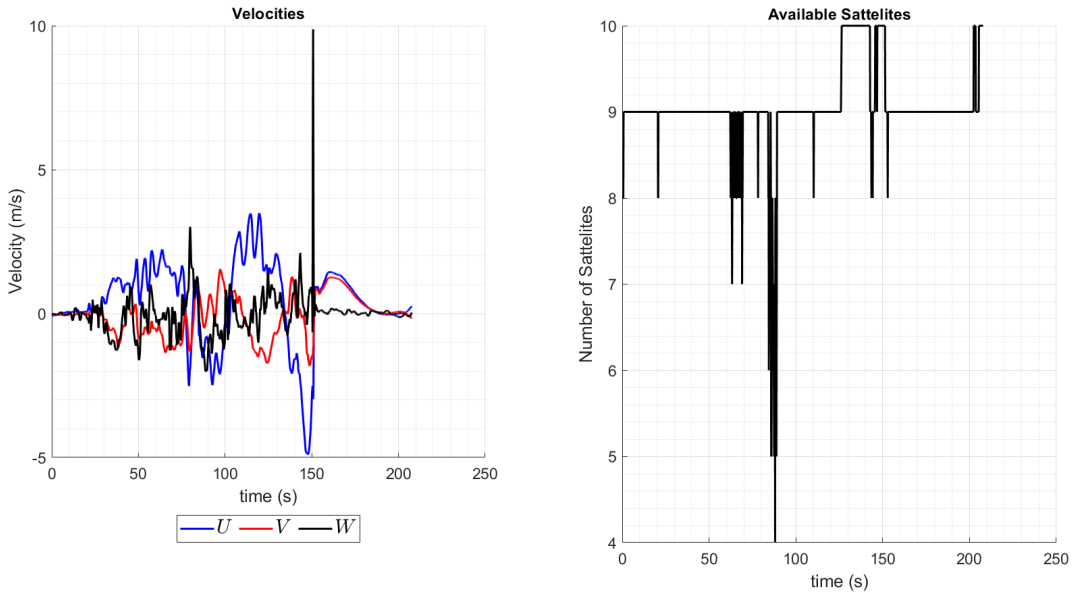

Figure 101 – Flight test, outdoor environment, aircraft velocities and available satellites.

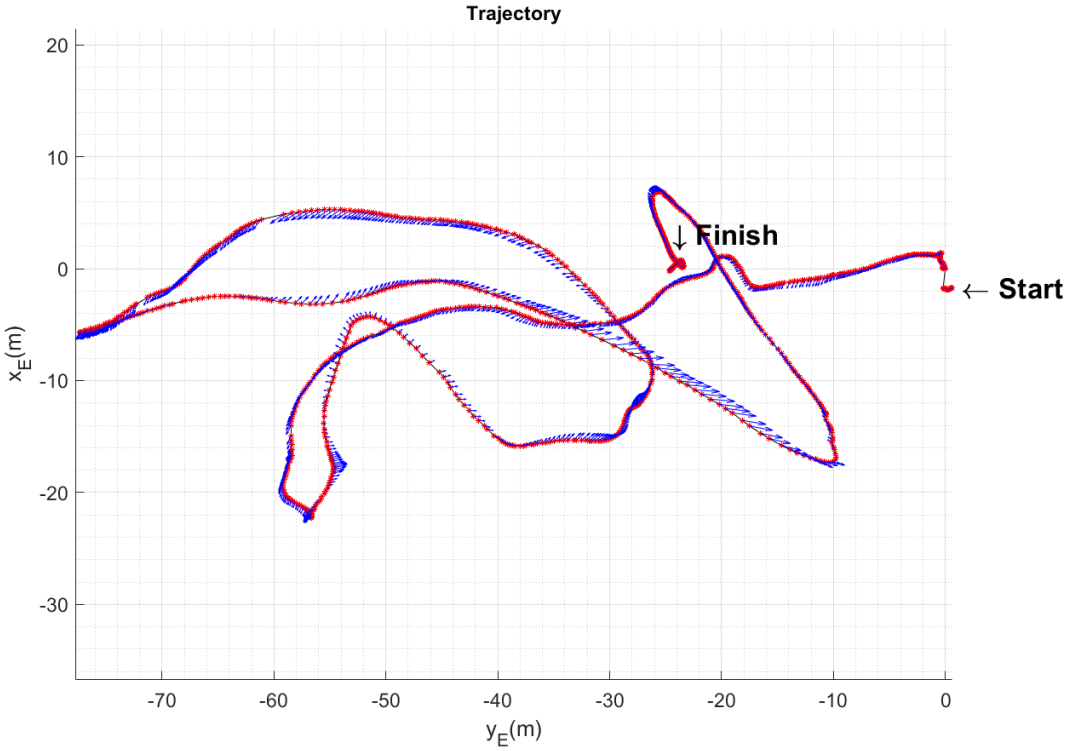

Figure 102 – Flight test, outdoor environment, aircraft computed trajectory

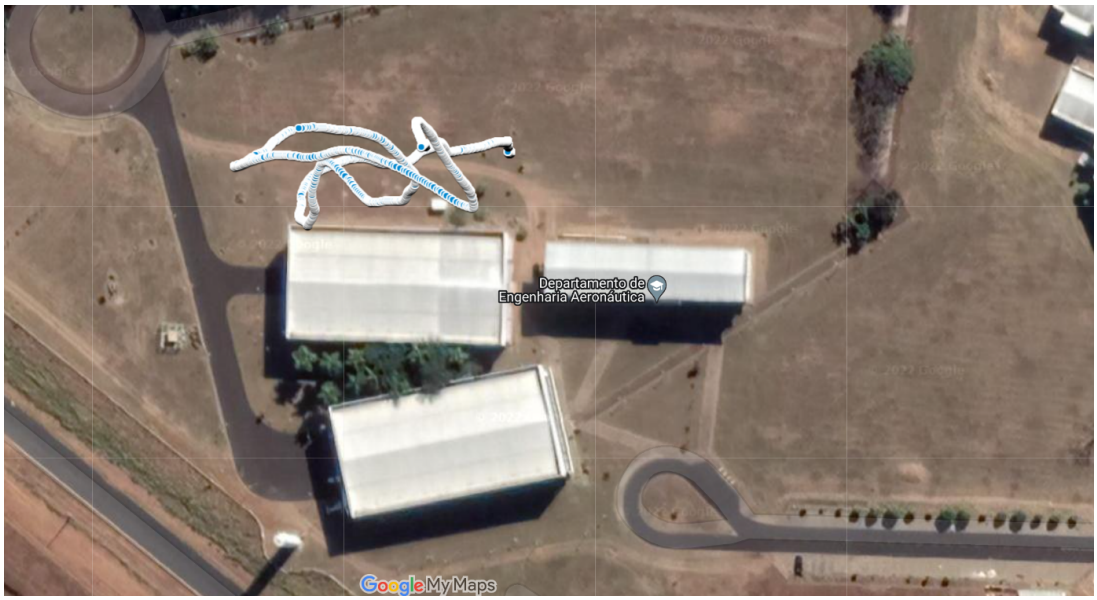

Figure 103 – Flight test, outdoor environment, aircraft trajectory in map.

10.3 Flight Test at Hovering Configuration, with Position Control and Transition Phase

At this stage of the project the aircraft had a crash with significant damage, therefore, the tests had to be interrupted for writing the thesis, repairing of the prototype and finalizing the project.

During a attitude plus altitude control test, the aircraft had a loss of attitude control, primarily in the yaw axis and consequently in roll and pitch axis, consequently the pilot lost control and turned off the motors during flight to avoid a serious accident. The possible causes of the loss of control might have been:

1. Low stiffness of the front motors supports, which may have twisted at a high load condition at the front propellers. So, a new and stiffer support for the front motors was manufactured.

2. The IMU's are positioned in the aircraft 'nose', together with the electronic systems integration board, therefore relatively far from the aircraft center of gravity, which is in the middle of the fuselage midway between the wing and front propellers at hovering configuration. Thus, it may not be measuring correctly the accelerations and angular velocities, mostly at inclined and oscillatory situations. So, a possible solution is to remove the IMU's from the integration board and install then at the base of the fuselage, much closer to the center of gravity.

11 CONCLUSIONS

This thesis presented a vertical take-off and landing unmanned aerial vehicle (VTOL UAV) configuration. It has the capacity to tilt the canard and wing along with two attached propellers. Additionally, there are two fixed front propellers pointing upwards. This configuration is somewhat a hybrid, or combination, between the tilt wing and lift plus cruise configurations, being that it may have the possibility for stable and controllable flight in any flight speed from hovering to horizontal flight in maximum speed.

A dynamic model for this configuration was derived using multi-body equations of motion, which was used to compute the transition trajectory, that is, the combination of states and controls that keep the aircraft in steady condition for the range of desired flight speeds (0 to 30 m/s). Also, a transition maneuver algorithm using gain-scheduled linear quadratic regulator (LQR) controller was developed in order to numerically simulate the transition flight from hover to cruise condition, and from cruise condition to hover. It's strategy is to switch between equilibrium states as the control system diminishes the state disturbances from the current equilibrium vector, as long as transition stability criteria threshold are satisfied. The numerical simulations showed that the model aircraft designed should have a smooth transition between flight speeds, with the exception of the situation where the wing is at its maximum lift coefficient. This movement from stalled wing at high angle of attack to tilt to a more horizontal and in the linear angle of attack range is the most critical of the transition maneuver, and makes the aircraft oscillate in attitude, altitude and even in the lateral directional flight states such as roll and yaw Euler angles and angular velocities, causing sideslip, which is a result of the gyroscopic moments. In order to have an accelerated transition the aircraft should keep a negative main body angle of attack in order to keep the front propellers thrust pointing upwards and forwards, whereas for the decelerated transition flight the aircraft main body should keep a positive angle of attack so that the front propellers points upwards and backwards, slowing down the vehicle.

An improvement of the mathematical model would be the inclusion of the blade element model similar to the modeling of helicopter rotors, applied mainly to the front propellers that are subject to situations of high angle of attack and horizontal flight speed. The very modification of the front propellers to helicopter rotors, with cyclic and collective control, by means of a swashplate, would be a substantial improvement.

Furthermore, an aircraft prototype of this configuration was built, being its airframe and on-board systems described, along with the microcontroller board, sensors, communication systems, actuators, motors, batteries and ground station.

In order to compute the flight states from the measurements provided by the on-board sensors, states estimation algorithms were derived using the discrete Kalman filter. The full algorithm can be divided in attitude discrete Kalman filter, altitude and vertical velocity discrete Kalman filter and position and horizontal velocity discrete Kalman filter, from which the full aircraft flight states can be derived.

Additionally, control algorithms to be applied in the aircraft were developed, mainly the hovering configuration attitude control, the hovering configuration attitude plus altitude control, the hovering configuration attitude plus altitude plus position control, and the transition control.

The on-board sensors readings, data handling, filtering, flight states estimation, radio inputs processing, control computations, telemetry data transmission and control signals outputs, are all actions to be performed by the vehicle microcontroller board through a embedded software, which were written in C programming language, and embedded in the on-board Arduino Due microcontroller board.

The systems were integrated in the aircraft prototype and flight tests were conducted in an indoor and outdoor environment. In the tests, flight data were effectively transmitted to the ground station which recorded the flight states time series for the hovering configuration using the attitude automatic control algorithm for both indoor and outdoor environments. The outdoor flight test lasted for 130 seconds and consumed 53% of the available propulsion batteries charge, therefore the autonomy of the prototype in the hovering configuration should be 245 seconds (4.0 minutes), which is low autonomy compared to quadcopters. This is because of the propulsion battery capacity rated at 5200 mmAh have in practice only 3000 mmAh. This configuration should be more efficient at higher flight speed, where the aircraft required power shall be much less, according to aircraft trim curves.

Moreover, it is reasonable that quadcopters are more efficient than this configuration considering only the hovering configuration, given that it has to carry the weight of the wing, canard, vertical tail, fuselage and tilting mechanisms that are not present in the quadcopters. Therefore, this configuration would be advantageous only in operations that require continuous forward flight speed.

During the hovering configuration outdoor flight tests the aircraft had a crash with significant damage, therefore, the tests had to be interrupted for writing the thesis, repairing of the prototype and finalizing the project. So, the hovering configuration with attitude plus altitude plus position control algorithm were not tested, as well as the flight transition algorithm.

The possible causes of the loss of attitude control were: low stiffness of the front motors supports, which may have twisted at a high load condition at the front propellers.

So, a new and stiffer support for the front motors was manufactured. And, the positioning of the on-board IMU's which are in the aircraft 'nose', therefore relatively far from the aircraft center of gravity, which is in the middle of the fuselage midway between the wing and front propellers at hovering configuration. Thus, it may not be measuring correctly the accelerations and angular velocities, mostly at inclined and oscillatory situations. So, a possible solution is to remove the IMU's from the integration board and install them at the base of the fuselage, much closer to the center of gravity.

Nonetheless, the author is committed to repairing the aircraft prototype and test the remaining flight control algorithms in the near future.

11.1 Contributions

As mentioned in section 1.2 the proposed VTOL vehicle configuration with tilt-wing along with propellers, tilt-canard and fixed upwards front propellers is in itself an important contribution of this thesis. The derivation of the dynamic model applicable for this configuration using multi-body equations of motion is also an important contribution. Moreover, the methodology and derivation of the equation of motion can be applied to air vehicles with tilting aerodynamic surfaces, as well as tilting rotating propellers.

The second contribution are the algorithms described to control the vehicle during transition flight from hovering to maximum horizontal speed, and from maximum horizontal speed to hovering condition, that is, both the methodology for calculating the sequence of equilibrium points as a function of flight speed, and the strategy to switch between reference states and controls, making use of cost functions that quantitatively represent the intensity of the disturbance in relation to the reference condition, in order to qualify if the aircraft is stable enough to continue the transition process, accelerating or decelerating the vehicle.

The numerical simulation results are also relevant contribution, where the flight states, controls and references are displayed in a time series for the complete flight transition process from hovering to maximum horizontal speed, and from maximum horizontal speed to hovering. This kind of results have not been presented this way in the literature so far, at least to the best of the author's knowledge.

The forth contribution are the prototype construction techniques for this kind of UAV described in the thesis, along with methodology to integrate the on-board systems, such as embedded sensors, microcontroller board, radio and telemetry system, motors and servos.

The last contribution are the prototype flight test results that not only showed the data measured by the on-board systems, as well as the perceived importance of the stiffness of motors supports for the vehicle control, and of sensors positioning in the vehicle

body, such as the Inertial Measurement Units (IMUs), which may have been causes of the crash of the prototype.

11.2 Suggestions for Future Works

The numerical simulations were performed using aerodynamic data estimated using the methods of (HOAK, 1960; HOERNER, 1965; HOUGHTON; CARPENTER, 2003), which can be validated via wind tunnel testing of the prototype, which is small enough to be tested full-size in a regular size wind tunnel. Furthermore, the propellers might have aerodynamic effects in the surfaces of the wing, canard and fuselage due to their wakes, which can be more properly measured in wind tunnels, or estimated via Computational Fluid Dynamics (CFD) simulations.

The propellers can be modeled using the blade element theory and vortex theory, which might have more precise results, especially for the front propellers, which operate most of the time at high angle of attack and horizontal flight speed. The very modification of the front propellers to helicopter rotors, with cyclic and collective control, by means of a swashplate, would be a substantial improvement to the vehicle configuration.

The positioning of the IMU's attached in the fuselage, close to vehicle center of gravity might result in better on-board measurements of the vehicle accelerations and angular velocities.

REFERENCES

APC. **APC Propellers Performance data**. 2022. Available at: http://https://www.apcprop.com/files/PER3_12x5.dat.

BACCHINI, A. *et al.* Impact of lift propeller drag on the performance of evtol lift+cruise aircraft. **Aerospace Science and Technology**, v. 109, p. 106429, 2021. ISSN 1270-9638. Available at: https://www.sciencedirect.com/science/article/pii/S1270963820311111.

BARRETO, J. *et al.* Drone-monitoring: Improving the detectability of threatened marine megafauna. **Drones**, v. 5, n. 1, 2021. ISSN 2504-446X. Available at: https://www.mdpi.com/2504-446X/5/1/14.

BENARBIA, T.; KYAMAKYA, K. A literature review of drone-based package delivery logistics systems and their implementation feasibility. **Sustainability**, MDPI, v. 14, n. 1, p. 360, 2021.

BENKHOUD, K.; BOUALL'EGUE, S. Modeling and lqg controller design for a quad tilt-wing uav. *In*: . [*S.l.: s.n.*], 2016.

BOLLARD, B. *et al.* Drone technology for monitoring protected areas in remote and fragile environments. **Drones**, v. 6, n. 2, 2022. ISSN 2504-446X. Available at: https://www.mdpi.com/2504-446X/6/2/42.

CARDOSO, D.; RAFFO, G.; ESTEBAN, S. Modeling and control of a tilt-rotor uav with improved forward flight. *In*: . [*S.l.: s.n.*], 2016.

CARON, F. *et al.* Gps/imu data fusion using multisensor kalman filtering: introduction of contextual aspects. **Information fusion**, Elsevier, v. 7, n. 2, p. 221–230, 2006.

CARUSO, M. J. Application of magnetoresistive sensors in navigation systems. *In*: CITESEER. **Sensors and Actuators, SAE SP-1220**. [*S.l.: s.n.*], 1997.

CETINSOY, E. *et al.* Design and construction of a novel quad tilt-wing uav. **Mechatronics**, v. 22, Issue 6, p. 723–745, 2012.

CZYBA, R. *et al.* Construction prototyping, flight dynamics modeling, and aerodynamic analysis of hybrid vtol unmanned aircraft. **Journal of Advanced Transportation**, Hindawi, v. 2018, 2018.

DAUD FILHO, A. C. **Flight Dynamics and Control Study of a VTOL UAV**. 2018. Dissertação (Mestrado) — São Carlos School of Engineering, University of São Paulo, São Carlos, 2018.

DAUD FILHO, A. C.; BELO, E. M. Flight dynamics modeling and trim curves of a conceptual semi-tandem wing vtol uav. *In*: **International Congress of the Aeronautical Sciences - ICAS**. [*S.l.: s.n.*]: ICAS, 2018.

DEIBE, Á. *et al.* A kalman filter for nonlinear attitude estimation using time variable matrices and quaternions. **Sensors**, MDPI, v. 20, n. 23, p. 6731, 2020.

DROANDI, G.; SYAL, M.; BOWER, G. Tiltwing multi-rotor aerodynamic modeling in hover, transition and cruise flight conditions. *In*: . [*S.l.: s.n.*], 2018.

ETKIN, B. **Dynamics of atmospheric flight**. [*S.l.: s.n.*]: Courier Corporation, 2012.

ETKIN, B.; REID, L. D. Dynamics of flight: Stability and control. *In*: _____. Third. [*S.l.: s.n.*]: John Wiley & Sons, Inc., 1996. p. 94–143.

EUSTON, M. *et al.* A complementary filter for attitude estimation of a fixed-wing uav. *In*: **2008 IEEE/RSJ International Conference on Intelligent Robots and Systems**. [*S.l.: s.n.*], 2008. p. 340–345.

FLAMMINI, F.; PRAGLIOLA, C.; SMARRA, G. Railway infrastructure monitoring by drones. *In*: . [*S.l.: s.n.*], 2016. p. 1–6.

FLORES, A.; OCA, A. M. de; FLORES, G. A simple controller for the transition maneuver of a tail-sitter drone. *In*: IEEE. **2018 IEEE Conference on Decision and Control (CDC)**. [*S.l.: s.n.*], 2018. p. 4277–4281.

FRANCO, G. D. *et al.* Modeling of actuators for uav control surfaces. *In*: ABCM. **19th International Congress of Mechanical Engineering**. [*S.l.: s.n.*], 2007.

FREDERICKS, W. J. *et al.* Greased lightning (gl-10) flight testing campaign. **Technical Memorandum NASA/TM-2017-219643, NASA**, 2017.

GREULICH, J. **Characterization and Identification of on-board servo motors using IMUs**. Freiburg: [*S.l.: s.n.*], 2016.

HAIXU, L.; XIANGJU, Q.; WEIJUN, W. Multi-body motion modeling and simulation for tilt rotor aircraft. **Chinese Journal of Aeronautics**, v. 23, Issue 4, p. 415–422, 2010.

HETéNYI, D.; GóTZY, M.; BLáZOVICS, L. Sensor fusion with enhanced kalman filter for altitude control of quadrotors. *In*: **2016 IEEE 11th International Symposium on Applied Computational Intelligence and Informatics (SACI)**. [*S.l.: s.n.*], 2016. p. 413–418.

HOAK, D. E. **USAF Stability and Control Datcom**. [*S.l.: s.n.*]: Air Force Flight Dynamics Laboratory, Wright-Patterson Air Force Base, Ohio, 1960.

HOERNER, S. F. **Fluid-Dynamic Drag: Practical Information on Aerodynamic Drag and Hydrodynamic Resistance**. [*S.l.: s.n.*]: Hoerner Fluid Dynamics, 1965.

HOUGHTON, E. L.; CARPENTER, P. W. **Aerodynamics for Engineering Students**. Fifth. [*S.l.: s.n.*]: Butterworth-Heinemann, 2003.

JURMAN, D. *et al.* Calibration and data fusion solution for the miniature attitude and heading reference system. **Sensors and Actuators A: Physical**, v. 138, n. 2, p. 411–420, 2007. ISSN 0924-4247. Available at: https://www.sciencedirect.com/science/article/pii/S0924424707003834.

KALMAN, R. E. A new approach to linear filtering and prediction problems. 1960.

KHAN, N. A. *et al.* Smart traffic monitoring system using unmanned aerial vehicles (uavs). **Computer Communications**, v. 157, p. 434–443, 2020. ISSN 0140-3664. Available at: https://www.sciencedirect.com/science/article/pii/S0140366420300189.

KULBACKI, M. *et al.* Survey of drones for agriculture automation from planting to harvest. *In*: **2018 IEEE 22nd International Conference on Intelligent Engineering Systems (INES)**. [*S.l.: s.n.*], 2018. p. 000353–000358.

KURKUTE, S. Drones for smart agriculture: A technical report. **International Journal for Research in Applied Science and Engineering Technology**, v. 6, p. 341–346, 04 2018.

LIU, D. *et al.* Preliminary virtual flight validation of a quad tilt rotor uav in wind tunnel. 2021.

LIU, Z. *et al.* Vtol uav transition maneuver using incremental nonlinear dynamic inversion. **International Journal of Aerospace Engineering**, Hindawi, v. 2018, 2018.

LIU, Z. *et al.* Control techniques of tilt rotor unmanned aerial vehicle systems: A review. **Chinese Journal of Aeronautics**, v. 30, n. 1, p. 135–148, 2017. ISSN 1000-9361. Available at: https://www.sciencedirect.com/science/article/pii/S1000936116302199.

LUQUE-VEGA, L. *et al.* Power line inspection via an unmanned aerial system based on the quadrotor helicopter. *In*: . [*S.l.: s.n.*], 2014. p. 393–397. ISBN 978-1-4799-2337-3.

LUSTOSA, L. R.; DEFAÿ, F.; MOSCHETTA, J.-M. Longitudinal study of a tilt-body vehicle: Modeling, control and stability analysis. *In*: **2015 International Conference on Unmanned Aircraft Systems (ICUAS)**. [*S.l.: s.n.*], 2015. p. 816–824.

MADGWICK, S. *et al.* An efficient orientation filter for inertial and inertial/magnetic sensor arrays. **Report x-io and University of Bristol (UK)**, v. 25, p. 113–118, 2010.

MAHONY, R.; HAMEL, T.; PFLIMLIN, J.-M. Nonlinear complementary filters on the special orthogonal group. **IEEE Transactions on Automatic Control**, v. 53, n. 5, p. 1203–1218, 2008.

MASAR, I.; STÖHR, E. Gain-scheduled lqr-control for an autonomous airship. *In*: **18th International Conference on Process Control**. [*S.l.: s.n.*], 2011. p. 14–17.

MASUDA, K.; UCHIYAMA, K. Robust control design for quad tilt-wing uav. **Aerospace**, v. 5, n. 1, 2018. ISSN 2226-4310. Available at: https://www.mdpi.com/2226-4310/5/1/17.

MATLAB. **R2018b**. Natick, Massachusetts: The MathWorks Inc., 2010.

MCSWAIN, R. G. *et al.* **Greased lightning (gl-10) performance flight research: Flight data report**. [*S.l.*], 2017.

MEIVEL, s. *et al.* Quadcopter uav based fertilizer and pesticide spraying system. *In*: . [*S.l.: s.n.*], 2016.

MERIAM, J. L.; KRAIGE, L. G. Engineering mechanics dynamics. *In*: _____. 7. ed. Hoboken, New Jersey: John Wiley & Sons, Inc., 2012. p. 5, 388.

MIKAMI, T.; UCHIYAMA, K. Design of flight control system for quad tilt-wing uav. *In*: **2015 International Conference on Unmanned Aircraft Systems (ICUAS)**. [*S.l.: s.n.*], 2015. p. 801–805.

MOGILI, U.; DEEPAK, B. Influence of drone rotors over droplet distribution in precision agriculture. 02 2021.

MURAOKA, K. *et al.* Transition flight of quad tilt wing vtol uav. *In*: **28th International Congress of the Aeronautical Sciences**. [*S.l.: s.n.*], 2012. p. 2012–11.

NARKHEDE, P. *et al.* Cascaded complementary filter architecture for sensor fusion in attitude estimation. **Sensors**, MDPI, v. 21, n. 6, p. 1937, 2021.

NELDER, J. A.; MEAD, R. A simplex method for function minimization. **Comput. J.**, v. 7, p. 308–313, 1965.

NEX, F.; REMONDINO, F. Uav for 3d mapping applications: A review. **Applied Geomatics**, v. 6, 03 2014.

NOORALISHAHI, P.; LóPEZ, F.; MALDAGUE, X. A drone-enabled approach for gas leak detection using optical flow analysis. **Applied Sciences**, v. 11, p. 1412, 02 2021.

OGATA, K. **Modern Control Engineering**. Fifth. [*S.l.: s.n.*]: Prentice Hall, 2010.

ÖNER, K. T. *et al.* Dynamic model and control of a new quadrotor unmanned aerial vehicle with tilt-wing mechanism. WASET (World Academy of Science, Engineering and Technology), 2008.

PAPACHRISTOS, C.; ALEXIS, K.; TZES, A. Design and experimental attitude control of an unmanned tilt-rotor aerial vehicle. *In*: **2011 15th International Conference on Advanced Robotics (ICAR)**. [*S.l.: s.n.*], 2011. p. 465–470.

PENG, K. *et al.* Design and implementation of an autonomous flight control law for a uav helicopter. **Automatica**, v. 45, n. 10, p. 2333–2338, 2009. ISSN 0005-1098. Available at: https://www.sciencedirect.com/science/article/pii/S0005109809003082.

QUAN, Q. **Introduction to multicopter design and control**. [*S.l.: s.n.*]: Springer, 2017.

RADOTICH, M. T. **Conceptual Design of Two Tiltrotor Aircraft for Urban Air Mobility**. [*S.l.: s.n.*]: University of Alaska Fairbanks, 2021.

RAJAMANI, M. R. **Data-based techniques to improve state estimation in model predictive control**. 2007. Tese (Doutorado) — Citeseer, 2007.

REMONDINO, F. *et al.* Uav photogrammetry for mapping and 3d modeling-current status and future perspectives. *In*: . [*S.l.: s.n.*], 2011. XXXVIII-1/C22.

ROSKAM, J. Airplane flight dynamics and automatic flight controls, part i. *In*: _____. Lawrence, KS: Design, Analysis and Research Corporation (DARcorporation), 2001. p. 3–34.

SIMMONS, B. M.; MURPHY, P. C. Aero-propulsive modeling for tilt-wing, distributed propulsion aircraft using wind tunnel data. **Journal of Aircraft**, American Institute of Aeronautics and Astronautics, p. 1–17, 2022.

SOBIESIAK, L. A. *et al.* Modelling and control of transition flight of an evtol tandem tilt-wing aircraft. *In*: **8th European Conference for Aeronautics and Aerospace Sciences (EUCASS)**. [*S.l.: s.n.*], 2019. p. 2019–7.

SOCIETY, T. V. F. **eVTOL Aircraft Directory**. 2022. Available at: https://evtol.news/aircraft.

SONKAR, S. *et al.* Real-time object detection and recognition using fixed-wing lale vtol uav. **IEEE Sensors Journal**, IEEE, 2022.

STEVENS, B. L.; LEWIS, F. L.; JOHNSON, E. N. **Aircraft control and simulation: dynamics, controls design, and autonomous systems**. [*S.l.: s.n.*]: John Wiley & Sons, 2015.

STEVENS, B. L.; LEWIS, F. L.; JOHNSON, E. N. **Aircraft Control and Simulation**. Third. [*S.l.: s.n.*]: John Wiley & Sons, Inc., 2016.

SU, J. *et al.* A multibody model of tilt-rotor aircraft based on kaneâ€™s method. **International Journal of Aerospace Engineering**, v. 2019, p. 1–10, 04 2019.

SUKKARIEH, S.; NEBOT, E.; DURRANT-WHYTE, H. A high integrity imu/gps navigation loop for autonomous land vehicle applications. **IEEE Transactions on Robotics and Automation**, v. 15, n. 3, p. 572–578, 1999.

TA, D. A.; FANTONI, I.; LOZANO, R. Modeling and control of a tilt tri-rotor airplane. *In*: **2012 American Control Conference (ACC)**. [*S.l.: s.n.*], 2012. p. 131–136.

TANG, C. P. Lagrangian dynamic formulation of a four-bar mechanism with minimal coordinates. *In*: . [*S.l.: s.n.*], 2010.

WAHDAN, A. *et al.* Magnetometer calibration for portable navigation devices in vehicles using a fast and autonomous technique. **IEEE Transactions on Intelligent Transportation Systems**, v. 15, n. 5, p. 2347–2352, 2014.

WALPOLE, R. E. *et al.* **Probability & statistics for engineers and scientists**. 8th. ed. Upper Saddle River: Pearson Education, 2007.

WALTERS, F. H. *et al.* **Sequential Simplex Optimization**. [*S.l.: s.n.*]: CRC Press LLC, 1991.

WELCH, G.; BISHOP, G. **An Introduction to the Kalman Filter**. USA, 1995.

YANG, X.; MEJIAS, L.; MOLLOY, T. Nonlinear h-infinity control of uavs for collision avoidance in gusty environments. **Journal of Intelligent and Robotic Systems**, v. 69, 08 2013.

ZHAO, W.; UNDERWOOD, C. Robust transition control of a martian coaxial tiltrotor aerobot. **Acta Astronautica**, v. 99, p. 111–129, 2014. ISSN 0094-5765. Available at: https://www.sciencedirect.com/science/article/pii/S0094576514000770.

APPENDIX

APPENDIX A – AERODYNAMIC DATA

In this Appendix the aerodynamic data of the fuselage, wing and canard, and the aerodynamic coefficients and derivatives of the transition trajectory, of the conceptual aircraft used in the simulations are displayed.

The wing and canard have constant chord Naca 0012 airfoils.

A.1 Fuselage Aerodynamic Data

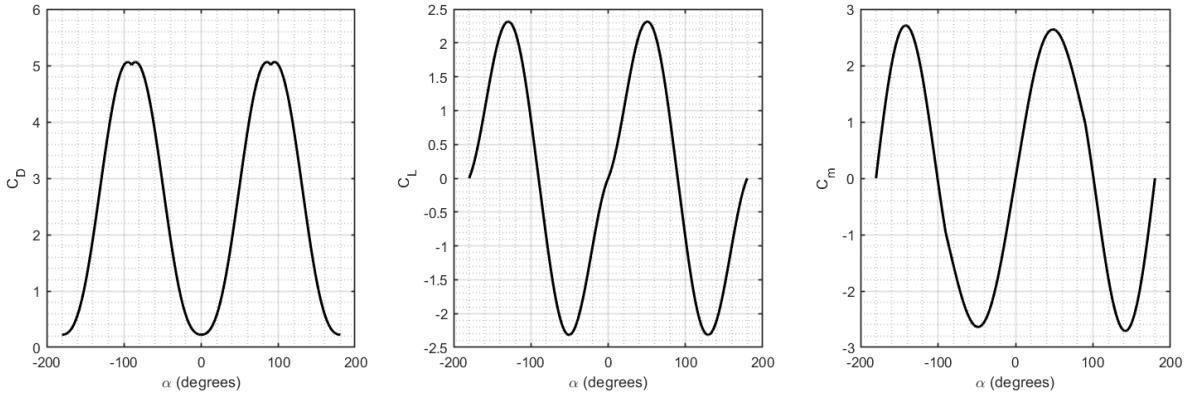

Figure 104 – Aircraft fuselage (main body) drag, lift and aerodynamic pitch moment coefficients.

A.2 Wing Aerodynamic Data

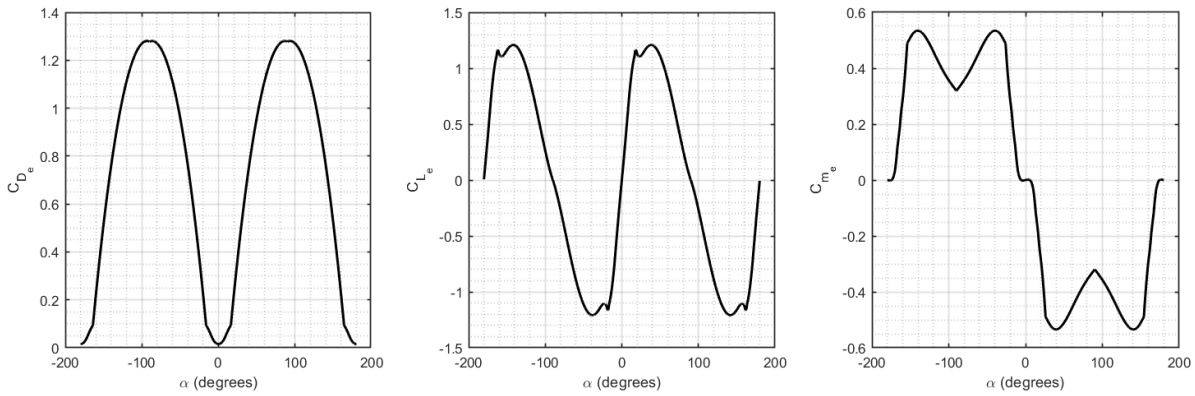

Figure 105 – Aircraft exposed wing drag, lift and aerodynamic pitch moment coefficients.

A.3 Canard Aerodynamic Data

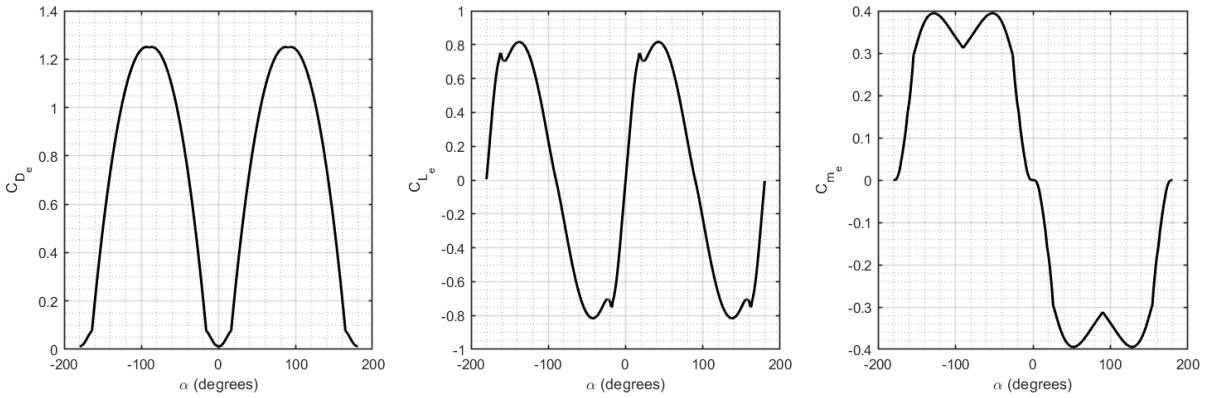

Figure 106 – Aircraft exposed canard drag, lift and aerodynamic pitch moment coefficients.

A.4 Aerodynamic Longitudinal Derivatives at Transition Trajectory

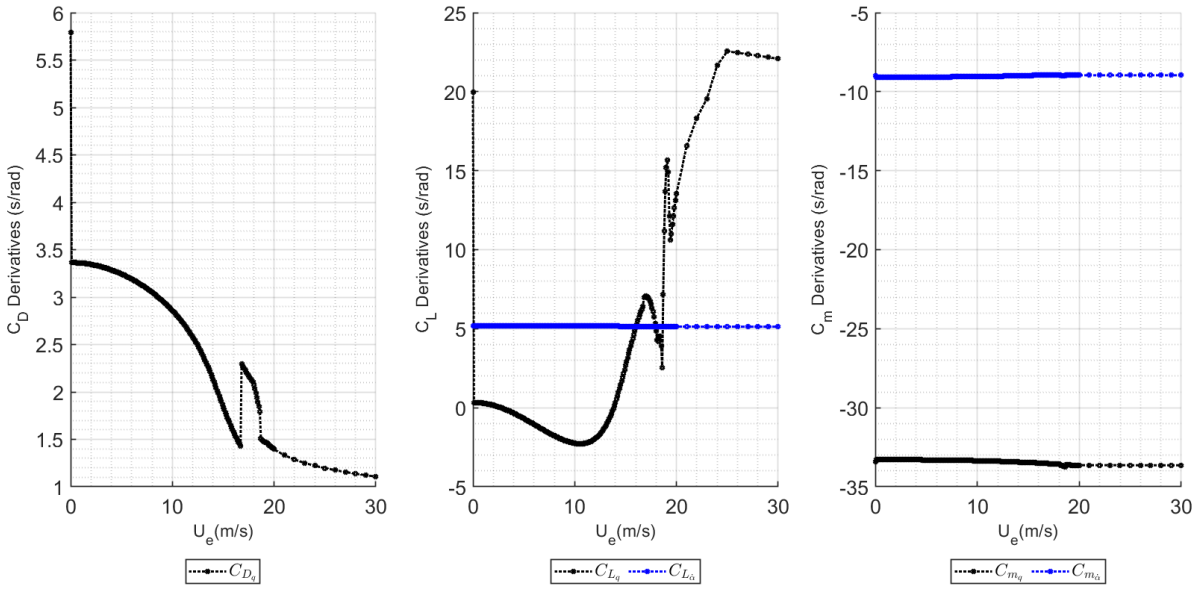

Figure 107 – Aerodynamic longitudinal derivatives at transition trajectory.

A.5 Aerodynamic Lateral Derivatives at Transition Trajectory

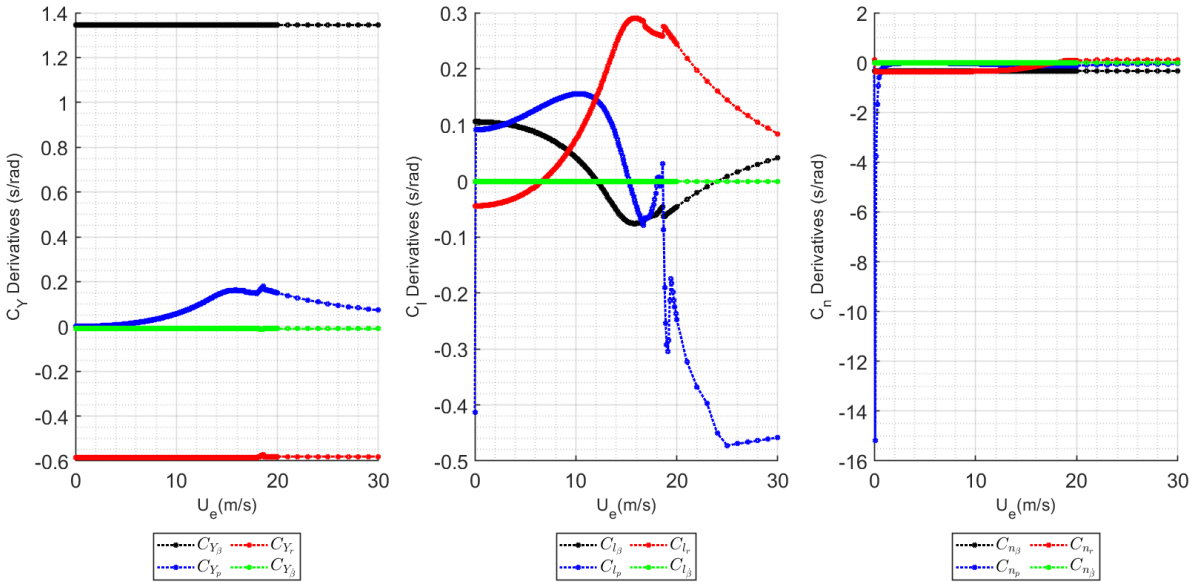

Figure 108 – Aerodynamic lateral derivatives at transition trajectory.

A.6 Aerodynamic Control Derivatives at Transition Trajectory

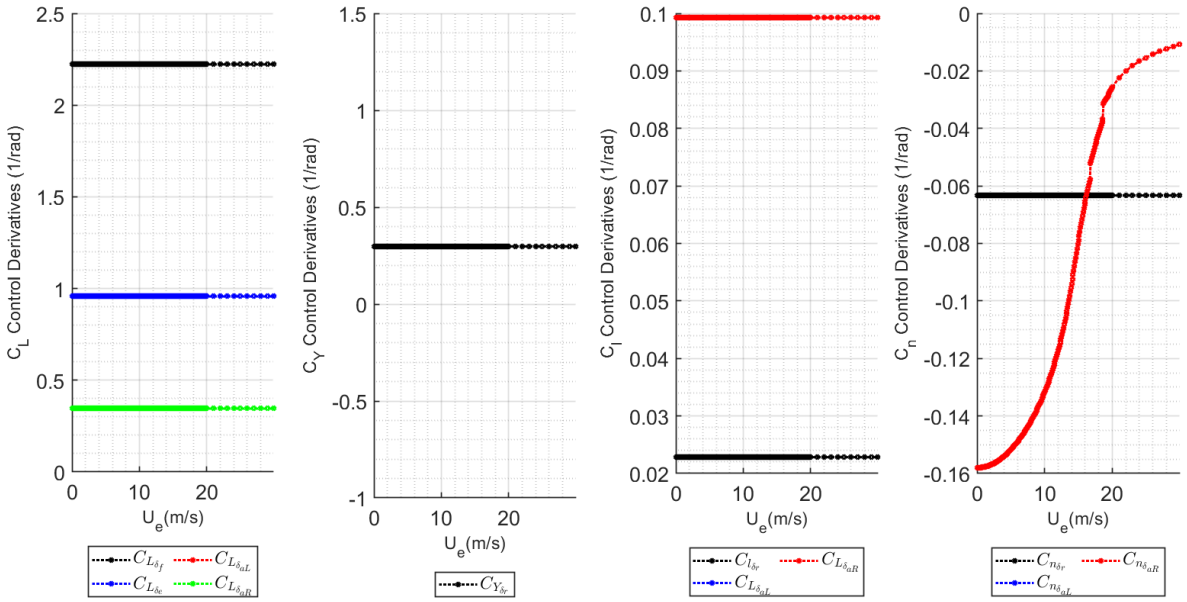

Figure 109 – Aerodynamic control derivatives at transition trajectory.

APPENDIX B – LATERAL STABILITY SIMULATIONS

Results of lateral dynamics simulation from an initial disturbance of 5° in roll angle at staring condition of reference flight speed reference U_e of 0, 7.5, 15, 22 and 30 m/s. Simulation of 30 seconds.

B.1 Starting at reference flight speed $U_e = 0\,m/s$, initial disturbance of 5° in roll angle.

In Figure 110 there are flight states dynamic response from an initial 5° disturbance in roll angle at hover condition $U_e = 0\,m/s$, and 30 seconds of simulation. In Figure 111 the controls.

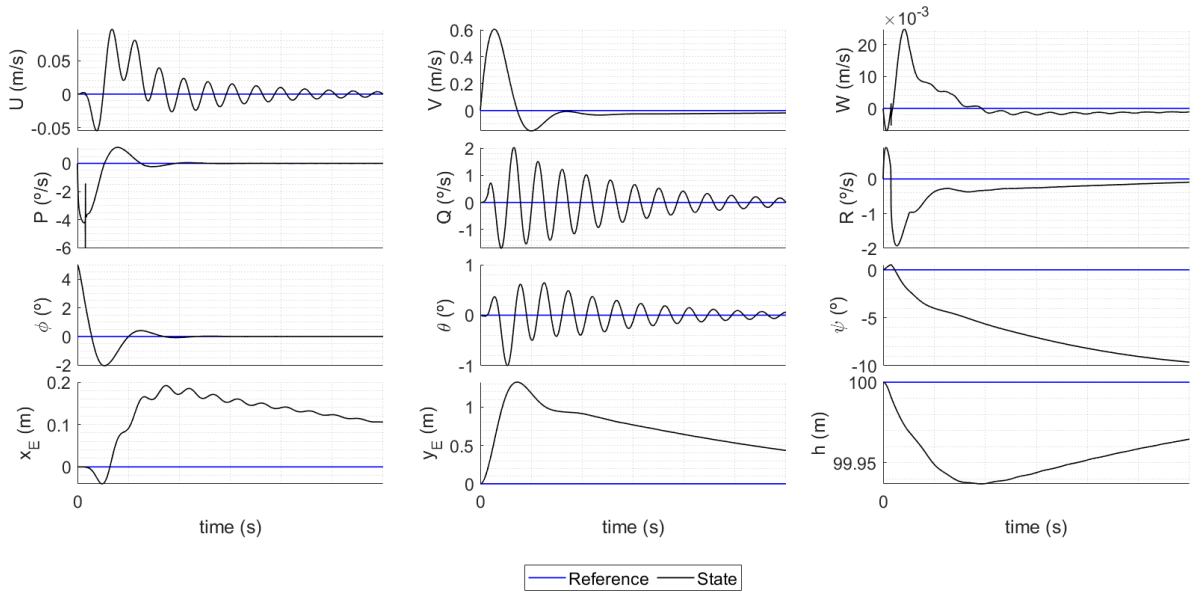

Figure 110 – Simulation lateral stability, flight states from 5° disturbance in roll angle (ϕ) at reference velocity $U_e = 0\,m/s$.

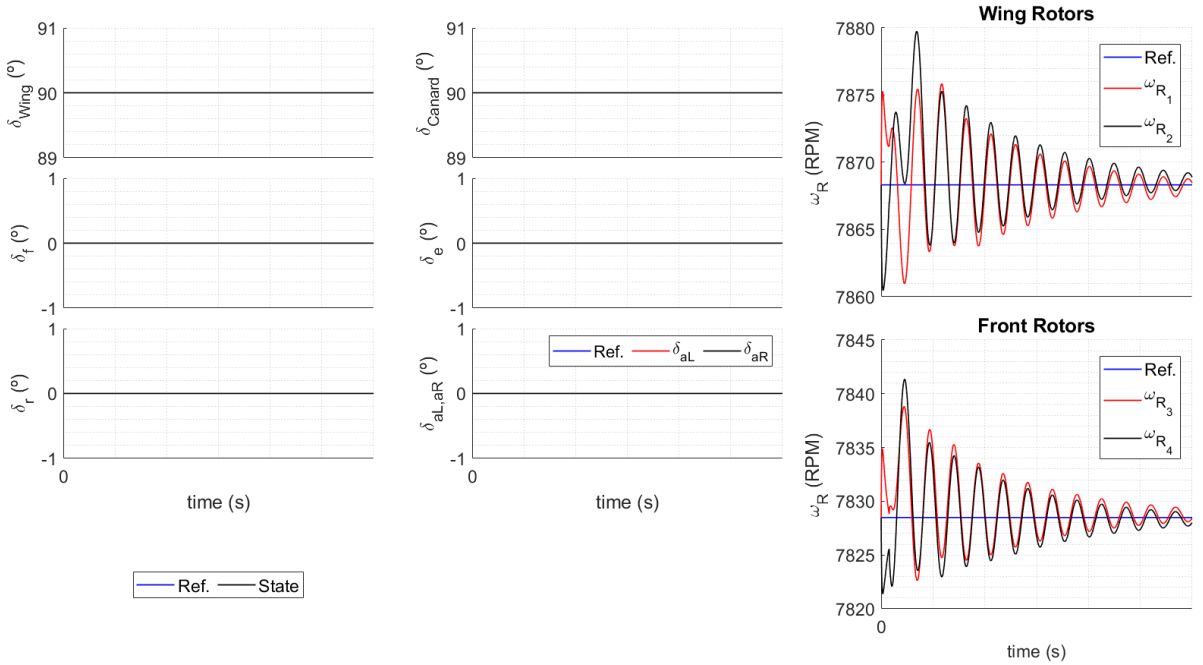

Figure 111 – Simulation lateral stability, controls from 5° disturbance in roll angle (ϕ) at reference velocity $U_e = 0\,m/s$.

B.2 Starting at reference flight speed $U_e = 7.5\,m/s$, initial disturbance of 5° in roll angle.

In Figure 112 there are flight states dynamic response from an initial 5° disturbance in roll angle at hover condition $U_e = 7.5\,m/s$, and 30 seconds of simulation. In Figure 113 the controls.

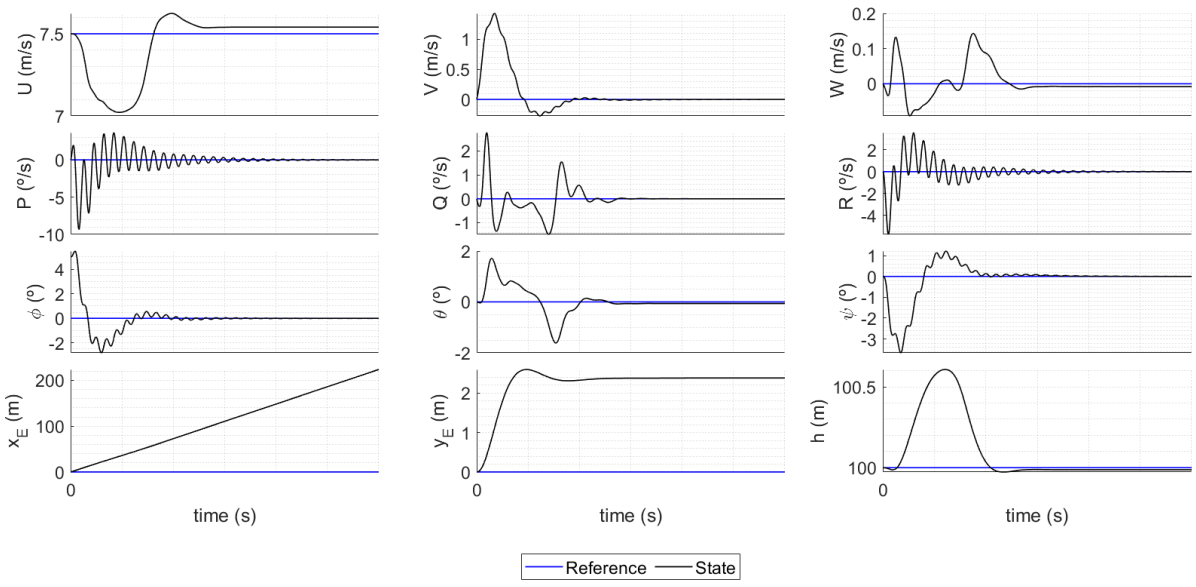

Figure 112 – Simulation lateral stability, flight states from 5° disturbance in roll angle (ϕ) at reference velocity $U_e = 7.5\,m/s$.

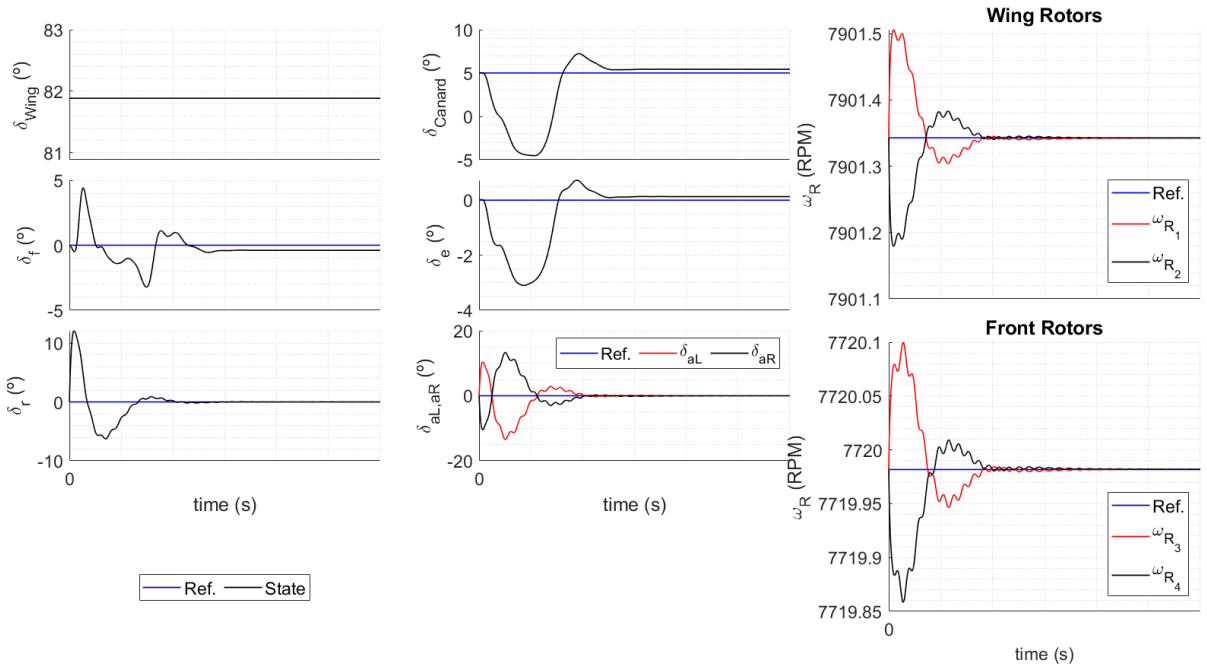

Figure 113 – Simulation lateral stability, controls from 5° disturbance in roll angle (ϕ) at reference velocity $U_e = 7.5\,m/s$.

B.3 Starting at reference flight speed $U_e = 15\,m/s$, initial disturbance of 5° in roll angle.

In Figure 114 there are flight states dynamic response from an initial 5° disturbance in roll angle at hover condition $U_e = 15\,m/s$, and 30 seconds of simulation. In Figure 115 the controls.

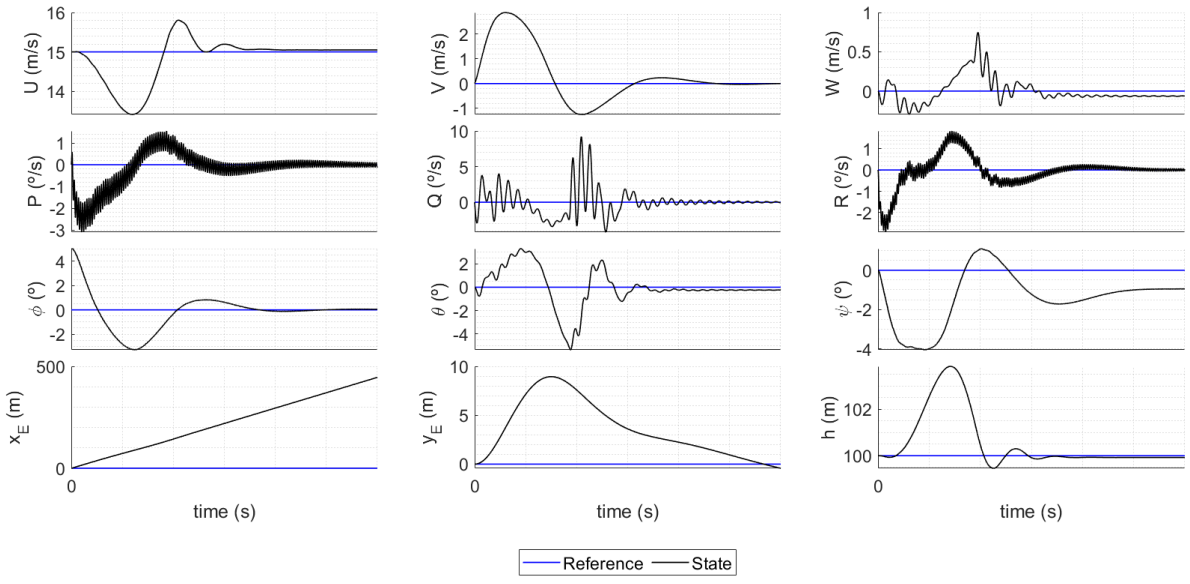

Figure 114 – Simulation lateral stability, flight states from 5° disturbance in roll angle (ϕ) at reference velocity $U_e = 15\,m/s$.

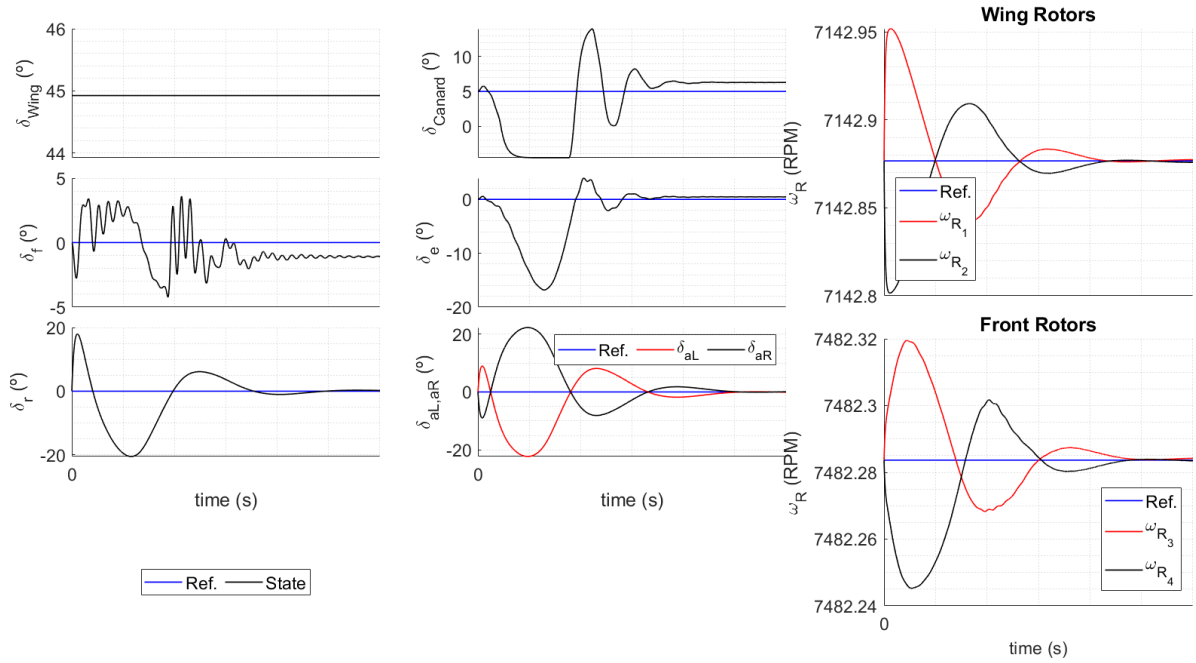

Figure 115 – Simulation lateral stability, controls from 5° disturbance in roll angle (ϕ) at reference velocity $U_e = 15\,m/s$.

B.4 Starting at reference flight speed $U_e = 22\,m/s$, initial disturbance of 5° in roll angle.

In Figure 116 there are flight states dynamic response from an initial 5° disturbance in roll angle at hover condition $U_e = 22\,m/s$, and 30 seconds of simulation. In Figure 117 the controls.

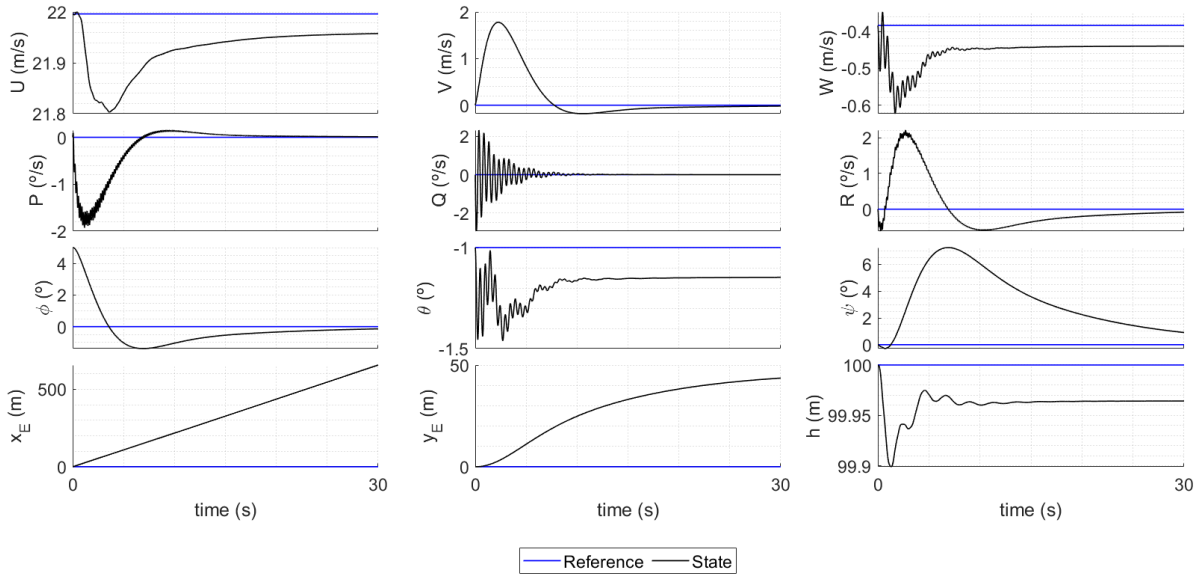

Figure 116 – Simulation lateral stability, flight states from 5° disturbance in roll angle (ϕ) at reference velocity $U_e = 22\,m/s$.

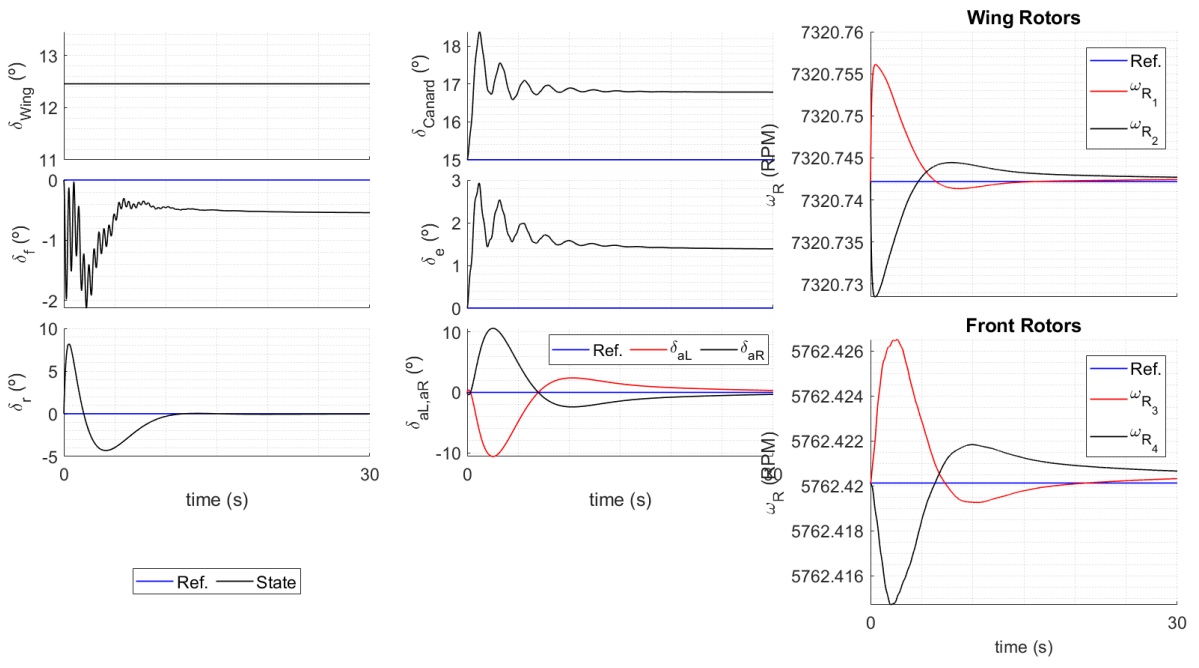

Figure 117 – Simulation lateral stability, controls from 5° disturbance in roll angle (ϕ) at reference velocity $U_e = 22\,m/s$.

B.5 Starting at reference flight speed $U_e = 30\,m/s$, initial disturbance of 5° in roll angle.

In Figure 118 there are flight states dynamic response from an initial 5° disturbance in roll angle at hover condition $U_e = 30\,m/s$, and 30 seconds of simulation. In Figure 119 the controls.

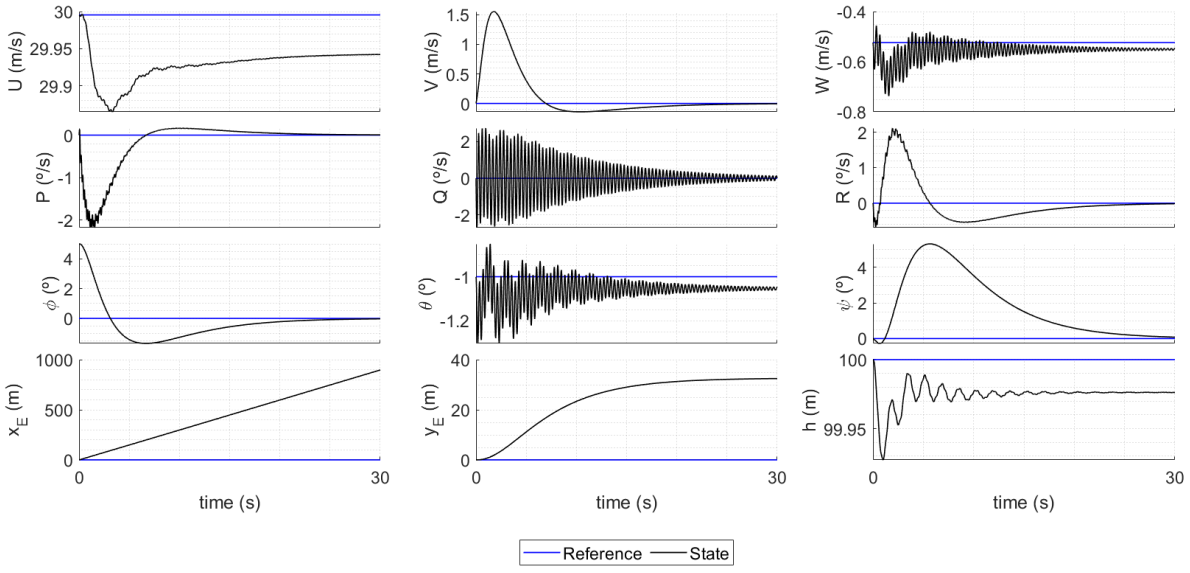

Figure 118 – Simulation lateral stability, flight states from 5° disturbance in roll angle (ϕ) at reference velocity $U_e = 30\,m/s$.

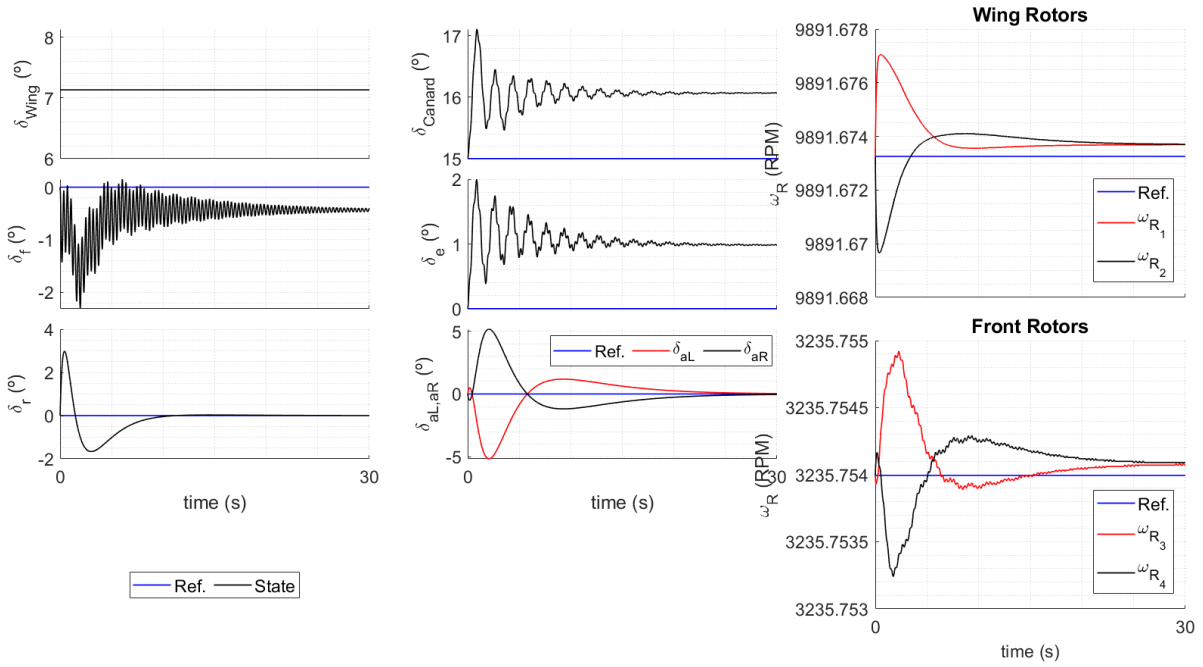

Figure 119 – Simulation lateral stability, controls from 5° disturbance in roll angle (ϕ) at reference velocity $U_e = 30\,m/s$.

APPENDIX C – SIMULATION CONTROLLER GAINS

In this Appendix are shown the controller gains used in the simulations. The gains are the terms of the longitudinal and lateral gain matrices, that result from the Linear Quadratic Regulator theory applied at the equilibrium condition.

The gain matrices are applied according to Eq.(C.1) and Eq.(C.2), being that, the equations are expanded in Eq.(C.3) and Eq.(C.4) respectively.

Therefore, the terms of the matrices are expressed in graphic form in Figure 120, Figure 121, Figure 122 and Figure 123 for the range of reference flight speed U_e applied in the simulations.

$$\mathbf{u}_{long} = -K_{long}\mathbf{x}_{long} \tag{C.1}$$

$$\mathbf{u}_{lat} = -K_{lat}\mathbf{x}_{lat} \tag{C.2}$$

$$\begin{bmatrix} u_{\delta_f} \\ u_{\delta_e} \\ u_{\delta_c} \\ u_{\omega_{R_1}} \\ u_{\omega_{R_2}} \\ u_{\omega_{R_3}} \\ u_{\omega_{R_4}} \end{bmatrix} = - \begin{bmatrix} k_{u_{\delta_f}} & k_{w_{\delta_f}} & k_{q_{\delta_f}} & k_{\theta_{\delta_f}} & k_{h_{\delta_f}} \\ k_{u_{\delta_e}} & k_{w_{\delta_e}} & k_{q_{\delta_e}} & k_{\theta_{\delta_e}} & k_{h_{\delta_e}} \\ k_{u_{\delta_c}} & k_{w_{\delta_c}} & k_{q_{\delta_c}} & k_{\theta_{\delta_c}} & k_{h_{\delta_c}} \\ k_{u_{\omega_{R_1}}} & k_{w_{\omega_{R_1}}} & k_{q_{\omega_{R_1}}} & k_{\theta_{\omega_{R_1}}} & k_{h_{\omega_{R_1}}} \\ k_{u_{\omega_{R_2}}} & k_{w_{\omega_{R_2}}} & k_{q_{\omega_{R_2}}} & k_{\theta_{\omega_{R_2}}} & k_{h_{\omega_{R_2}}} \\ k_{u_{\omega_{R_3}}} & k_{w_{\omega_{R_3}}} & k_{q_{\omega_{R_3}}} & k_{\theta_{\omega_{R_3}}} & k_{h_{\omega_{R_3}}} \\ k_{u_{\omega_{R_4}}} & k_{w_{\omega_{R_4}}} & k_{q_{\omega_{R_4}}} & k_{\theta_{\omega_{R_4}}} & k_{h_{\omega_{R_4}}} \end{bmatrix} \begin{bmatrix} u \\ w \\ q \\ \theta \\ h \end{bmatrix} \tag{C.3}$$

$$\begin{bmatrix} u_{\delta_r} \\ u_{\delta_{aL}} \\ u_{\delta_{aR}} \\ u_{\omega_{R_1}} \\ u_{\omega_{R_2}} \\ u_{\omega_{R_3}} \\ u_{\omega_{R_4}} \end{bmatrix} = - \begin{bmatrix} k_{u_{\delta_r}} & k_{v_{\delta_r}} & k_{p_{\delta_r}} & k_{r_{\delta_r}} & k_{\phi_{\delta_r}} & k_{\psi_{\delta_r}} \\ k_{u_{\delta_{aL}}} & k_{v_{\delta_{aL}}} & k_{p_{\delta_{aL}}} & k_{r_{\delta_{aL}}} & k_{\phi_{\delta_{aL}}} & k_{\psi_{\delta_{aL}}} \\ k_{u_{\delta_{aR}}} & k_{v_{\delta_{aR}}} & k_{p_{\delta_{aR}}} & k_{r_{\delta_{aR}}} & k_{\phi_{\delta_{aR}}} & k_{\psi_{\delta_{aR}}} \\ k_{u_{\omega_{R_1}}} & k_{v_{\omega_{R_1}}} & k_{p_{\omega_{R_1}}} & k_{r_{\omega_{R_1}}} & k_{\phi_{\omega_{R_1}}} & k_{\psi_{\omega_{R_1}}} \\ k_{u_{\omega_{R_2}}} & k_{v_{\omega_{R_2}}} & k_{p_{\omega_{R_2}}} & k_{r_{\omega_{R_2}}} & k_{\phi_{\omega_{R_2}}} & k_{\psi_{\omega_{R_2}}} \\ k_{u_{\omega_{R_3}}} & k_{v_{\omega_{R_3}}} & k_{p_{\omega_{R_3}}} & k_{r_{\omega_{R_3}}} & k_{\phi_{\omega_{R_3}}} & k_{\psi_{\omega_{R_3}}} \\ k_{u_{\omega_{R_4}}} & k_{v_{\omega_{R_4}}} & k_{p_{\omega_{R_4}}} & k_{r_{\omega_{R_4}}} & k_{\phi_{\omega_{R_4}}} & k_{\psi_{\omega_{R_4}}} \end{bmatrix} \begin{bmatrix} u \\ v \\ p \\ r \\ \phi \\ \psi \end{bmatrix} \tag{C.4}$$

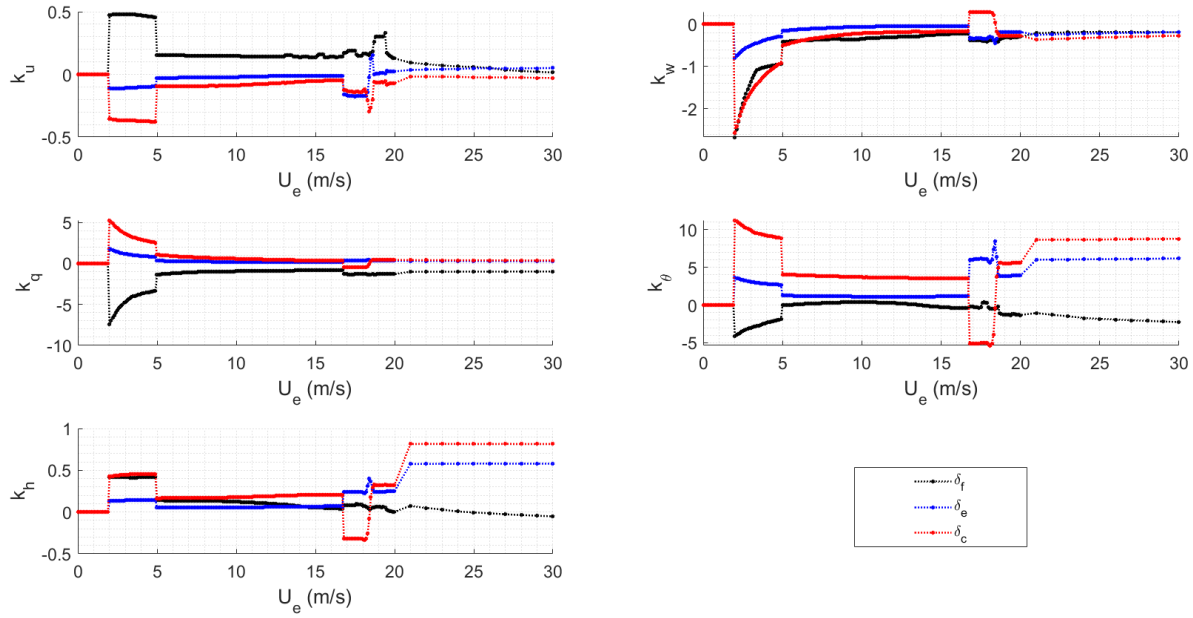

Figure 120 – Simulation controller gains, longitudinal system, aerodynamic controls.

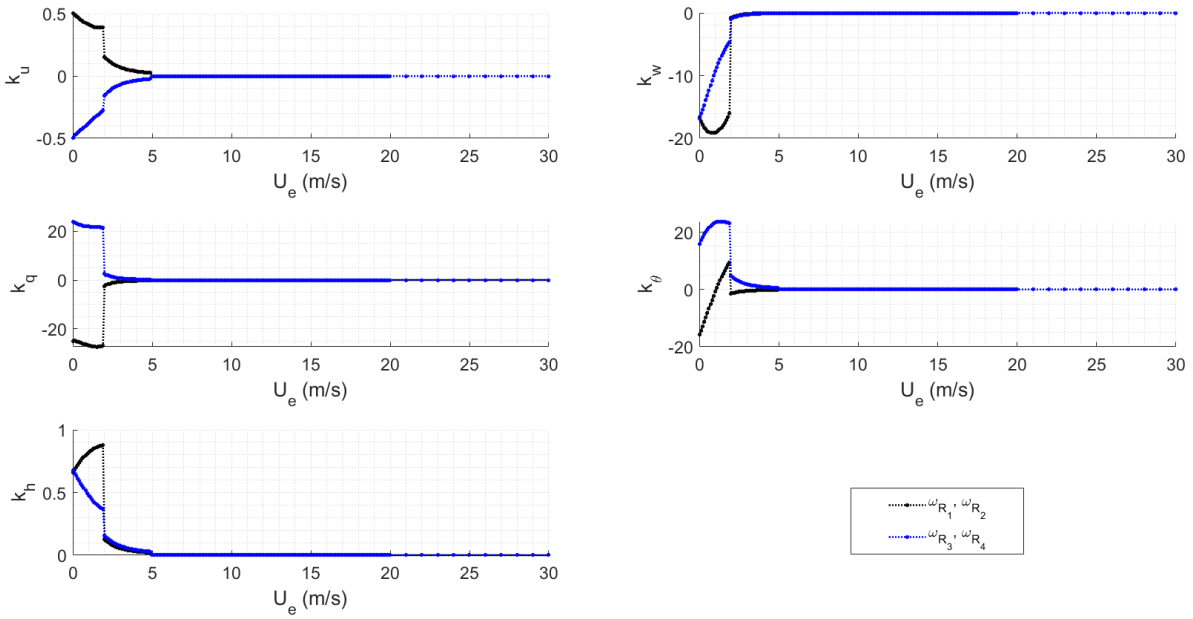

Figure 121 – Simulation controller gains, longitudinal system, propellers.

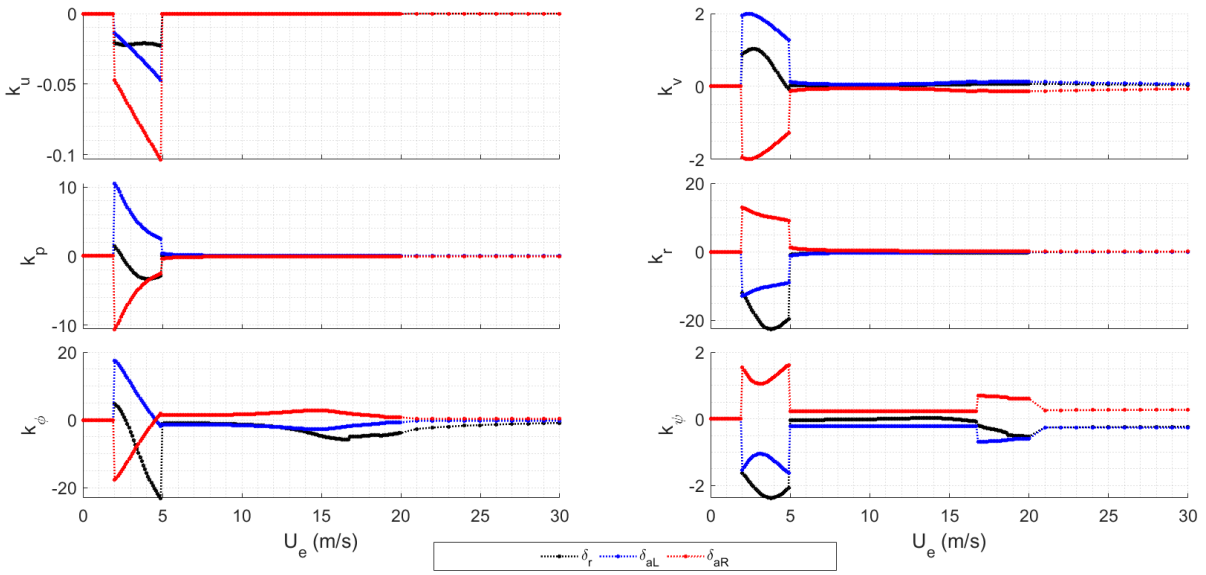

Figure 122 – Simulation controller gains, lateral directional system, aerodynamic controls.

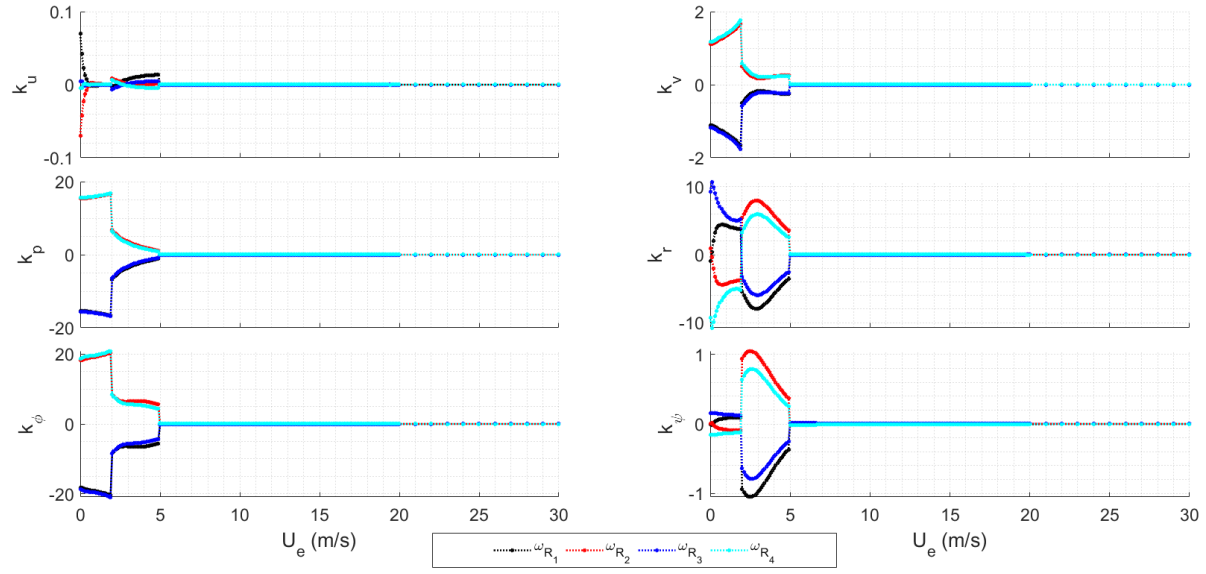

Figure 123 – Simulation controller gains, lateral directional system, propellers.

APPENDIX D – FLIGHT TESTS EMBEDDED SOFTWARE PARAMETERS

In this Appendix are shown the parameters used in the aircraft prototype embedded control software.

Table 36 – Control Gains

Axis	k_P	k_I	k_D	$PID_{max}(\mu s)$	$P_{max}(\mu s)$	$I_{max}(\mu s)$
roll (ϕ)	0.5	0	12	350	-	0
pitch (θ)	0.6	0	12	350	-	0
yaw (ψ)	4.0	0.01	12	300	-	100
height (h)	12	0	24	25	15	0

Table 37 – Control Parameters

$k_1(\phi)$	16.4 $\mu s/°$
$k_1(\theta)$	16.4 $\mu s/°$
$k_2(\phi)$	3.0 $\mu s.s/°$
$k_2(\theta)$	3.0 $\mu s.s/°$
$k_2(\psi)$	3.0 $\mu s.s/°$
$\phi_{desired_{max}}$	30 °
$\theta_{desired_{max}}$	30 °
$\Delta Throttle_{lean_{max}}$	20 μs

Table 38 – Angular velocities discrete Kalman filter parameters

Q_{ω_x}	1	$P_{0_{\omega_x}}$	1
Q_{ω_y}	1	$P_{0_{\omega_y}}$	1
Q_{ω_z}	1	$P_{0_{\omega_z}}$	1

The attitude discrete Kalman filter uses the following Eq. (D.1) to start the state uncertainty covariance.

$$P_0 = \begin{bmatrix} 1 & 0 & 0 \\ 0 & 1 & 0 \\ 0 & 0 & 1 \end{bmatrix} \tag{D.1}$$

The altitude and position discrete Kalman filter uses the following Eq. (D.2) to start the state uncertainty covariance.

$$P_0 = \begin{bmatrix} 1 & 0 \\ 0 & 1 \end{bmatrix} \tag{D.2}$$